RESEARCH TRIANGLE INSTITUTE

4378-1009-F

NASA CR-145307

CONTINUED INVESTIGATION OF POTENTIAL APPLICATION OF OMEGA NAVIGATION TO CIVIL AVIATION

by

Ernest G. Baxa, Jr.

Research Triangle Institute
Research Triangle Park, NC 27709

Contract NAS1-13290

March 1978

NASA

National Aeronautics and Space Administration

Langley Research Center
Hampton, Virginia 23665

RESEARCH TRIANGLE PARK, NORTH CAROLINA 27709

ACKNOWLEDGEMENTS

This report was prepared by the Research Triangle Institute, Research Triangle Park, North Carolina, under contract NAS1-13290. The work is being administered by the Electromagnetics Research Branch of the Flight Electronics Division, Langley Research Center.

This report describes results of evaluation studies of the OMEGA navigation system and its potential application for airborne use. The Research Triangle Institute has worked closely with Mr. C. D. Lytle, Mr. E.S. Bradshaw and Mr. E. M. Bracalente of the Electromagnetics Research Branch under the direction of Mr. J. H. Schrader. Computer programming support has been provided by personnel of the LTV Aerospace Corporation under contract to NASA at Langley Research Center and assigned to this project. This report is intended to present the results of the efforts of the various organizations involved with the total program.

RTI staff members participating in this study are as follows:

E. G. Baxa, Jr., Project Leader
C. L. Britt, Jr. Laboratory Supervisor
K. W. Leland, Engineer
S. L. Wheelock, Mathematician
M. E. Gordon, Research Assistant and Secretary
A. B. Murray, Scientific Programmer

Page
Intentionally
Left Blank

"Page missing from available version"

TABLE OF CONTENTS

Page
Intentionally
Left Blank

"Page missing from available version"

LIST OF ILLUSTRATIONS

LIST OF ILLUSTRATIONS
(Continued)

LIST OF ILLUSTRATIONS
(Continued)

LIST OF ILLUSTRATIONS
(Continued)

LIST OF ILLUSTRATIONS
(Continued)

LIST OF ILLUSTRATIONS
(Continued)

LIST OF TABLES

Page
Intentionally
Left Blank

ABSTRACT

This final report under Contract NAS1-13290 documents work done in support of a NASA program designed to evaluate the utility of the OMEGA navigation system. With support from the Research Triangle Institute, NASA personnel at the Langley Research Center began an extensive experimental program in 1973. Particular emphasis was placed on collecting statistically significant quantities of OMEGA data to determine through analysis the achievable accuracies with the differential and composite modes of operation and to define the major contributing factors to differential OMEGA error. One objective of this study has been to investigate the potential application of OMEGA navigation to civil aviation use. This report is the conclusion of the analysis from which preliminary results were presented in an earlier final report prepared under Contract NAS1-12043.

Major attention in this report is given to an analysis of receiver repeatability in measuring OMEGA phase data. In this work, repeatability is defined as the ability of two like receivers which are co-located to achieve the same LOP phase readings. In the context of differential OMEGA this limits the achievable position error. In an early phase of the experimental program, modal interference of the North Dakota OMEGA signal caused extremely large differential errors, particularly during nighttime hours. Specific data analysis is presented in this report in support of this conclusion. A propagation model is described which has been used in the analysis of propagation anomalies. Composite OMEGA analysis is presented in terms of carrier phase correlation analysis and the determination of carrier phase weighting coefficients for minimizing composite phase variation. Differential OMEGA error analysis is presented for receiver separations of up to 600 n.mi. Three frequency analysis includes LOP error and position error based on three and four OMEGA transmissions. Finally, results of phase-amplitude correlation studies are presented.

CHAPTER 1

INTRODUCTION

Since 1972 the NASA Langley Research Center at Hampton, Virginia has been involved with an investigation of the OMEGA navigation system. This investigation has been designed to determine applicability of the system for general aviation use. An experimental program involving collection of OMEGA data and subsequent analysis was initiated in September 1973. OMEGA data were recorded according to this plan through 1975. The Research Triangle Institute has supported this NASA program under a previous contract, NAS1-12043 (ref. 1), and under this current contract, NAS1-13290. Associated work involving development and analysis of navigation accuracies using a feasibility model of a low-cost general aviation airborne OMEGA processor is currently supported by RTI under contract NAS1-14005 (ref. 2).

This report serves to provide a comprehensive analysis of OMEGA position estimate errors considering various modes of operation using data recorded by NASA personnel. Analysis of receiver system errors are also included. Propagation anomalies, including particular emphasis on inaccuracies resulting from time-varying modal interference in the OMEGA VLF propagation, has been a major concern of this study. This has led to development by RTI personnel of a VLF propagation prediciton model which is capable of calculating PPC (propagation prediction corrections) for OMEGA phase considering all significant modes of propagation.

Considerable effort under this contract has been associated with supporting NASA personnel in reducing OMEGA data, preparing plots of data for visual editing, editing data, and summarizing the data in a form suitable for position estimation and error evaluation. Data plots were so voluminous that a limited number have been prepared for NASA-Langley and are not presented in this report. Much of the LOP analysis, differential error analysis, and position error analysis results are also not included. These have been summarized in this report in support of the conclusions made.

Use has been made of regression analysis and analysis of variance procedures to present results of a parametric analysis of the differential OMEGA navigation mode. An attempt has been made to generalize these results beyond the particular geographical region in which data were accumulated. In completing this analysis, a significant, unexplained error contribution was observed in the receiver/recording system as evidenced by the side-by-side test results. In the experimental plan, these were originally intended to allow for possible needed calibration of the receivers. Ultimately, these showed that random variations in receiver performance were a limiting factor in obtaining definitive results from regression analysis. An understanding of the fundamental source of the side-by-side phase difference variations is not complete. One hypothesis involving receiver phase measurement variation with signal amplitude is discussed. Although the two receivers used to record the OMEGA data do not have the same characteristics, there appears to be little, if any, correlation between variation in amplitude differences at the two receivers and measured phase variations with the receivers co-located.

In this report Chapter 2 describes the overall data gathering experimental program and analyzes the results of side-by-side tests with particular emphasis on receiver repeatability. Also, phase-amplitude correlation results are discussed. Chapter 3 discusses the results of differential OMEGA studies. These two chapters relate to tasks 1 and 2 of the contract. In Chapter 4, the VLF propagation model development is discussed which relates to task 4 of the contract. Chapter 5 describes results of composite OMEGA studies as per contract tasks 1, 2 and 3. Using actual data and the propagation model, propagation anomalies are discussed in Chapter 6 relating to contract task 5. Tasks 6 and 7 of the contract are described briefly in Chapter 2. Under task 8, two publications which relate to these studies (refs. 3 and 4) describe parametric analysis of differential OMEGA and time varying modal interference.

Several appendices are included giving supporting data and analysis results described within the report.

CHAPTER 2

DIFFERENTIAL OMEGA EXPERIMENTAL PROGRAM

To evaluate the OMEGA navigation system a two-year data gathering experimental program was undertaken. Beginning in September, 1973, two OMEGA receiver sets with associated digital recording equipment were used to collect phase and amplitude data at all three OMEGA frequencies. With a four station capability (A-Norway, B-Trinidad (segment G through March 1978), C-Hawaii, D-N. Dakota) one of the receivers was maintained in a laboratory environment at the Langley Research Center (LRC), Hampton, Virginia. The other receiver system was mounted in a travel trailer and periodically moved from Hampton to each of twelve different remote locations at varying distances from Hampton. Additionally, six locations extending into Florida were used on a one-time basis. Figure 2-1 illustrates the various locations used. Several visits to each of the twelve primary locations were made during the course of the data gathering. During each visit, both the "base" receiver at Hampton and the "remote" receiver were operated simultaneously for a period of three to five days.

This plan was designed for the primary purpose of obtaining data suitable for analysis of the differential mode. Of course there are sufficient data to evaluate other modes including ordinary OMEGA, composite OMEGA, and to investigate the effects of modal interference and other anomalous behavior. A previous report (ref. 1) has described the plan in more detail and also elaborates on the receivers used including an analysis of receiver performance. The plan was not complete at the time of the earlier report, therefore, this description will include the entire plan.

In the course of experiment design, two primary objectives were defined. One was to make measurements to adequately determine the variation of differential OMEGA with respect to receiver pair separation range and relative orientation. The second was to collect adequate data to gain insight about temporal variations, i.e., hour-to-hour variation, day-to-day repeatability, and seasonal variations. Previous differential tests (refs. 5, 6 and 7) had examined geometric effects in other local areas, but generally the conclusions were limited because relatively few receiver locations were used.

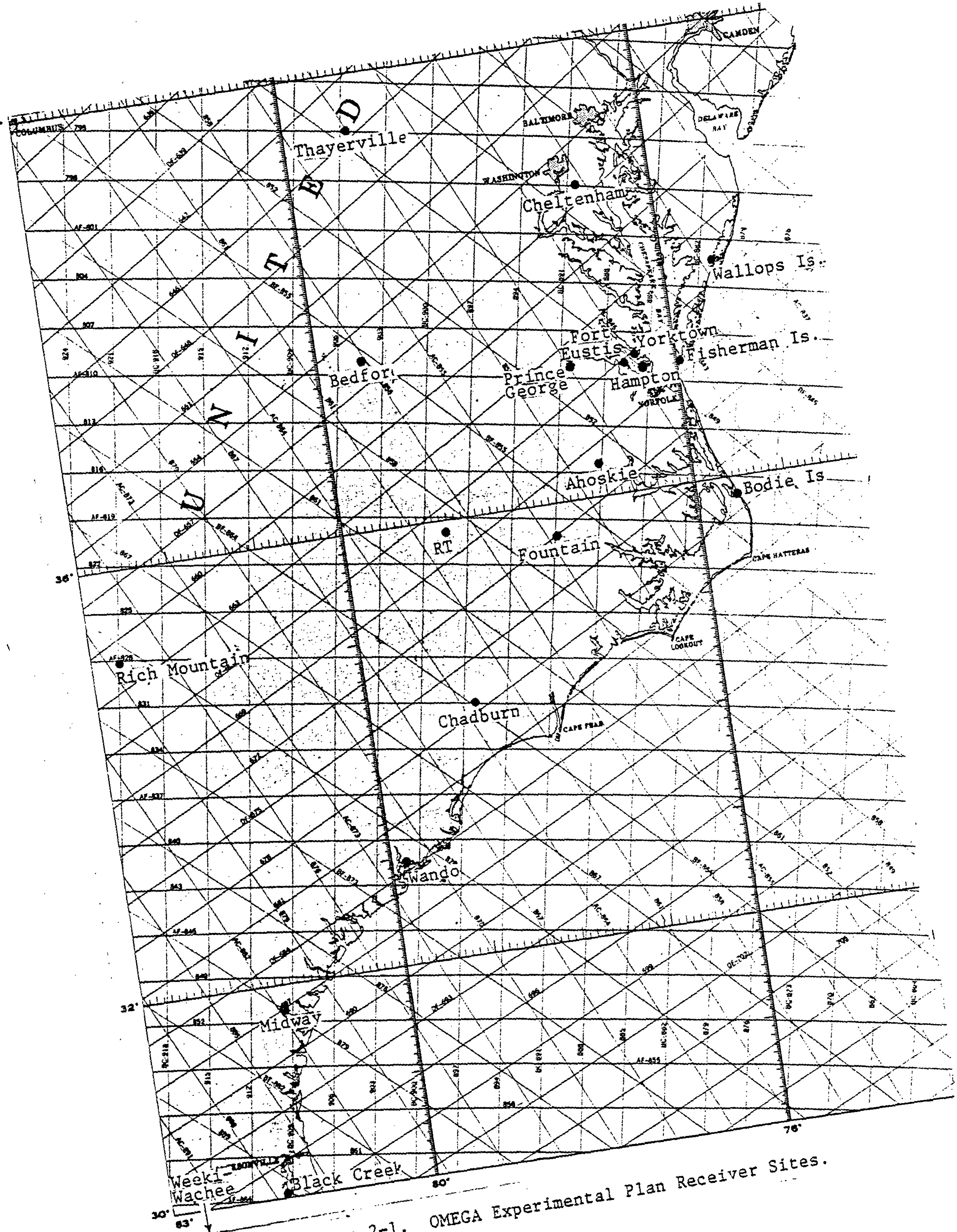

Figure 2-1. OMEGA Experimental Plan Receiver Sites.

Figure 2-2 illustrates the thirteen primary locations used (see Figure 2-5 in ref. 1) with the separation range and azimuth from Hampton. Table 2-1 is a schedule of site visits for the remote receiver system. As described in a previous report (ref. 1), each receiver system includes a Tracor 599R OMEGA receiver. The numeral within each darkened area of Figure 2-3 indicates the frequency selected on the Tracor receiver (1-10.2 kHz, 3-13.6 kHz). Figure 2-3 displays the distribution of receiver separation ranges, azimuths, and the site revisitation period.

During data gathering the N. Dakota transmission at full power and the Trinidad transmission at under 1 kw were the only signals continuously available. Norway data were available during about seventy-five percent of the time and Hawaii was on the air for at least one visit to each of the receiver sites during the latter stages of the experiment. The major problems with the OMEGA signals were fairly regular occurrences of modal interference on the North Dakota transmission, particularly at night, (ref. 3) and poor signal strength on the Norway transmission.

There were 83 data sets generated through repositioning of the remote receiver. Of these, six were not analyzed because of severe problems with the recording system or other equipment related problems. Six of the remaining sets were for separation ranges which extended beyond the conventional "differential region." Overall, seventeen sets (22% of the good data sets) provide measurements with the receivers co-located or side-by-side (SxS). These were interspersed throughout the experiment to allow some measure of inherent receiver repeatability (differential repeatability). A significant portion of the subsequent analysis has been relative to the SxS situation. Some significant random variations in the mean differential error between data periods were observed. A detailed analysis of these observations follows.

2.1 Receiver Repeatability

Receiver repeatability has been used in a strict sense (refs. 8 and 9) to mean capability of a receiver to indicate the same phase measurements given the same input signal phase at different times. With respect to this analysis, receiver repeatability is used in a differential sense. The capability of a differential pair of receivers when co-located to yield a differential phase measurement which is not dependent upon

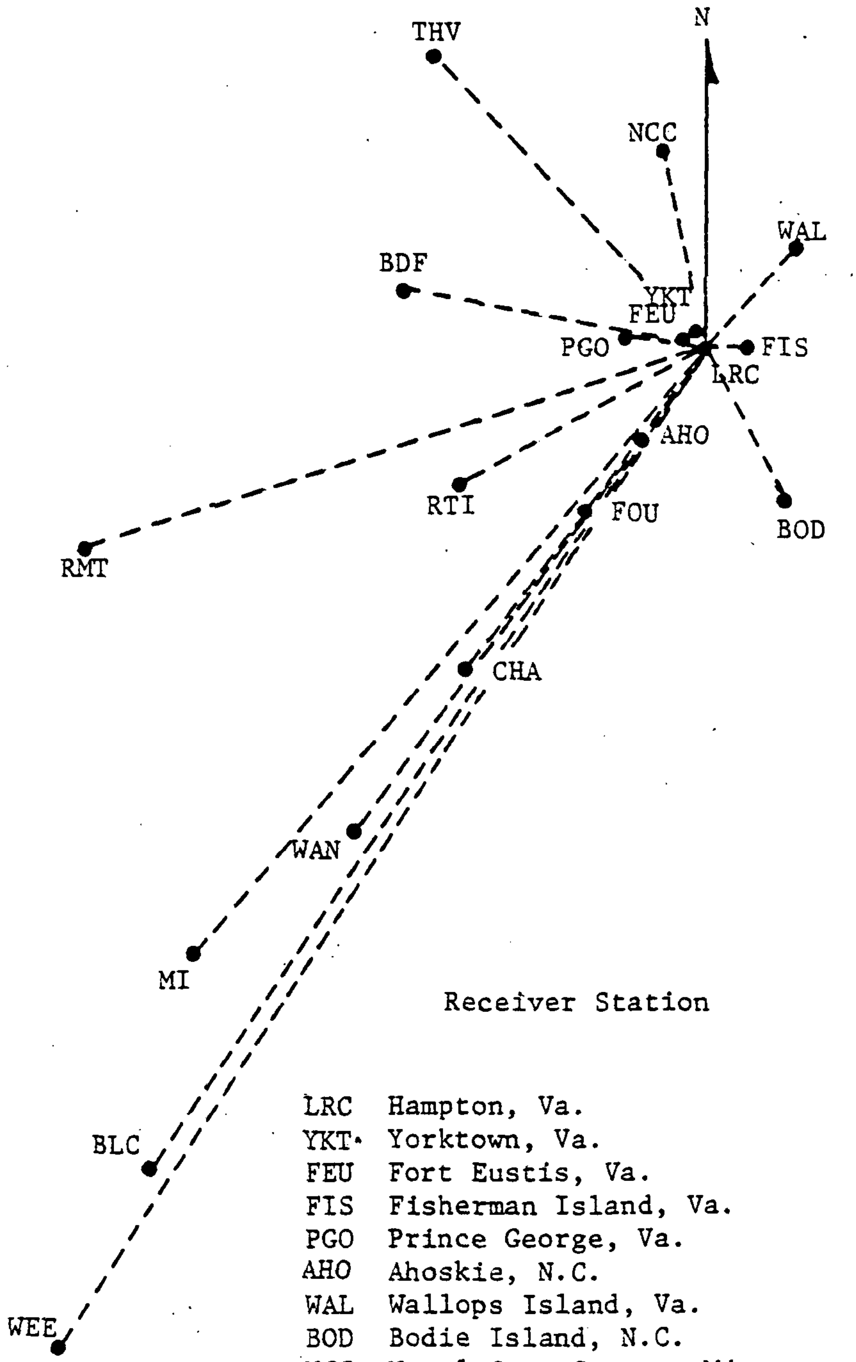

	Receiver Station	Range n.mi.	Range Km	Azimuth Degrees
LRC	Hampton, Va.	0	0	----
YKT	Yorktown, Va.	8.3	15.37	328.6
FEU	Fort Eustis, Va.	11.2	20.74	286.4
FIS	Fisherman Island, Va.	19.2	35.56	90.8
PGO	Prince George, Va.	40.0	74.08	277.4
AHO	Ahoskie, N.C.	56.9	105.38	213.2
WAL	Wallops Island, Va.	66.0	122.23	40.8
BOD	Bodie Island, N.C.	85.2	157.79	152.3
NCC	Naval Comm Center, Md.	101.3	187.61	347.4
FOU	Fountain, N.C.	103.1	190.86	216.3
RTI	Research Triangle, N.C.	139.8	258.91	239.9
BDF	Bedford, Va.	151.8	281.13	280.5
THV	Thayerville, Md.	200.0	370.4	317.4
CHA	Chadburn, N.C.	204.0	377.81	216.2
WAN	Wando, S.C.	301.1	577.64	215.4
RMT	Rich Mountain, N.C.	326.9	605.40	251.26
MI	Midway, Ga.	405.9	751.73	219.6
BLC	Black Creek, Fla.	499.2	924.52	213.8
WEE	Weeki-Wachee, Fla.	598.9	1109.16	212.9

Figure 2-2. Experimental Plan Receiver Site Locations.

Table 2-1. Site Schedule for Remote Receiver

	1973				1974												1975							
	SEP	OCT	NOV	DEC	JAN	FEB	MAR	APR	MAY	JUN	JUL	AUG	SEP	OCT	NOV	DEC	JAN	FEB	MAR	APR	MAY	JUN	JUL	AUG
Hampton, Va. LRC	1	1	1	1		3	3	3		1		1	1		1			1		3	3	3	3	
Yorktown, Va. YKT		1					3				1											3		
Ft. Eustis, Va. FEU				1				3					1									3		
Fisherman Island, Va. FIS				1/3				3														3		
Prince George, Va. PGO		1/3	1/3				3				1											3		
Ahoskie, N.C. AHO	1/3					3				1											3			
Wallops Island, Va. WAL					1				3				1						3	3				
Bodie Island, N.C. BOD						3				1				1					3					
Cheltenham, Md. NCC					1/3				3				1					3	3					
Research Triangle Park, N.C. RTI						3				1				1		1	1							
Bedford, Va. BDF			1/3				3					1								3				
Thayerville, Md. THV								3					1								3			
Rosman, N.C. RMT											3			1						3				
Fountain, N.C.																								1
Chadburn, N.C.																								1
Wando, S.C.																								1
Midway, Ga.																								1
Black Creek, Fla.																								1
Weeki-Wachee, Fla.																								1

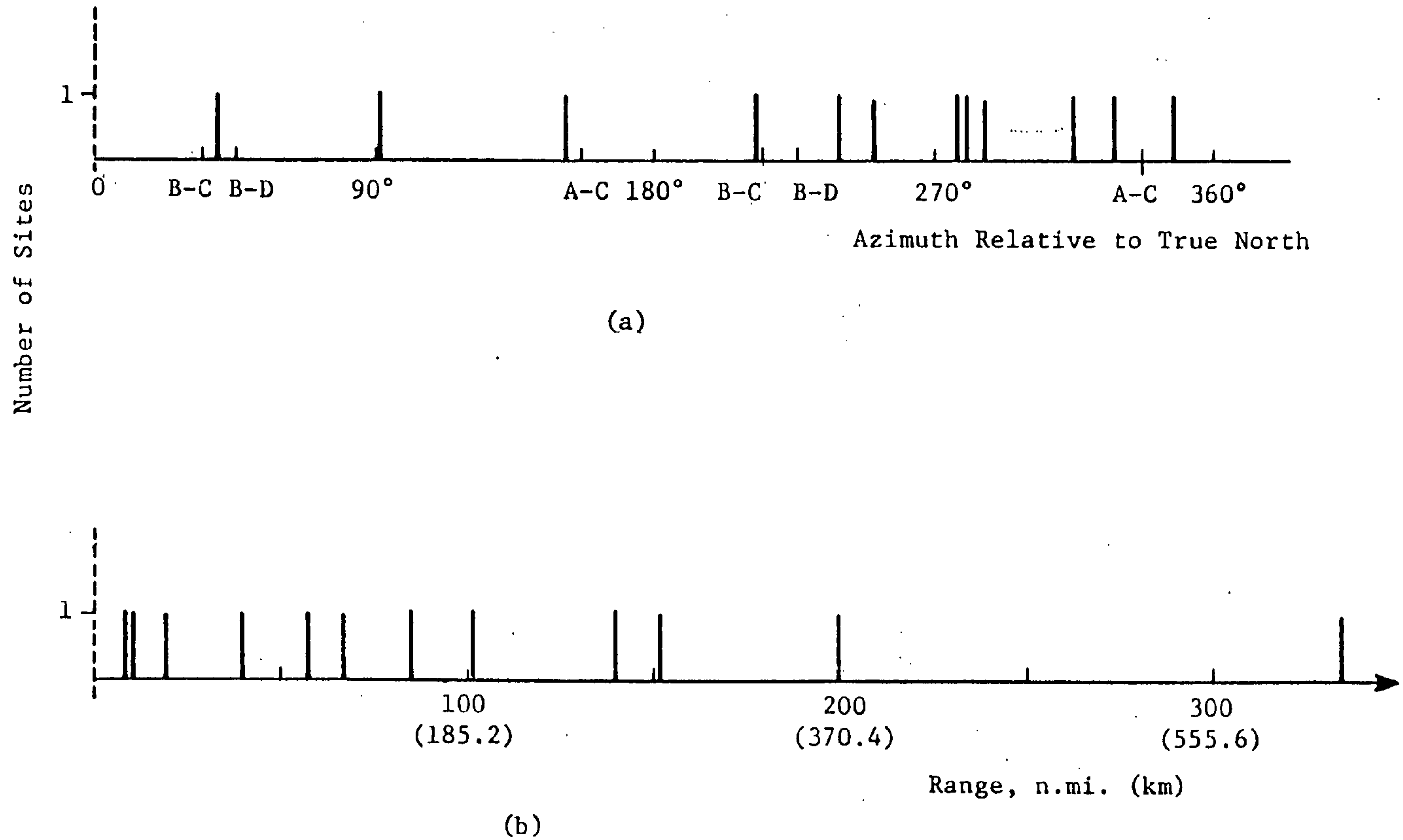

Figure 2-3. For Twelve Primary Sites of Remote Receiver: (a) Histogram of Azimuths from Hampton, Va. to Various Sites, (b) Histogram of Differential Ranges, (c) Histogram of Site Revisit Delay, (d) Cumulative Distribution of Revisit Delay Time.

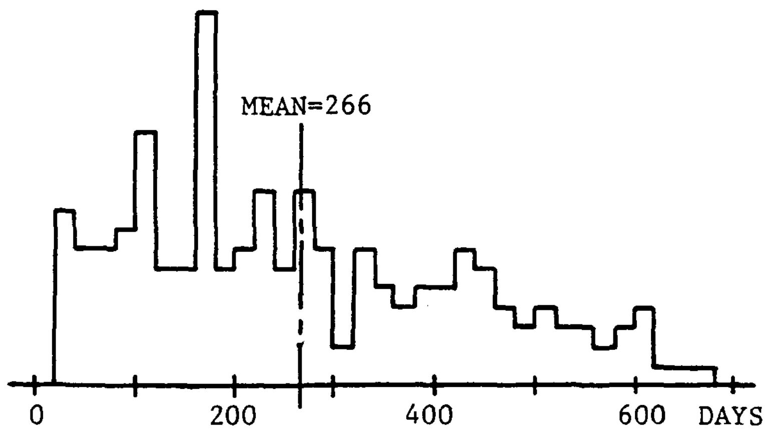

(c) Histogram of Site Revisit Delay

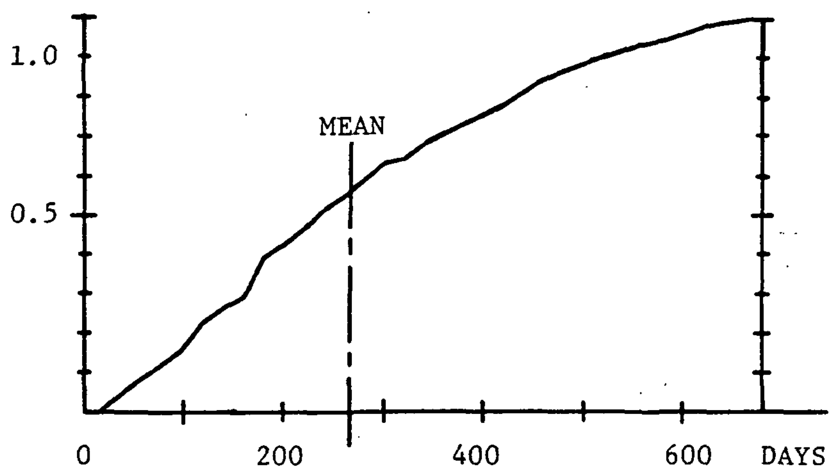

(d) Cumulative Distribution of Revisit Delay Time

Figure 2-3. Concluded.

time. When used in this sense, receiver repeatability is determined by the capability of each individual receiver to independently indicate the same measure of the same phase at different times as well as any differences in S curve type error which may exist between receivers. Repeatability error is typically random so that in a differential sense both correlated and uncorrelated (between receivers) contributions to error are included. Any mutual coupling between antenna configurations can also affect repeatability.

Receivers used in this experimental plan were co-located (SxS set-up) at frequent intervals so that a good estimate of differential receiver repeatability could be obtained. Any drift in phase measurement could conceivably be accounted for through this "calibration" procedure.

As data have been analyzed, a random repeatability error has been observed. This error for any given receiver SxS set-up generally has a small variation about the mean (< 1.0 cec) however, there is a rather large variation in the mean between periods ($\sim$ 2 cec). The variation in the period means as well as the range of the mean values does change with frequency. Following is a discussion of this analysis.

The SxS data have been analyzed primarily on the basis of one-hour averages of 10-second sample values of phase. This corresponds to low-pass filtering on data recorded from a receiver which has a phase measurement time constant of approximately one minute. The resolution of the phase measurement circuitry in each digital receiver is 0.25 cec at 10.2 kHz, 0.28 cec at 11.3 kHz, and 0.33 cec at 13.6 kHz. Figures 2-4, 2-5, and 2-6 are plots of hourly average differential LOP phase for approximately 75% of the SxS situations. These plots show full 24-hour period data with data sets overlaid. Daytime periods at Hampton, Va., correspond approximately to GMT hours 12-20 with exact times dependent on time of year. Figure 2-4 shows LOP B-D (TRI-N.DK) differential measurements at all three frequencies. More overall spread is evident in the 13.6 kHz data with a slightly positive overall bias in the 11.3 kHz data and slightly negative at 13.6 kHz. The 10.2 kHz data is rather evenly spread between $\pm$ 1.0 cec. Although it is not illustrated very well in these figures, variations in day-to-day repeatability are small compared to the overall variations. At

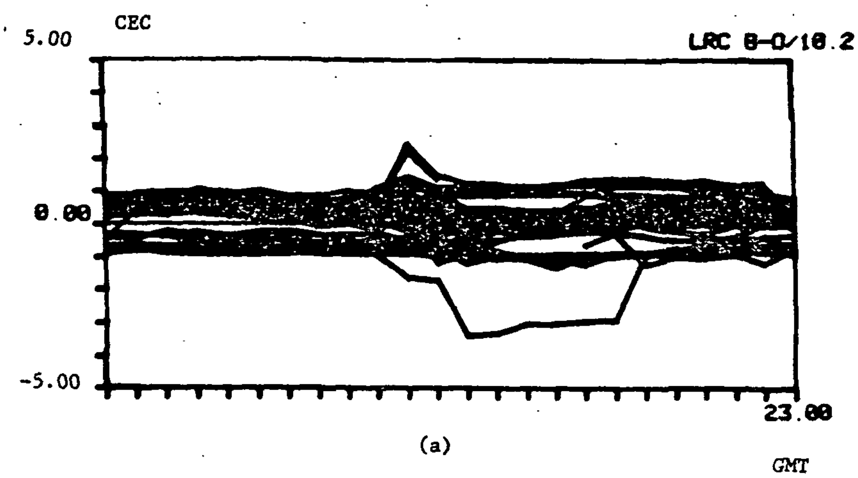

(a)

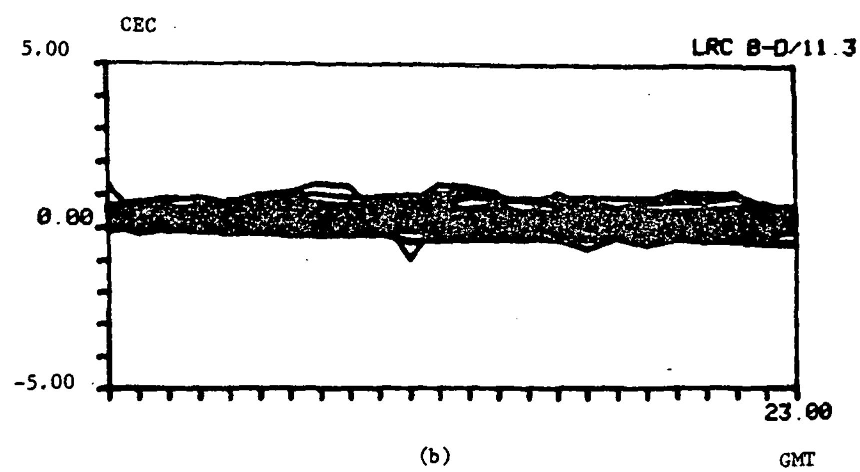

(b)

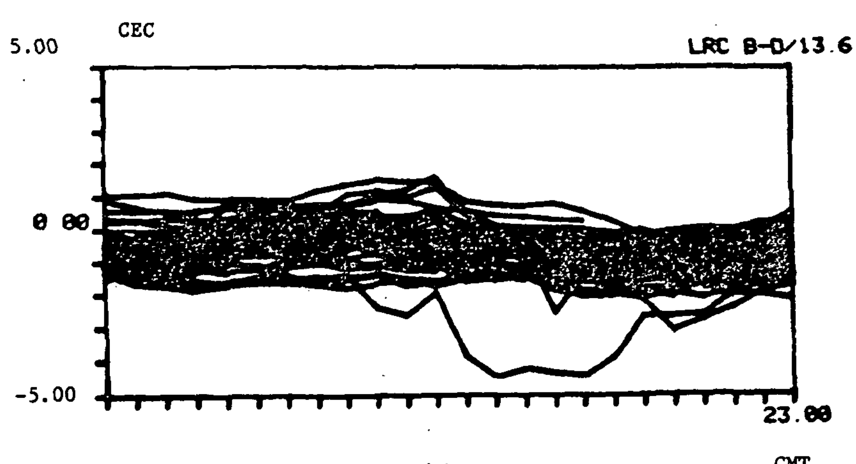

(c)

Figure 2-4. Overlay of SxS Hourly Differential Error Mean Values for LOP TRI-NDK (a) 10.2 kHz, (b) 11.3 kHz, (c) 13.6 kHz.

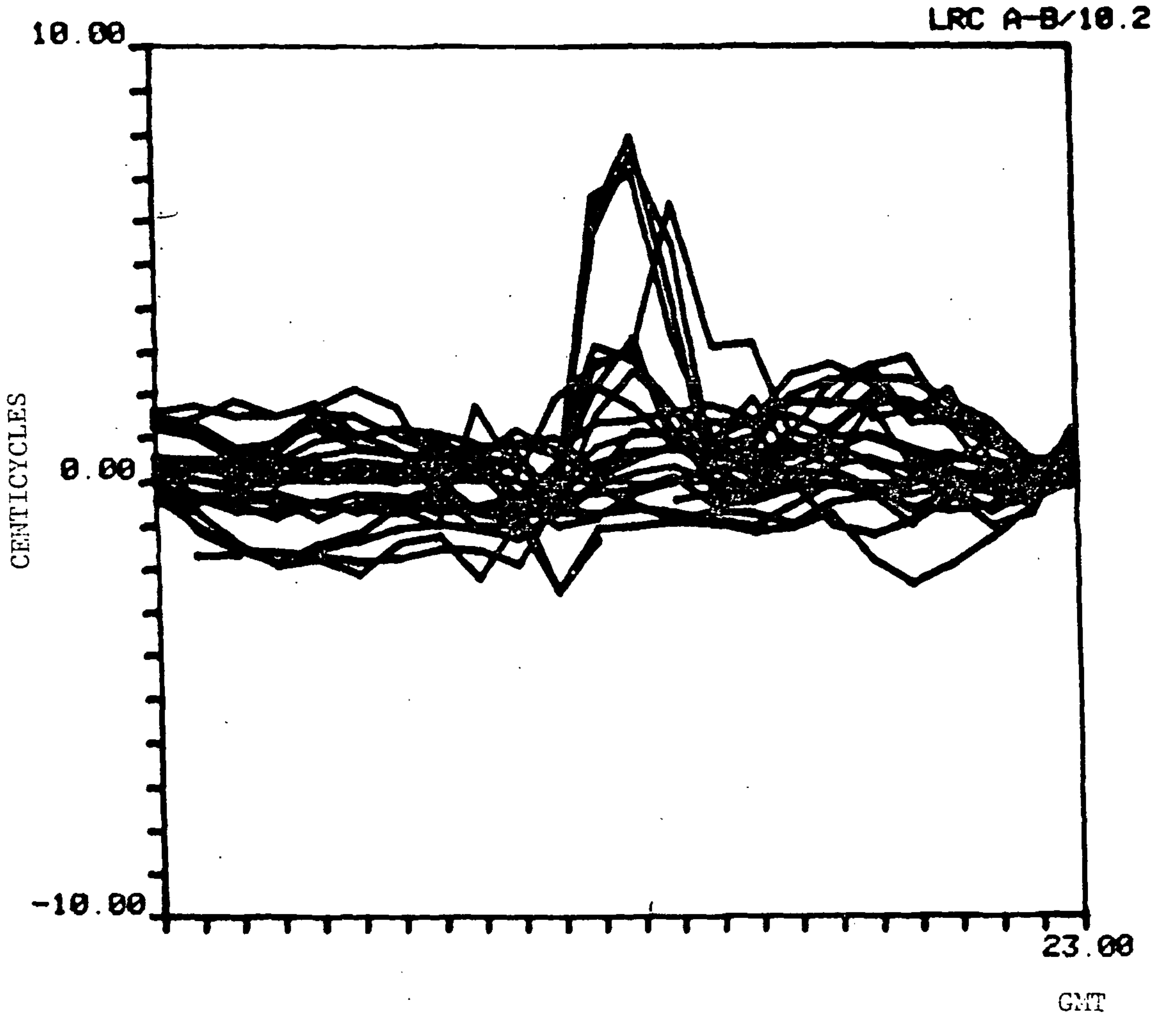

(a)

Figure 2-5. Overlay of SxS Hourly Differential Error Mean Values for LOP NOR-TRI (a) 10.2 kHz, (b) 11.3 kHz, (c) 13.6 kHz.

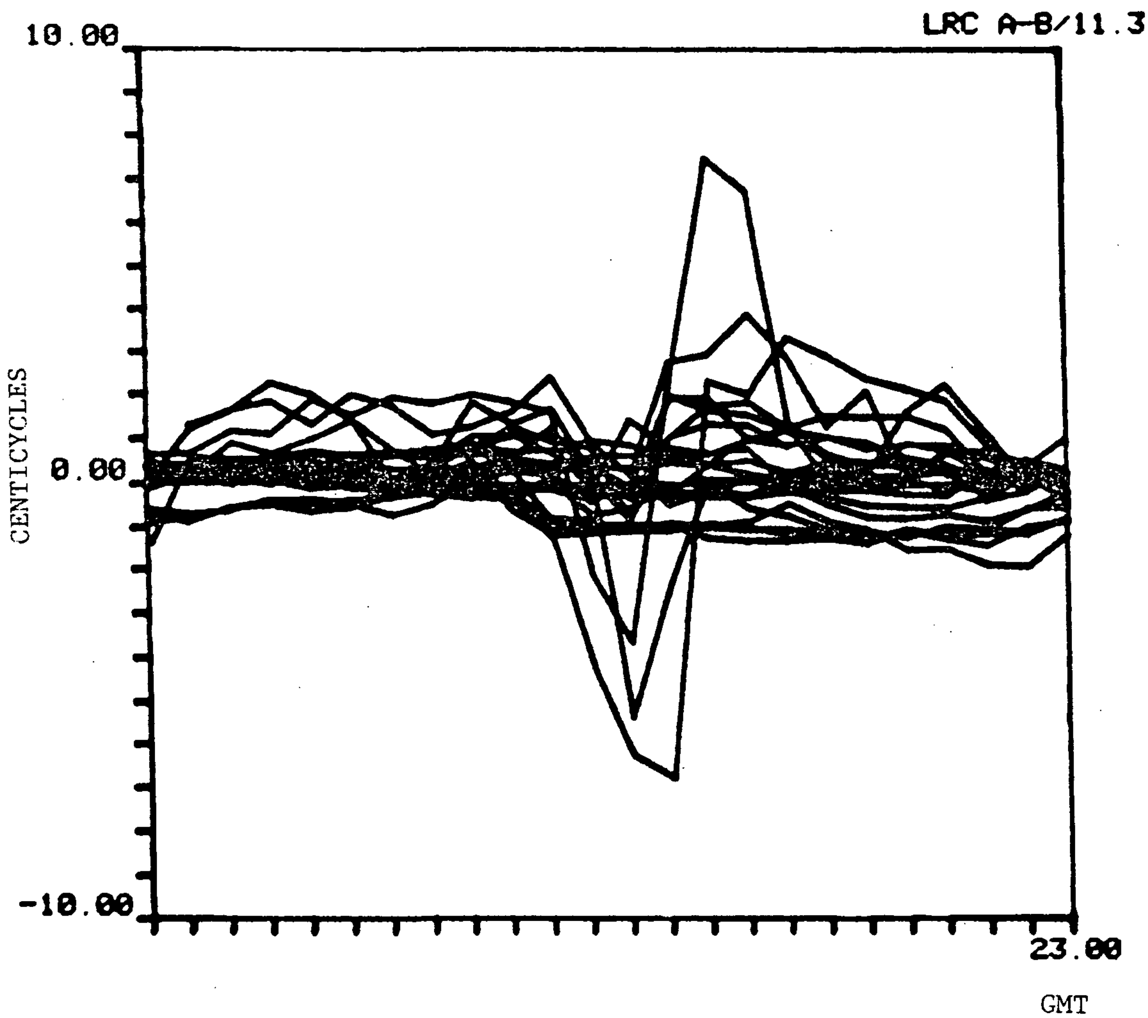

(b)

Figure 2-5. Continued.

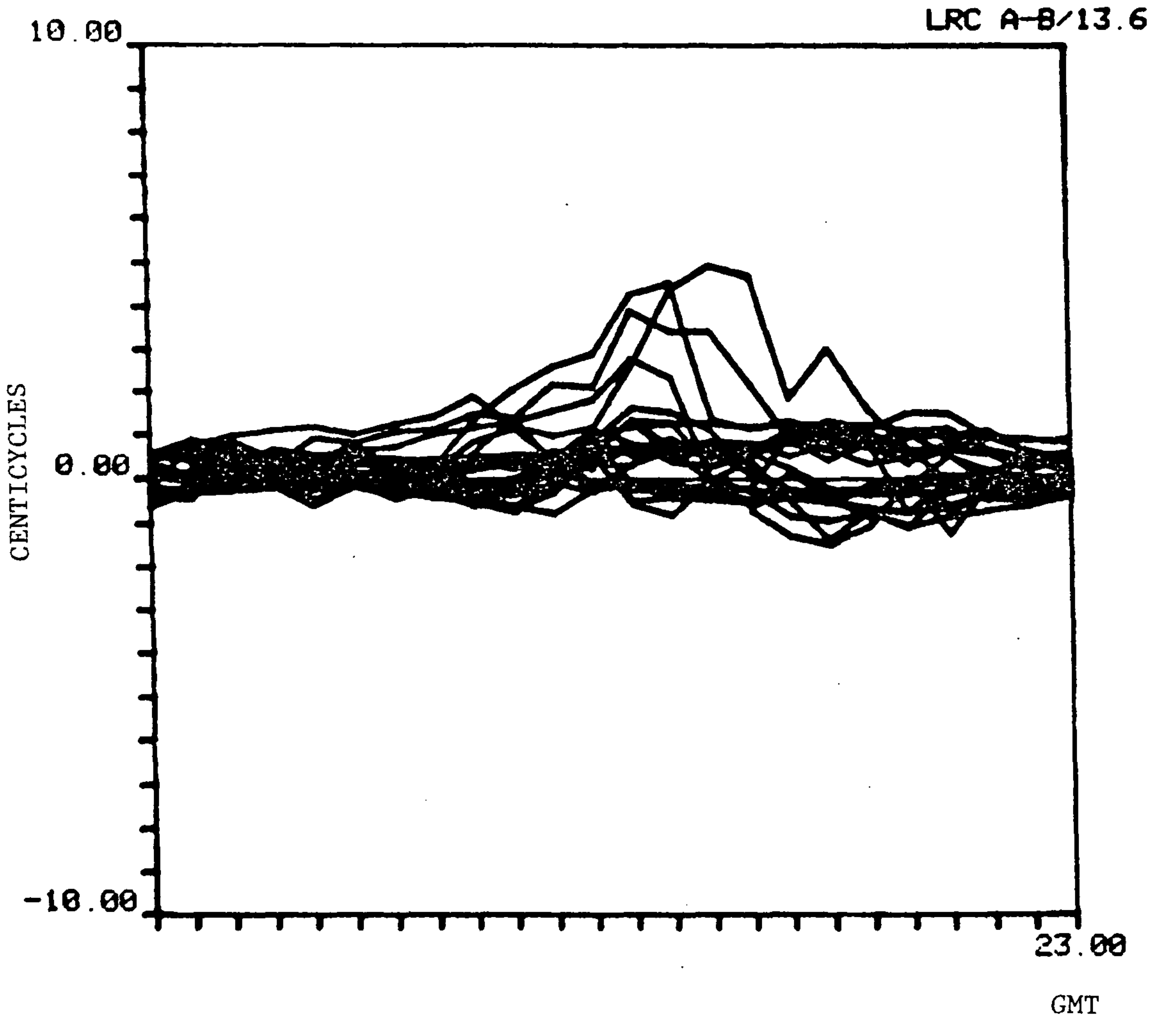

(c)

Figure 2-5. Continued.

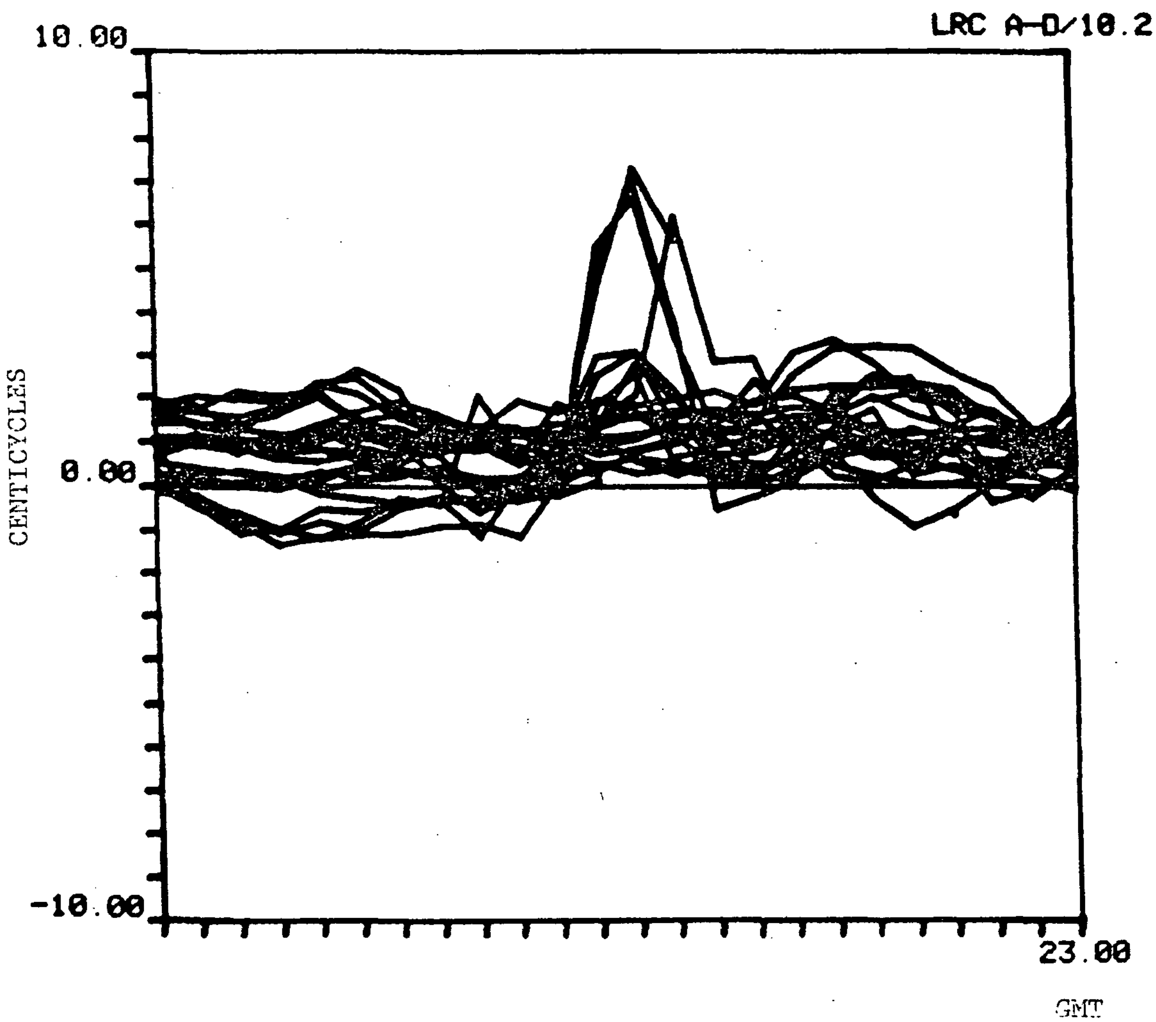

(a)

Figure 2-6. Overlay of SxS Hourly Differential Error Mean Values for LOP NOR-NDK (a) 10.2 kHz, (b) 11.3 kHz, (c) 13.6 kHz.

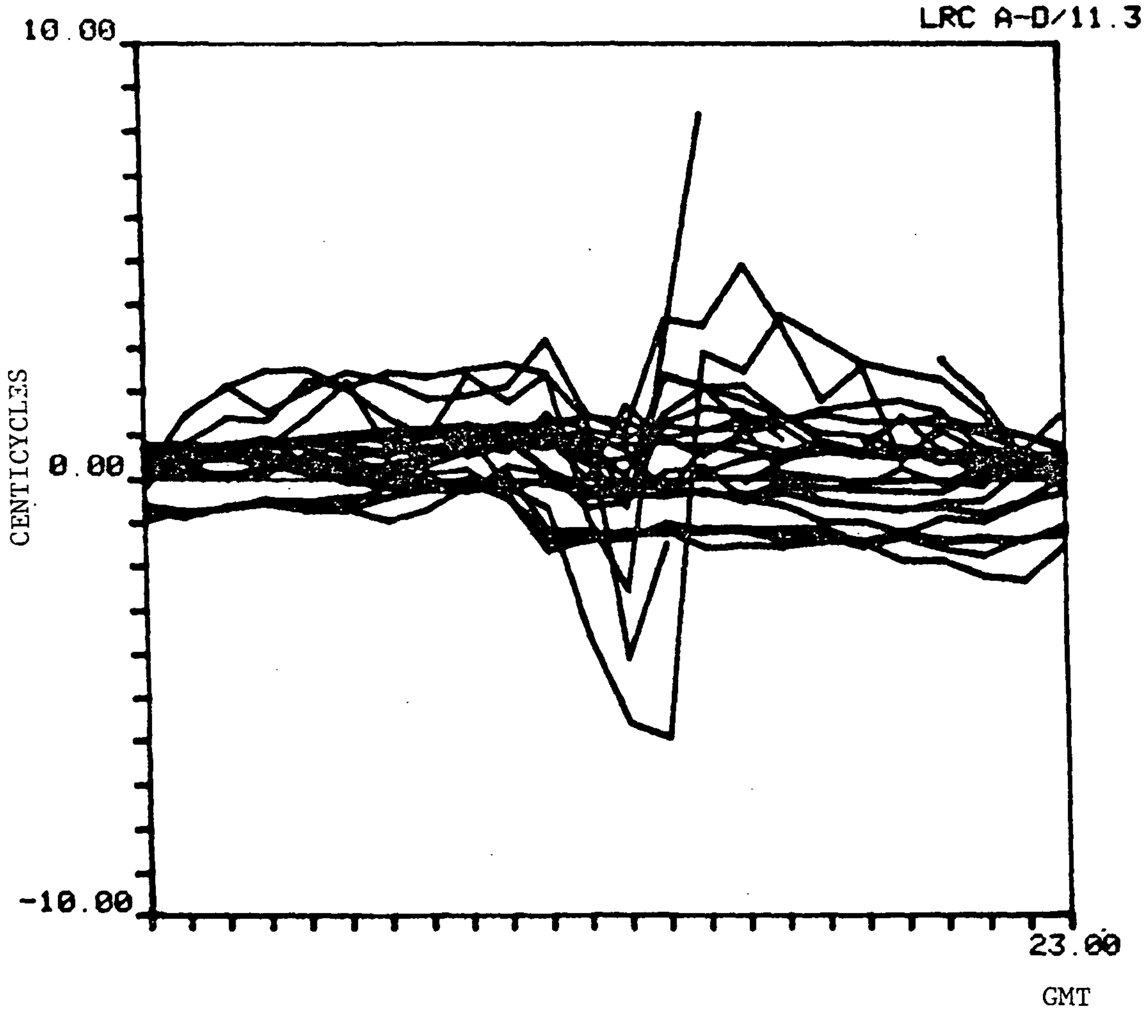

(b)

Figure 2-6. Continued.

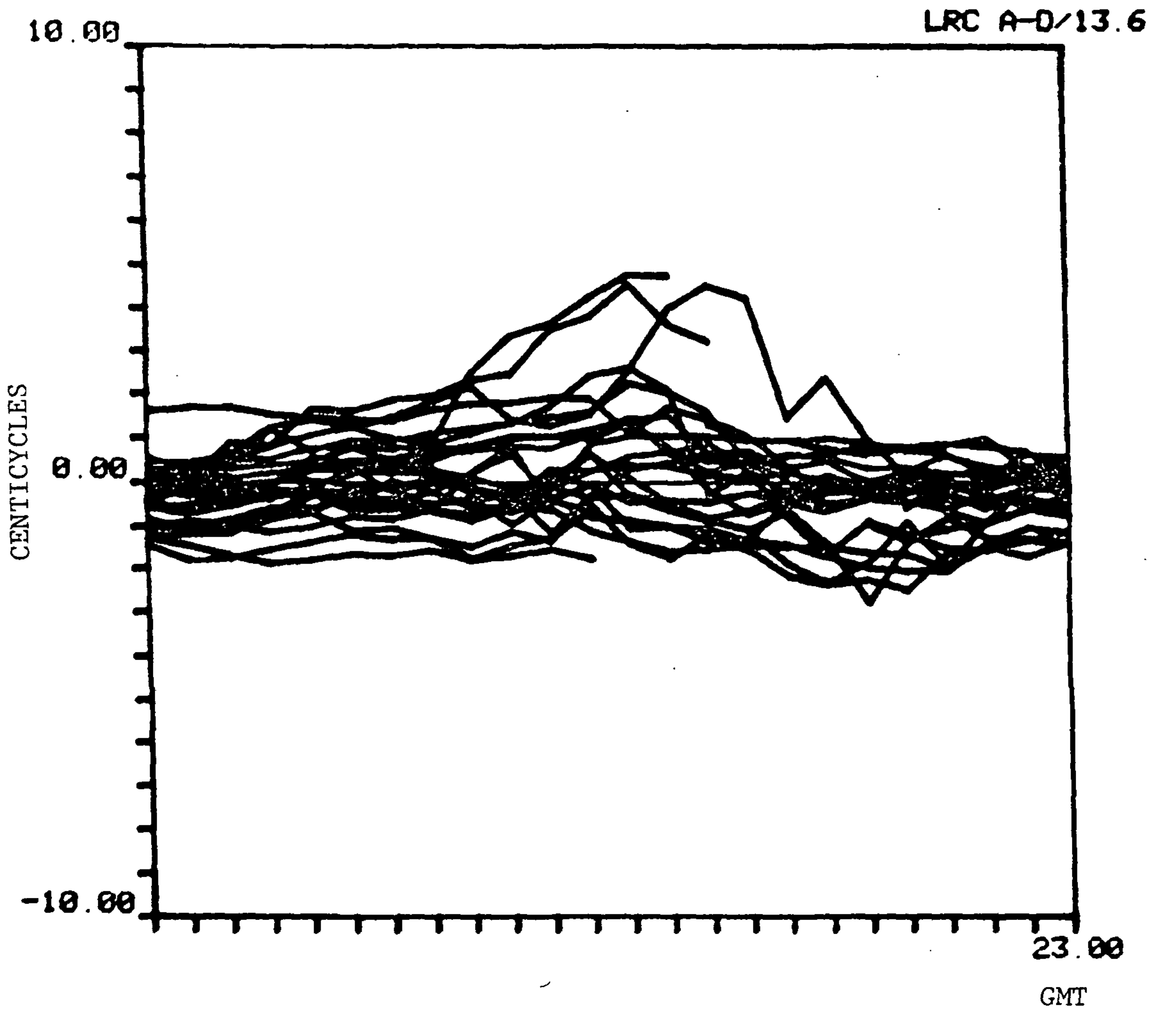

(c)

Figure 2-6. Continued.

10.2 and 13.6 kHz there is one transition period during which the differential phase error is definitely outside the envelope. This is not explained. From these data the 11.3 kHz signal appears to be the most repeatable. In Figures 2-5 and 2-6, LOPs A-B (NOR-TRI) and A-D (NOR-NDK) are shown for the same data. These show somewhat more overall variation and can be attributed to the receiver performance tracking the Norway signal which is generally 40-50 dB below N. Dakota at the Hampton, Va. location. These low SNR conditions also resulted in typically larger hourly standard deviation of differential LOP phase values for those LOPs shown. Any hours with phase standard deviation greater than 4.0 cec have been deleted from these presentations. No one frequency is consistently best, however, the A-B 13.6 kHz nighttime repeatability is particularly good. Figure 2-7 provides a plot of the Tracor 599R receiver differential data to illustrate the relative quality of the NASA digital receiver performance.

No apparent trends are identifiable in the data set to data set variations. This period-to-period randomness is further illustrated in Table 2-2 with data set means and standard deviations. Here XMN refers to the average hourly mean value for the data set and STD is the standard deviation of hourly mean values.

Data from station C (HAW) was not available until approximately December 1974 and has not been used in this discussion of period-to-period randomness versus within period repeatability.

In analyzing repeatability error, of particular concern in the differential mode is the effect of this error on position estimation. These same data have been analyzed in combination form in terms of relative position error. This represents a baseline error contribution which is dependent on the receiver system itself and is independent of those parameters which may be of greater interest in evaluating the concept: receiver separation distance and azimuth; phase dispersion; and local conditions. Position error here is used in the sense of east-west (x) and north-south (y) variation from the true position assuming that the differential LOP phase errors are used to estimate a position fix relative to the true position. Let

$$\Delta\phi^T = [\Delta\phi_1, \Delta\phi_2, \ldots \Delta\phi_n]$$

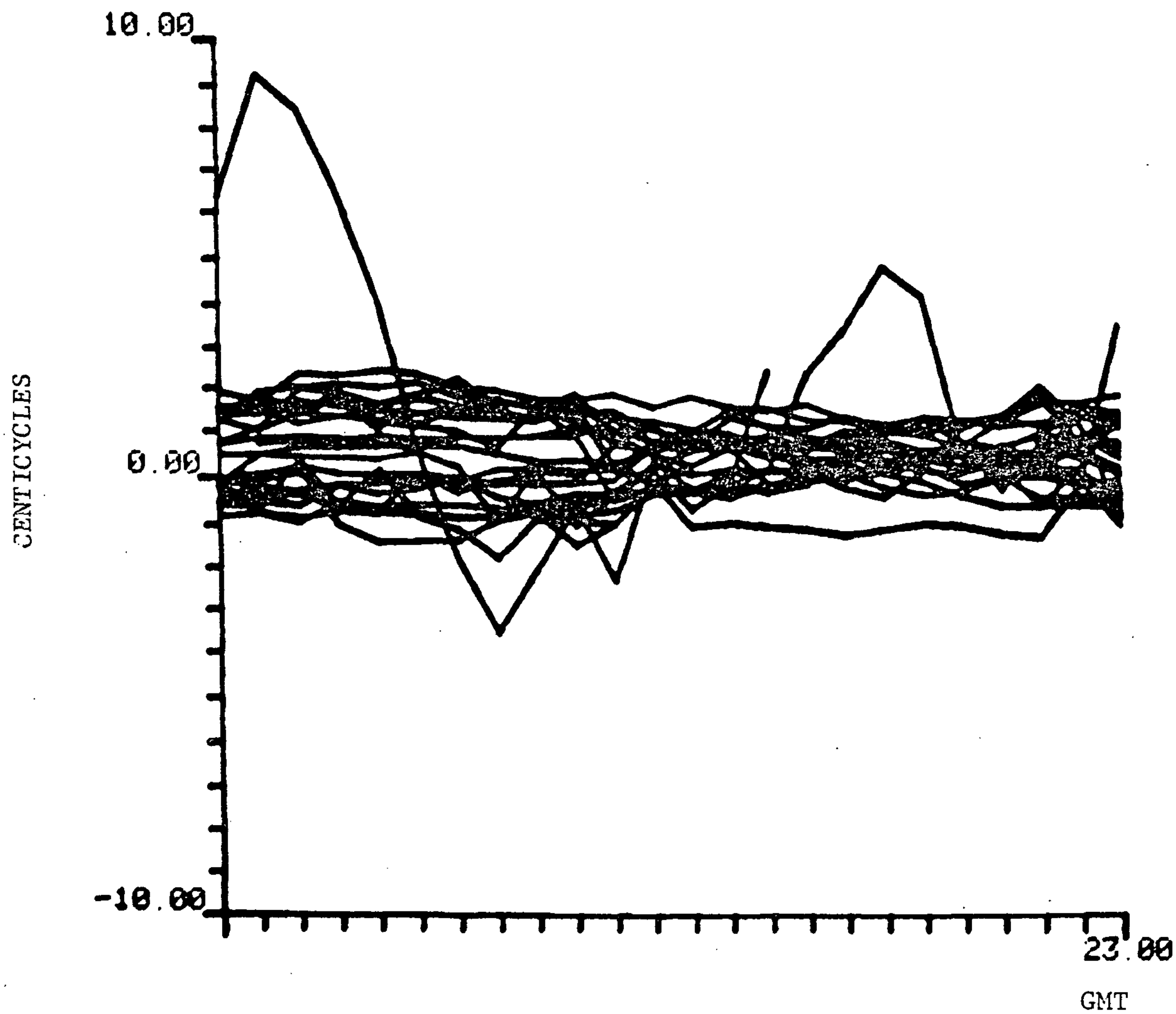

Figure 2-7. SxS Hourly Average Differential LOP Phase Values from TRACOR 599R Receiver for TRI-NDK at 10.2 kHz.

Table 2-2. Side-by-Side Average Hourly Mean and Hourly Mean Standard Deviation by Data Set (Full Period).

	NOR-TRI						NOR-HAW						NOR-NDK					
	10.2		11.3		13.6		10.2		11.3		13.6		10.2		11.3		13.6	
DSN	XMN	STD	XMN	STD	XMN	STD	XMN	STD	XMN	STD	XMN	STD	XMN	STD	XMN	STD	XMN	STD
1																		
2																		
3																		
4	0.84	1.35	0.23	0.39	-.33	0.59							1.38	2.06	0.63	0.93	-1.23	1.84
5																		
6	0.42	1.29	0.16	0.62	0.25	0.63							1.14	1.81	0.51	1.02	-.79	1.27
7	0.19	0.80	-.82	1.25	0.44	0.71							1.15	1.71	-1.02	1.53	-.18	0.41
8	0.26	0.49	-.03	0.28	0.42	0.81							1.11	1.60	0.02	0.33	0.27	0.62
9	0.16	0.95	0.56	0.99	0.24	0.54							0.54	1.06	0.77	1.25	0.59	1.09
10	0.61	2.60	0.89	2.42	1.01	2.02	0.53	2.25	1.34	2.78	0.85	2.16	0.74	2.32	1.40	2.83	1.19	2.31
11	3.28	6.63	1.11	1.94	-.18	3.77	3.13	6.43	1.54	2.48	0.53	4.74	2.68	5.64	1.41	2.37	1.78	4.36
12	0.62	2.25	2.40	3.61	0.18	1.55	0.72	1.96	3.41	5.05	-.38	1.78	0.77	1.84	3.25	4.86	0.44	1.63
13	-.05	1.71	2.44	3.62	0.24	1.15	0.12	1.43	3.42	5.02	-.44	1.47	0.22	1.27	3.34	4.91	0.60	1.41
14	-.79	2.88	-0.77	2.98	0.33	1.09	-.33	1.52	-.04	0.97	0.48	1.37	0.03	0.97	0.18	0.95	2.10	3.38

	TRI-HAW						TRI-NDK						HAW-NDK					
	10.2		11.3		13.6		10.2		11.3		13.6		10.2		11.3		13.6	
DSN	XMN	STD	XMN	STD	XMN	STD	XMN	STD	XMN	STD	XMN	STD	XMN	STD	XMN	STD	XMN	STD
1							-.86	1.22	0.55	0.78	-1.01	1.52						
2							-.81	1.30	.77	1.13	-1.61	2.40						
3							0.31	0.51	0.57	0.81	-0.62	0.94						
4							0.54	0.79	0.39	0.56	-.89	1.34						
5							0.27	0.45	0.49	0.71	-.51	0.84						
6							0.73	1.13	0.35	0.52	-1.05	1.52						
7							0.96	1.40	-.19	0.29	-0.62	0.94						
8							0.85	1.21	0.05	0.13	-.15	0.38						
9							0.39	0.63	0.22	0.36	0.36	0.66						
10	0.02	0.60	0.45	0.79	-.14	0.77	0.41	1.82	0.56	0.85	0.24	0.61	0.21	0.48	0.07	0.45	0.34	0.75
11	-.40	1.14	0.42	0.75	1.00	2.28	-.71	1.38	0.28	0.51	1.97	2.90	-.29	0.91	-.14	0.42	1.05	2.16
12	0.10	0.66	1.01	1.55	-.57	0.97	0.16	0.81	0.85	1.26	0.27	0.50	0.05	0.45	-.16	0.67	0.84	1.37
13	0.17	0.59	0.99	1.50	-.68	1.04	0.27	0.75	0.90	1.32	0.36	0.56	0.09	0.39	-.08	0.64	1.04	1.54
14	0.41	1.77	0.52	3.04	0.36	0.82	0.98	3.56	0.73	3.22	1.78	2.78	0.48	1.78	0.17	0.41	0.83	1.87

represent a vector of differential LOP phase measurements from the SxS data. These can be described in terms of a vector $\overline{\varepsilon} = [\varepsilon_E \; \varepsilon_N] \equiv [x,y]$ as

$$\Delta\phi = [M]\;\overline{\varepsilon} \tag{2-1}$$

where

$$[M] = \begin{bmatrix} \gamma_1\cos\beta_1 & -\gamma_1\sin\beta_1 \\ \gamma_2\cos\beta_2 & -\gamma_2\sin\beta_2 \\ \cdot & \cdot \\ \cdot & \cdot \\ \cdot & \cdot \\ \gamma_n\cos\beta_n & -\gamma_n\sin\beta_n \end{bmatrix}$$

with β_i the CW angle which is 90° less than the angle between north and the LOP gradient at the true position. The γ_i values are LOP gradients in cec/km at the respective frequency of consideration. Considering stations NOR, TRI HAW, and NDK, the β_i and γ_i values at Hampton, Virginia, are given in Table 2-3.

Given (2-1) the least squares estimate of position error is

$$\hat{\varepsilon} = [M^T M]^{-1} M^T \overline{\Delta\phi} \quad . \tag{2-2}$$

Since only LOP data are available, the vector $\overline{\Delta\phi}$ can never have more than three linearly independent elements and $[M^T M]^{-1}$ is 2x2. Table 2-4 summarizes (2-2) for all the combinations of three linearly independent LOPs taken from four transmitter phase measurements at the Hampton site.

For the situation when only three transmitter phase measurements are available, there can be only two independent LOP measurements, [M] is 2x2, and (2-2) reduces to

$$\hat{\varepsilon}' = [M]^{-1} \overline{\Delta\phi} \quad . \tag{2-3}$$

Table 2-3. LOP Angle and Gradient Values at Hampton, Va.

LOP	β (degrees cn)	Gradient Values (cec/km) γ 10.2 kHz	γ 11.3 kHz	γ 13.6 kHz
AB*	89.07°	5.86	6.50	7.81
AC	155.76°	5.43	6.03	7.26
AD	167.70°	4.44	4.98	5.97
*BC	216.09°	6.25	6.94	8.35
*BD	227.93°	6.68	7.43	8.92
CD	294.62°	1.38	1.57	1.86

*B is TRIN

Table 2-4. Position Estimate Transformations at Hampton, Va. for 10.2 kHz, 4 Transmitters

Position Error	Differential LOP Phase Measurement Error AB*	AC	AD	*BC	*BD	CD
E_x	-.0229	-.1266			-.0845	
E_y	-.0960	-.0576			.0618	
E_x	.0778	-.1995				.0110
E_y	-.1636	.0001				.0278
E_x	-.0424		-.1165	-.0985		
E_y	-.1329		-.0547	.0448		
E_x	.0415		-.2254			.0231
E_y	-.1629		.0006			.0315
E_x	-.1083			-.1941		.0553
E_y	-.1583			.0023		.0459
E_x	-.1636				-.2170	.0844
E_y	-.1557				.0034	.0513
E_x		-.1187		-.0795		.0211
E_y		-.1510		.1563		.0707
E_x		-.1378			-.0684	.0244
E_y		-.1174			.1367	.0492
E_x			-.1557	-.0580		.0502
E_y			-.1920	.1802		.1224
E_x			-.1753		-.0465	.0492
E_y			-.1467		.1538	.0785

* B is Trinidad

Table 2-5 summarizes the transformations applicable to (2-3). Given a set of differential LOP measurements which represent all of the possible combinations of LOP values from a given transmitter set, any of several transformations can be used to get a position error estimate. The position estimate will be independent of which LOP pair is selected. Station triplets are selected on the basis of ability to track phase and geometric coverage.

Figures 2-8 through 2-13 provide three and four station SxS hourly position error plots based on the measured differential LOP errors. Also shown on these figures is the overall RMS error for the hourly values and the CEP (circle of equal probability) radius for each set. Data for all three OMEGA frequencies is illustrated. It can be noted that the most significant spread in the position errors is generally in the direction of station A (NOR). The signal received from A has the largest phase variation and no other available station provides good geometric coverage in the direction of A.

In analyzing these results, the differential RMS position error is consistently within 0.5 km. Generally the 13.6 kHz derived position error is the best. The maximum resolution error is on the order of 0.1 km and is dependent upon the transmitters selected.

In these figures the position estimates derived from the differential LOP error values are bounded by superimposed LOP segments to indicate the range of the LOP values corresponding to the various position points. In Figure 2-8 position points are derived from the LOP pair NOR-HAW and TRI-HAW. At 10.2 kHz it can be seen that the range of differential error in LOP TRI-HAW is approximately symmetric about the zero value (orgin of EAST-NORTH coordinates). The points spread into the southwest quadrant indicate several error values on the NOR-HAW LOP difference which are positive. The position points are spread along the line which corresponds to the azimuth of the TRI-HAW LOP which happens to be in the general direction of NOR (29°E). The same general characteristics are true at the other frequencies. At 13.6 kHz the range of errors in the NOR-HAW is not as large.

In Figure 2-9 position points are obtained without using NOR yet the larger deviation is along the TRI-HAW LOP direction. This is a geometric

Table 2-5. Position Estimate Transformations at Hampton, Va. for 10.2 kHz, 3 Transmitters (ABD)

Position Error	Differential LOP Error AB*	AD	BD*
E_x	.0371	-.2297	
E_y	-.1701	-.0037	
E_x	-.1925		-.2275
E_y	-.1738		-.0037
E_x		-.1926	.0367
E_y		-.1739	.1685

* B is Trinidad

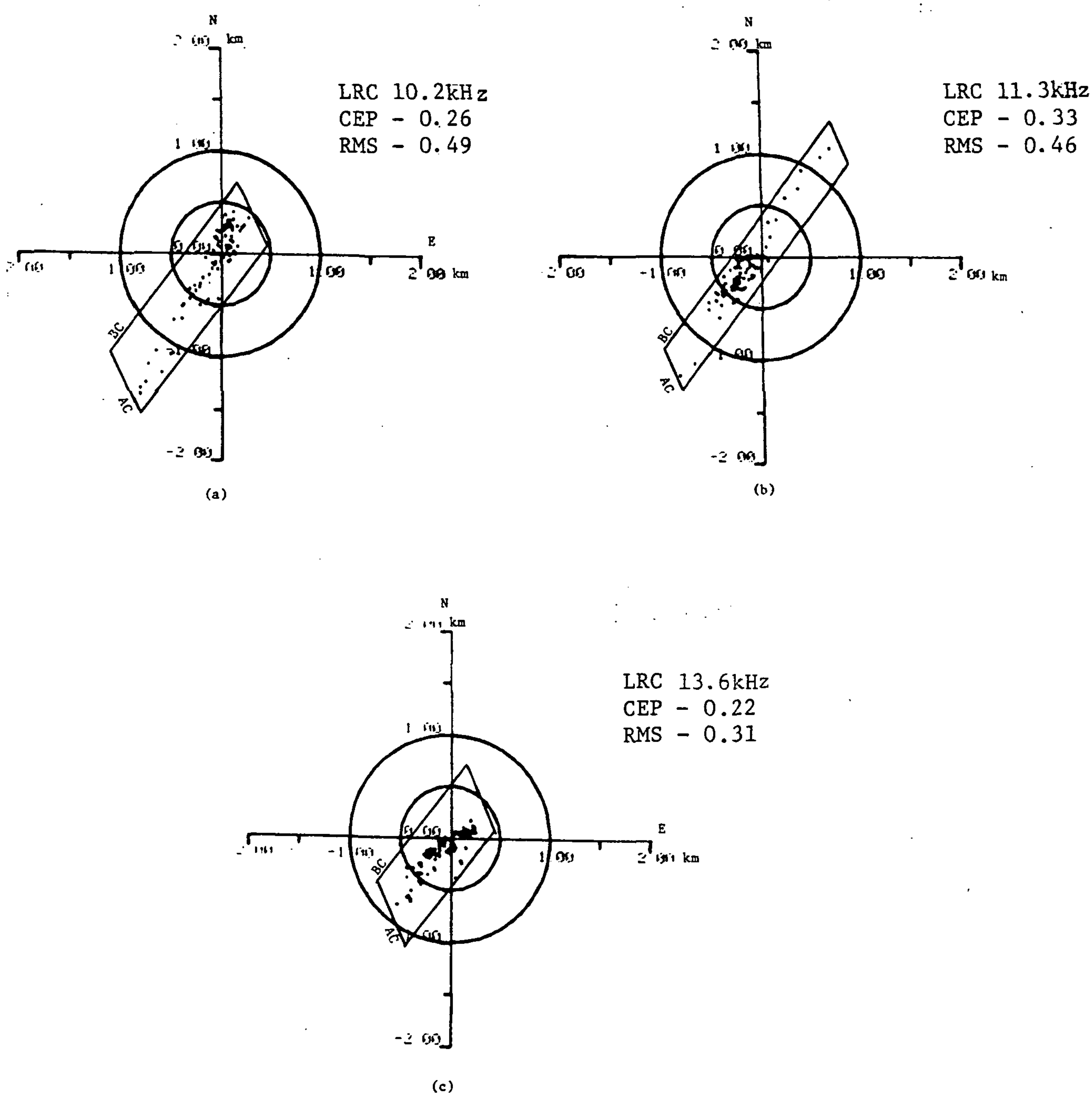

Figure 2-8. Side-by-Side Position Error Considering LOPs NOR-HAW and TRI-HAW (a) 10.2 kHz, (b) 11.3 kHz, (c) 13.6 kHz.

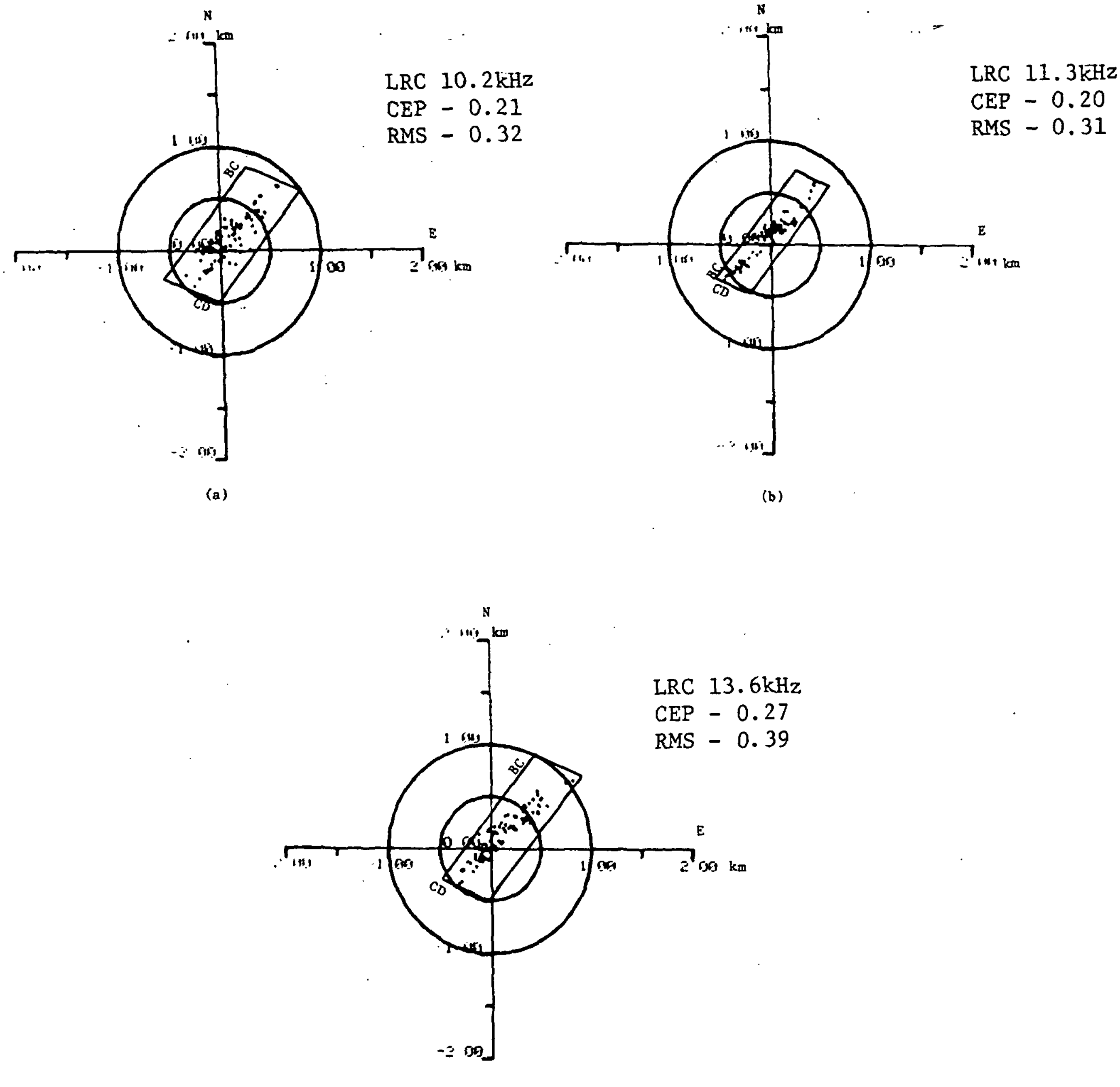

Figure 2-9. Side-by-Side Position Error Considering LOPs TRI-HAW and HAW-NDK
(a) 10.2 kHz, (b) 11.3 kHz, (c) 13.6 kHz.

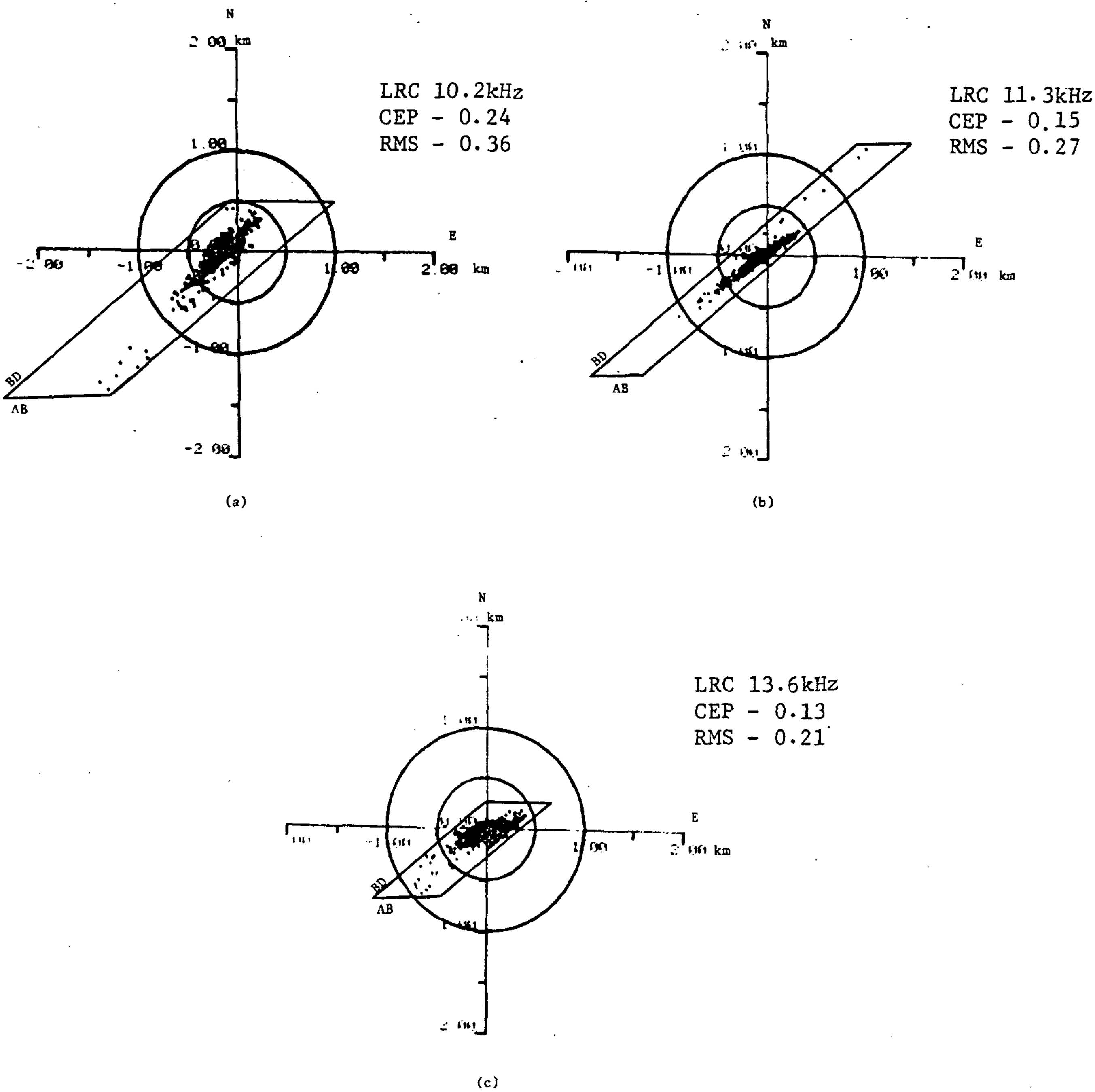

Figure 2-10. Side-by-Side Position Error Considering LOPs NOR-TRI and TRI-NDK (a) 10.2 kHz, (b) 11.3 kHz, (c) 13.6 kHz

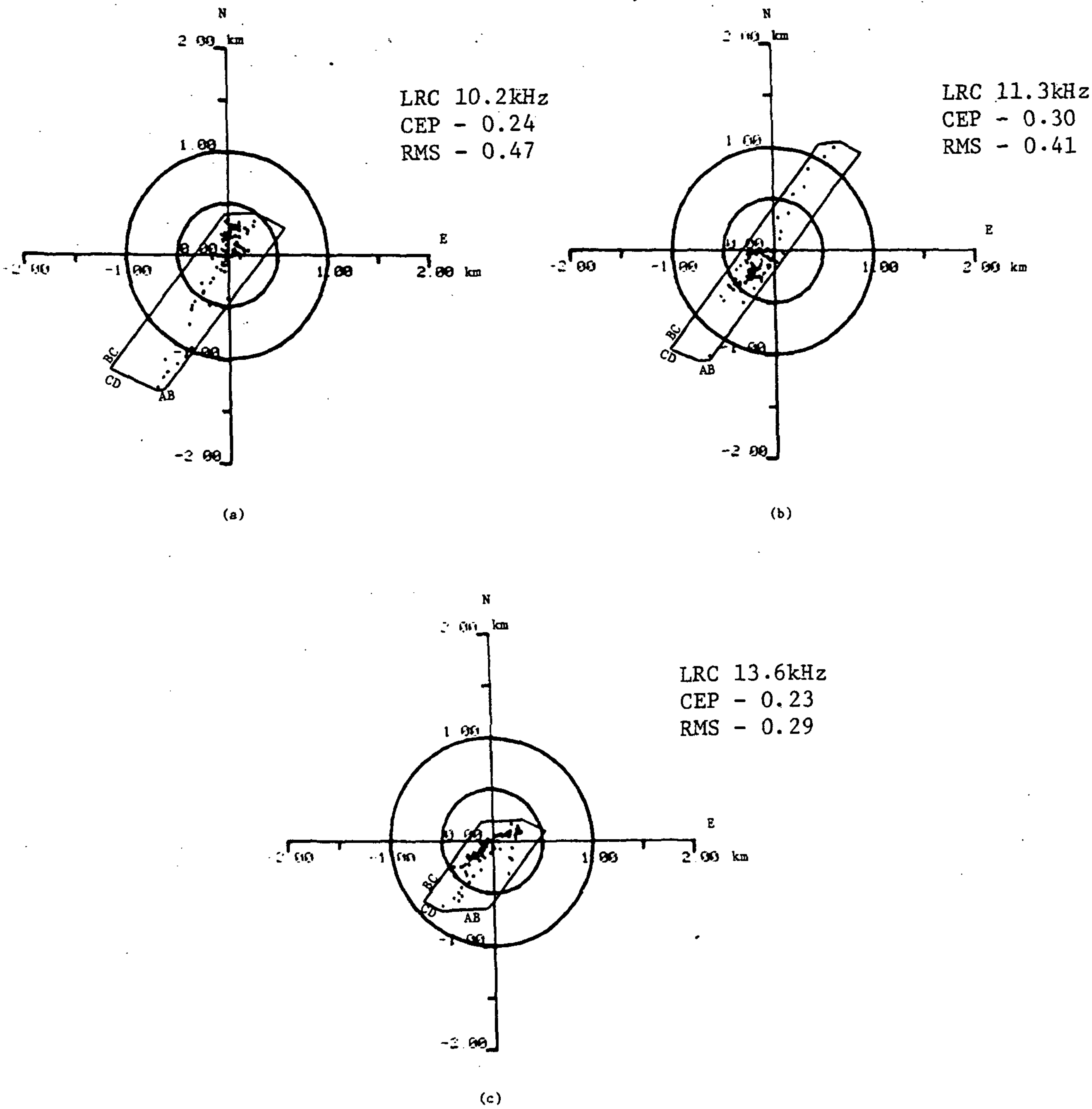

Figure 2-11. Side-by-Side Position Error Considering LOPs NOR-TRI, TRI-HAW, and HAW-NDK. (a) 10.2 kHz, (b) 11.3 kHz, (c) 13.6 kHz

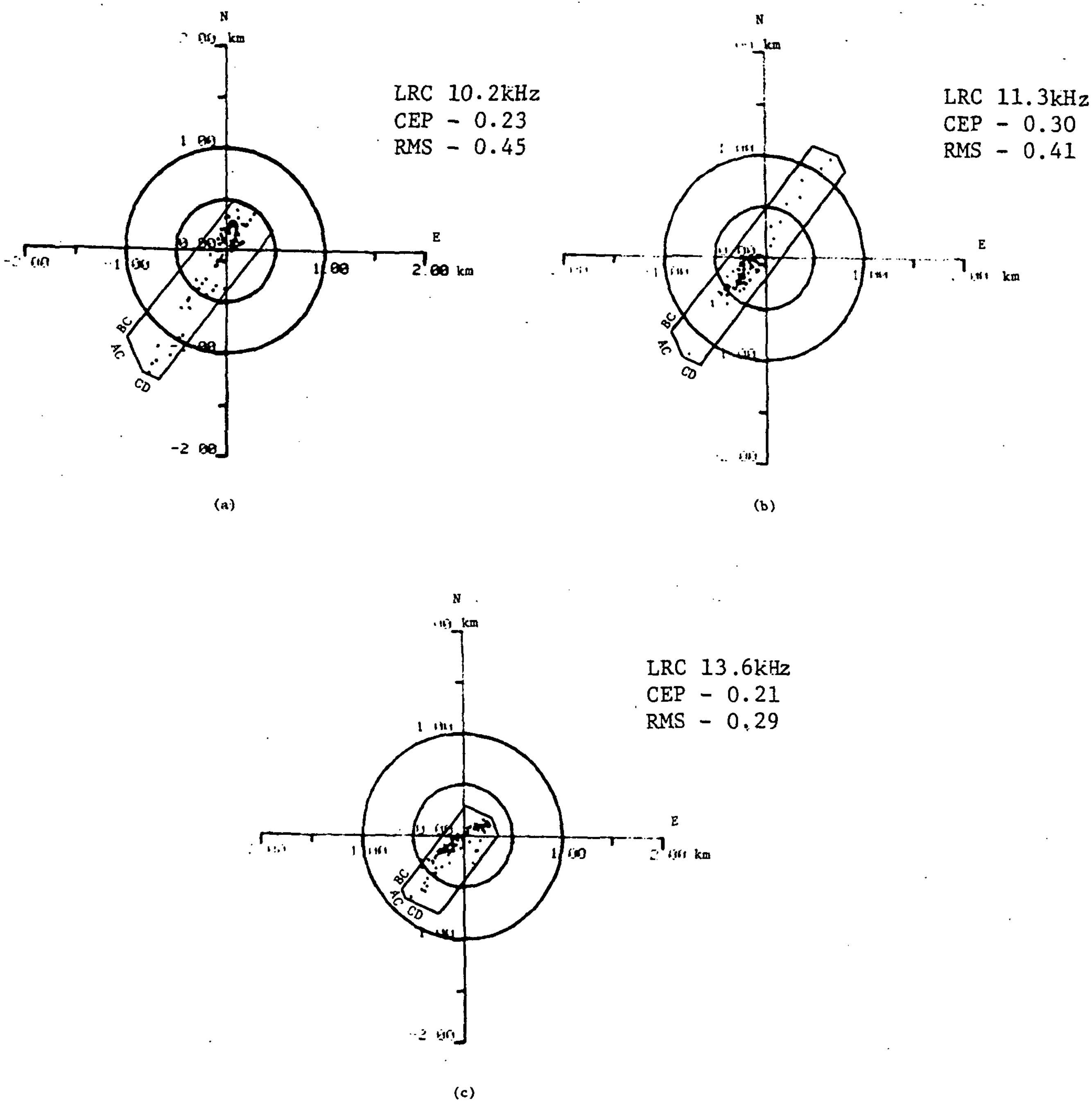

Figure 2-12. Side-by=Side Position Error Considering LOPs NOR-HAW, TRI-HAW, and HAW-NDK. (a) 10.2 kHz, (b) 11.3 kHz, (c) 13.6 kHz

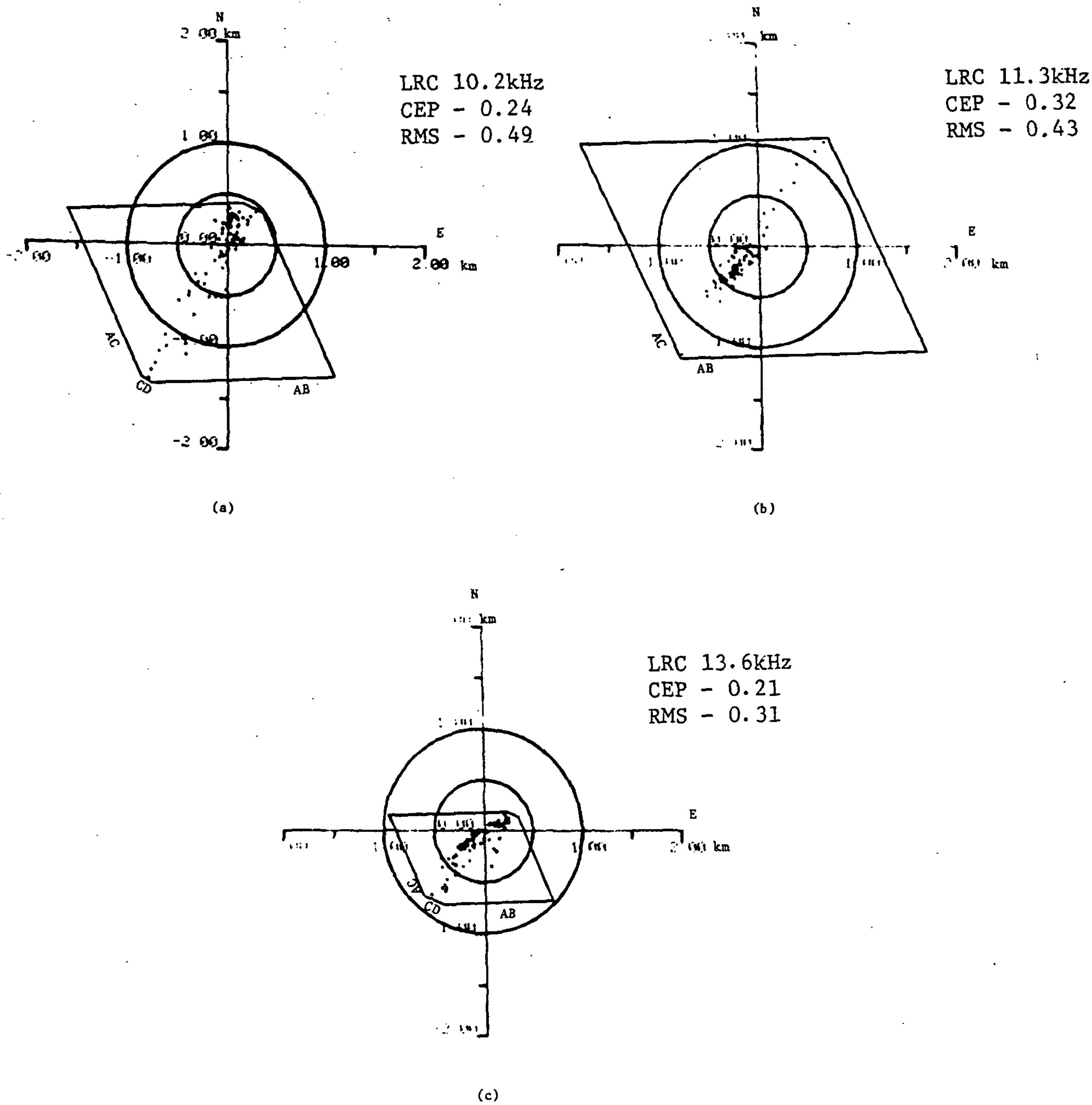

Figure 2-13. Side-by-Side Position Error Considering LOPs NOR-TRI, NOR-HAW and HAW-NDK. (a) 10.2 kHz, (b) 11.3 kHz, (c) 13.6 kHz

problem in that phase errors in the HAW-NDK LOP represent a spatial error more than four times as great as the same phase error in TRI-HAW. This is because of the distance of Hampton, Virginia, from the HAW-NDK baseline. Therefore, even though the differential LOP phase error in HAW-NDK is smaller than the TRI-HAW error, the position error range is greater.

In Figure 2-10 the error in NOR is again predominant with the larger position error spread along the TRI-NDK LOP. The reduced error in NOR at 13.6 kHz is again evident. The extreme position points correspond to a slightly larger phase error in the NOR-TRI LOP than was evident in the NOR-HAW LOP differential phase difference.

Considering the least square position error estimate using three differential LOP error values, three combinations are illustrated. In Figure 2-11 the HAW-NDK geometric dilution of precision error coupled with the NOR error is evident at 10.2 and 11.3 kHz. The reduced HAW-NDK error and the reduced NOR error at 13.6 kHz are apparent. Very little change occurs in Figure 2-12 where NOR-HAW is used instead of NOR-TRI. Figure 2-13 illustrates a somewhat different situation. The two LOPs involving NOR yield correlated position errors forcing the spread along the bisector of the angle between the two LOPs. This is also the general direction of the gradient of HAW-NDK, compounding the situation.

Summarizing this presentation, the hourly mean differential error lower bound as represented by the SxS data is random within about $\pm$ .5 km based on a position error analysis. During transition periods the error can extend to $\pm$ 1.0 km. With better transmitter coverage in terms of signal strength and geometry, this error could be held within $\pm$ 0.5 km.

2.2 OMEGA Receiver Amplitude-Phase Correlation

The recorded OMEGA data include amplitude values as measured by the TRACOR 599R receiver at the frequency for which this receiver is set. Appendix A details receiver amplitude measurement variation as a function of input signal strength. These curves have been used in conjunction with recorded amplitude values to estimate the received signal strength at each of the receivers for several of the SxS situations. Correlation analysis of received phase and amplitude has been used to determine if amplitude variations between set-ups might contribute to observed variations in the differential phase error mean values. This analysis includes a determination of the effect of received signal amplitude on phase measurement output for each receiver and provides a comparison of receivers.

The most significant phase variation in the OMEGA signal is diurnal as is the case with amplitude. Of specific interest is short term correlation between phase and amplitude so that it is necessary to confine this analysis to discrete periods of general phase stability within each day so as to eliminate the effect of the diurnal.

A phase-amplitude correlation test was run on several sets of OMEGA data taken in a SxS receiver environment. Analysis for each data period which may include 3 to 5 days of data is run for the union set of all full daytime records and the union set of all full nighttime records within each data period. Data from each receiver is analyzed separately.

Correlation tests consist of scatter plots of phase measurements vs. amplitude measurements for each data set as well as a listing of mean and standard deviation values for phase and amplitude within the set and a calculated measure of correlation

$$\rho_{xy} = \frac{E\{(x - \bar{x})(y - \bar{y})\}}{\sigma_x \sigma_y}$$

where $\bar{x}$ indicates mean of x, σ_x indicates standard deviation of x, $E\{\cdot\}$ is the expected value operator, and x and y represent the phase and amplitude variations with time. The coefficient ρ_{xy} is a measure of the linear correlation of the variables x and y, i.e., the nearer in magnitude to 1 the more linearly correlated. The scatter plot provides a measure of linear correlation to the extent that points are collected in a tight pattern along a "best fit" straight line. A measure of non-linear correlation is afforded if the data tend to collect around some non-linear curve.

Amplitude measurements at each 10 second sample time correspond to one of four transmitters. These recorded amplitude values are converted to a measure of signal strength (see Appendix A). Phase values are transformed to remove reference oscillator drift as follows.

Using the strongest signal which is most stable at the Hampton receiver site, the NDK (Sta. D) phase values for each daytime period are averaged to determine a daytime mean μ_i for the ith daytime record (i=1, 2, ..., N) where N is the number of daytime records in a data period. Using N values of μ_i, a set of times t_i (t_1=0, t_2=8640, t_3=17280, etc.) is defined so that each value μ_i is displaced in time by 8640 10-second time periods. An estimate of reference oscillator drift is then derived according to the slope of a least squares line through the points $\{\mu_i, t_i\}$

$$\hat{\gamma} = \frac{N\sum_i t_i\mu_i - \left(\sum_i t_i\right)\left(\sum_i \mu_i\right)}{N\sum_i t_i^2 - \left(\sum_i t_i\right)^2}$$

where $\hat{\gamma}$ is drift estimate in centicycles per 10-second period.

For the entire data period the reference phase drift is removed from the individual transmitter phase data according to

$$\phi_{NEW}(t) = \phi_{OLD}(t) - \frac{\hat{\gamma}}{10}\left[t - t_{start}\right]$$

where t_{start} may be chosen arbitrarily (all times in seconds). $\phi_{OLD}(t)$ represents the originally recorded phase value at time t and $\phi_{NEW}(t)$ represents the drift removed value used in the correlation tests.

Independent drift removal is accomplished for phase measurements corresponding to each OMEGA transmitter contained in the data period. Drift estimation is made using the NDK data only.

Once the phase data and corresponding amplitude data are transformed each data set is used in a correlation analysis for each transmitter at the frequency of the amplitude measurements. Separate analyses are run for receivers 1 and 2.

Table 2-6 summarizes results from analysis of two of the data sets at the 13.6 kHz frequency. Data set 56 was obtained in late March 1974 and data set 91 during April 1975. It can be noted that no consistent

Table 2-6. Results of Phase-Amplitude Correlation Analysis for Two Data Sets at 13.6 kHz

	DAY 1			DAY 2			DAY 3			NIGHT 1			NIGHT 2			NIGHT 3			NIGHT 4		
1.56	TRI	HAU	NDK	TRI	HAW	NDK	TRI	HAW	NKD	TRI	HAW	NDK	TRI	HAW	NDK	TRI	HAW	NDK	TRI	HAW	NDK
Mean Phase $\bar{\phi}$	12.91		17.33	11.88		16.14	13.79		17.41	47.31		48.22	45.64		47.86	45.59		47.05	49.58		50.16
Mean Amp. $\bar{A}$	-14.33		5.15	-14.55		4.34	-14.60		4.12	-15.65		0.17	-14.46		4.01	-15.9		-0.45	-14.28		-0.92
Corr. Coef. ρ	-0.60		-0.74	-0.34		-0.48	-0.62		0.15	0.07		0.37	-0.27		0.15	0.27		0.62	0.18		-0.29
2.56																					
Mean Phase $\bar{\phi}$	55.73		59.58	55.45		59.02	56.70		59.58	89.54		90.43	89.79		91.62	88.99		90.10	90.35		90.23
Mean Amp. $\bar{A}$	-16.42		3.85	-16.31		3.87	-16.23		3.13	-17.75		-2.77	-16.15		1.83	-17.47		-3.14	-16.03		-2.62
Corr. Coef. ρ	-0.74		-0.85	-0.40		-0.47	-0.67		0.34	0.09		0.30	-0.49		0.09	0.21		0.57	-0.05		-0.33
1.91																					
Mean Phase $\bar{\phi}$	10.45	75.25	12.56	11.19	70.36	12.25				45.45	61.05	43.75	44.70	59.37	43.99						
Mean Amp. $\bar{A}$	-13.55	-18.96	1.01	-13.37	-20.29	1.03				-13.91	-12.25	-2.45	-12.31	-11.52	-2.00						
Corr. Coef. ρ	-0.09	-0.28	-0.04	-0.17	-0.87	0.04				0.44	-0.19	0.52	0.66	0.25	0.24						
2.91																					
Mean Phase $\bar{\phi}$	2.06	83.92	5.87	1.00	64.73	4.81				34.00	51.67		35.11	51.14	36.32						
Mean Amp. $\bar{A}$	-15.41	-19.52	-0.54	-15.65	-20.22	-0.42				-15.81	-12.74	-5.06	-14.68	-12.83	-3.99						
Corr. Coef. ρ	-0.59	-0.49	-0.66	-0.48	-0.94	0.23				0.27	-0.08	-0.20	0.52	0.36	0.39						

Notes: 1) Phase values are in cec relative to local oscillator with drift removed.
2) Amplitude values are in dB relative to "normal" daytime North Dakota signal level.

correlation between phase and amplitude was observed for either daytime or nighttime periods. The TRI amplitude was on the order of 18-20 dB below that of NDK during both daytime and nighttime periods of data set 56. The TRI-NDK LOP mean value was on the order of -0.50 cec. For data set 91 there was about 14-16 dB difference in the amplitude of the TRI and NDK signals. The mean TRI-NDK LOP phase was near 2 cecs. The scatter plots and calculated mean and standard deviation estimates for phase and amplitude are included in Appendix A. These show very close agreement in the general characteristics between receivers for any selected period.

Based on this analysis, if the correlation between phase and amplitude were consistently high for the hourly values, a definite relationship between received signal amplitude and phase measurement bias could be established. Thus when comparing situations where the average signal strength is significantly different, a predictable phase measurement bias should appear in the differential phase as an error. This analysis does not support any relationship between received signal strength variations and the observed period-to-period mean differential error variations.

2.2.1 Pseudo-lane counting with the OMEGA data.— In analyzing OMEGA phase data, either LOP data or individual transmitter station data, it is necessary to reinsert lane count information so that statistical calculations will be valid. OMEGA phase data as recorded is a measure of phase in centicycles (cec) modulo 100 at the frequency of interest. All measurements are samples at 10-second intervals of received signal phase relative to the local oscillator phase (reference). Each relative phase measurement is some value in the interval (0,100) at the respective carrier frequency. When making a statistical analysis of the data, a transition from, for example, 60 cec in one lane to, say, 20 cec in the next lane would appear numerically as a -40 cec change instead of a + 60 cec shift. In order to preserve the correct direction, magnitude, and average value, it is necessary to track the phase change as it crosses the lane boundary (100 cec = 0 cec). This section describes the procedure used in the statistical analysis of data to accomplish lane counting or "pseudo-lane counting" as it will be termed since it is simply a procedure for post analysis to maintain lane identity in the recorded data relative to the starting lane. The starting lane is dependent on supplementary information concerning either known position or a position estimate of the receiver.

With the first order digital phase-locked loop receiver tracking an OMEGA signal no more than a 4 cec phase shift can be successfully tracked during a 10-second sampling interval. Any phase changes in the received signal which are more rapid will inherently cause a loss of lock condition. For the stationary receiver this generally is no problem. In fact, when analyzing the recorded receiver output with the receiver locked on the incoming signal this limitation can be used to advantage. As phase measurements are interpreted, a comparison of successive pairs of values can readily reveal in which direction the loop is tracking. To illustrate how this can be used to determine lane changes, assume that two successive phase values are 99 and 1 cec, respectively. If the receiver is in lock, this must correspond to a lane boundary crossing which means a phase change from 99 to 101 cec, i.e., a +2 cec change instead of a -98 cec change within the same lane. From this reasoning it is possible to define a pseudo lane counting algorithm.

For the beginning relative phase value in a data set for a particular transmitter and frequency, an arbitrary lane value is assigned. A lane count of zero can be assigned and lane values can be shifted to their true value by simply adding a constant after relative shifts have been determined within a data set. A lane count register is assigned to the initial setting, i.e., LCNT = 0. The initial phase sample is then interpreted as

$$\phi_o = SAMVAL_o + LCNT_o * 100$$

where SAMVAL is the sample value of recorded phase in cec and ϕ_o is the true value of phase within the defined lane structure. The next successive 10-second phase sample is then determined using

$$\phi_i' = SAMVAL_i + LCNT_{i-1} * 100$$

where i = 1, 2, ... to the last sample in the data set. Comparing the ith sample with the (i-1)st sample and comparing the difference to some predetermined threshold value

$$|\Delta\phi_i| = |\phi_{i-1} - \phi_i'| \lesseqgtr T$$

yields the sample to sample change. If $\Delta\phi_i$ is > T then $LCNT_i = LCNT_{i-1} + SGN\ (\phi_{i-1} - \phi_i')$ where the SGN (·) function has a value of +1 or -1 depending on the sign of $\Delta\phi_i$. If $\Delta\phi_i$ < T then $LCNT_i = LCNT_{i-1}$. Once the lane value corresponding to the ith phase value is determined then ϕ_i' is replaced by

$$\phi_i = SAMVAL_i + LCNT_i * 100$$

where ϕ_i reflects the true phase of the ith sample value in whole cycles and fractional cycles (cec) relative to the first point in the data set.

To determine an appropriate value of the threshold T it is necessary to consider not only the receiver characteristics in the ideal situation, but also the results of receiver noise on the recorded phase values. As was stated, the first order loop can respond, in-track, to no more than a 4 cec input phase change during a 10-second sampling interval. Digital noise internal to the receiver and the effect of editing must also be considered when defining the maximum possible recorded phase shift from one sample to the next within a lane.

An automated editing computer program is used to pre-process the data. Through analysis of raw data, situations have been observed where large instantaneous phase shifts do occur in the recorded output due to internal receiver noise. These events are of at least two types. One type is generally peculiar to one particular loop on any given occurrence. Note that there are twelve loops within the receiver, one for each of four transmitters at each of three frequencies. Loop assignments are determined by the receiver timing and control logic synchronized to the OMEGA format. The loop noise normally is recognizable as an instantaneous phase jump at a given sample point and then a phase drift back to the earlier level characteristic of a sudden loss of lock and recovery. Recovery is normally accomplished within six minutes. The editing algorithm searches for these "spikes" in the data and simply removes six minutes of data from the data set beginning with the leading edge discontinuity. These values are tagged as bad data and not considered for further analysis. Figure 2-14 illustrates

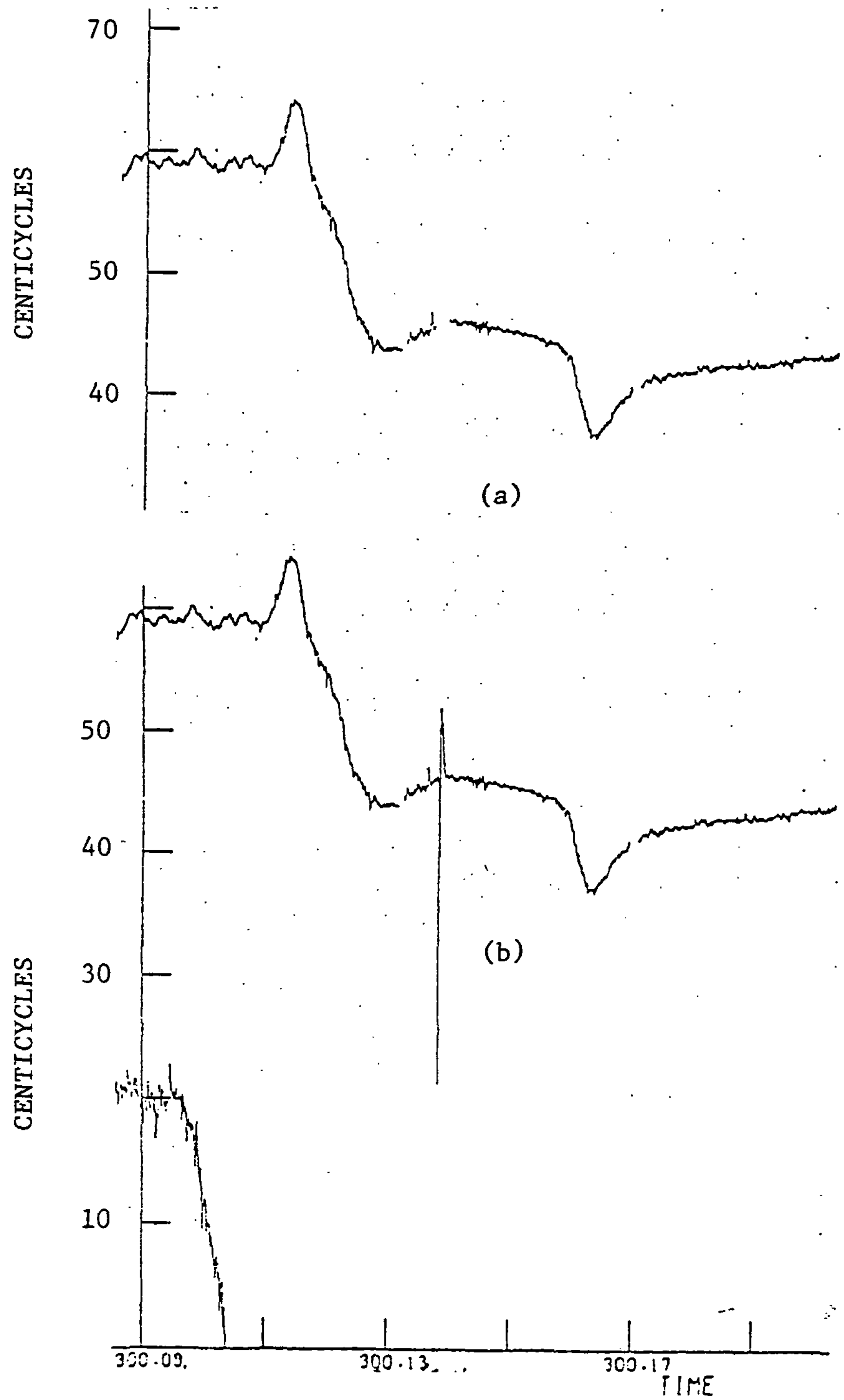

Figure 2-14. Phase of NDK 10.2 kHz Illustrating the Effect of Spike Editing Accomplished with a Computer Algorithm: (a) Phase history with spike removed during hour 13, (b) Original phase history recorded at Yorktown, Va.

an event of this type with a plot of the phase data with a "spike" and a plot of the data after editing. The edited data simply appears as a gap in the plot. There are situations when such phase spikes have occurred in succession so that the edited data may have more than a six minute gap. Within a six minute period a uniform input phase change of approximately 144 cec could conceivably be tracked by the loop (using 4 cec per 10-second sample). Thus, if successive phase changes are compared in a lane counting algorithm, it is necessary to make the sample-to-sample comparison threshold T large enough to allow for within lane changes over at least a six minute period. For the stationary receiver the input relative phase should never change more than 10-15 cec even with appreciable reference oscillator drift.

A second type of noise in recorded phase data generally affects all loops. The effect appears as if an instantaneous shift in reference oscillator phase takes place. Sometimes those phase shifts are recovered, but more often they are not. The recorded phase suddenly experiences a step shift without any apparent loss of track. At some later time the phase may suddenly shift back to an earlier level. Figure 2-15 illustrates two situations described. One involves a recovered situation and one does not. These shifts are normally less than 10 cec but can be up to 50 cec. Note that any shift greater than 50 cec in one direction can be interpreted as a shift of less than 50 cec in the opposite direction since no lane counting is inherently a part of the receiver. In any continuous analysis of individual transmitter phase data, it is necessary to detect these apparent reference phase shifts and correct for them.

It should also be noted that some of the early phase data was taken with the receiver loops configured as second order digital loops. In the second order loops, the output phase could conceivably track up to a 29 cec phase shift from one 10-second sample to the next. This does not, of course, affect expected transitions of input phase but does affect the threshold criterion used to detect and edit "spikes" in the data.

To provide for reasonable capability to track the lane changes in relative OMEGA phase when there are periods of missing data through editing, it seems reasonable to use a threshold value T = 50 cec. Thus if $|\Delta\phi| > 50$ the lane count is changed, otherwise the lane count remains the same. Even

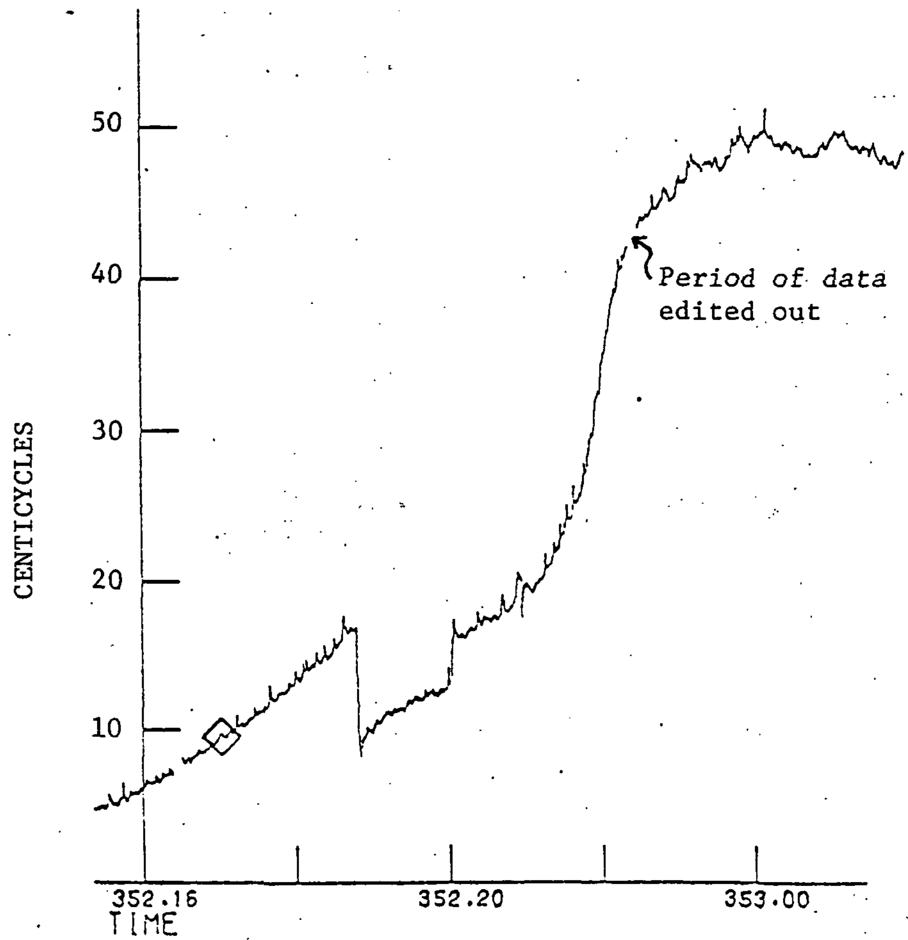

Figure 2-15. (a) Phase History of TRI 10.2 kHz at Hampton, Va. Illustrating the Effect of Apparent Reference Phase Shifts. A shift during hour 18 is essentially recovered in hour 20 without a lane error.

(b) Phase Histories of NOR, TRI, and NDK 13.6 kHz at Rich Mountain, N.C. Illustrating an Apparent Reference Phase Shift During Hour 14 Which is not Recovered. A lane error would be introduced in the NDK and NOR phase at the time of this shift.

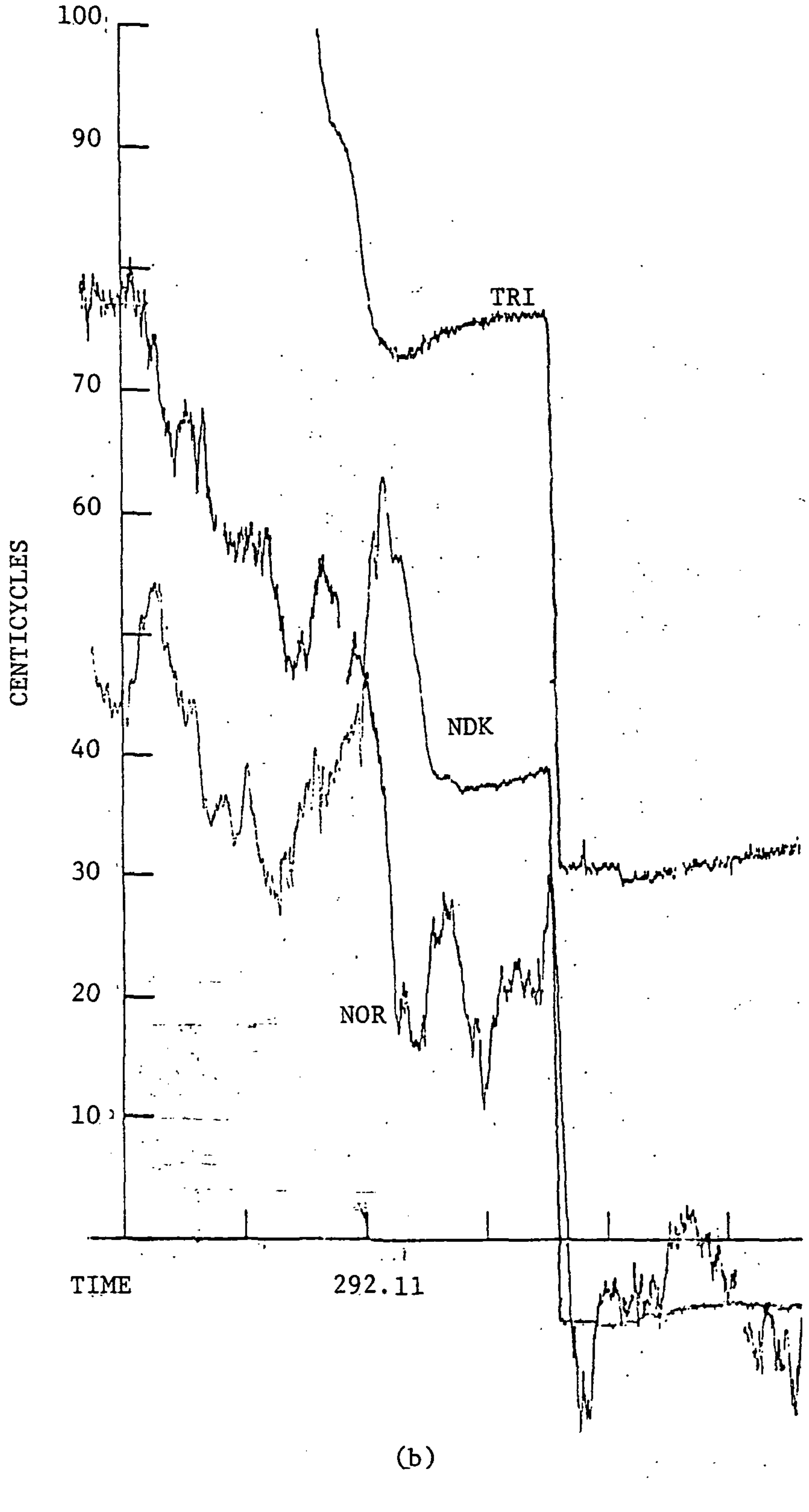

(b)

Figure 2-15. Continued.

with this choice there are situations which will render lane changes invalid. These can be attributed primarily to situations where the reference oscillator phase changes instantaneously. Further editing is necessary to correct for these. Figure 2-16 illustrates a situation in which a valid lane change is tracked correctly. Figure 2-15(b) illustrated a situation where a reference phase jump caused an incorrect lane change.

This pseudo-lane counting algorithm is designed to yield phase data which is consistent on an absolute scale within a data set. When calculating statistical summaries on recorded phase data and on LOP data, this is necessary so that calculation of mean values are valid. Even with lane counting incorporated it is necessary to visually inspect the data to insure correctness. It would require extremely sophisticated and complex routines to yield better results than the method described and even then absolutely error-free lane counting would not be guaranteed.

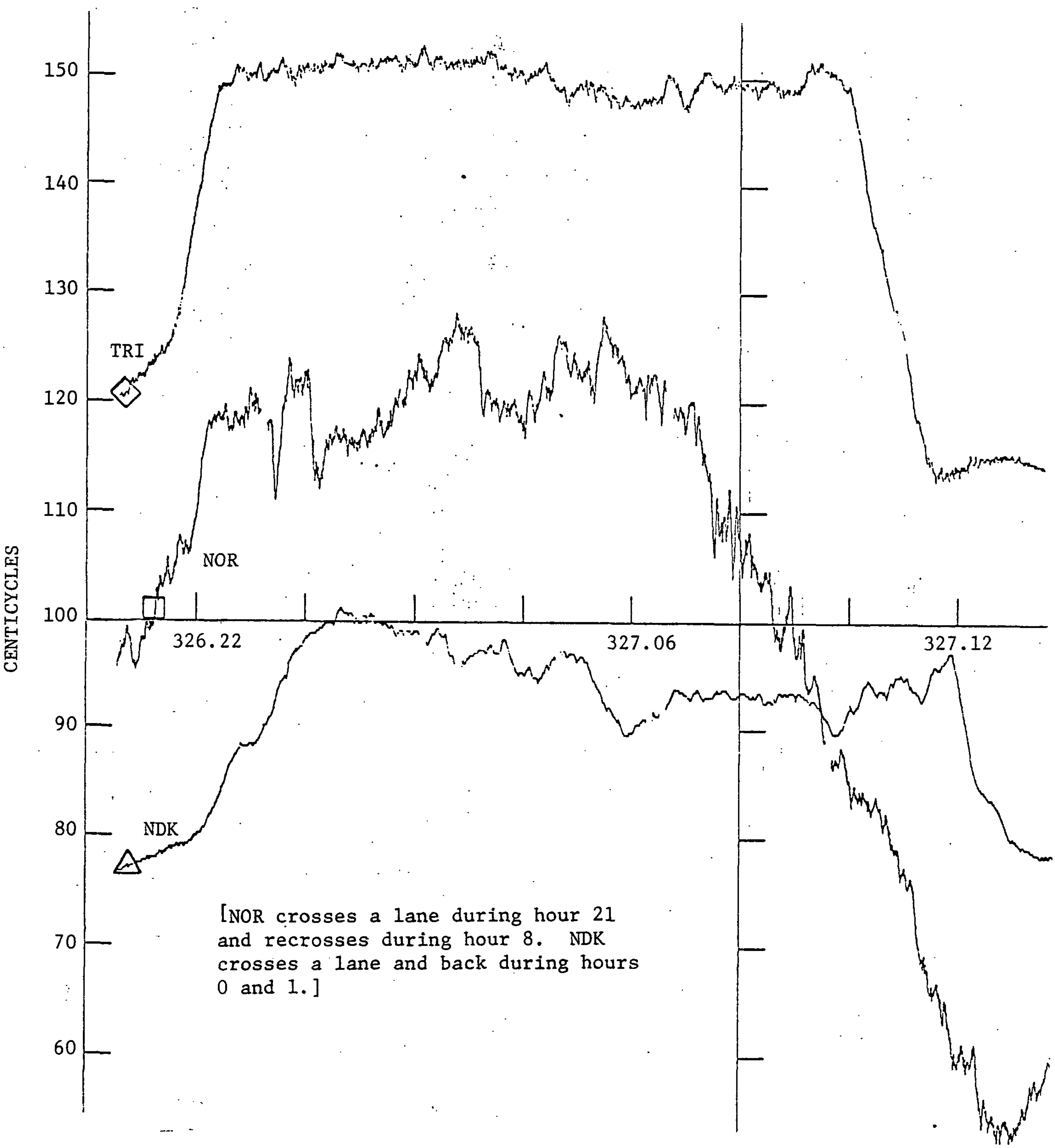

Figure 2-16. Phase History of NOR, TRI, and NDK at Hampton, Va. Illustrating Lane Counting in the Data Which is Valid.

CHAPTER 3

ANALYSIS OF DIFFERENT OMEGA ERROR

Data accumulated over the duration of the ground-based experimental program were reduced to hourly mean phase values for further analysis. One primary reason for this is simply the magnitude of the total data set makes it very difficult to process ten-second samples. Also by using data averaging the low-frequency variations in differential OMEGA, *error can be analyzed essentially independent of any high frequency effects* which may be receiver dependent. For navigation, particularly in an airborne environment, a maximum instantaneous type error description will not be available. However, these are very often largely a function of the receiver, its time-constant, and the effects of receiver vehicle movement. The time constant of the NASA-Langley reciever is by design too large (≈60 seconds) to gain information concerning instantaneous error information relative to the airborne environment. On the other hand, general characteristics of the OMEGA error can be well analyzed. The essence of the analysis to be presented involves evaluation of individual LOP differential phase measurement errors, position estimate errors based upon pairs of LOP measurement, i.e., three station OMEGA data, and position estimate errors using least-square methods of combining LOP measurements from four station OMEGA data. Generally, mean, rms and CEP (circle of error probability) summaries of the various errors are used. In the parametic analysis of differential OMEGA receiver separation, range is of particular interest. Presentation of much of the analysis is segregated by receiver site location for the remote receiver relative to the Hampton location. Three frequency results are presented so that comparison is made at the various OMEGA carrier frequencies.

3.1 Differential Mean

The differential mean phase errors were calculated from ten second differential phase error measurements. Hourly mean values were initially calculated. These were averaged over various periods of the day for each data set according to whether the data hour was transition period, full daylight, or nighttime. Full data set mean values were also calculated. Mean values have been segregated on the basis of LOP station pair and frequency. Values obtained from the Tracor phase measurements are treated separately from those with the digital receivers. In each of Figures 3-1 through 3-6 the independent variable is the square-root of separation range between Hampton, Virginia, and the respective remote receiver site. At each range value, one point is plotted as the mean of each available data set at the location. The curves represent connected straight line segments between the mean error considering all data sets available at each site.

In Figures 3-1 through 3-6 the leftmost range value in each of these plots corresponding to LRC is $\Delta R=0$ or side-by-side (SxS). The spread in these mean values from data set to data set is generally less than 5.0 cec at any frequency but appears greater in the full daylight condition than for other time periods. For other ranges this time of day characteristic is not generally true. It should be noted that only one data set was available for six of the sites: FOU, CHA, WAN, MID, BLC, and WEE. Therefore, no information relative to variations in the mean is shown. For large ΔR, the RMT location was used for several data periods in Figure 3-1. For LOP AB there is a definite negative mean phase error and the magnitude correlates with frequency. It can be noted that this error is generally larger in magnitude than at closer ranges, although the sign of the mean error does fluctuate for closer ranges. This same effect may be observed in Figures 3-2 and 3-3 also. With LOP BD (Figure 3-5) the mean values are generally smaller, which can be expected with the stronger OMEGA signals. Also, the RMT mean values are positive except for 13.6 kHz. This appears to be the result of a modal interference shift at 13.6 kHz in North Dakota. Similar effects are observed at BDF, NCC and THV, which are all very near a critical distance from North Dakota. Similar negative means are observed at these sites for LOP BC in Figure 3-4. However, with LOP BC there exists more correlation between frequencies. The nighttime shift of North Dakota on 13.6 kHz is quite apparent in Figure 3-6(c) on LOP CD.

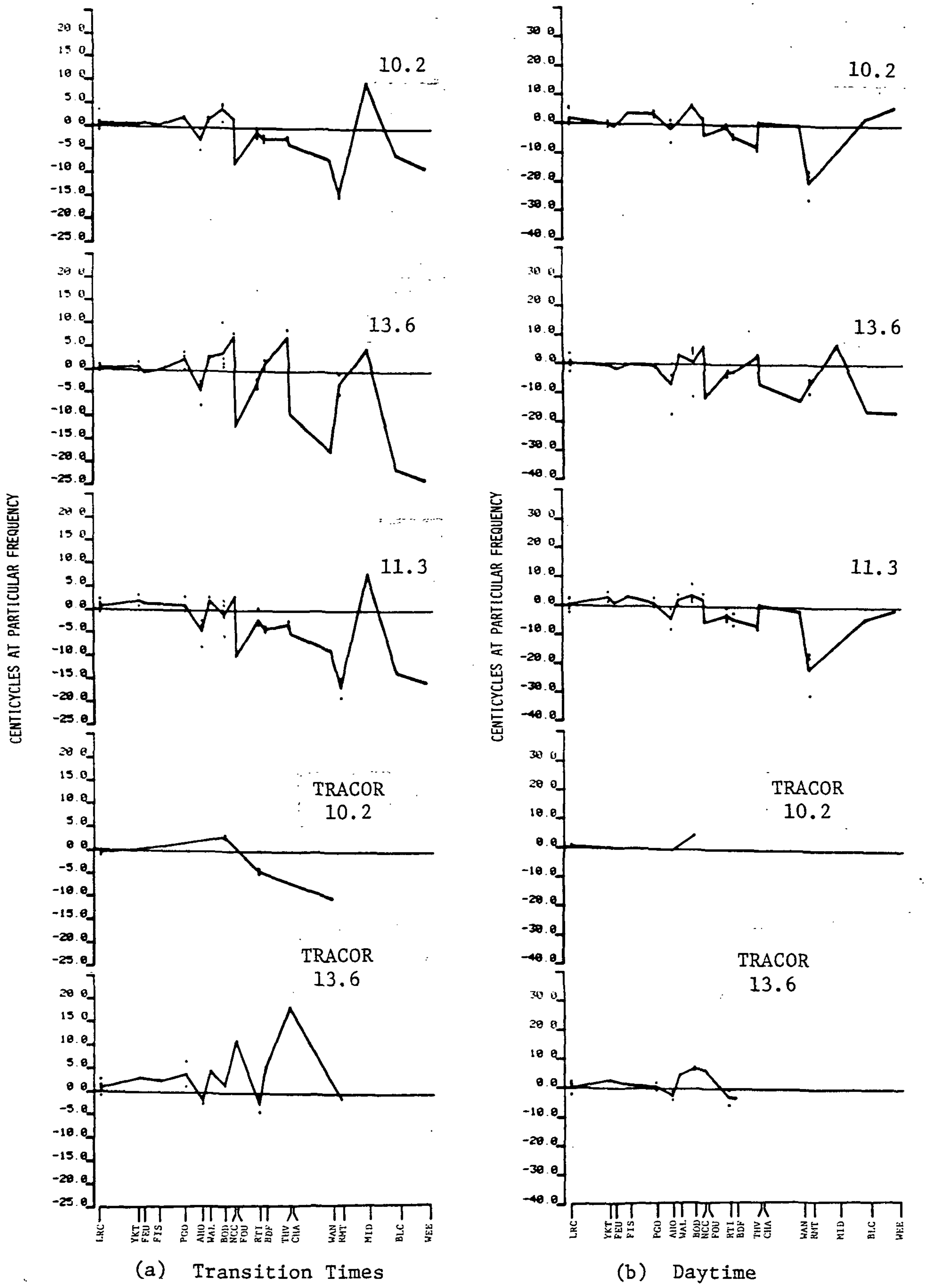

Figure 3-1. Data Set Mean Differential Error vs. Separation Range for Norway-Trinidad LOP.

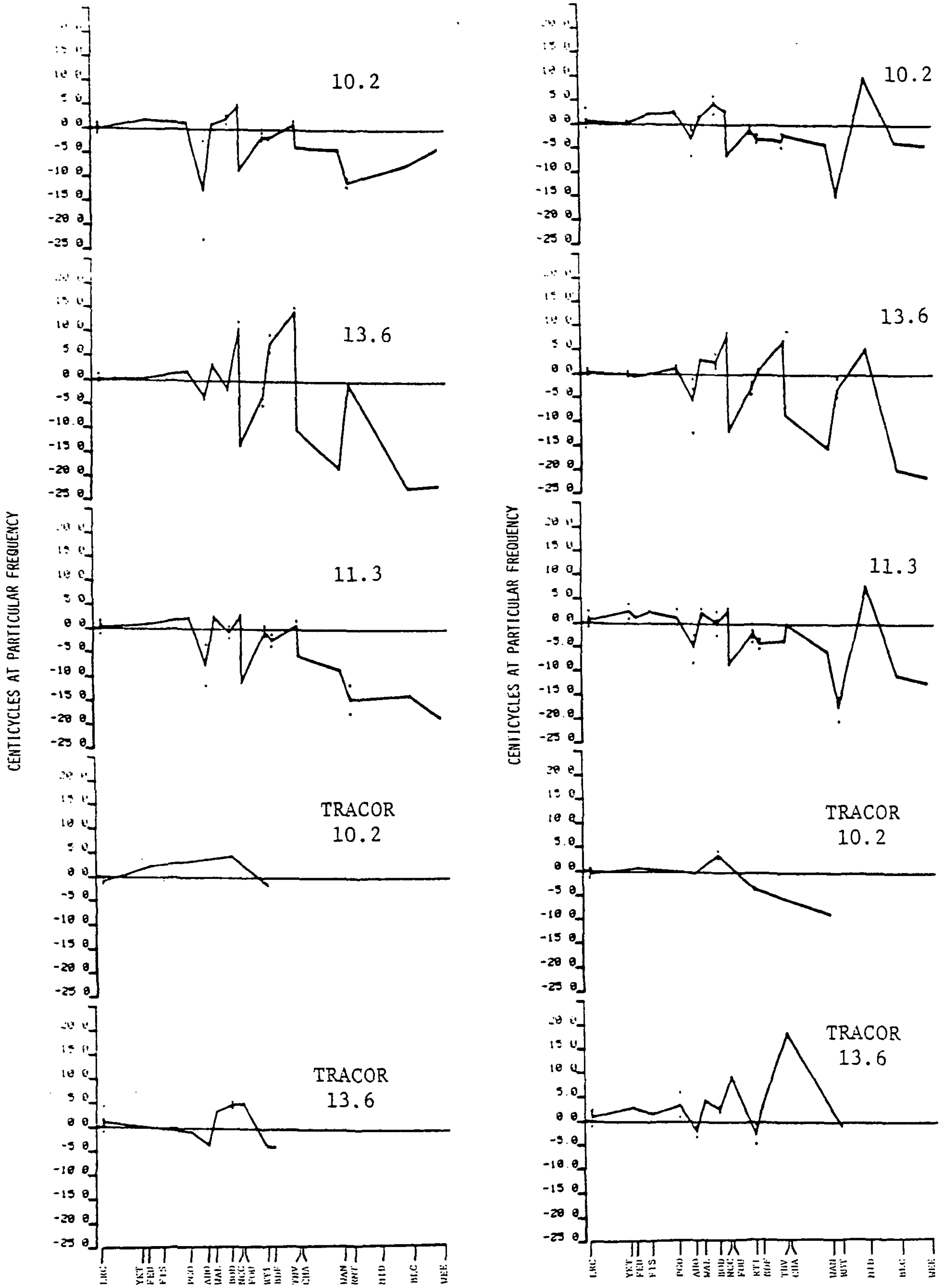

(c) Nighttime

(d) Total Time

Figure 3-1. Continued

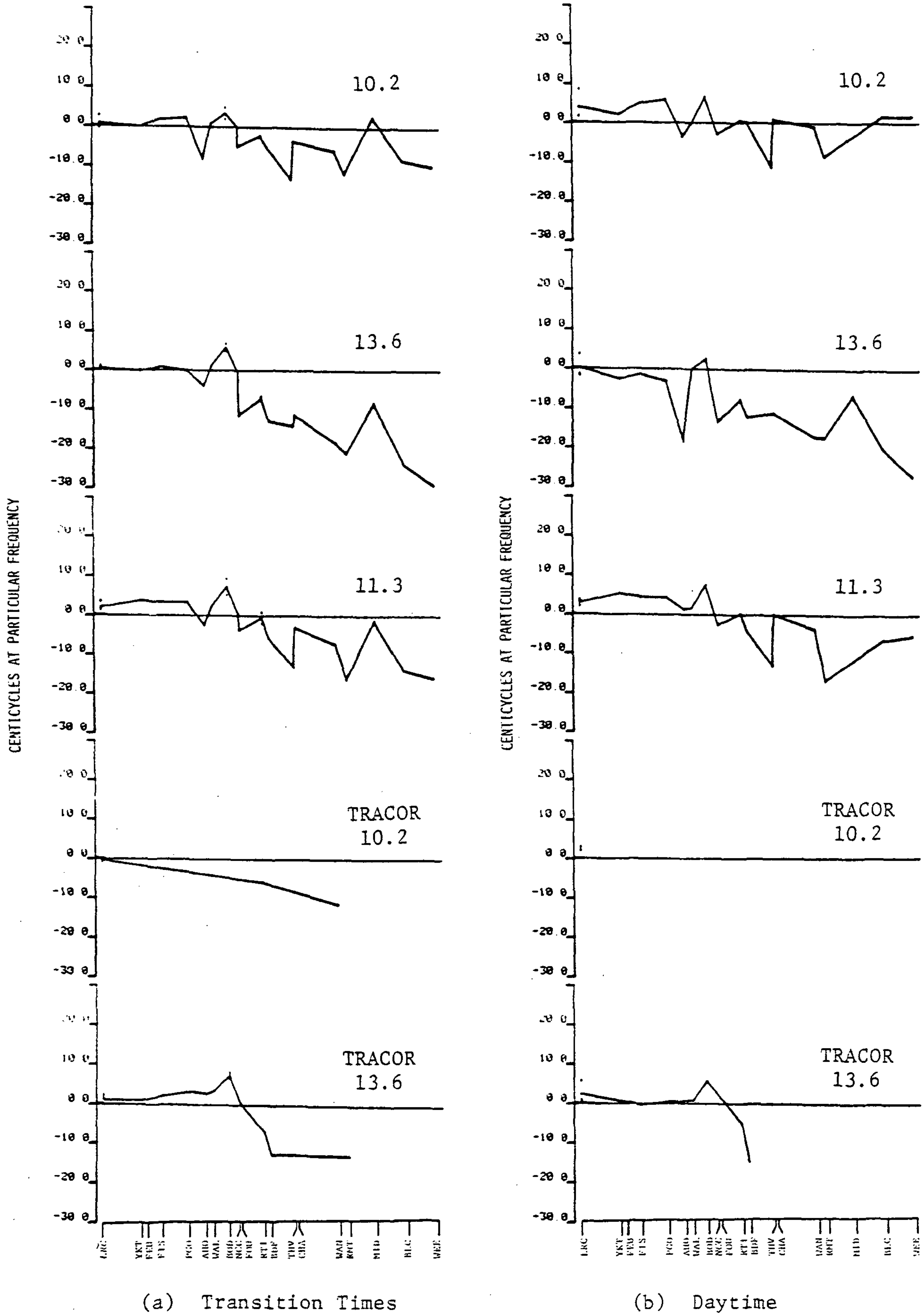

Figure 3-2. Data Set Mean Differential Error vs. Separation Range for Norway - Hawaii LOP.

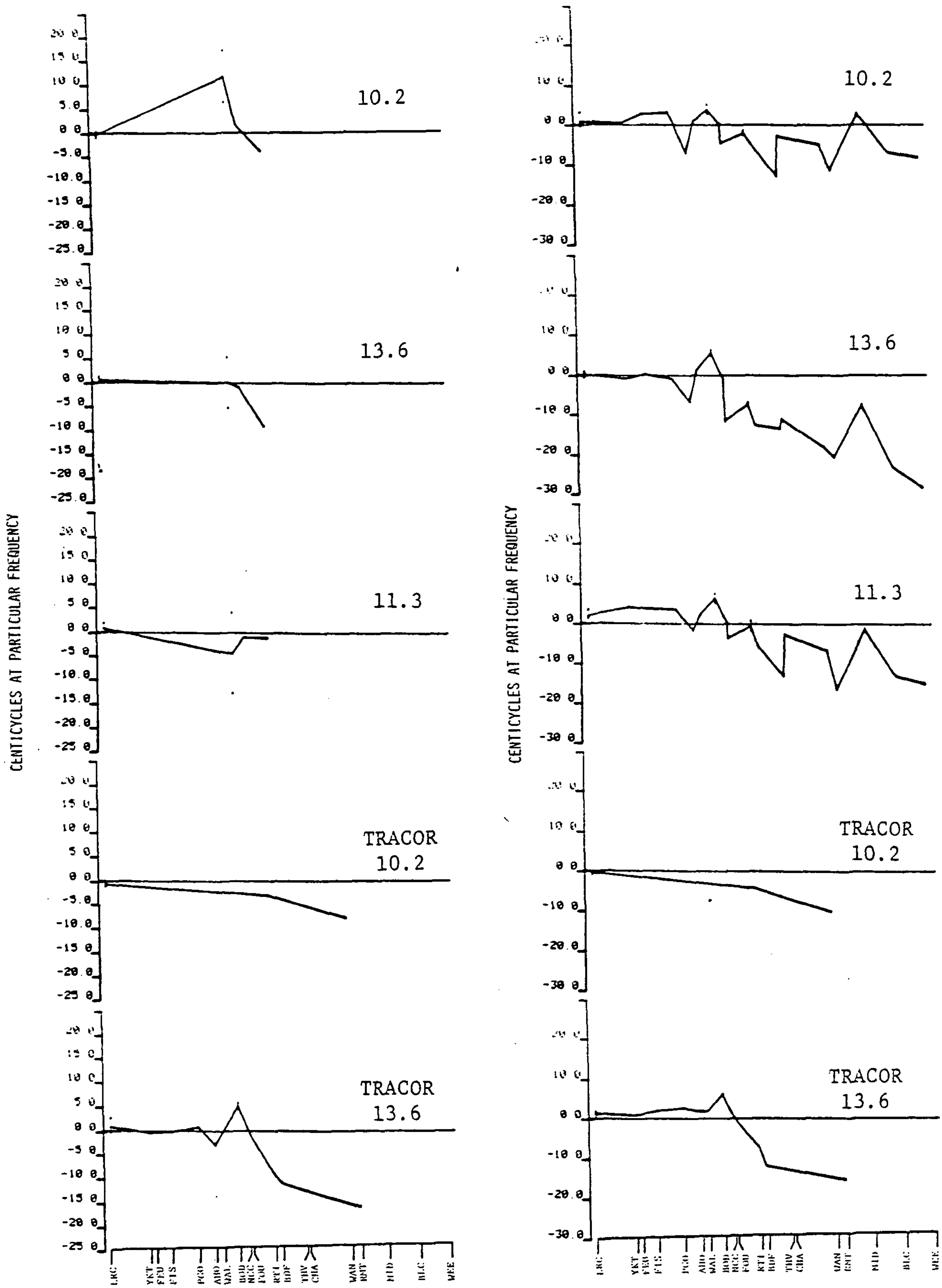

(c) Nighttime

(d) Total Time

Figure 3-2. Continued

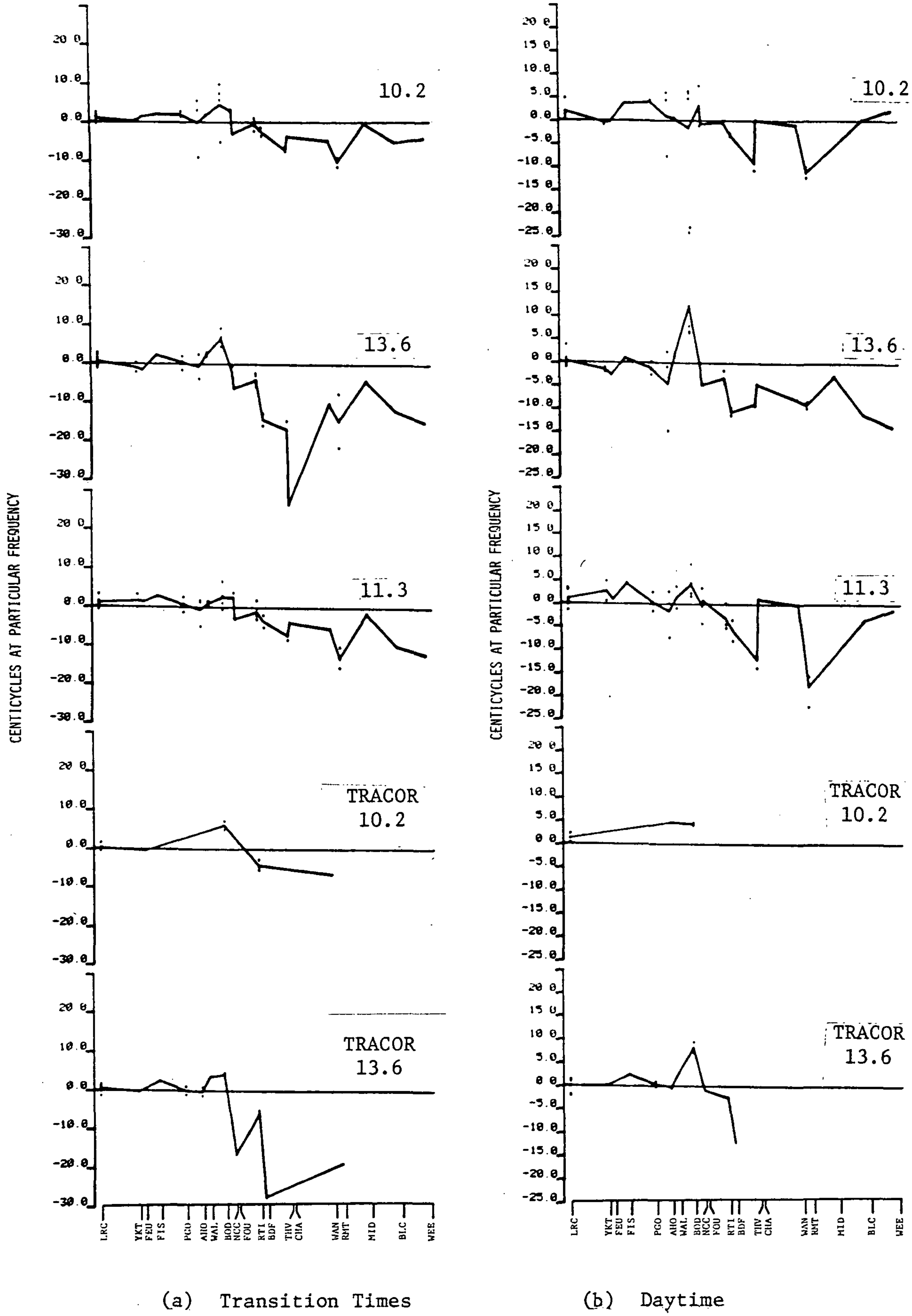

Figure 3-3. Data Set Mean Differential Error vs. Separation Range for Norway - N. Dakota LOP.

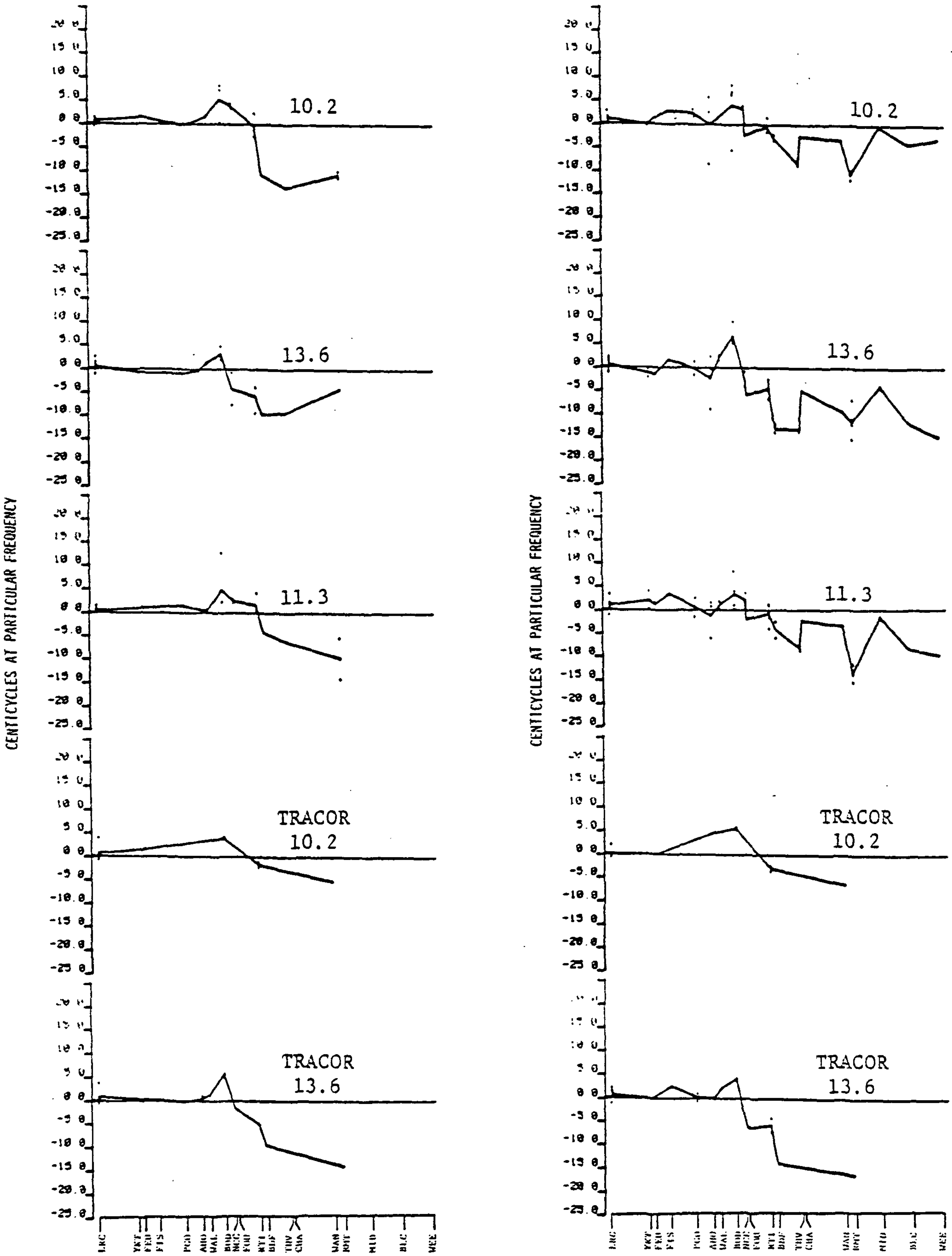

(c) Nighttime

(d) Total Time

Figure 3-3. Continued

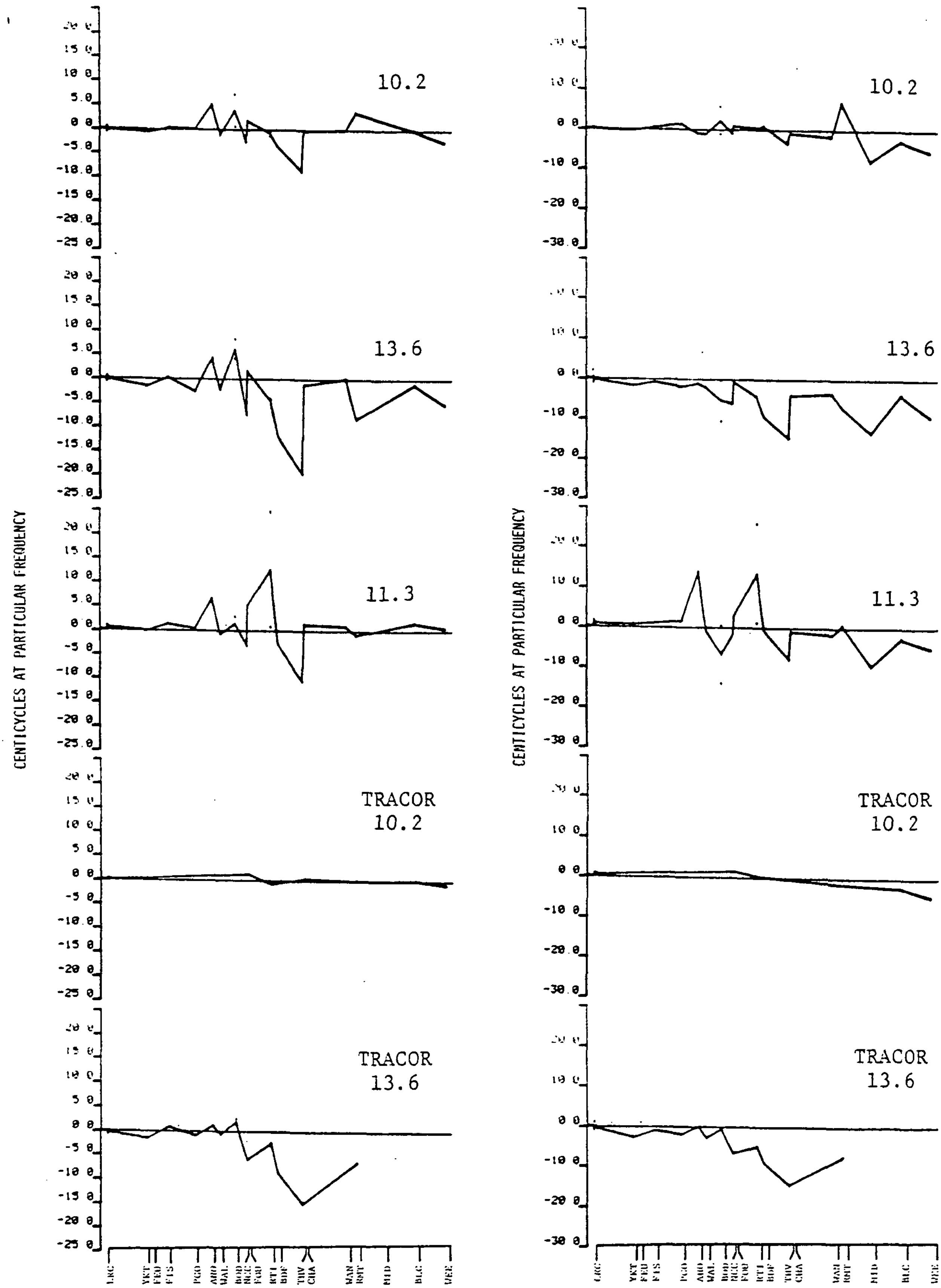

(a) Transition Times (b) Daytime

Figure 3-4. Data Set Mean Differential Error vs. Separation Range for Trinidad - Hawaii LOP.

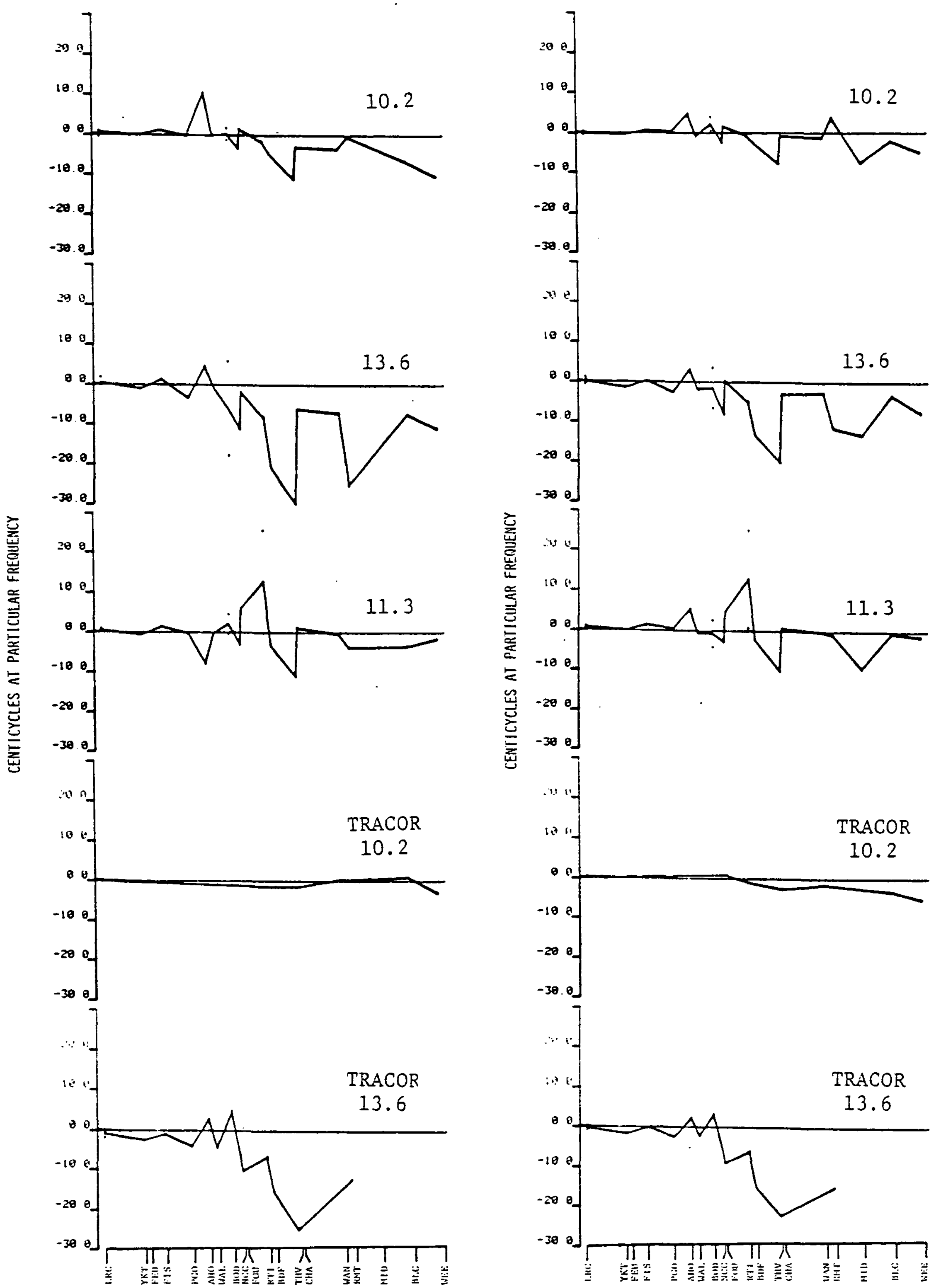

(c) Nighttime

(d) Total Time

Figure 3-4. Continued.

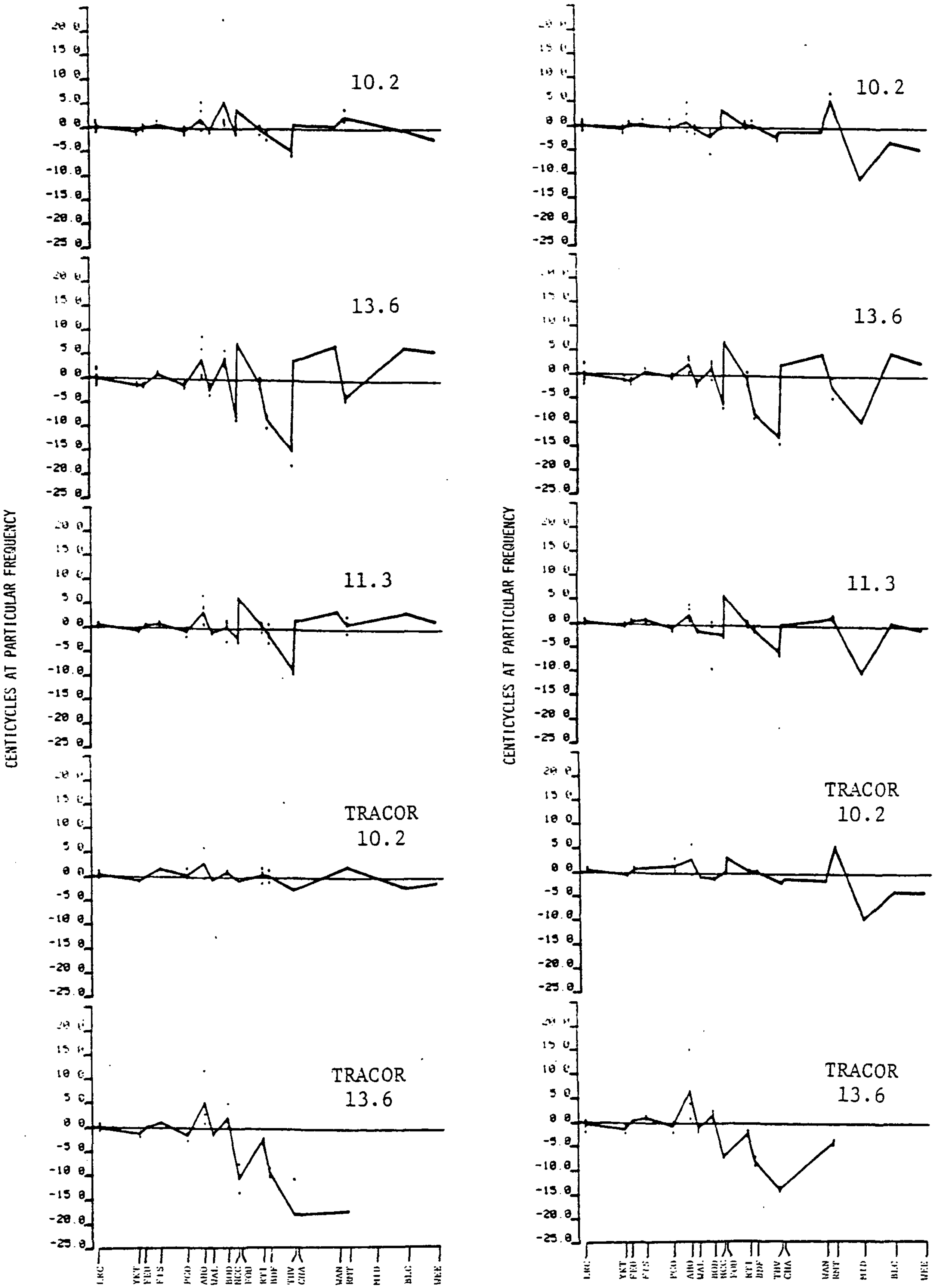

(a) Transition Times

(b) Daytime

Figure 3-5. Data Set Mean Differential Error vs. Separation Range for Trinidad - N. Dakota LOP.

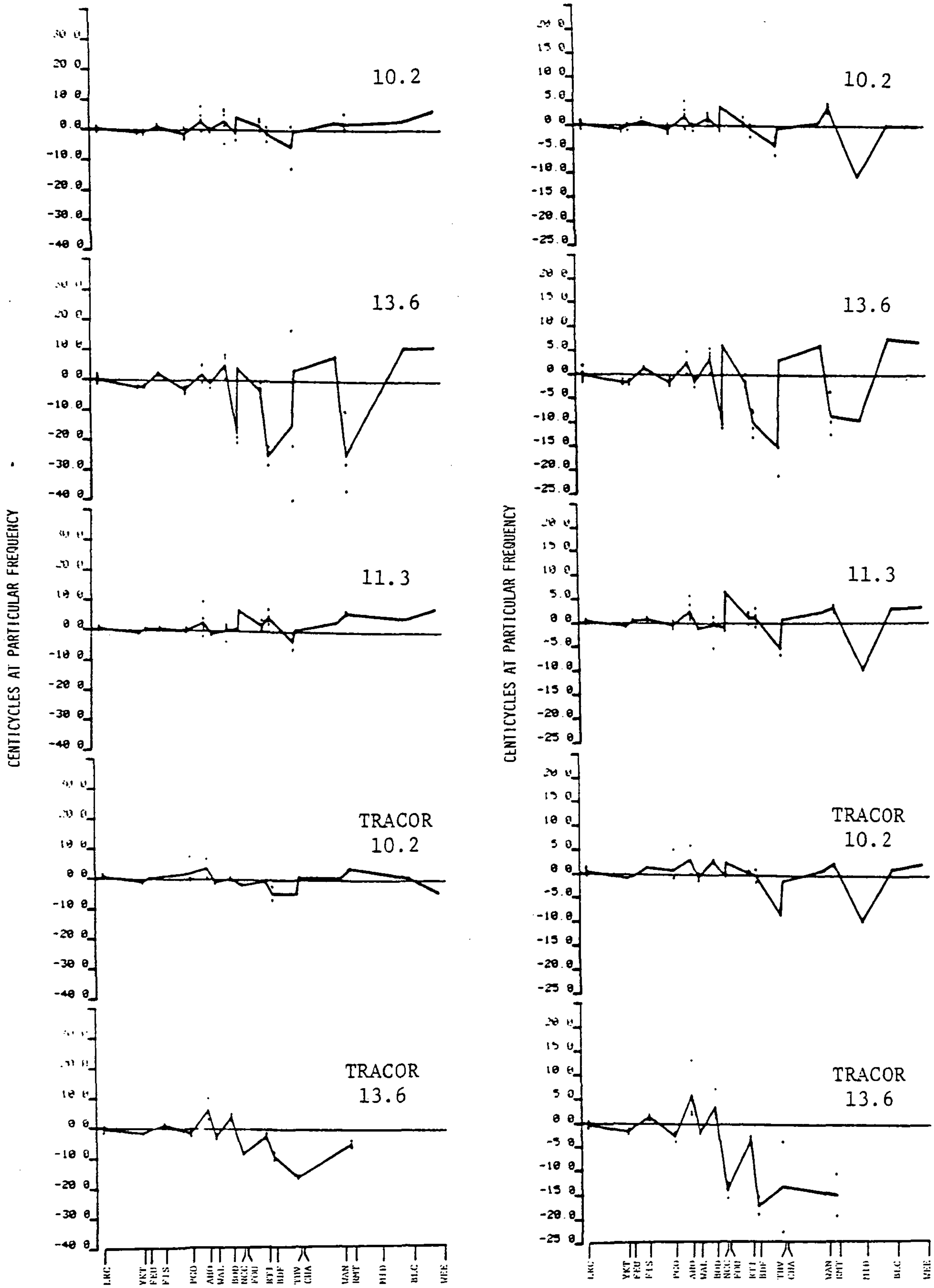

(c) Nighttime

(d) Total Time

Figure 3-5. Continued.

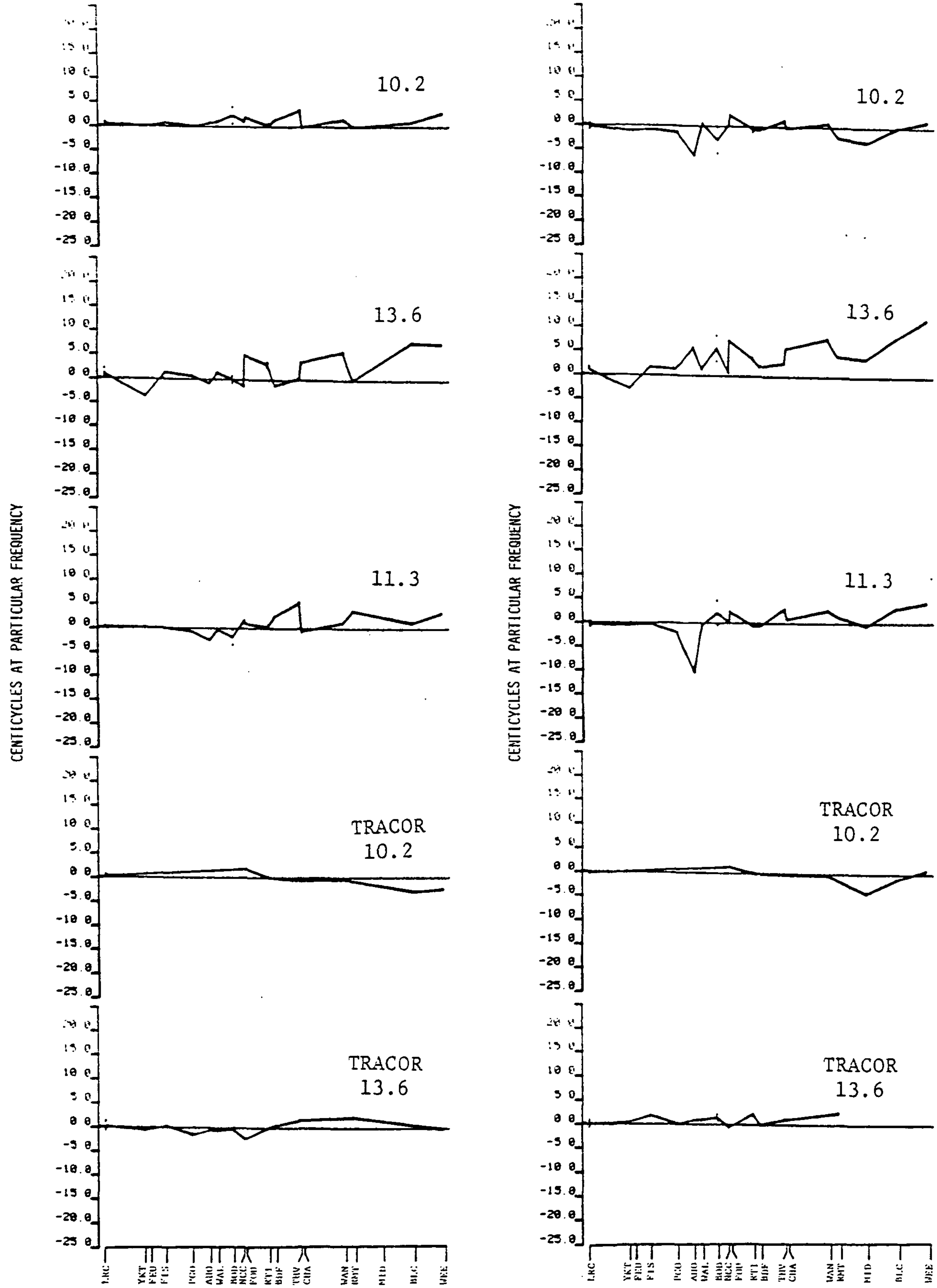

(a) Transition Times (b) Daytime

Figure 3-6. Data Set Mean Differential Error vs. Separation Range for Hawaii - N. Dakota LOP.

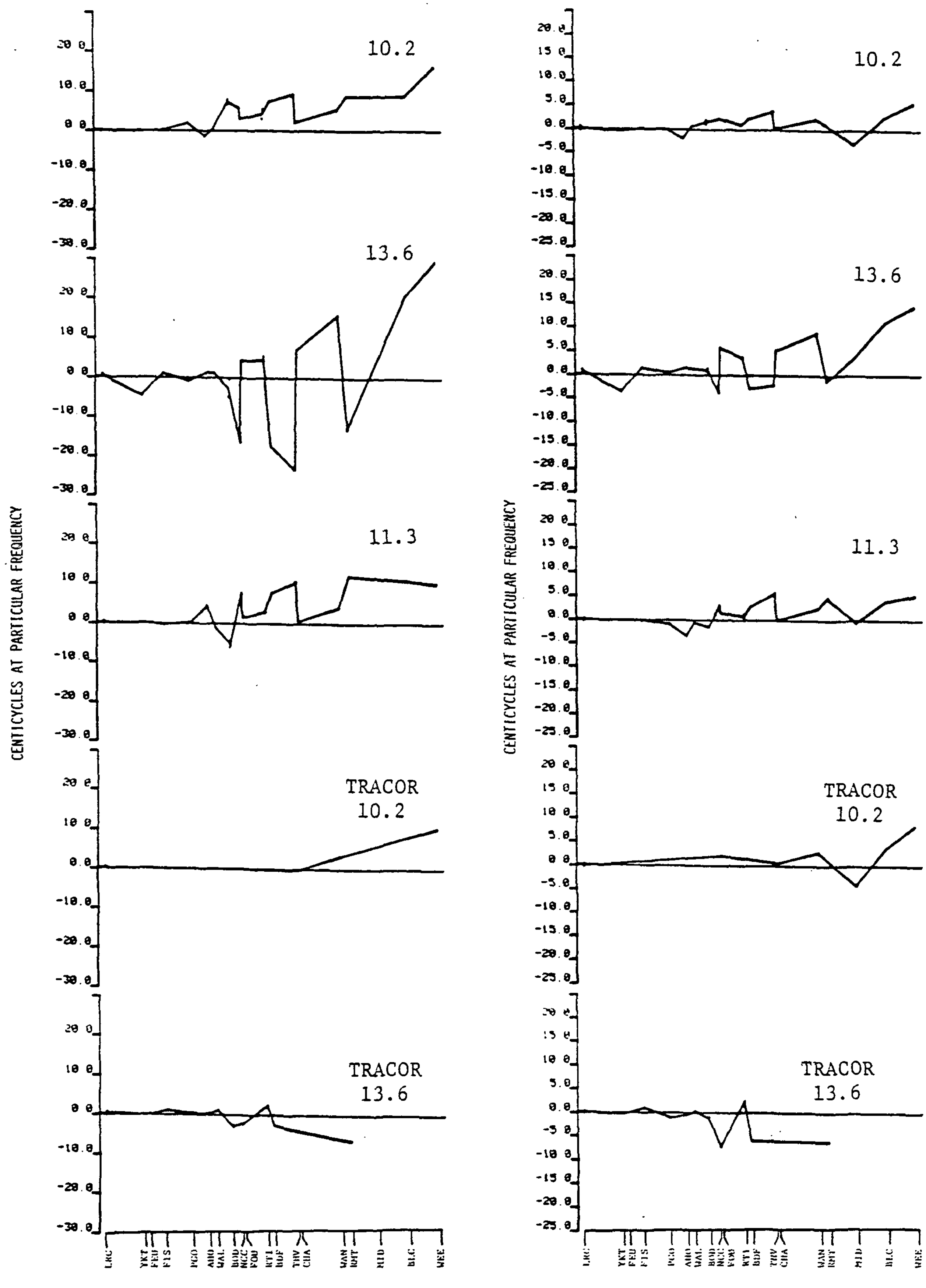

(c) Nighttime

(d) Total Time

Figure 3-6. Continued.

Although the data are more limited for the Tracor receiver and the variation in the data set means is larger, there is good correlation with the DPLL receiver data. For all LOPs the mean error within a 50 mile range is almost always less than 3-5 cec, which is a significant result. Beyond that range, the inability to predict the mean due to dispersion, local effects, and primarily decorrelation error introduces significant variation in accuracy. Further discussion will follow relative to navigation position errors with differential OMEGA, which probably are more relevant.

In Figures 3-7 through 3-12 the standard deviation of hourly differential mean values for each data set is shown. These represent full period statistics and are plotted against differential range square root for each LOP and frequency. The solid lines are straight line segment connections between the overall mean value of this standard deviation value at each site. Two locations have predominantly large variations on all LOPs: Ahoskie and Bodie Island. This large variation is apparent at all frequencies which would seem to prelude a local effects problem, such as power line interference, as a contributing factor. For LOPs involving Norway, the variation in mean values for the side-by-side situation is on the order of 3-5 cec at each frequency, with the 11.3 kHz frequency showing the smallest standard deviation values and the least variation. With the Trinidad-Hawaii LOP all three frequencies show variations within 2 cec for side-by-side with an outlier at 11.3 kHz. For Trinidad-N. Dakota, the 13.6 kHz shows the least variation while for Hawaii-N. Dakota, the 11.3 kHz shows the smallest variation.

Overall, there is some increase in standard deviation with separation range, but it is not very significant. In fact, the Midway location was an unusually low standard deviation for all LOPs. There is only limited data available for this site however. The Tracor receiver data is not as extensive as for the other receiver because only one frequency was tracked during each set-up. It is difficult to conclude that the Tracor measurements have less mean variation than was exhibited by the digital receiver.

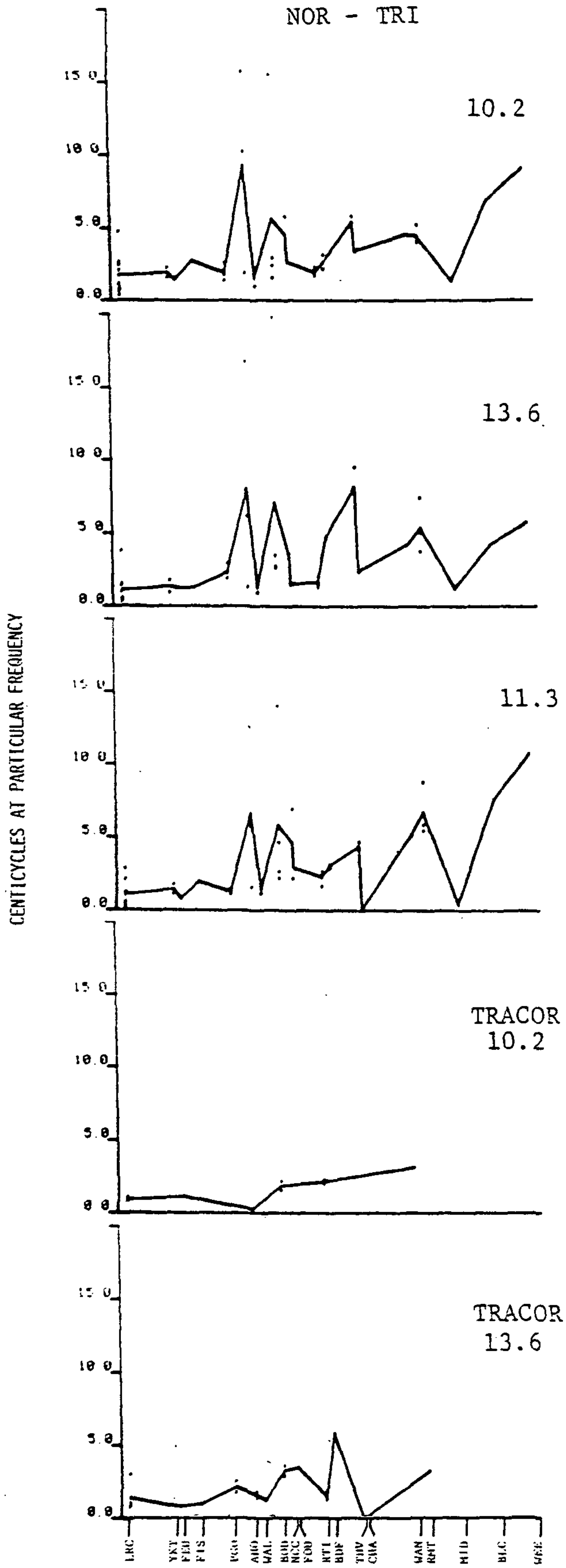

Fig. 3-7. Norway-Trinidad LOP Standard Deviation of Hourly Differential Mean for Each Data Set.

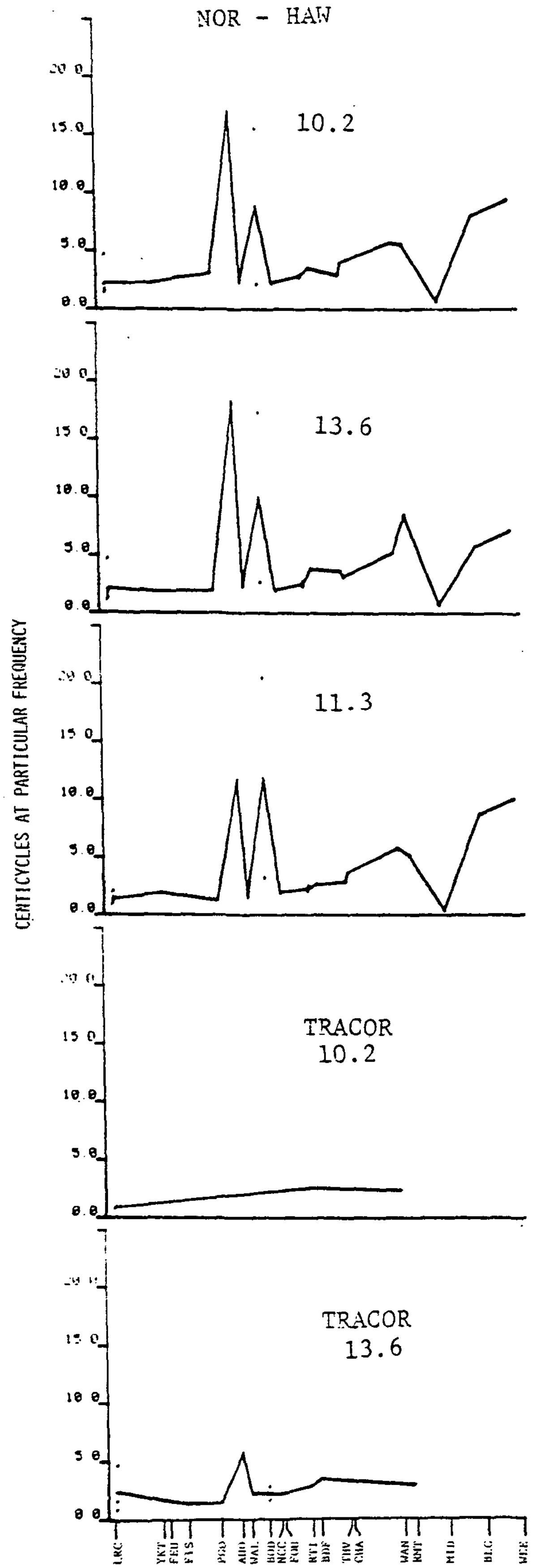

Fig. 3-8. Norway-Hawaii LOP Standard Deviation of Hourly Differential Mean for Each Data Set.

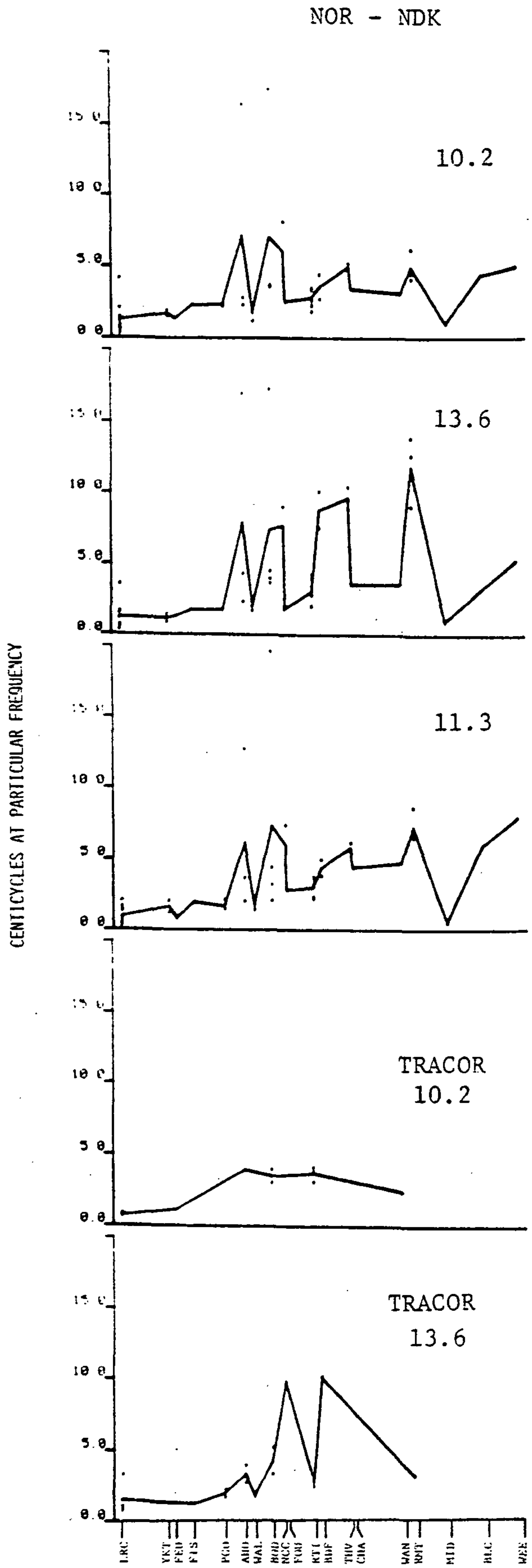

Fig. 3-9. Norway-N. Dakota LOP Standard Deviation of Hourly Differential Mean for Each Data Set.

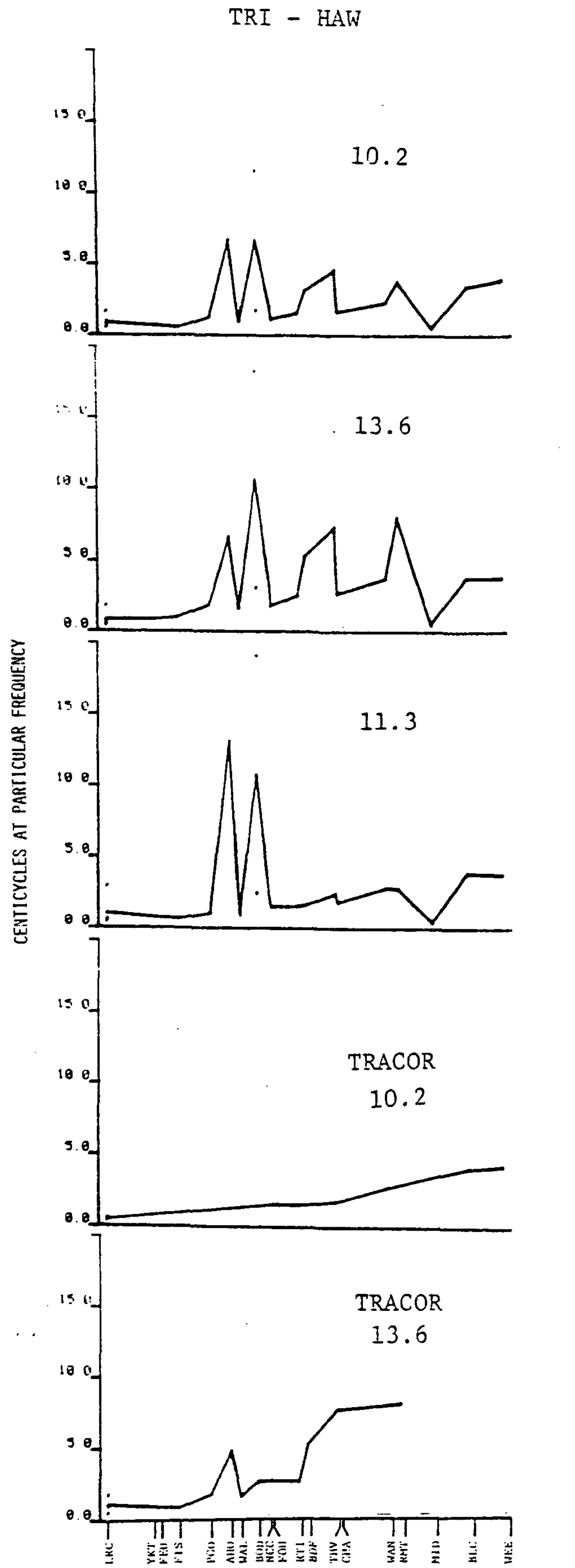

Fig. 3-10. Trinidad-Hawaii LOP Standard Deviation of Hourly Differential Mean for Each Data Set.

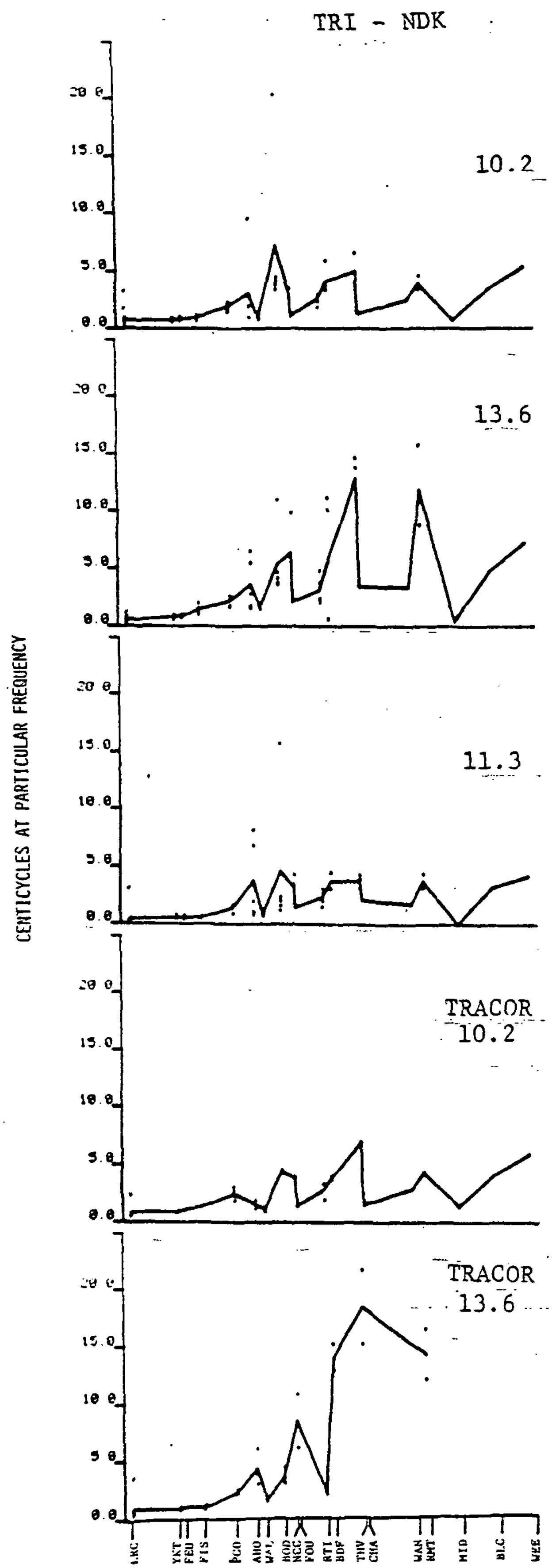

Fig. 3-11. Trinidad-N. Dakota LOP Standard Deviation of Hourly Differential Mean for Each Data Set.

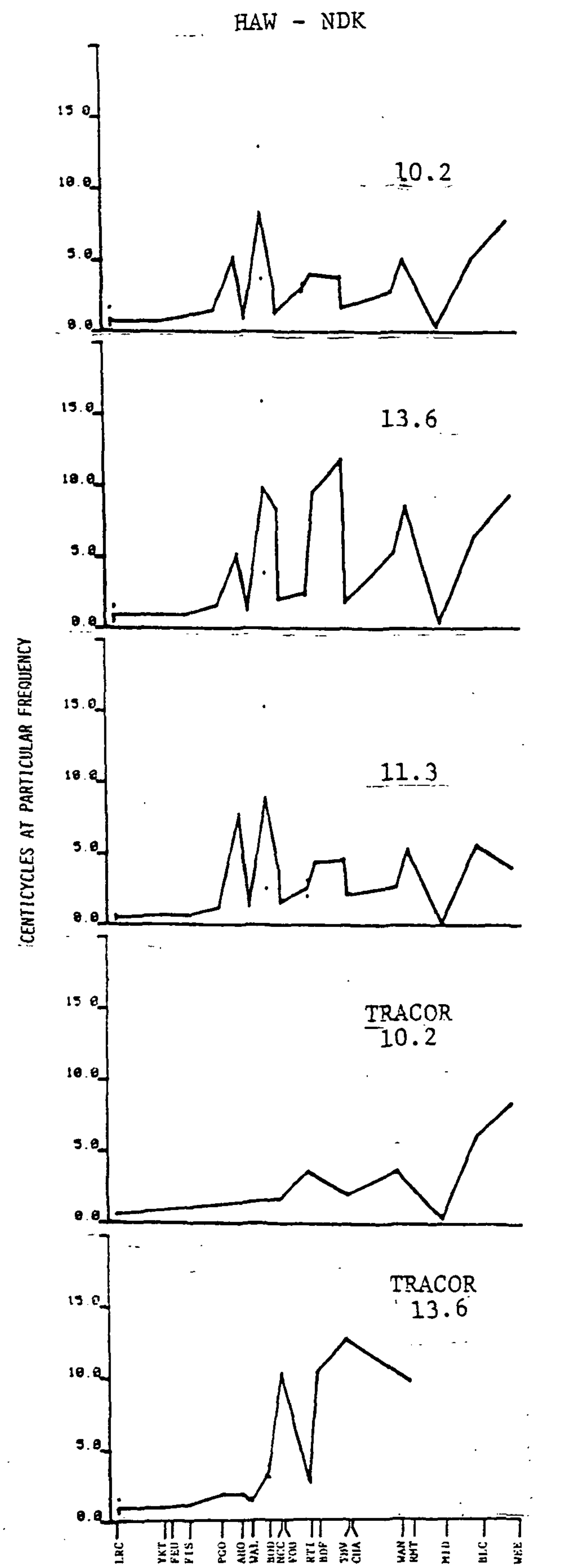

Fig. 3-12. Hawaii-N. Dakota LOP Standard Deviation of Hourly Differential Mean for Each Data Set.

3.2 Differential Average Hourly Error Standard Deviation

The differential phase error analysis included calculation of an hourly standard deviation for each hour at each receiver location. These standard deviation values were averaged over various time periods to arrive at daytime, nighttime, transition period, and full 24-hour period average hourly standard deviations. These values have been organized by LOP and frequency, and are presented as a function of the square root of separation distance between the respective receiver sites and Hampton, Virginia. Plots of these analyses are presented in Figures 3-13 through 3-18. These presentations represent the effects of statistical decorrelation error and inherent receiver repeatability type error. Individual data points at the ranges indicate the average for a particular receiver set-up (data period), while the curves are straight line segments interconnecting the mean of each of these data points at the respective separation range.

There is a general trend for the average hourly standard deviation of differential phase error to increase with receiver separation range. However, the increase with range is not significant. The linear variation of these plots does indicate an exponential relationship between differential phase error standard deviation and receiver separation range. Local effects are quite evident in these presentations and appear to be a dominating effect. The Wallops Island, Virginia location is consistently very quiet in that the average hourly error standard deviation is generally less than all other locations except side-by-side. The side-by-side standard deviation is a good measure of the uncorrelated receiver error and is generally less than 1 cec at each frequency with the digital receivers. With the Tracor receiver this error is larger on the average, generally between 1 and 2 cec. Signal-to-noise ratio is an important consideration with the Tracor receiver since the LOPs involving Norway (A) generally have larger side-by-side errors. It can be noted that the BD LOP errors on Tracor compare more favorably with the digital receiver, particularly during the daytime at 13.6 kHz. These are the two stongest signals and with the digital receiver there is very little variation in

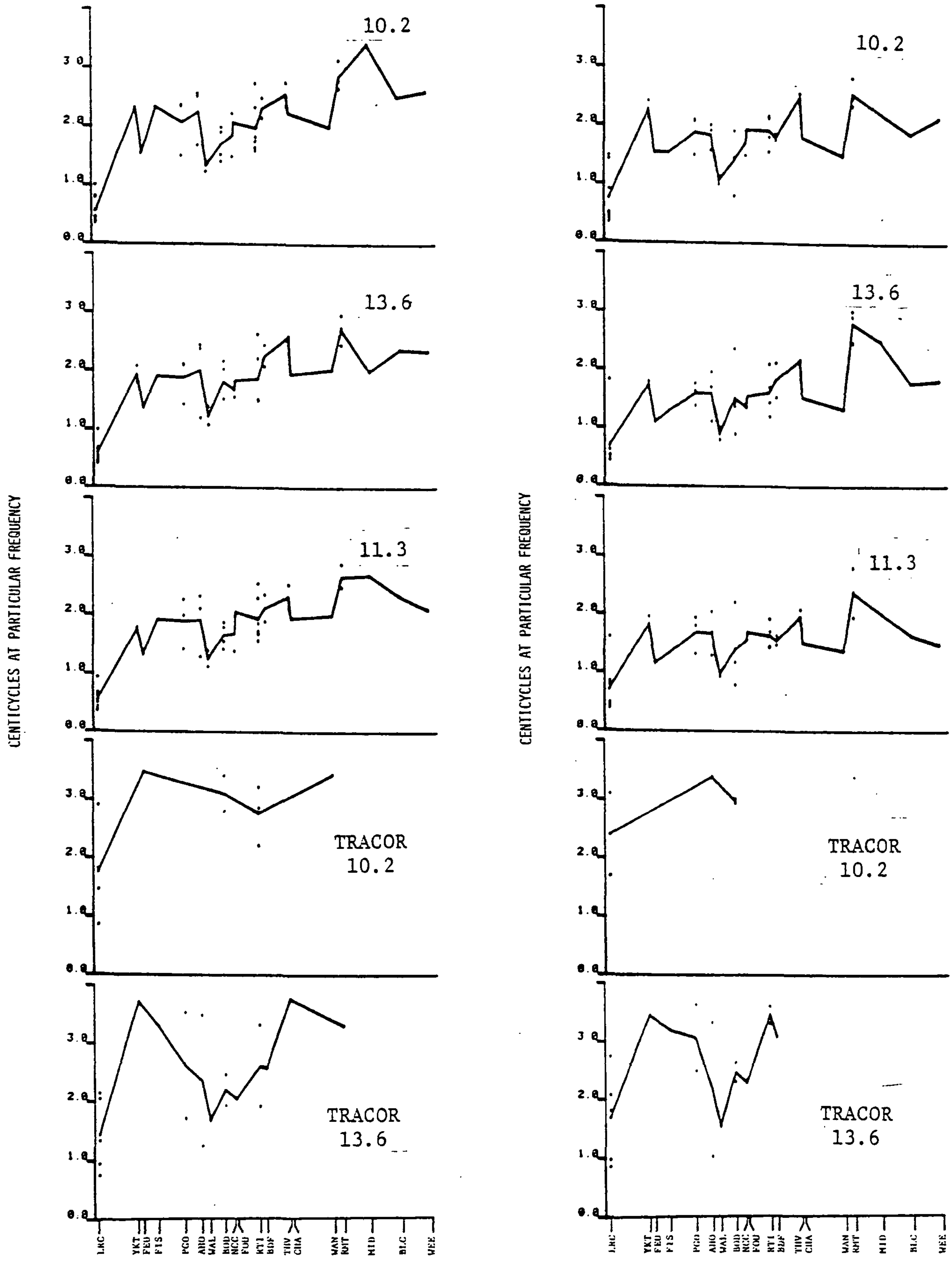

(a) Transition Time (b) Daytime

Figure 3-13. Data Set Differential Average Hourly Error Standard Deviation vs. Separation Range for Norway - Trinidad LOP.

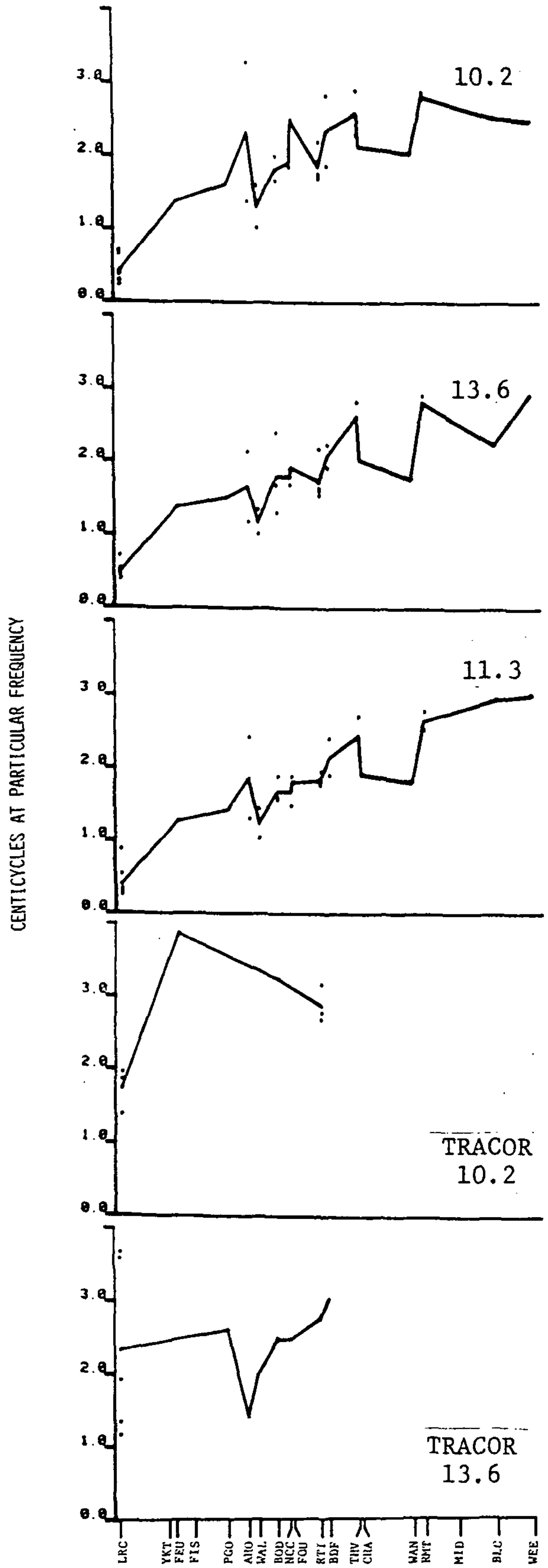

(c) Nighttime

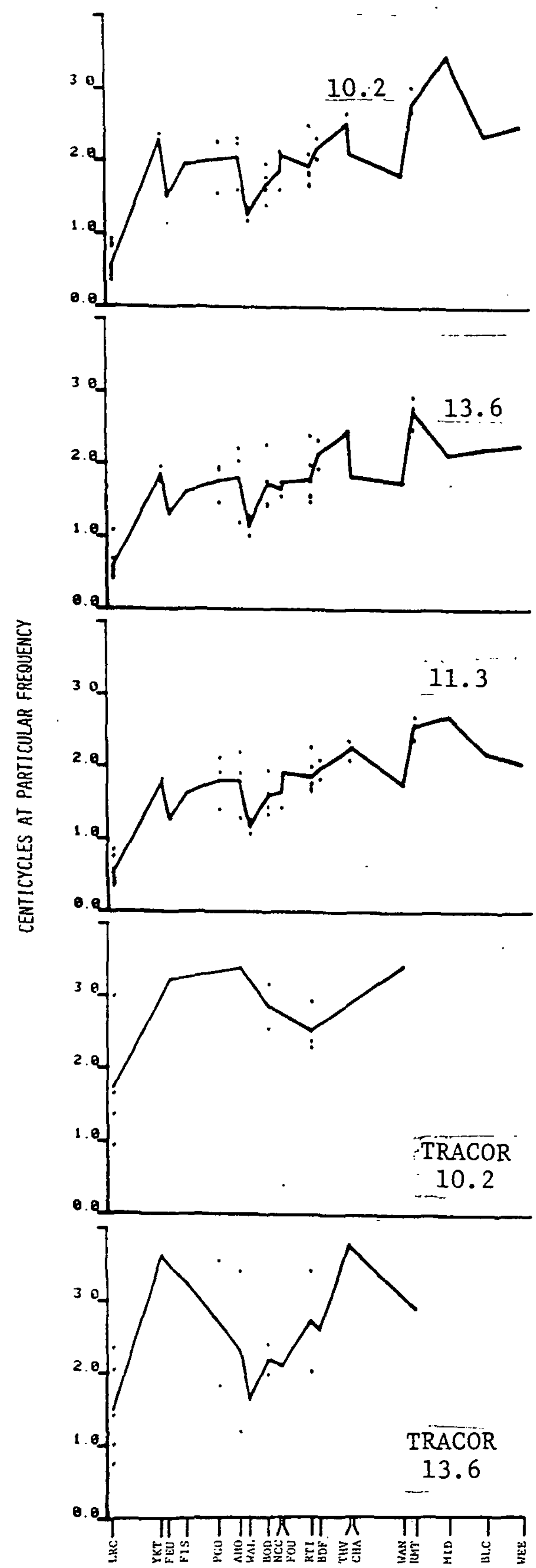

(d) Total Time

Figure 3-13. Continued.

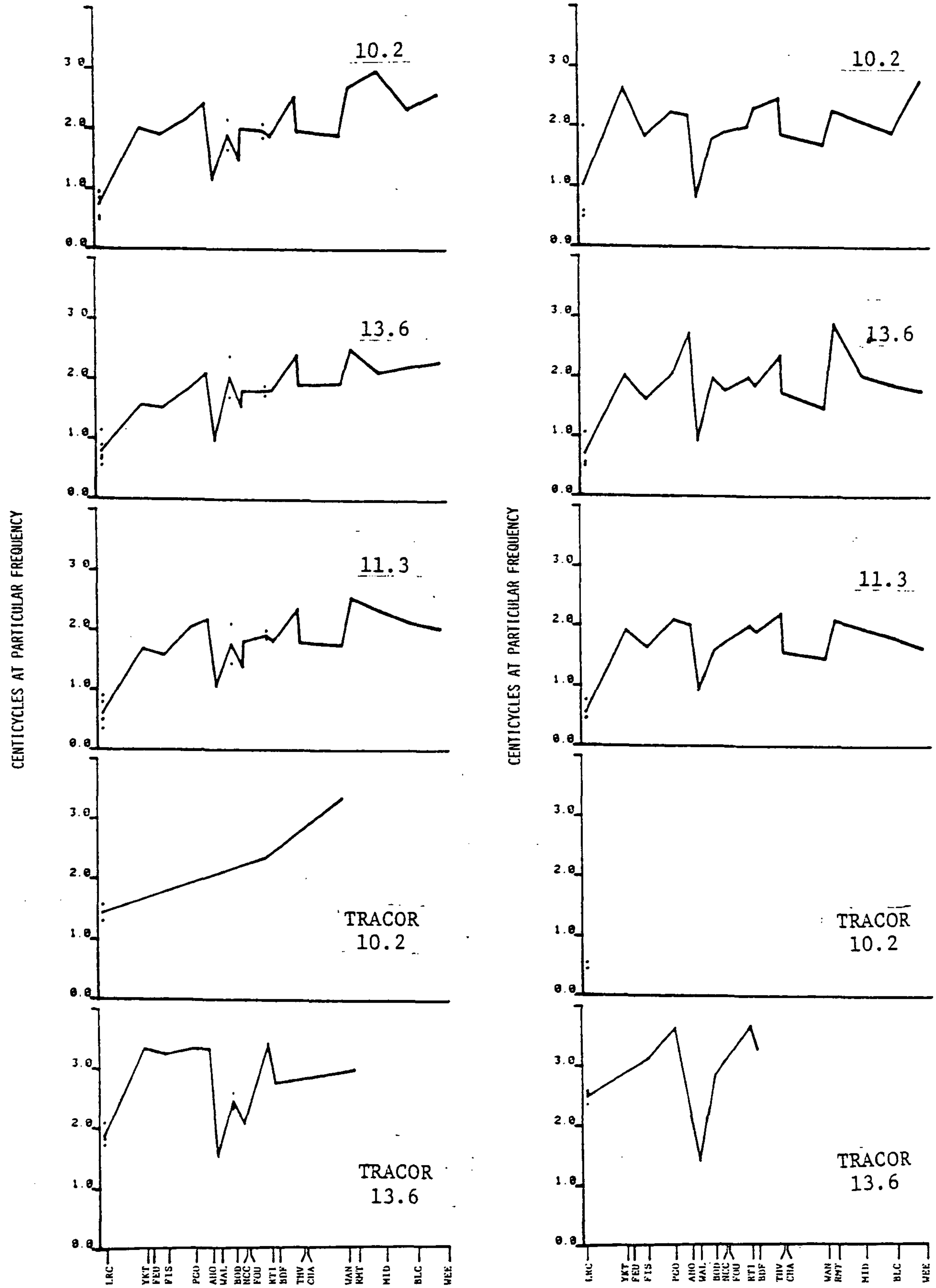

(a) Transition Time (b) Daytime

Figure 3-14. Data Set Differential Average Hourly Error Standard Deviation vs. Separation Range for Norway - Hawaii LOP.

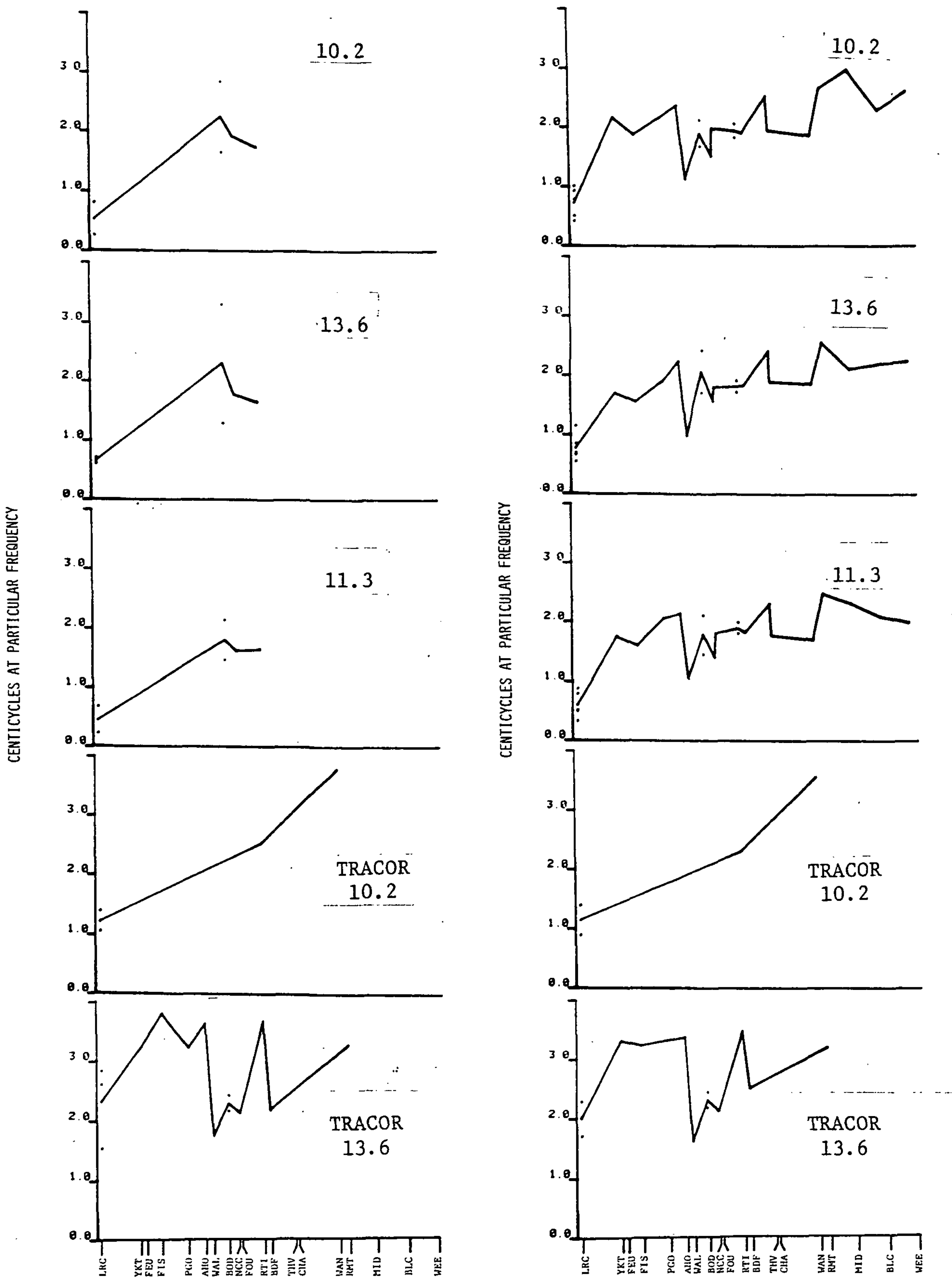

(c) Nighttime

(d) Total Time

Figure 3-14. Continued.

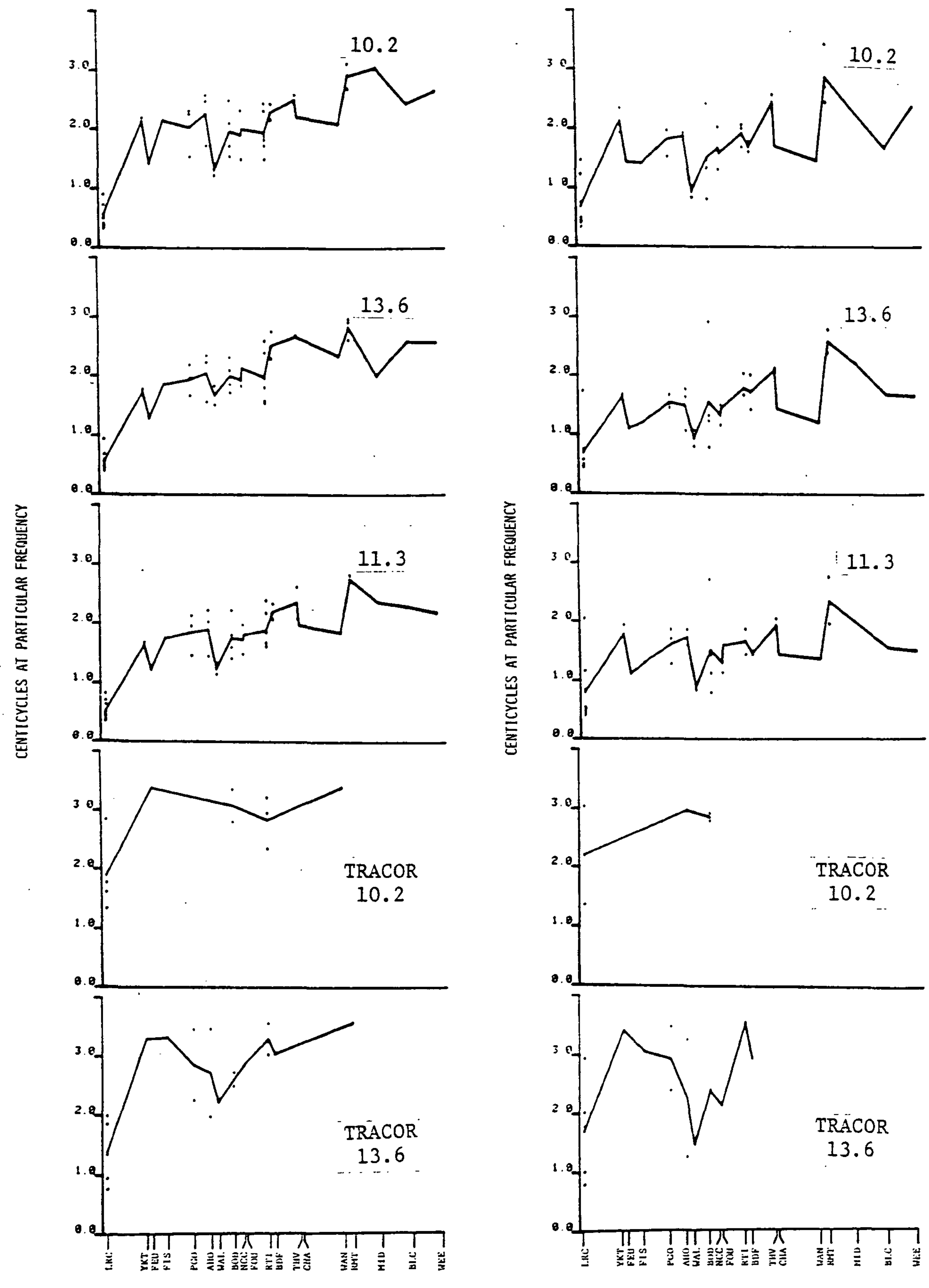

(a) Transition Time (b) Daytime

Figure 3-15. Data Set Differential Average Hourly Error Standard Deviation vs. Separation Range of Norway - N. Dakota LOP.

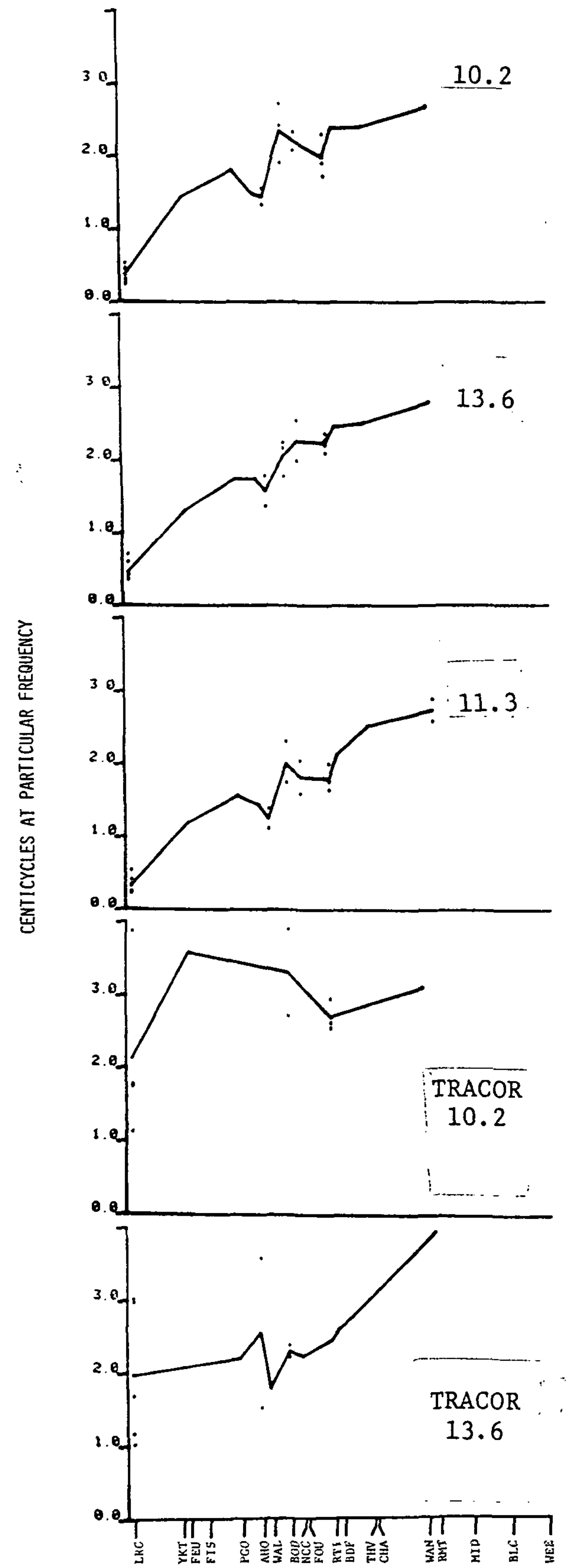

(c) Nighttime

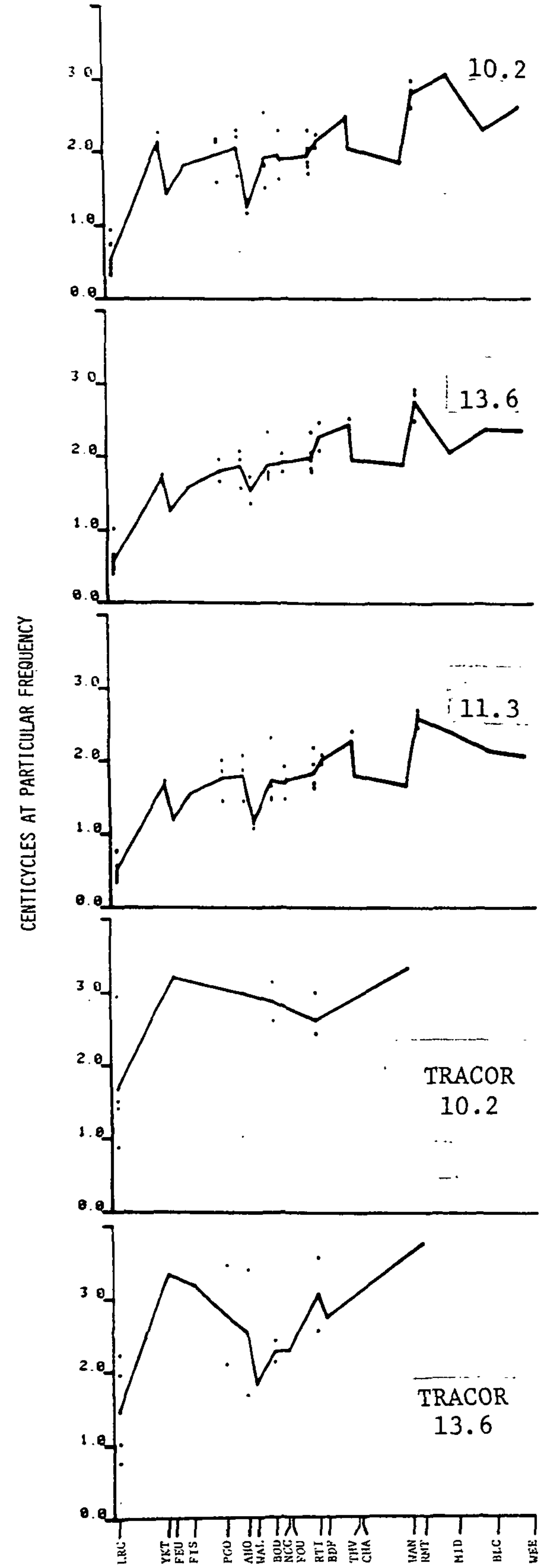

(d) Total Time

Figure 3-15. Continued.

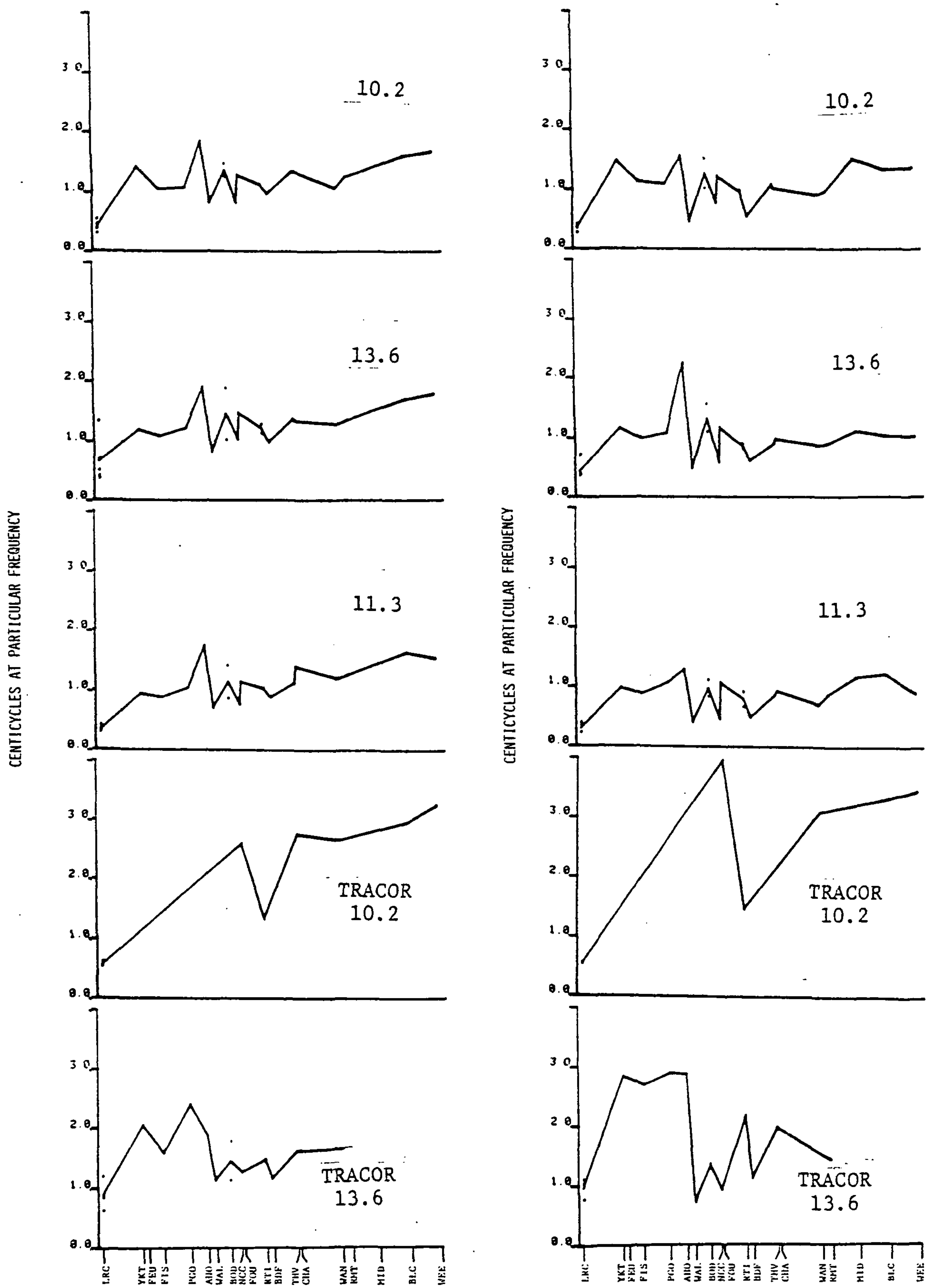

Figure 3-16. Data Set Differential Average Hourly Error Standard Deviation vs. Separation Range for Trinidad - Hawaii LOP.

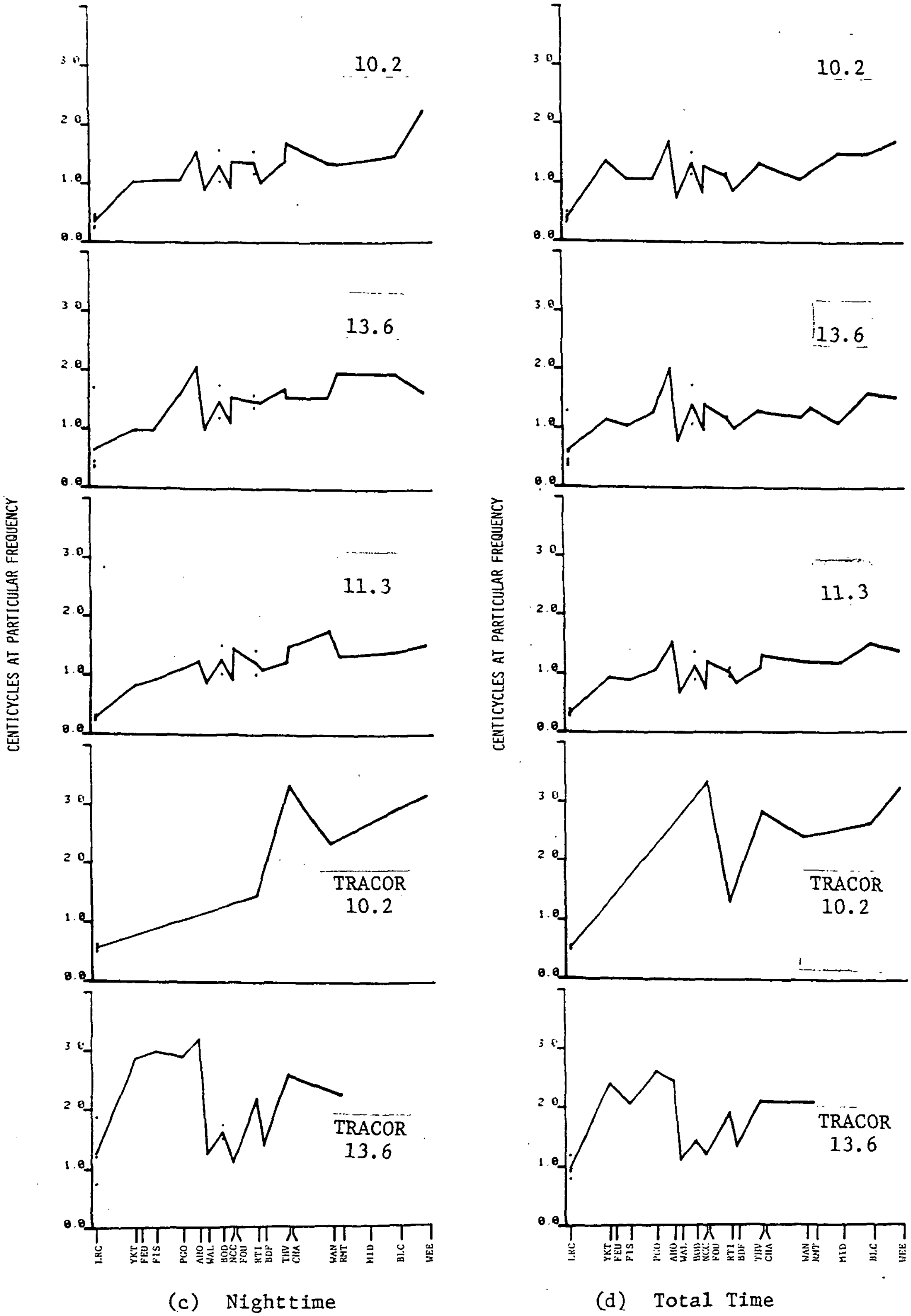

Figure 3-16. Continued.

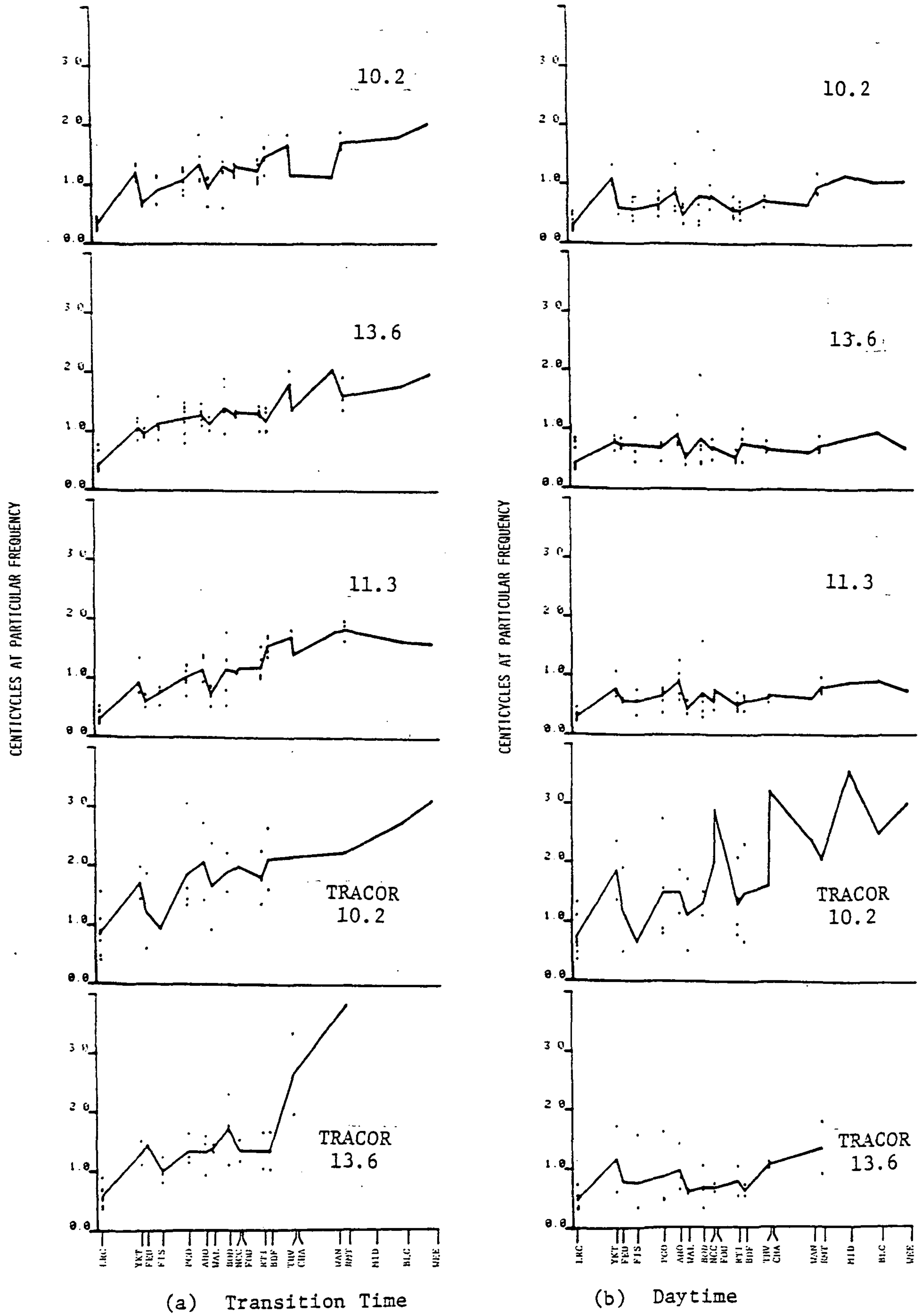

Figure 3-17. Data Set Differential Average Hourly Error Standard Deviation vs. Separation for Trinidad - N. Dakota LOP.

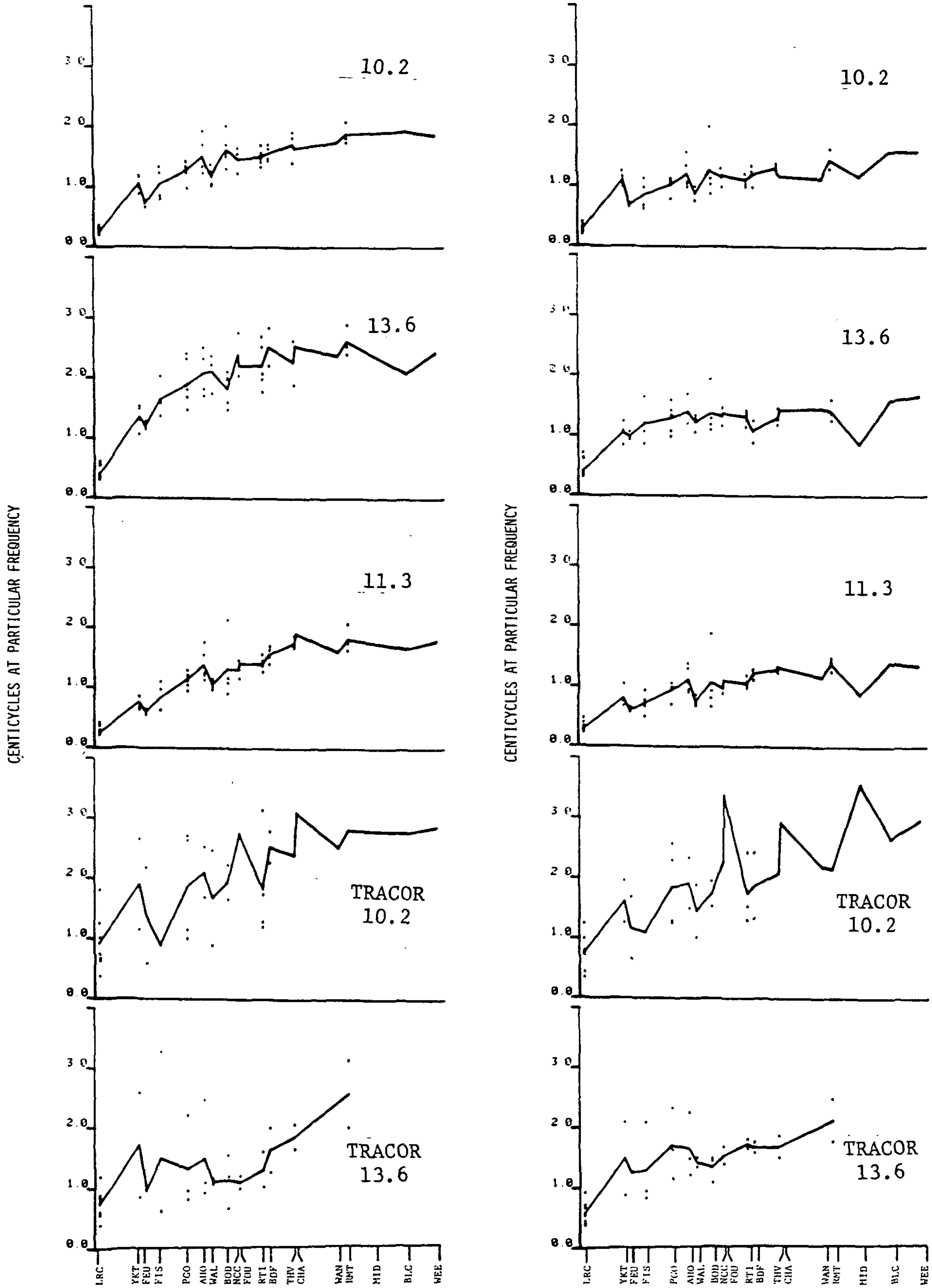

(c) Nighttime

(d) Total Time

Figure 3-17. Continued.

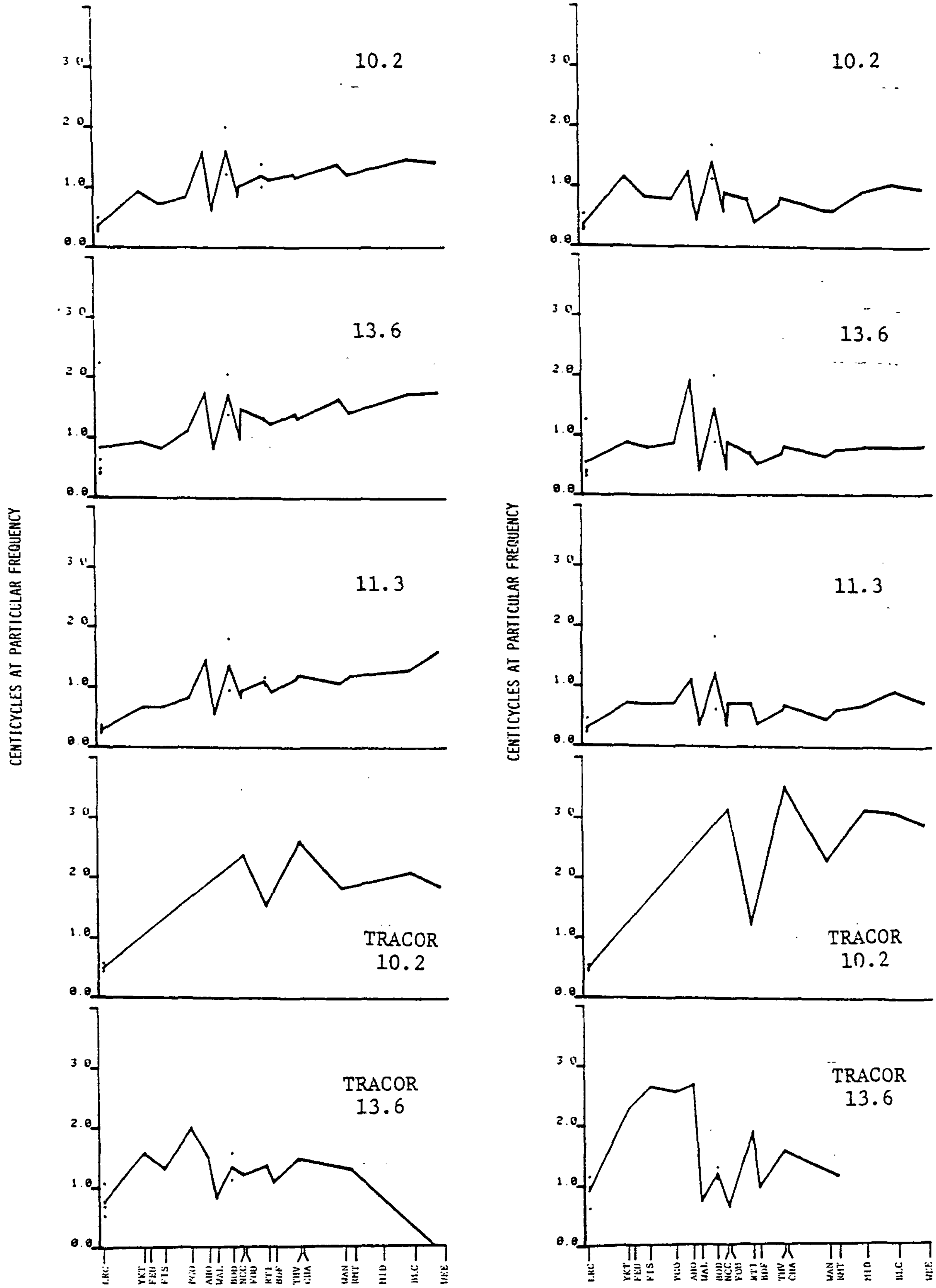

(a) Transition Time (b) Daytime

Figure 3-18. Data Set Differential Average Hourly Error Standard Deviation vs. Separation Range for Hawaii - N. Dakota LOP

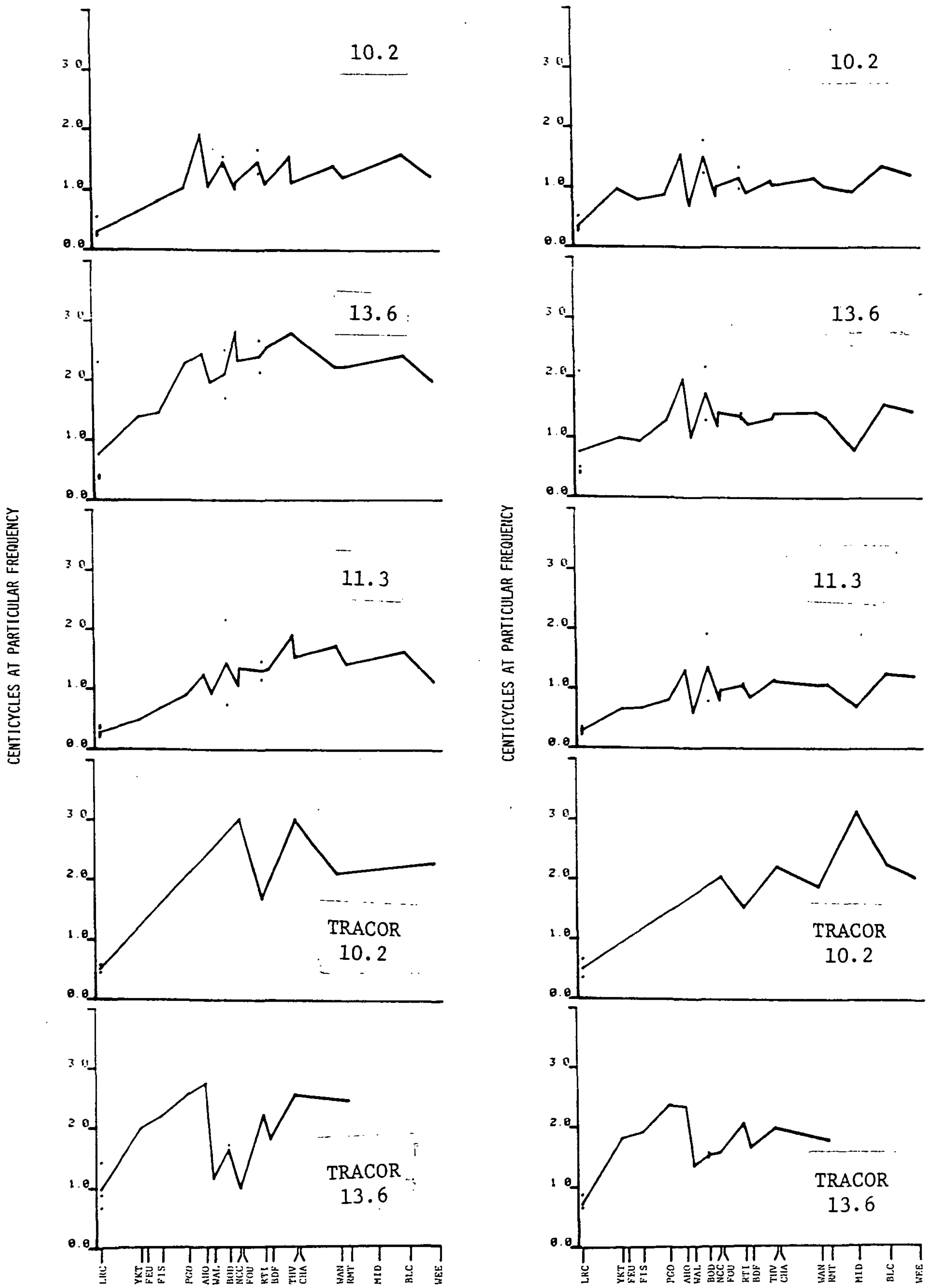

(c) Nighttime

(d) Total Time

Figure 3-18. Continued.

the error with separation range. This indicates good correlation between received phase values at the two receivers, even for separation ranges of 600 n.mi.

In general, the slope of the Tracor receiver error is greater than for the digital receivers. The reason for this is not clear. One contributing factor is that the set-up to set-up variation (receiver repeatability) is markedly worse with the Tracor receiver. With more variation in the individual data points the curve of the means appears steeper.

3.3 Differential Position Error

Using the transformations discussed in Chapter 2, both two LOP (three-station) and three LOP (four-station) differential position error has been investigated. It should be noted that with three stations a unique position estimate is obtained. With four stations the position estimate is not unique. The error is dependent on the LOP choice. For four-station data several LOP triplets have been used for some of the following analysis and the position error illustrated is the smallest in a least-square sense.

In Figure 3-19 several data sets were combined to yield a set of hourly differential position error estimates using the Norway, Trinidad and North Dakota phase measurements at 10.2 kHz. The RTI site differential data were used corresponding to a receiver separation range of 258.9 km. The RTI site is in a rural area with the whip antenna mounted on the roof of a one story building. The position estimate RMS value was 0.60 km with a CEP value of 0.41 km. Figure 3-20 is a histogram of the magnitude of the position error values. It may be noted that the position errors are relatively evenly distributed directionally and yield quite good accuracy at this separation range.

To compare ordinary OMEGA accuracy (No SWC) with differential accuracy, Figures 3-21 through 3-26 illustrate RMS and CEP position error using stations Norway, Trinidad and North Dakota at each of the carrier frequencies and each of the 13 primary receiver sites. These plots are

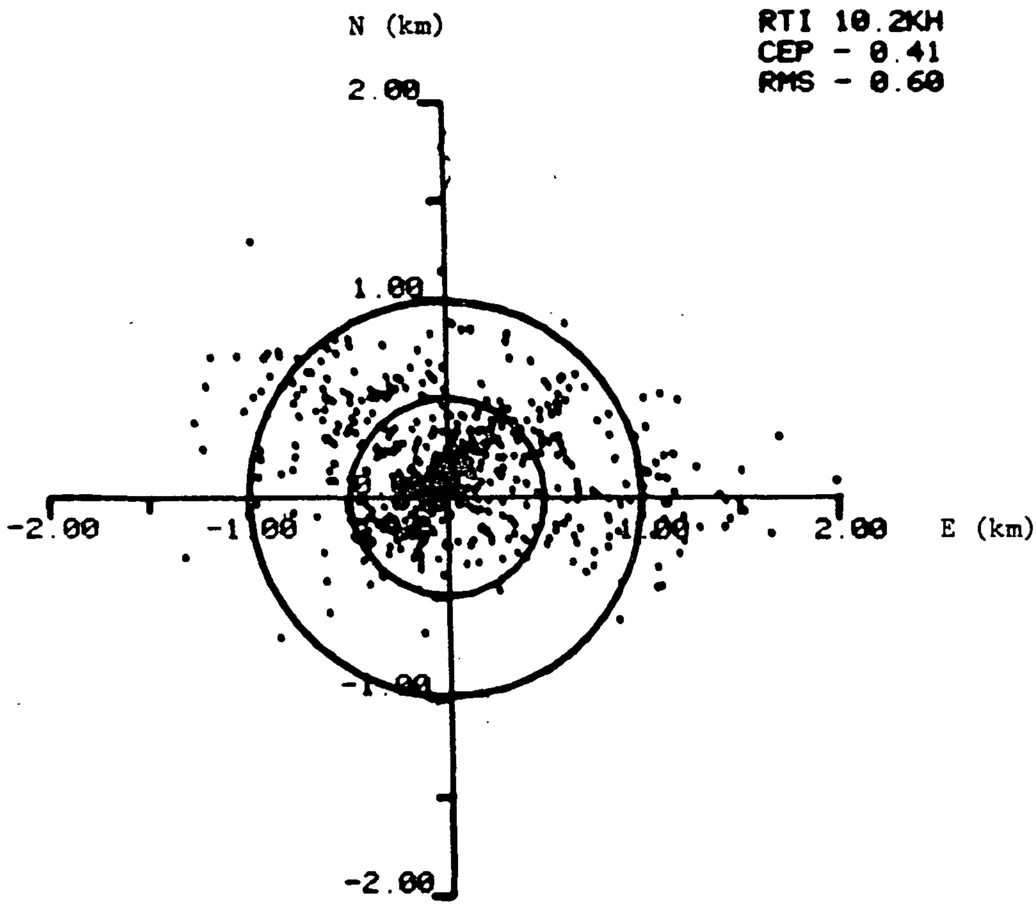

Figure 3-19. Hourly Differential OMEGA Position Error at RTI Site for LOPs NOR-NDK and TRI-NDK at 10.2 kHz.

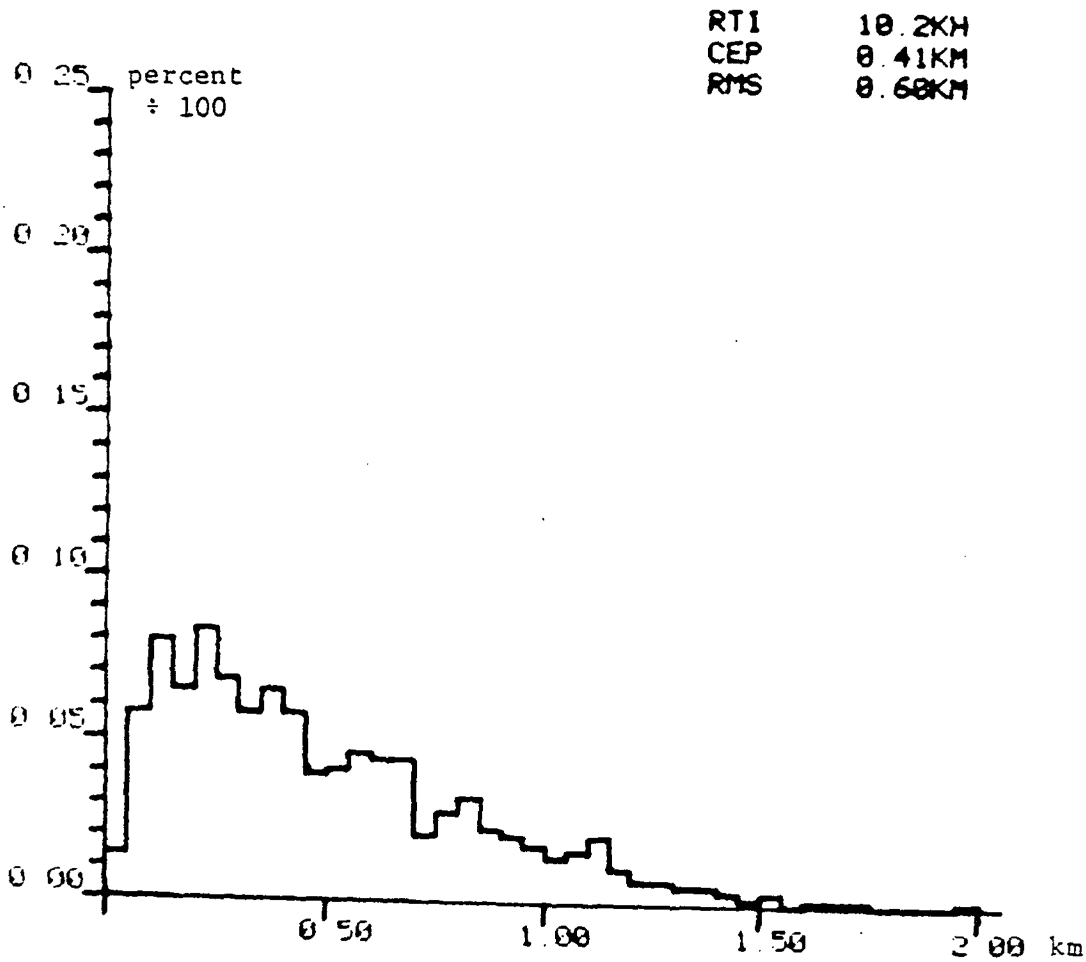

Figure 3-20. Histogram of Hourly Differential OMEGA Position Error (Magnitude) at RTI Site for LOP's NOR-NDK and TRI-NDK. 10.2 kHz.

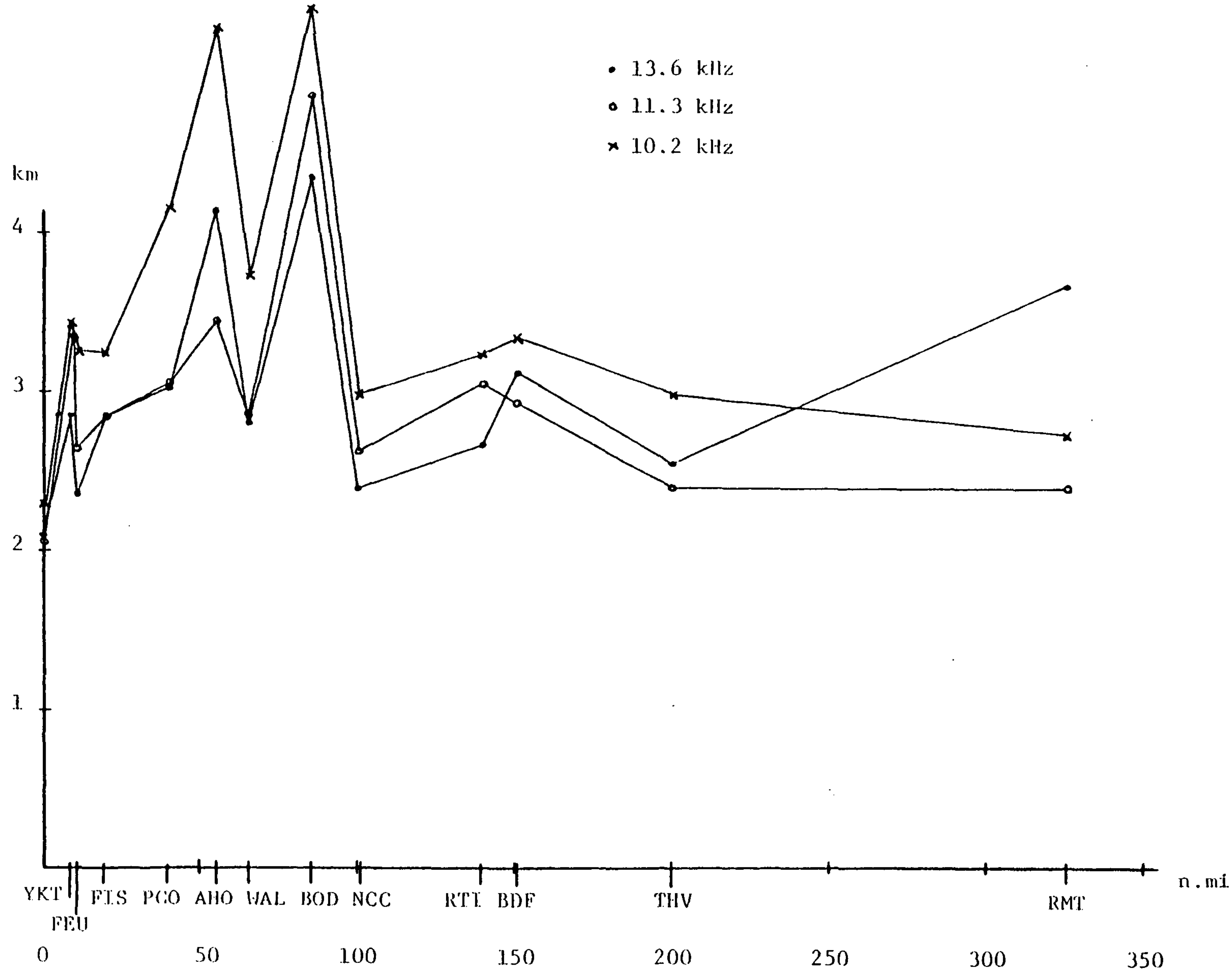

Figure 3-21. OMEGA RMS Position Error (km) at Various Receiver Sites Relative to Hampton, Virginia Site. No SWC.

LOP's NOR-NDK and TRI-NDK.

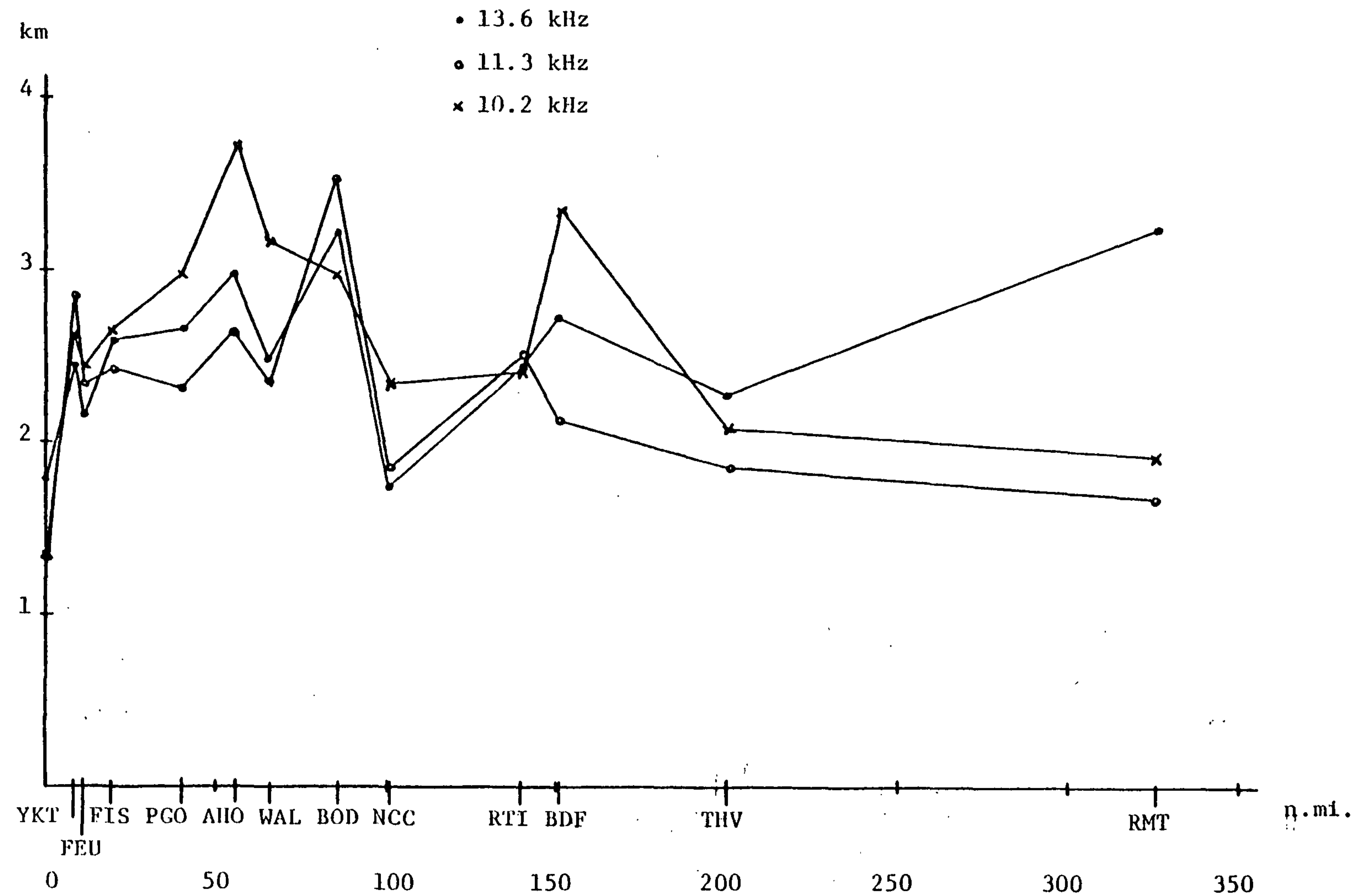

Figure 3-22. OMEGA Position CEP (km) at Various Receiver Sites Relative to Hampton, Virginia Site. No SWC.
LOP's NOR-NDK and TRI-NDK.

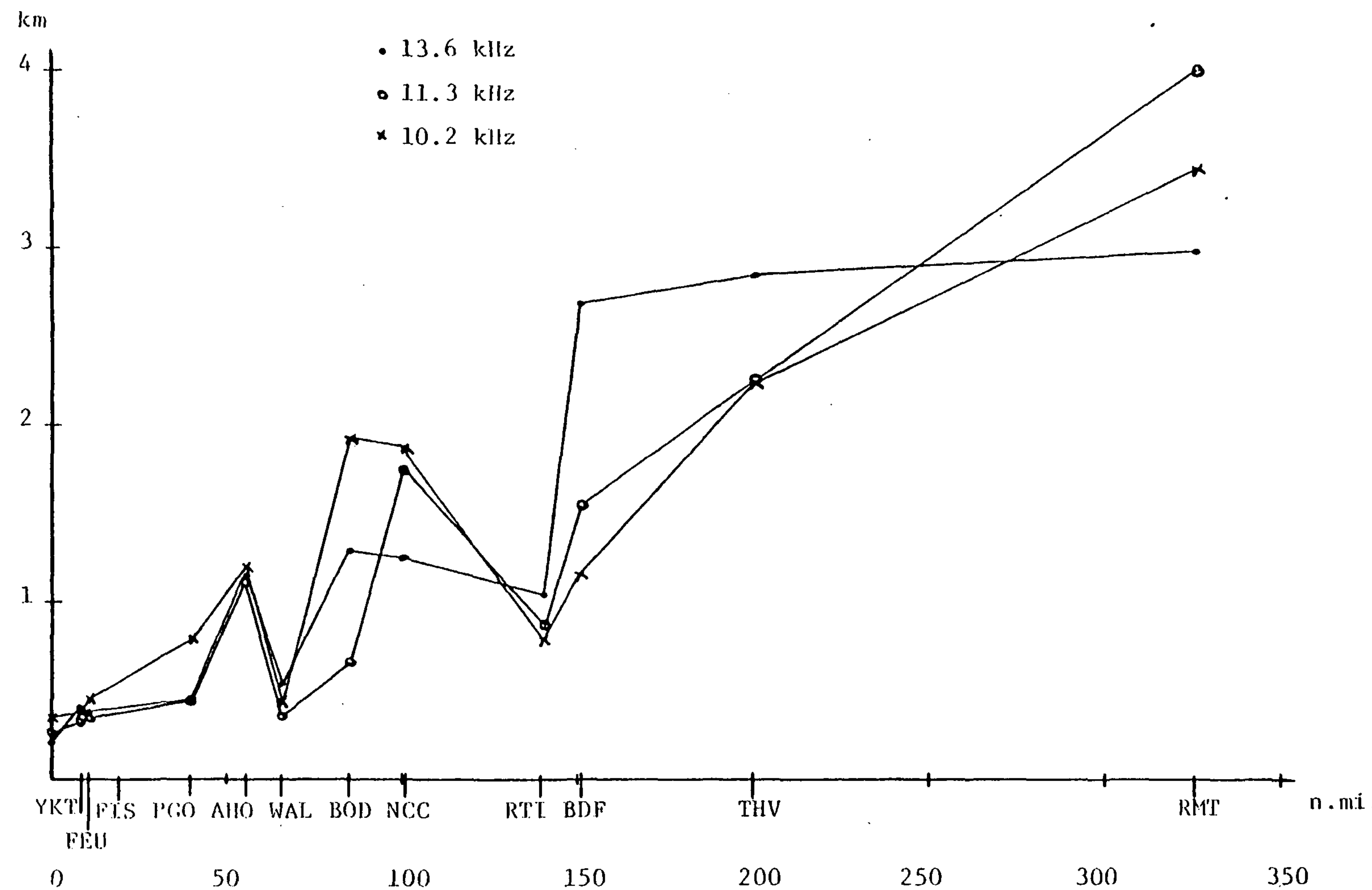

Figure 3-23. Differential RMS Position Error (km) vs. Distance Between Receivers (n.mi.).

LOP's NOR-NDK and TRI-NDK.

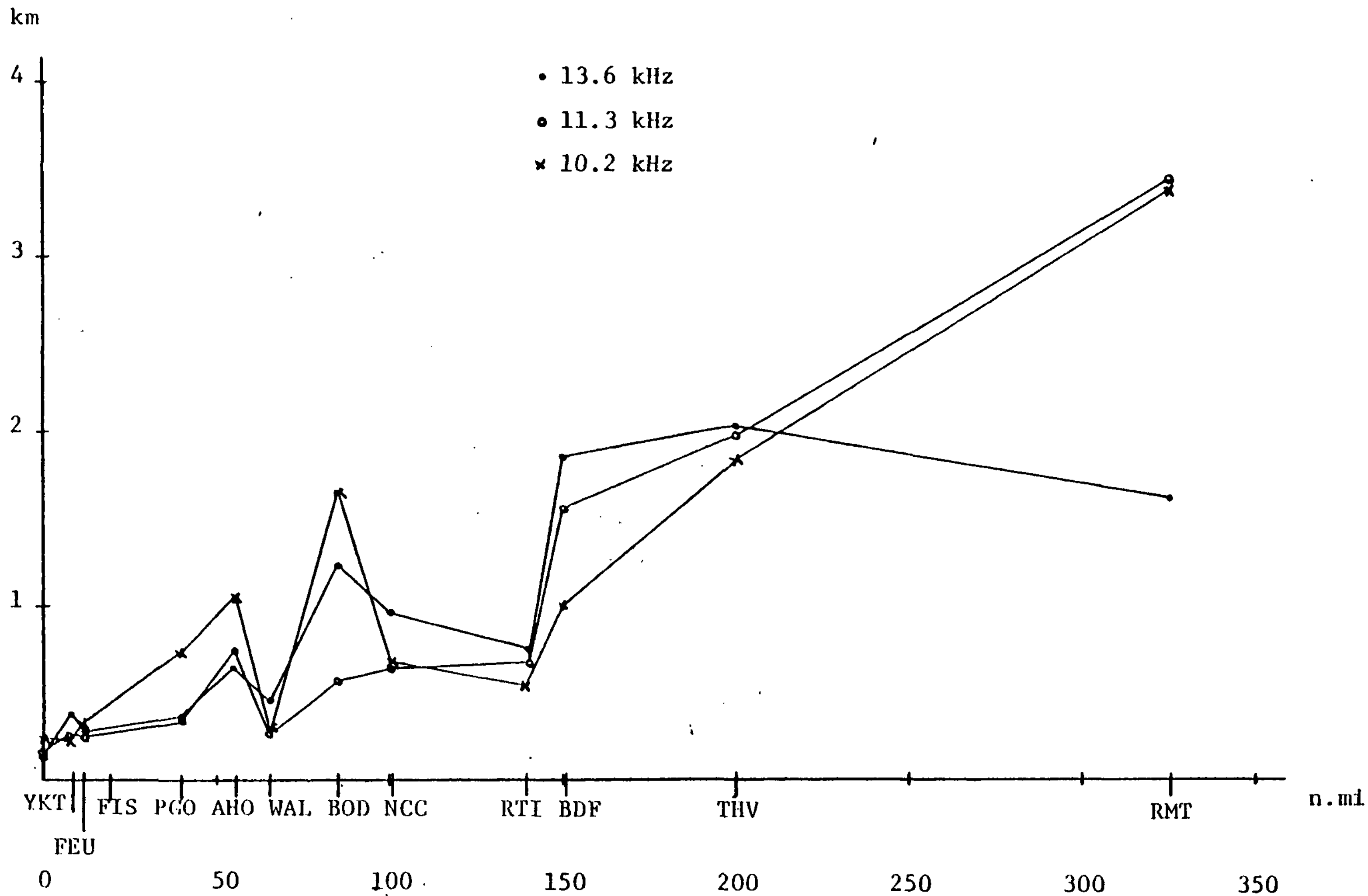

Figure 3-24. Differential Position CEP (km) vs. Distance Between Receivers (n.mi.).

LOP's NOR-NDK and TRI-NDK.

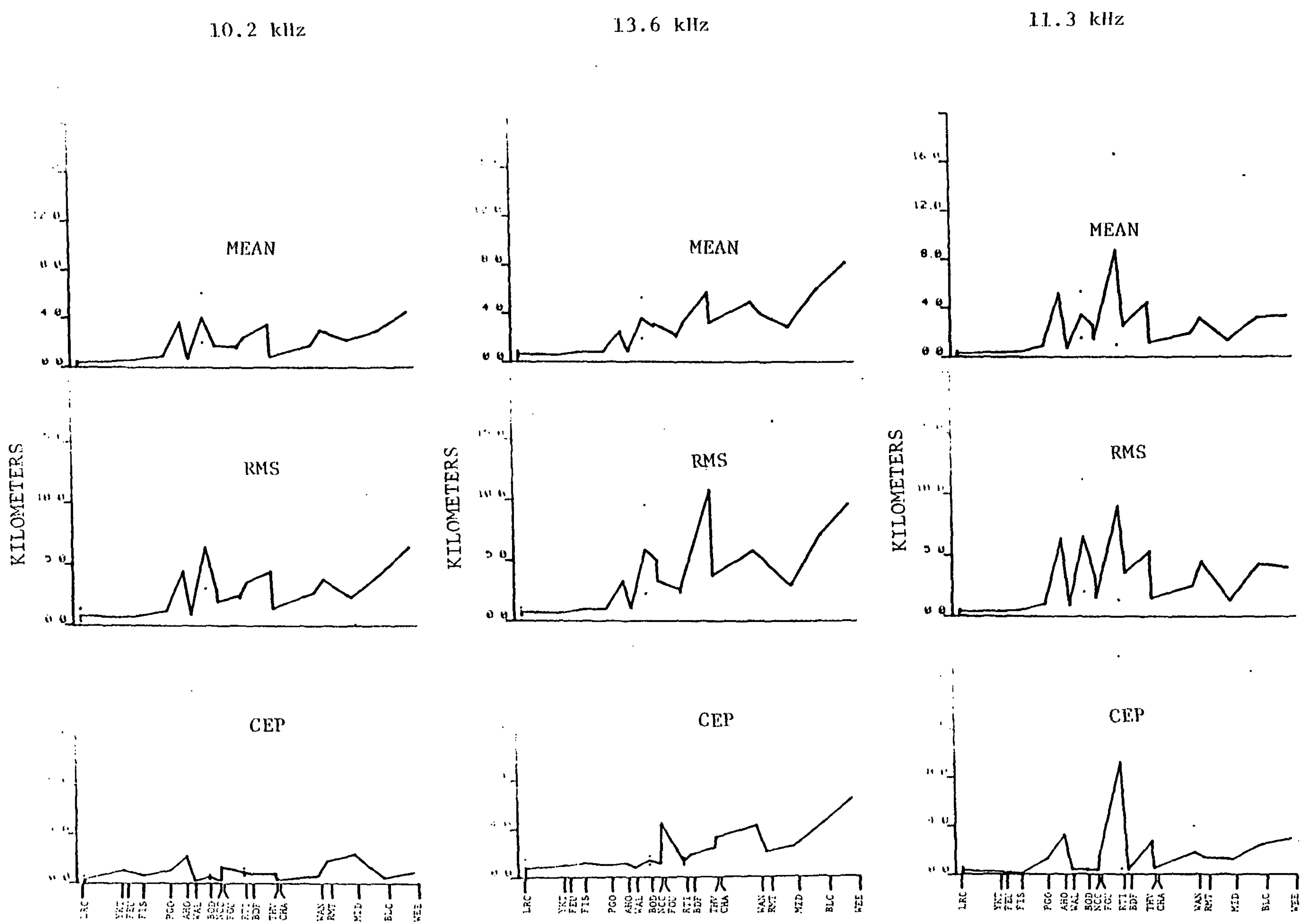

Figure 3-25. Differential Position Error with Trinidad-Hawaii and Trinidad-N. Dakota LOP's.

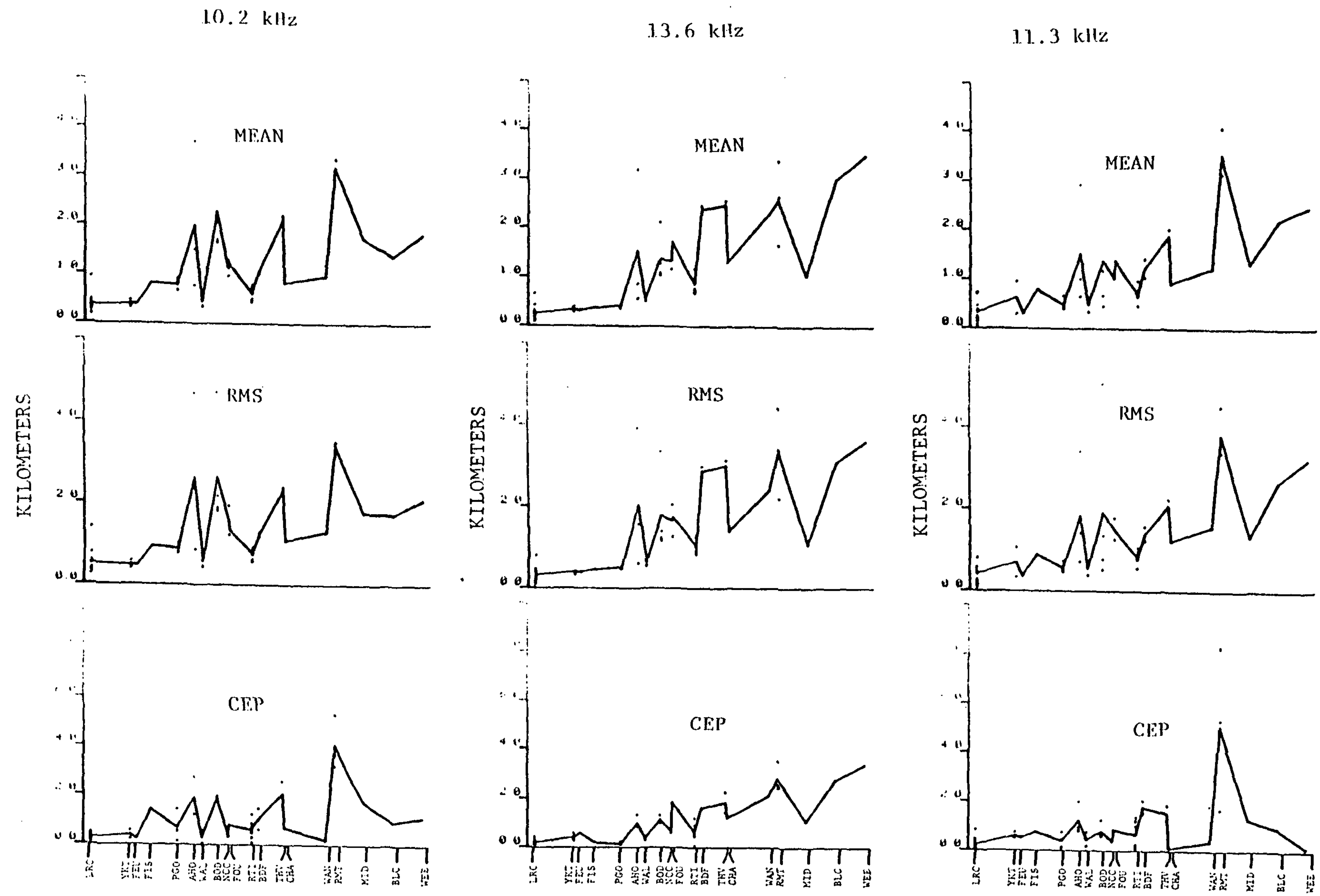

Figure 3-26. Differential Position Error with Norway-Trinidad and Trinidad-N. Dakota LOP's.

based on RMS and CEP position error over all hours in several data sets at each receiver site. The range values are relative to Hampton, Virginia, which is at a zero range value. Comparing ordinary to differential, the effect of the differential correction is graphically apparent. For receiver separation of up to 278 km (150 n.mi.) the differential correction offers a significant improvement in position error. Beyond that range there was little, if any, noticeable improvement. There appear to be some local effects contributing to position error at both AHO and BOD, which exist in both the ordinary and differential position error plots. The effect of frequency on the error is not clear, although the ordinary OMEGA error appears very slightly larger at 10.2 kHz at virtually all sites. In Figure 3-27 the overall mean differential position error is shown at each site. The 10.2 kHz mean at BOD is particularly large and illustrates further what is probably a local effect problem. Note that the RTI location which was addressed in Figures 3-19 and 3-20 is particularly good. Considering four-station data, Figures 3-28 through 3-30, compare ordinary (No SWC) and differentially corrected position errors using the minimum least squares position error LOP triplet at each site. With uncorrected OMEGA there is essentially no advantage using LOP triplets over the LOP pairs used in Figures 3-21 and 3-22. However, with differential corrections, an advantage does appear.

3.4 Summary

Recognizing that any analysis of differential OMEGA accuracy is dependent upon the receiver equipment, this analysis does confirm the differential concept as a means of providing for usable accuracy. Certainly the differential correction can be valid with up to 275 km (150 n.mi.) separation of receivers under many conditions. Even at extended separations beyond this, good accuracy is possible, as demonstrated with these results. This analysis considered only real-time corrections. Other studies have indicated that significant time delay in corrections is costly in terms of accuracy. Even so, with real-time corrections, position estimate accuracies do vary with time of day, and based on these results, are

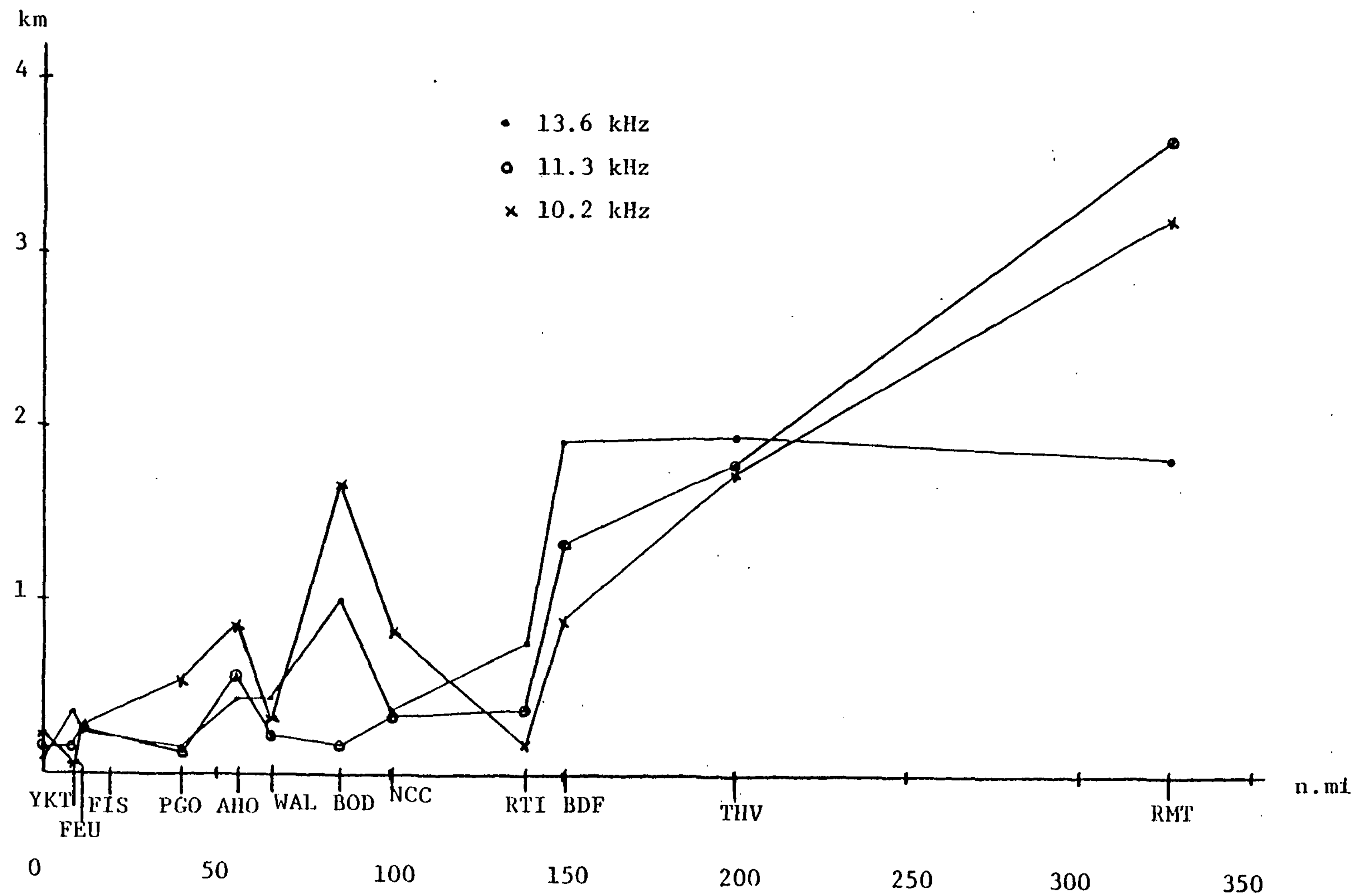

Figure 3-27. Mean Differential Position Error (km) vs. Distance Between Receivers (n.mi.).

LOP's NOR-NDK and TRI-NDK.

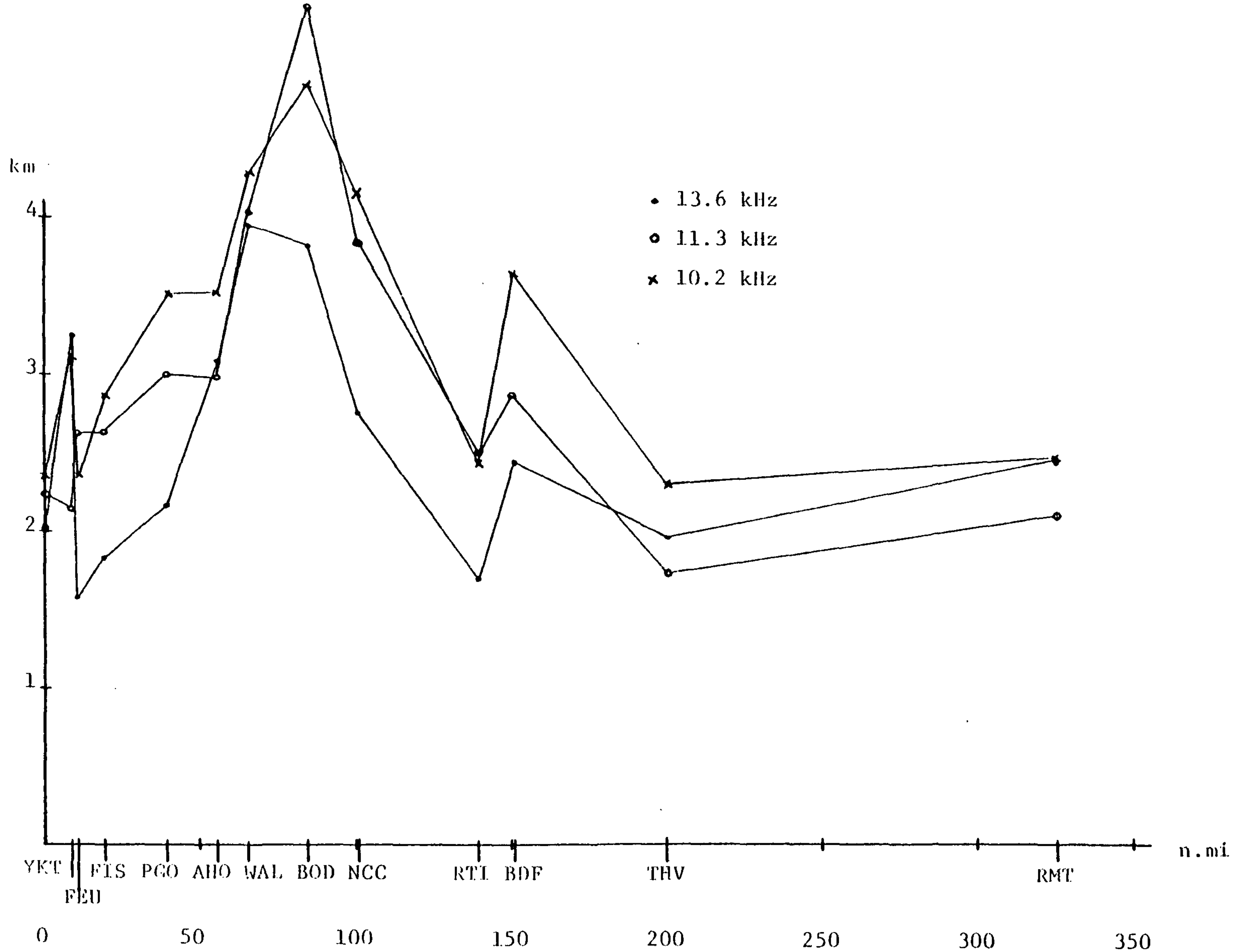

Figure 3-28. OMEGA RMS Position Error (km) at Various Receiver Sites Relative to Hampton, Virginia Site Considering LOP Triplets NOR-TRI, NOR-HAW, HAW-NDK; NOR-TRI, TRI-HAW, HAW-NDK; NOR-HAW, TRI-HAW, HAW-NDK.

Values Correspond to Triplet with Minimum Least Squares Position Error.

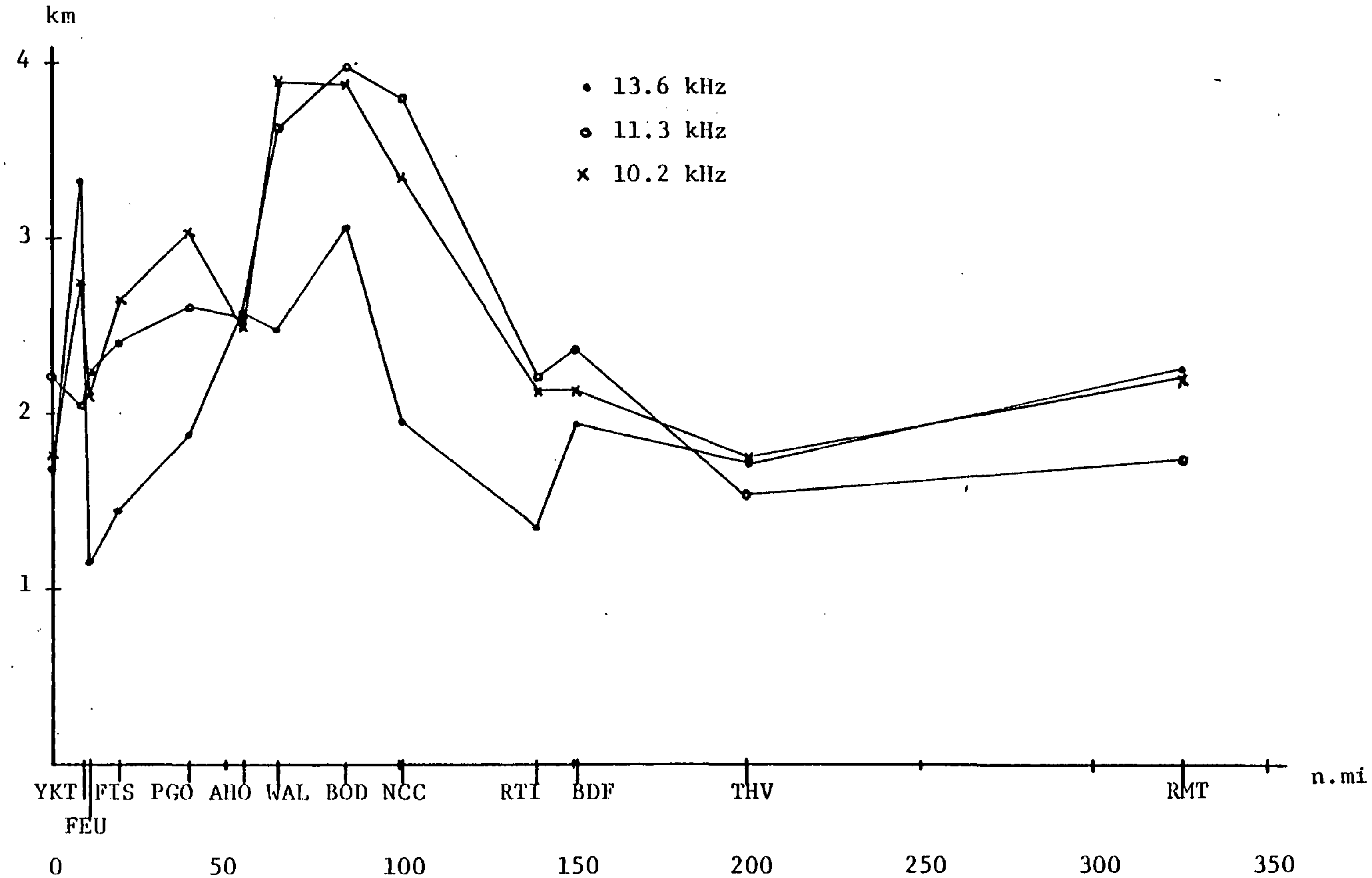

Figure 3-29. OMEGA Position CEP (km) at Various Receiver Sites Relative to Hampton, Virginia Site Considering LOP Triplets NOR-TRI, NOR-HAW, HAW-NDK; NOR-TRI, TRI-HAW, HAW-NDK; NOR-HAW, TRI-HAW, HAW-NDK.

Values Correspond to Triplet with Minimum Least Squares Position Error.

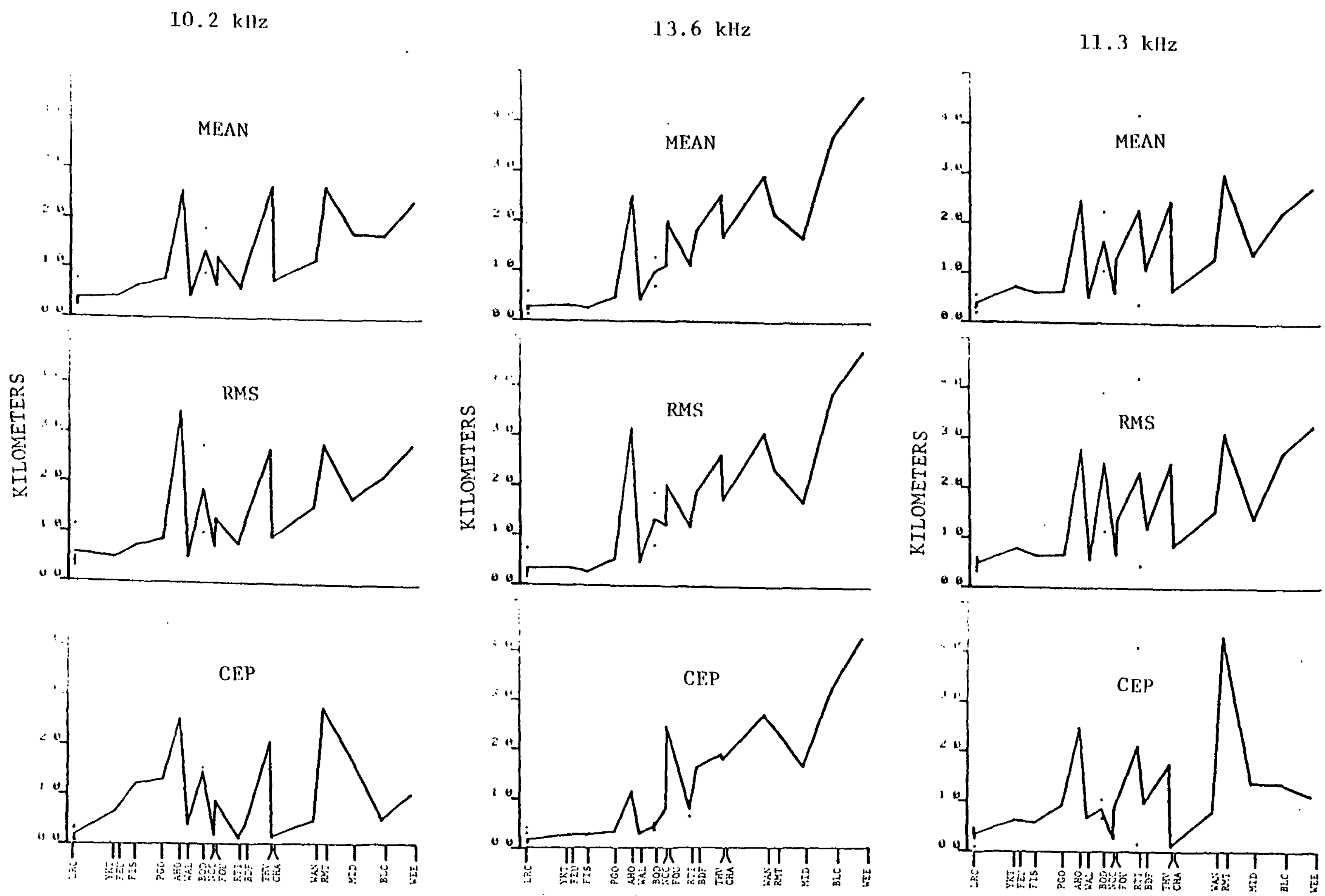

Figure 3-30. Four Station Differential Position Error with Norway-Trinidad, Trinidad-Hawaii, and Hawaii-N. Dakota LOP's.

influenced significantly by receiver repeatability. It is very difficult to draw conclusions concerning local effects problems and how these affect repeatability error. Repeatability error was significant even for the side-by-side tests, when the receivers and associated antennas were co-located.

CHAPTER 4

VLF PROPAGATION

4.1 General

A VLF propagation model was developed to identify and better understand those phase error mechanisms that are related to propagation anomalies such as modal interference. Although a complete analysis of phase data requires a statistical approach, a deterministic model of propagation under average conditions is required to utilize known physics to explain important error mechanisms and to provide predictive information to guide the statistical analysis.

4.2 The Propagation Model: Development of Theory

Intrinsic to the waveguide theory of VLF propagation is the representation of the EM fields as a sum of propagating modes. This mode sum is made tractable by introducing a notation to represent the different functional characteristics of the solution, as defined by Wait (ref. 10) and subsequently extended by Galejs (ref. 11).

For a Vertical Dipole Source, the mode sum becomes

$$E_r(h,d) = \frac{-\eta I d s e^{-i\pi/4}}{h\sqrt{a\lambda \sin(d/a)}} \sum_q S_q^{1.5} \Lambda_q^e G_q^e(h_s) G_q^e(h) \exp\{ik_o S_q d) \qquad (4\text{-}1)$$

where h is the distance above the ground surface; Λ_q^e is the excitation efficiency factor of the qth mode; $G_q^e(h_s)$ and $G_q^e(h)$ are the source and receiver height gain functions respectively; k_o is the freespace wave number; d is the distance along the earth's surface from transmitter to receiver; Ids is the dipole current moment of the source; a is the earth's radius; λ is the freespace wavelength. The propagation factor S_q for the qth mode can be considered as the sine of the complex angle of incidence at the ground, which is commonly used in the literature [refs. 11,12,13). The superscript e in (4-1) indicates the vertical polarization of the source antenna. A waveguide mode as formulated in (4-1) has both TM and TE field components, due to the anisotropy of the ionosphere. However, at

VLF frequencies, the field components of one type are usually dominant, lending to descriptive terms such as quasi-TM and quasi-TE for the individual modes (ref. 14). To characterize the ground level field patterns of a VLF source located on the ground, the excitation factor and propagation parameter must be evaluated for each important mode. The height gain functions for this situation are defined to be unity.

An approach based on the work of Budden (ref. 12) represents the waveguide in rectangular coordinates and accounts for the effect of earth curvature in the airspace by artificially modifying the permittivity with increasing height. The ionosphere is treated, in this approach, using a planar geometry. This leads to a "transition" region in which the earth's curvature cannot be neglected but which must also be treated as part of the ionosphere. A method by which this transition region can be treated for daytime conditions is discussed by Gossard (ref. 13).

Another approach, used in this work, represents the earth ionosphere waveguide in cylindrical coordinates so as to take into account the curvature of the earth in the direction of propagation. The analysis of the problem is divided into two parts. The first describes the fields in the airspace below the ionosphere, that region between the ground and the height, h_i, below which the ionosphere can be completely neglected. The second part describes the fields in the ionosphere, that is, above region 1, up to a height, h_u, where the continuing variation in the ionosphere is taken to be homogeneous. The technique used in the ionosphere region could be extended to ground level; but since the airspace solution offers a considerable reduction in complexity of analysis, the two region approach is used.

4.2.1 Fields in the airspace.— In analyzing VLF propagation in the airspace region, the TM and TE fields are uncoupled when represented in a cylindrical coordinate system, and therefore can be treated independently. The TM fields are H_z, E_ϕ, E_r, and the TE fields are E_z, H_ϕ, H_r, for propagation in the ϕ direction. Figure 4-1 illustrates the coordinate system within the earth ionosphere waveguide.

To solve for the fields in the airspace region, it is convenient to characterize the upper and lower boundaries in terms of impedance relationships at each boundary. A smooth, homogeneous surface can be represented

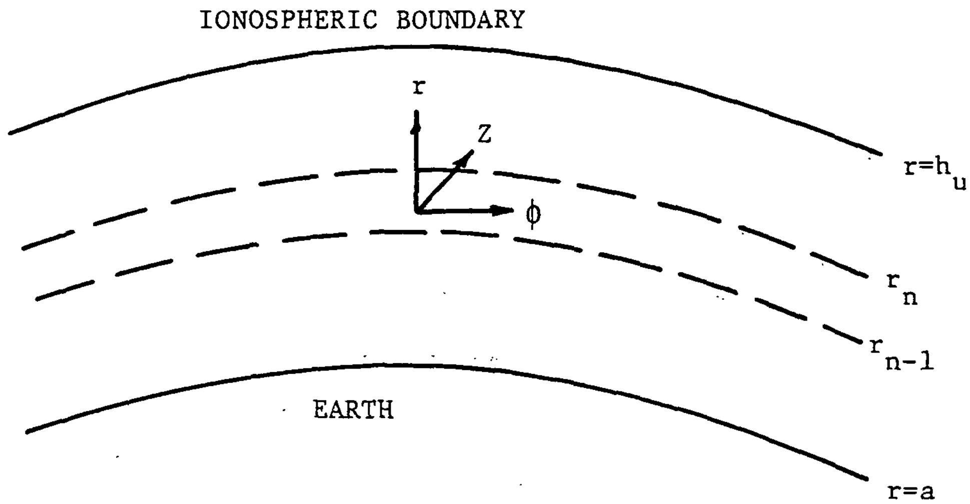

Figure 4-1. Earth-Ionospheric Waveguide Illustrating Coordinate System

by separate surface impedances for TM and TE incident waves. It has been established that an effective surface impedance for the ground provides a good approximation to the actual physical situation at VLF (ref. 10). The TM and TE ground surface impedances are dependent on the angle of incidence or propagation parameter. The surface impedances in the limit of grazing incidence are

$$
\begin{aligned}
Zg(TM) &= \frac{E_z(a)}{H_\phi(a)} = \sqrt{\frac{-i\omega\mu_o}{\sigma+i\omega\varepsilon}} \sqrt{1 + \frac{i\omega\varepsilon_o}{\sigma+i\omega\varepsilon}} \\
Zg(TE) &= \frac{-E_r(a)}{H_z(a)} = \sqrt{\frac{-i\omega\mu_o}{\sigma-i\omega\varepsilon}} \Big/ \sqrt{1 + \frac{i\omega\varepsilon_o}{\sigma-i\omega\varepsilon}}
\end{aligned}
\qquad (4\text{-}2)
$$

which are expressed in terms of ground conductivity σ. These impedances are numerically close in value to the intrinsic impedance of the media at VLF.

The conditions necessary for a mode to propagate are that the impedance condition at the ground is satisfied and that similar conditions be met at the interface separating the airspace from the ionosphere. If assumptions are made, which lead to an isotropic ionosphere (transverse horizontal magnetic field) the TM and TE components are also uncoupled in the ionosphere.

In the isotropic situation a TE and TM ionosphere surface impedance can be written in terms of physical ionosphere parameters. TM modes which solve the TM boundary conditions can be solved for, independently of TE modes. The analytical field solutions which involve Hankel functions of large order and argument can be approximated by Airy functions or Hankel functions of order 1/3. A modal equation can then be written in terms of these Airy functions and the TM boundary conditions. This equation can be solved iteratively for the propagation parameters of allowable TM modes. The TE modes are found in similar fashion. This method may be extended for an anisotropic ionosphere by coupling the TM and TE modal equations to satisfy the more complex boundary condition at the ionosphere. This condition can be expressed by Budden's four reflection coefficients, for example (ref. 12). An alternate approach (ref. 11) used in this work is to transfer the TM and TE impedances from the ground to the ionosphere in vertical steps corresponding to thin cylindrical layers. The functions representing the radial variation of the fields can then be approximated by exponentials. The fields at the boundary of one layer are transformed to the next layer boundary by a TM or TE transmission matrix E or H respectively. For the TM case the analytic solution yields:

$$\begin{bmatrix} E_r(r) \\ H_z(r) \end{bmatrix} = \begin{bmatrix} \frac{-\nu}{\omega\varepsilon_o r} \left\{A_e H_\nu^{(1)} (kr) + B_e H_\nu^{(2)} (kr)\right\} \\ A_e H_\nu^{(1)} (kr) + B_e H_\nu^{(2)} (k_r) \end{bmatrix} = \begin{bmatrix} a_n(r) \end{bmatrix} \begin{bmatrix} A_e \\ B_e \end{bmatrix} \quad (4\text{-}3)$$

where $H_\nu^{(1)}$ and $H_\nu^{(2)}$ are Hankel functions of the first and second kind, and of order ν. The fields can be approximated over a thin layer using:

$$\begin{bmatrix} a_n(r) \end{bmatrix} \approx \begin{bmatrix} K_1/\omega\varepsilon_o & K_2/\omega\varepsilon_o \\ 1 & 1 \end{bmatrix} \bullet \begin{bmatrix} e^{iK_1 r} & 0 \\ 0 & e^{iK_2 r} \end{bmatrix} \quad (4\text{-}4)$$

where $K_1, K_2 = \pm\frac{i}{2r_m} \sqrt{K_o^2 - \frac{\nu^2 + .25}{r_m^2}}$; $\nu = S\, k_o a$; r_m = the mean radius of the layer.

This result follows by representing the radius as average layer radius where it appears as a coefficient in the differential equation of the analytic solution. For the nth layer of average radius $(r_n + r_{n+1})/2$, A_e and B_e can be eliminated to give:

$$\begin{bmatrix} E_r(n+1) \\ H_2(r_n+1) \end{bmatrix} = [a_n] \begin{bmatrix} e^{iK_1\Delta r} & o \\ o & e^{iK_2\Delta r} \end{bmatrix} [a_n] \begin{bmatrix} E_r(r) \\ H_2(r) \end{bmatrix} \quad (4\text{-}5)$$

$$= [E_h] \begin{bmatrix} E_r(r-\delta) \\ H_z(r-\delta) \end{bmatrix} \quad (4\text{-}6)$$

Similarly a transmission matrix can be defined for the TE field components. These results are dependent on the propagation parameter S.

The transmission matrices can be cascaded by multiplication to form an overall transmission matrix for the TE and TM modes which will give the TM and TE impedances at the upper airspace boundary for a given mode, since the ground impedance is known. For the TM case:

$$\begin{bmatrix} E_r(r_i) \\ H_z(r_i) \end{bmatrix} \quad \begin{bmatrix} E_n \end{bmatrix} \begin{bmatrix} E_{n-1} \end{bmatrix} \cdots \begin{bmatrix} E_1 \end{bmatrix} \begin{bmatrix} E_o \end{bmatrix} \begin{bmatrix} E_r(r_g) \\ H_z(r_g) \end{bmatrix} \tag{4-7}$$

The analysis in the ionosphere region yields coefficients, a_{ij}, that relate the TE and TM impedances Z_e and Z_h, respectively, at the lower ionosphere boundary.

$$Z_e = \frac{a_{11} + a_{12}Z_h}{a_{21} + a_{22}Z_h} \quad \text{or} \quad Z_h = \frac{a_{11} - a_{21}Z_e}{a_{12} - a_{22}Z_e} \tag{4-8}$$

These coefficients can also be expressed uniquely in terms of the four Budden reflection coefficients (ref.11). Given the airspace boundary information, it is then possible to solve iteratively for a value of S which provides transformed impedances at the ionosphere that fit the impedance relation determined by the ionosphere solution.

4.2.2 Fields in the anisotropic ionosphere.— A thin layer approach is also used in the ionosphere to determine the ionosphere lower boundary impedance relation. However, here it is not possible to separate the TM and TE field components. Consequently, a transmission matrix is used which transforms the four fields E_ϕ, H_z, H_ϕ, E_z across a thin cylindrical layer. The same coordinate system as that used in the airspace is kept. The fields in the ionosphere are expressed in terms of two upgoing and two downgoing magneto-ionic modes. The individual wavenumbers are obtained from an expression analogous to the Booker quartic. For an assumed time variation of the form $e^{-i\omega t}$, Maxwell's equations can be written for the ionosphere as:

$$\nabla \times E = i\omega\mu H \tag{4-9}$$

$$\nabla \times H = -i\delta\varepsilon_o[\varepsilon] \cdot E \tag{4-10}$$

where $k_1 = \omega\sqrt{\mu_o\varepsilon_o}$. As in the airspace, the radial dependence is approximated as a complex exponential in a thin layer. The field variation in a layer is assumed of the form:

$$E = E_o \exp(-i\omega t + ikr + i\nu\phi) \tag{4-11}$$

Equations (4-9), (4-10) and (4-11) are combined to give:

$$0 = [A]\ E \tag{4-12}$$

This is satisfied if the determinant of A vanishes. The determinant of A is expressed as a quartic polynomial in k which can be equated to 0 and solved to specify the radial wavenumber (k) for each of the magneto-ionic modes.

The field components can then be written in terms of these modes as:

$$\begin{bmatrix} E_\phi(r) \\ H_z(r) \\ H_\phi(r) \\ E_z(r) \end{bmatrix} = \begin{bmatrix} & & & \\ & C_n & & \\ & & & \\ & & & \end{bmatrix} \begin{bmatrix} A_1 e^{ik_1 r} \\ A_2 e^{ik_2 r} \\ A_3 e^{ik_3 r} \\ A_4 e^{ik_4 r} \end{bmatrix} \tag{4-13}$$

where A_1 through A_4 are the amplitudes associated with each mode. For the purpose of determining the coefficients of C_n, the amplitudes A_1 through A_4 can be taken to be the magneto-ionic mode components of a single spatial field component such as given in (4-11). This formulation will not allow a transition to isotropic regions as all four field components will not be coupled with the one selected. Therefore, to allow numerical transition to an isotropic environment, two ionospheric modes are defined as components of E_z. Evaluation of the elements of C_n then proceeds from Maxwell's equations and equation (4-12). The transmission matrix T for a layer is defined in terms of the field components at radius r and r + Δr, where Δr is the layer thickness.

$$\begin{bmatrix} E_\phi(r+\Delta r) \\ H_z(r+\Delta r) \\ H_\phi(r+\Delta r) \\ E_z(r+\Delta r) \end{bmatrix} = \begin{bmatrix} T \end{bmatrix} \begin{bmatrix} E_\phi(r) \\ H_z(r) \\ H_\phi(r) \\ E_z(r) \end{bmatrix} \tag{4-14}$$

The transmission matrix T is derived from (4-13) and (4-14) and can be written as

$$T = \begin{bmatrix} C_n \end{bmatrix} \begin{bmatrix} e^{ik_1\Delta r} & & & \\ & e^{ik_2\Delta r} & & 0 \\ & & e^{ie_3\Delta r} & \\ 0 & & & e^{ik_4\Delta r} \end{bmatrix} \begin{bmatrix} C_n \end{bmatrix} \tag{4-15}$$

where the exponential terms were collected to emphasize the dependence on layer thickness and eliminate the need for numerical calculation of exponentials with large arguments such as $e^{ik_1 r}$. To express the fields at the bottom of the ionosphere in terms of the modes at the top of the varying ionosphere a matrix Q is defined following Galejs (ref.11) with the relation:

$$\begin{bmatrix} E_\phi(r_i) \\ H_z(r_i) \\ H_\phi(r_i) \\ E_z(r_i) \end{bmatrix} = \begin{bmatrix} Q \end{bmatrix} \begin{bmatrix} A_1 \\ 0 \\ A_3 \\ 0 \end{bmatrix} \tag{4-16}$$

where it is assumed there are only upgoing waves in the region above h_ν. Equation (4-16) can be rearranged to give the boundary relationship for the ionospheric surface impedances as

$$Z_e = \frac{a_{11} + a_{12} Z_h}{a_{21} + a_{22} Z_h} \qquad \text{or} \qquad Z_h = - \frac{a_{11} - a_{21} Z_e}{a_{12} - a_{22} Z_e} \tag{4-17}$$

where a_{11} through a_{22} are expressed in terms of the elements of Q as

$$\begin{aligned} a_{11} &= q_{11} q_{43} - q_{13} q_{41} \qquad & a_{12} &= q_{11} q_{33} - q_{13} q_{31} \\ a_{21} &= q_{21} q_{43} - q_{23} q_{41} \qquad & a_{22} &= q_{21} q_{23} - q_{23} q_{31} \end{aligned} \tag{4-18}$$

The results of this model based on a thin layer approximation technique in cylindrical coordinates have been compared with the Galejs model. Galejs (ref.11) analyzed the ionosphere in rectangular coordinates and accounted for earth's curvature by decreasing the horizontal propagation parameter, S, with increasing height for each layer. This was similar to the modification of permittivity with height adopted by Budden and necessarily places a limit on maximum layer thickness for the approach to account for curvature in an acceptably accurate manner.

The mode parameters, parameters produced by the method of Galejs and the method presented here, are in excellent agreement, with a small deviation occurring as the layer thickness is increased. It has been determined that a cylindrical layer analysis using exponential approximation for the radial cylinder functions gives accuracy comparable to that of the Airy function solution for a layer thickness of 10-20 km in the airspace. This indicates that a determination of shell thickness in the ionosphere region should be based on the resolution in available ionosphere profiles and possible consideration of unwanted reflection from layer boundaries.

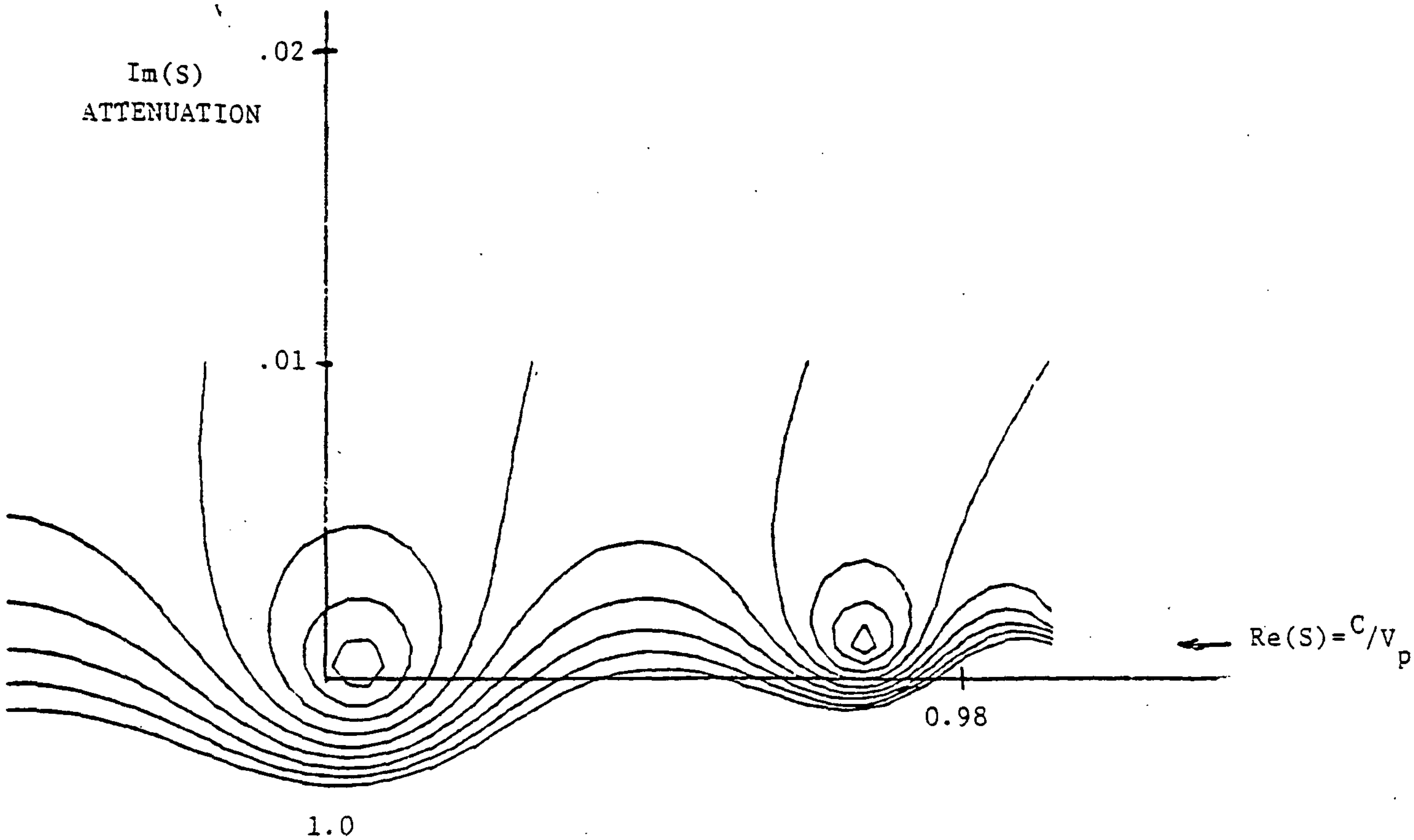

Figure 4-2. Root Position Contour Map.

4.3 The Propagation Model: Computational Algorithms

The preceding section provides the theoretical basis for a numerical model developed to study the effects of modal interference on VLF navigation. The model determines the propagation parameters and the excitation factor Λ which are required by (4-1) to characterize the propagation of each mode. The mode parameters can be used to evaluate the extent of phase and amplitude interference to the primary mode along a particular propagation path. The ionosphere, which is considered as a series of concentric cylindrical layers, is taken to be homogenous within an individual layer. Within such a layer, the electron density and electron collision frequency are required to characterize the ionosphere by a permittivity tensor $[\varepsilon]$. Profiles of these two ionospheric parameters which are arbitrary or of exponential form can be used. Reference profiles evaluated by Deeks from experimental data have also been included. The orientation of the earth magnetic field with respect to the propagation path is specified to the model by the magnetic dip angle and the azimuth angle of the propagation path with respect to Magnetic East. The earth magnetic field strength along with its orientation complete the terrestrial parameters necessary to determine $[\varepsilon]$ for a given layer. The earth boundary is characterized to the model by an equivalent ground conductivity and relative permittivity.

The propagation parameter S is solved for iteratively for each mode in two nested stages which require that particular boundary conditions be matched. Since the boundary impedence relationship obtained from the ionosphere solution is less sensitive to S than the match below in the airspace and is also by far the lengthier in run time, the algorithm is written to minimize the number of passes through the ionosphere. An initial estimate of S is taken from the startup algorithm to be subsequently described and is passed to the ionosphere solution along with the physical inputs mentioned previously. The parameters A_{11} through A_{14}, which relate the TE impedance to the TM impedance at the lower ionosphere boundary by (4-17), are the results from this solution. This relationship characterizes the upper boundary of the airspace so that a refined value of S that satisfies the airspace boundary conditions can be solved for iteratively.

This refined estimate is used as a new initial estimate, and the process is repeated until S converges within preset specification.

In the airspace for an estimate of S, the ground impedance can be transformed radially for the TM and TE case to give the wave impedances at the upper airspace boundary $Z_e'(S)$ and $Z_h'(S)$, respectively. These impedances can be tested against (4-17) to establish match indexes which can be written

$$M_E(S) = \frac{A_{11} + A_{12}Z_H'}{A_{21} + A_{22}Z_H'} - Z_E' \tag{4-19}$$

$$M_H(S) = -\frac{A_{11} - A_{21}Z_E'}{A_{12} - A_{22}Z_E'} - Z_H' \tag{4-20}$$

Both (4-19) and (4-20) approach 0 as a match is obtained and can be used to find the mode parameters S_q with a standard complex root-finding algorithm such as Muller's method. A contour map of $|M_E(S)|$ is given in Figure 4-2 showing the first two TM modes.

In the nearly isotropic case Z_E and Z_H are only loosely coupled. Therefore, the zero finding routine tends to bypass the roots of one wavetype depending on the criteria used, unless the initial estimates are good to begin with. This problem is avoided by refining the rough TM estimates using (4-19) and the rough TE estimates using (4-20). These rough estimates are obtained by selecting values of S along the real line corresponding to local minima of $M_E(S)$ and $M_H(S)$ for quasi TM and quasi TE propagation parameter estimates, respectively.

The number of cylindrical layers in each region determines the layer thickness and the closeness of the approximation to the theoretical model, given sufficient computing precision. The number of layers and the thickness of the varying ionosphere, determined by h_i and h_u, are minimized for run-time economics. The ionosphere calculations represent the greatest contribution to run-time, hence the number of layers in the airspace can be chosen sufficiently large and fixed. The repeated multiplication of the layer transmission matrices, especially in the ionosphere, is subject to a buildup of numerical error. However, the steps described above to reduce run-time are effective in minimizing error buildup. For a machine with

16 place significance, there is wide latitude allowed in the selection of an h_u for which the solution in the airspace at VLF is not dependent. This region of independence from h_u ranges from approximately 110-140 km.

Results from this model were compared to those of Galejs over a wide range of frequency, ground conductivity and ionosphere profiles. The results indicate essentially exact agreement for shell widths of 15 kilometers or less. Comparison calculations were based on the various ionosphere profiles of Deeks. Agreement of the propagation parameter was to 1 part in 10^5 for phase velocity and one hundredth of a decibel per kilometer for the attenuation factor. The excitation factors also agreed to within .01 dB. It appears that the two versions converge to identical results in the limit of zero shell thickness. The propagation model also gives excellent agreement with published results from the NELC Waveguide program. Results from a typical comparison are shown in Table 4-1. The specific conditions for the comparison at 15.567 kHz are those used by Morfitt (ref.14) in a similar comparison of propagation models. These conditions correspond to mid-latitude propagation under an assumed exponential nighttime ionosphere. The agreement in phase velocity and attenuation is limited only by the tolerance that was used for iteration cut-off in the RTI program. The excitation factor is subject to somewhat more variation because it depends on the derivative of an ionosphere impedance "match" characteristic with respect to the propagation parameter. A discussion of this with the researchers at NELC disclosed that due to the variation in direction and increment size in taking the numerical complex derivative they would expect as much as 1-2 db of variation in the excitation factors for runs made with different initial postulated propagation parameter values.

Table 4-1. Comparison of Propagation Models

Mode Identification		RTI LONGWAVE	NELC WAVEGUIDE
TM1	c/v	.99636	.99632
	α db/mm	.27	.28
	$\lvert\Lambda\rvert$ db	-8.31	-7.81
TM2	c/v	1.00703	1.007128
	α	1.46	1.508
	$\lvert\Lambda\rvert$	.04	.91
TE1	c/v	.99802	.99800
	α	1.44	1.49
	$\lvert\Lambda\rvert$	-20.46	-20.28

Page Intentionally Left Blank

CHAPTER 5

COMPOSITE OMEGA ANALYSIS

Composite OMEGA is a mode of operation whereby phase measurements at two or more carrier frequencies are combined to form a composite frequency phase. In reference 1 this concept was discussed considering composite phase as a linear combination of carrier phase measurements. One problem that was addressed involved mapping composite phase values to position locations. With no constraints on the carrier phase weighting this can result in ambiguities. In this chapter weighting coefficient constraints are considered and related to work done by Pierce and Baltzer (refs. 15, 16, 17, and 18), so that the composite phase may be directly related to standard charts. A second section discusses determination of combination weights to minimize measured composite phase variations.

5.1 Composite OMEGA Weighting Coefficients

Assume that a composite OMEGA phase measurement consists of a linear combination of 13.6 kHz and 10.2 kHz phase measurements in units of the respective OMEGA frequencies. The composite phase, ϕ_c, can then be represented as

$$\phi_c = a_1\phi_{13.6} + a_2\phi_{10.2} \tag{5-1}$$

where (a_1, a_2) are arbitrary in the range $-\infty \leq a_1, a_2 \leq \infty$. Phase units of the composite measure will be determined by the relationship of a_1 and a_2 so that only when $a_2 = 1 - \frac{4}{3} a_1$ will ϕ_c be in units of cecs at 10.2 kHz (ref. 15). For other (a_1, a_2) pairs the phase units of ϕ_c will be in units of wavelengths at other frequencies. When comparing various composite phase measures, e.g., comparing the navigation errors associated with different weightings, the units of ϕ_c for any given (a_1, a_2) pair must be calculated because it is necessary to express the various composite phase values in the same phase units. It is, of course, particularly convenient to use cec of 10.2 kHz since navigation charts are available in these units.

For any choice (a_1, a_2) it is possible to derive a conversion factor so that ϕ_c is always in units of cec at 10.2 kHz. Let K be such that

$$\phi_c' = K\phi_c \tag{5-2}$$

where ϕ_c is as given in (5-1) and ϕ_c' is in units of cec at 10.2 kHz. Then using (5-2) to rewrite (5-1)

$$\phi_c' = Ka_1\phi_{13.6} + Ka_2\phi_{10.2} \tag{5-3}$$

where $Ka_2 = -\frac{4}{3} Ka_1$ is required normalization for ϕ_c' to be in the desired 10.2 kHz units. This yields

$$K = [a_2 + \frac{4}{3} a_1]^{-1} . \tag{5-4}$$

Thus, the expression for composite phase in 10.2 kHz phase units for any choice of (a_1, a_2) weighting coefficients becomes

$$\phi_c' = [a_2 + \frac{4}{3} a_1]^{-1} \left\{a_1\phi_{13.6} + a_2\phi_{10.2}\right\} \tag{5-5}$$

where (a_1, a_2) can be arbitrarily chosen.

Equation (5-5) can be expanded and rewritten to yield

$$\phi_c' = \frac{3}{4} m\phi_{13.6} - (m-1)\phi_{10.2} \tag{5-6}$$

which is the composite form used by Pierce (refs. 16 and 17). In

(5-6)

$$m = \frac{\frac{4}{3} a_1}{a_2 + \frac{4}{3} a_1} = \frac{\frac{4}{3} a_1/a_2}{1 + \frac{4}{3} a_1/a_2} \quad . \tag{5-7}$$

From (5-7) it can be seen that any choice of (a_1,a_2) can be mapped to a particular value of m. In fact, m is only dependent on the ratio of (a_1/a_2) which is given in Figure 5-1. This result means that there is in effect a many-to-one mapping of the a_1, a_2 plane onto a line $a_2 = 1 - \frac{4}{3} a_1$ brought about by conversion of composite phase units to cec of 10.2 kHz. Actually each line $a_1 = \beta a_2$ with slope β and going through the origin is mapped to a single point on the line $a_2 = 1 - \frac{4}{3} a_1$ which is the intersection of lines $a_1 = \beta a_2$ with the line $a_2 = 1 - \frac{4}{3} a_1$. A small subset of these lines is illustrated in Figure 5-2.

When evaluating the composite phase variation as a function of a_1 and a_2 all formulations of ϕ_c, when transformed to units of cec at 10.2 kHz, will be equivalent for each pair of the set $\{a_1, a_2\}$ corresponding to a particular β value when $a_1 = \beta a_2$. Thus, it is only necessary to consider variations of composite phase as a function of β and the variations of composite phase over the entire a_1, a_2 plane are characterized. From Figure 5-1 it was illustrated that for each β there is a unique value of m. Thus, one can use (5-6) to evaluate the composite phase variations as a function of m and consequently will have considered all possible pairs of weighting coefficients given in (5-1).

This observation is illustrated in Figure 5-3. Real data obtained at NASA-Langley were used to form composite phase readings. It was desired to determine what weighting coefficients would yield a minimum standard deviation of composite phase when measures of phase from a given transmitter at 13.6 kHz and 10.2 kHz were combined linearly. The composite phase was calculated as

$$\phi_c = A\left\{\frac{3}{4} \phi_{13.6}\right\} - B\phi_{10.2} \tag{5-8}$$

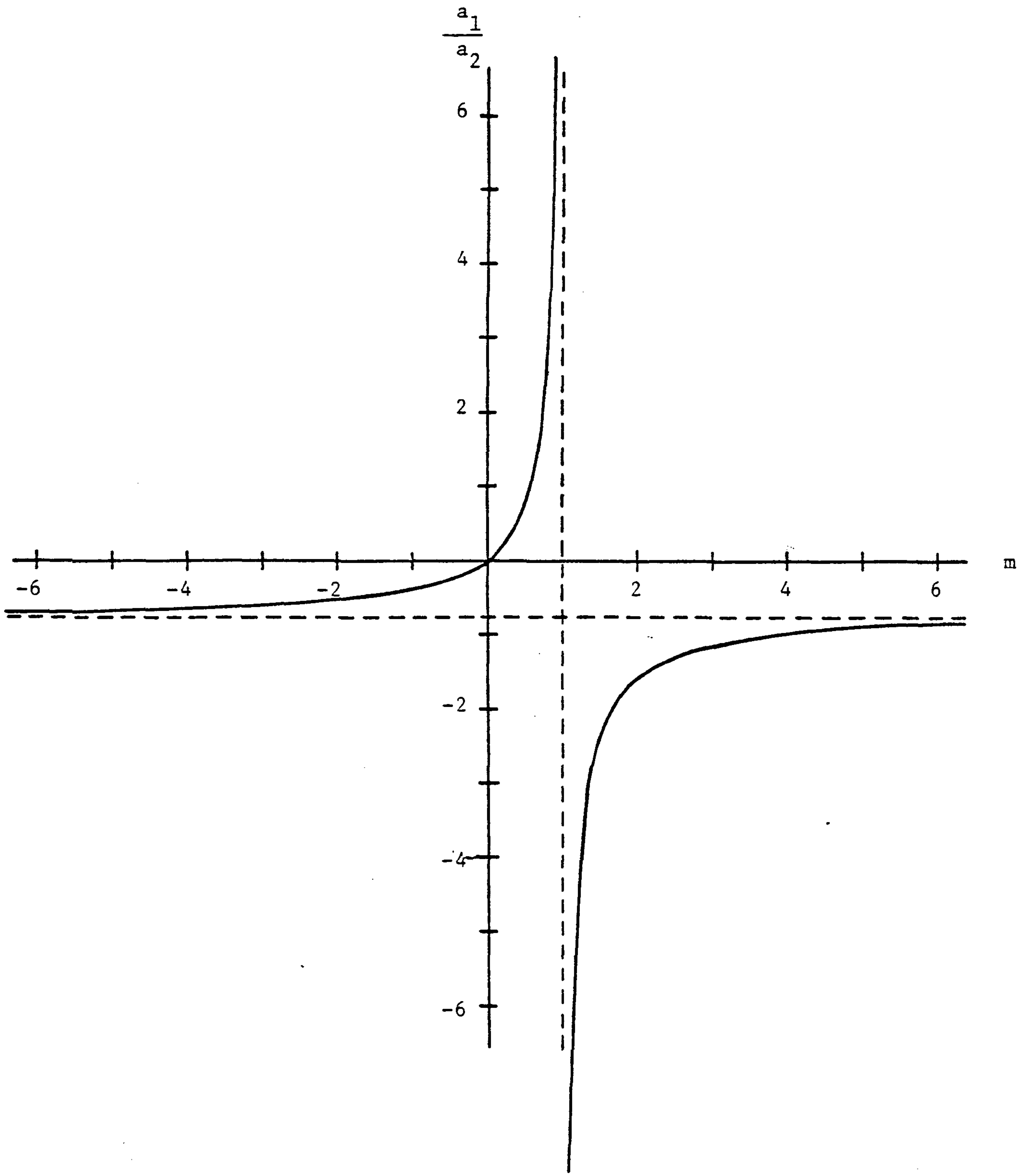

Figure 5-1. Composite Phase Weighting Coefficient Ratio vs. m

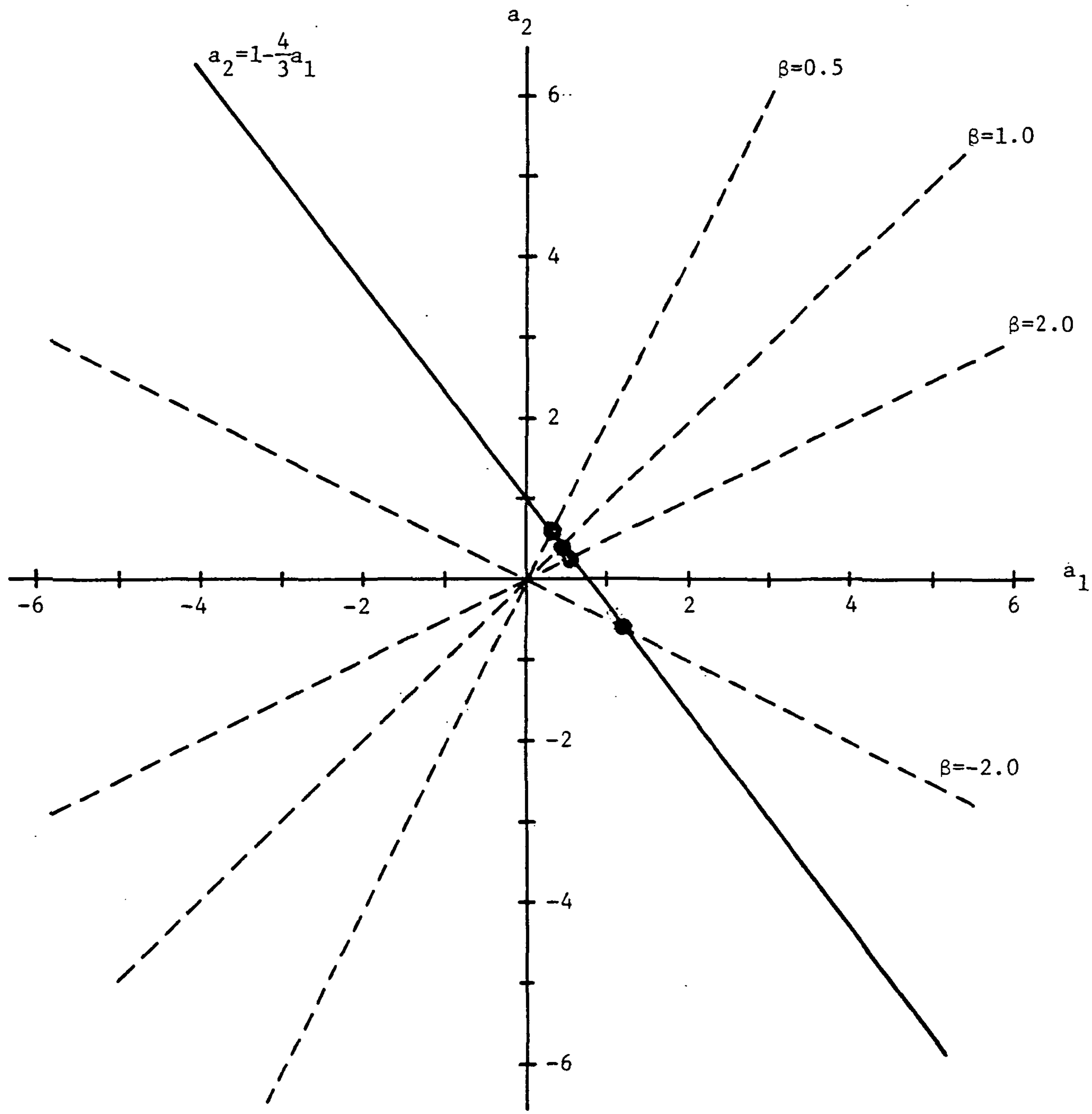

Figure 5-2. Mapping the a_1, a_2 Plane into the Line $a_2=1-\frac{4}{3}a_1$. ($\beta=a_1/a_2$)

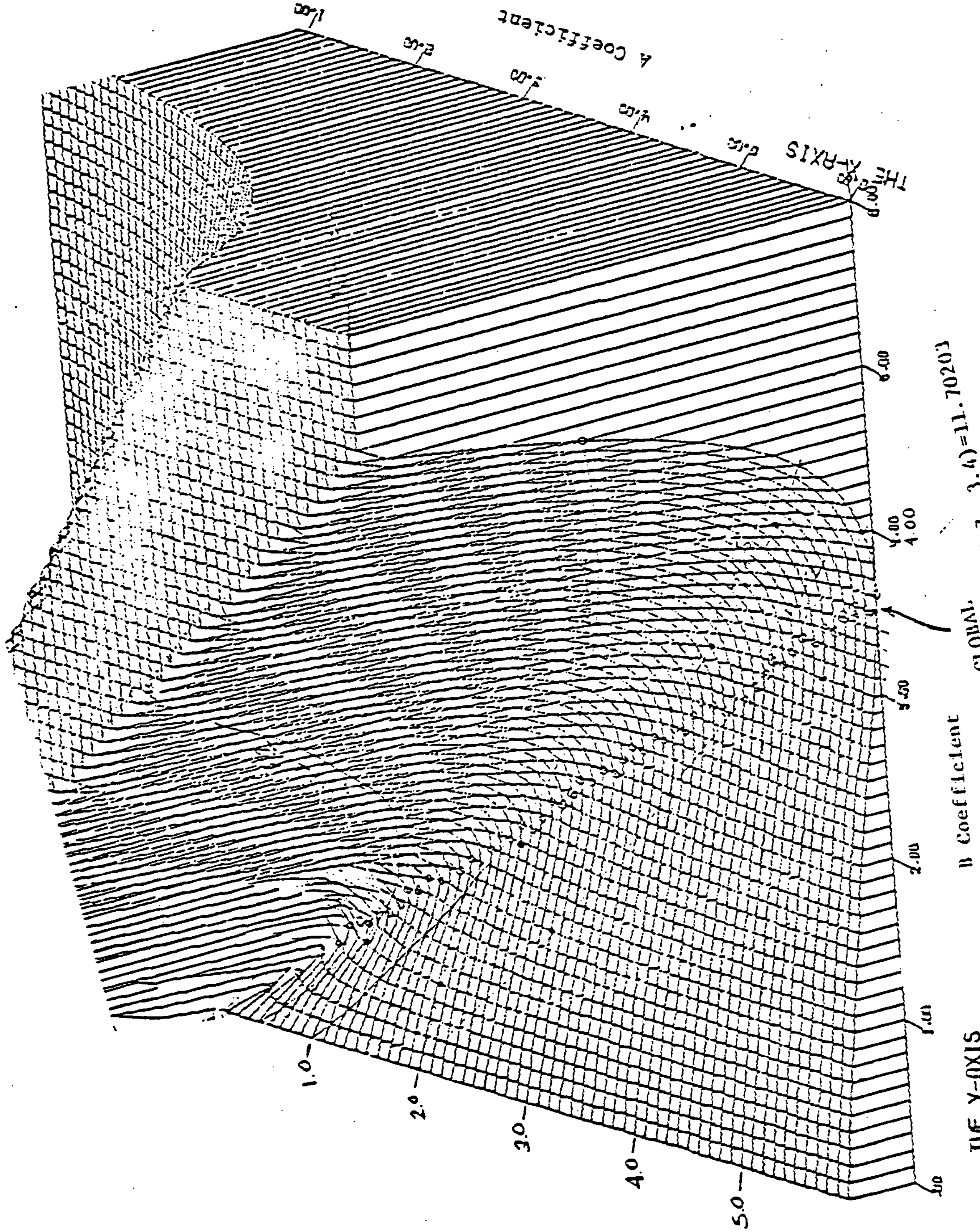

Figure 5-3. Composite Phase Standard Deviation vs. Relative Weighting of 13.6 kHz and 10.2 kHz Phase.

where phase readings are in cec at each respective frequency. Equation (5-8) is equivalent to (5-1) where $a_1 = \frac{3}{4}A$ and $a_2 = -B$. Then, to insure that ϕ_c is in cec units of 10.2 kHz, (5-8) is expressed as in (5-5) as

$$\phi_c' = [A-B]^{-1} \{\frac{3}{4} A\phi_{13.6} - B\phi_{10.2}\} \quad . \tag{5-9}$$

Using measurements of $\sigma_{13.6}$, $\sigma_{10.2}$, and τ_{12} from a five day period of data collected from the Norway station, the standard deviation of ϕ_c' (i.e. σ_c') given by (5-9) was used to calculate and plot σ_c' for a range of A,B ($0 \leq A \leq 6$, $0 \leq B \leq 6$). The resulting three dimensional plot is given in Figure 5-3. The valley of minimum is actually parallel to the A-B plane with $\sigma_c' = 11.7$ cec at 10.2 kHz and is along the line $B \simeq 0.6A$. The estimated standard deviation from the data for 10.2 kHz was 22.9863 cec and for 13.6 kHz was 22.6189 cec. The data estimate of $\tau_{12}\sigma_{10.2}\sigma_{12.6}$ was 513.92. It is desired to estimate the value of m corresponding to the weighting of (5-6) for which the minimum standard deviation of the composite phase is 11.7 cec.

It can be noted that with $B = A-1$, (5-9) yields (5-6) with $m = A$ and, as has been discussed in this section, the variation of ϕ_c' along the line $B = A-1$ will contain all the information about the variation of σ_c' in the A,B weighting coefficient plane.

Using (5-6)

$$(\sigma_c')^2 = \frac{9}{16} m^2\sigma_{13.6}^2 + (m-1)^2\sigma_{10.2}^2 - \frac{3}{2} m(m-1)\tau_{12}\sigma_{10.2}\sigma_{13.6} \quad . \tag{5-10}$$

With $R_{12} = \tau_{12}\sigma_{10.2}\sigma_{13.6}$

$$\sigma_c' = \{\frac{9}{16} m^2\sigma_{13.6}^2 + (m-1)^2\sigma_{10.2}^2 - \frac{3}{2} m(m-1)R_{12}\}^{-\frac{1}{2}} \quad . \tag{5-11}$$

The minimum value of σ_c' may be found by differentiating (5-10) with respect to m and equating this to zero. This results in

$$m_0 = \left[\frac{2\sigma^2_{10.2} - 3/2R_{12}}{9/8\sigma^2_{12.6} + 2\sigma^2_{10.2} - 3R_{12}} \right] . \tag{5-12}$$

With a minimum σ_c' of 11.7 cec the cross-correlation R_{12} may be expressed as a function of m using (5-11) to yield

$$R_{12} = \frac{3}{8}\left[\frac{m}{m-1}\right]\sigma^2_{13.6} + \frac{2}{3}\left[\frac{m-1}{m}\right]\sigma^2_{10.2} - \frac{2}{3}\frac{(11.7)^2}{m(m-1)} . \tag{5-13}$$

The intersection of (5-12) and (5-13) yields a point (m_0, R_{12}) which allows a minimum $\sigma_c' = 11.7$ cec. Ideally, the R_{12} solution should be that which was calculated from the data (513.92). However, due to errors in estimating $\sigma_{10.2}$, $\sigma_{13.6}$, R_{12}, and min $[\sigma_c']$, there is a slight difference. Figure 5-4 is a plot of the two relationships between m_0 and R_{12} given by (5-12) and (5-13). The intersection yields a solution of $m_0 = 2.638$. Thus, (5-9) becomes

$$\phi_c' = \frac{3}{4}(2.638)\phi_{13.6} - 1.638\phi_{10.2} \tag{5-14}$$

yielding the composite phase measurement which has minimum variance for this data set. For the value of R_{12} obtained from Figure 5-4, Figure 5-5 is a plot of σ_c' vs. m as given by (5-11) which gives the same information as Figure 5-3. The minimum at m = 2.638 is the global minimum for any possible linear combination of $\phi_{13.6}$ and $\phi_{10.2}$ for this particular data set. It is of interest to note that this value of m corresponds very closely to values observed by Pierce for the Norway signal at Cambridge, Massachusetts (ref. 17).

5.2 The Effect of Carrier Phase Correlation on Composite Phase

It has been shown that the linear weighting coefficient plane for a composite phase measure involving 13.6 kHz and 10.2 kHz is completely characterized by the "m-value" weighting of carrier phase values.

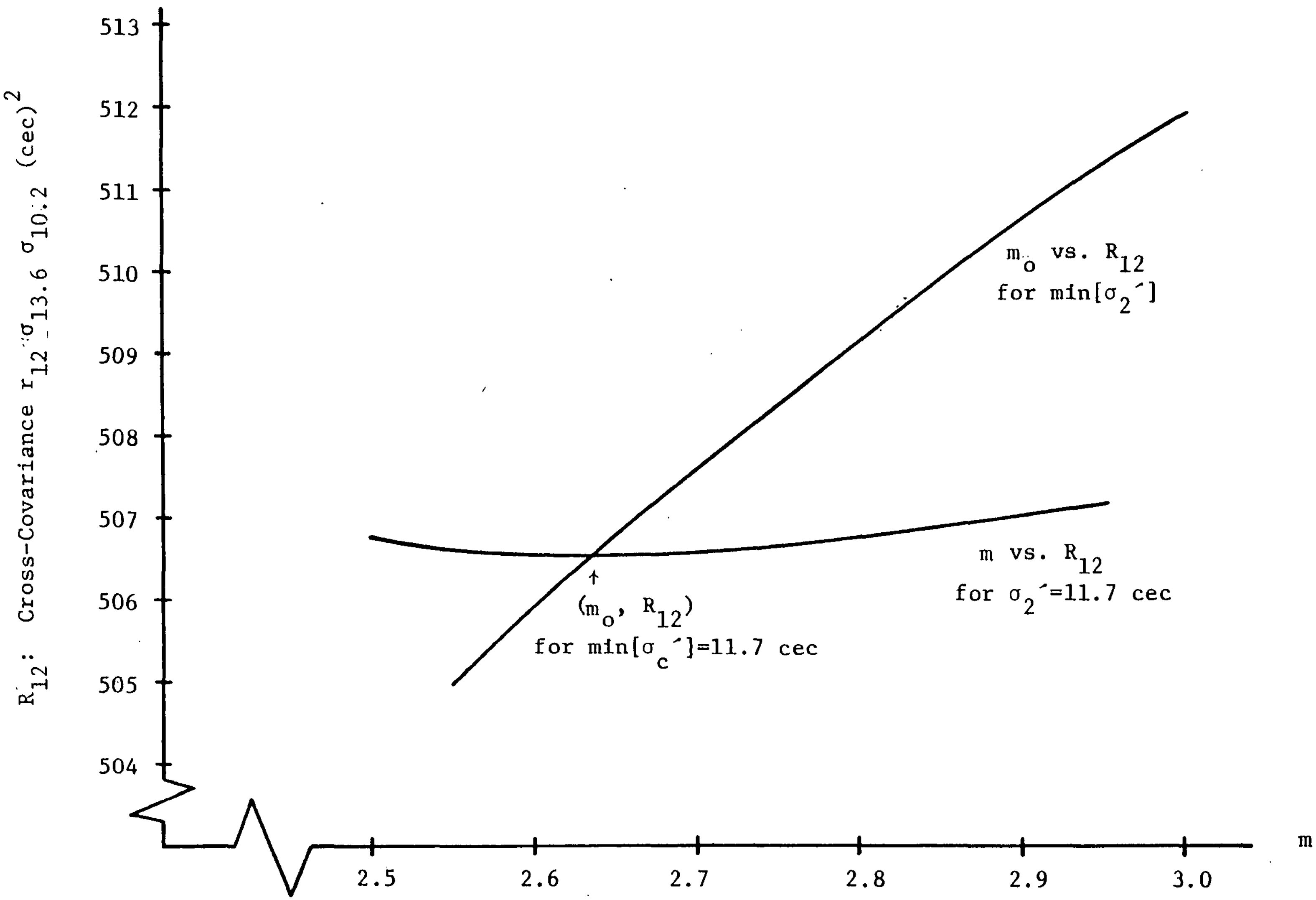

Figure 5-4. Data Determined R_{12} and m_o for $\mathrm{Min}[\sigma_c']$=11.7 cec

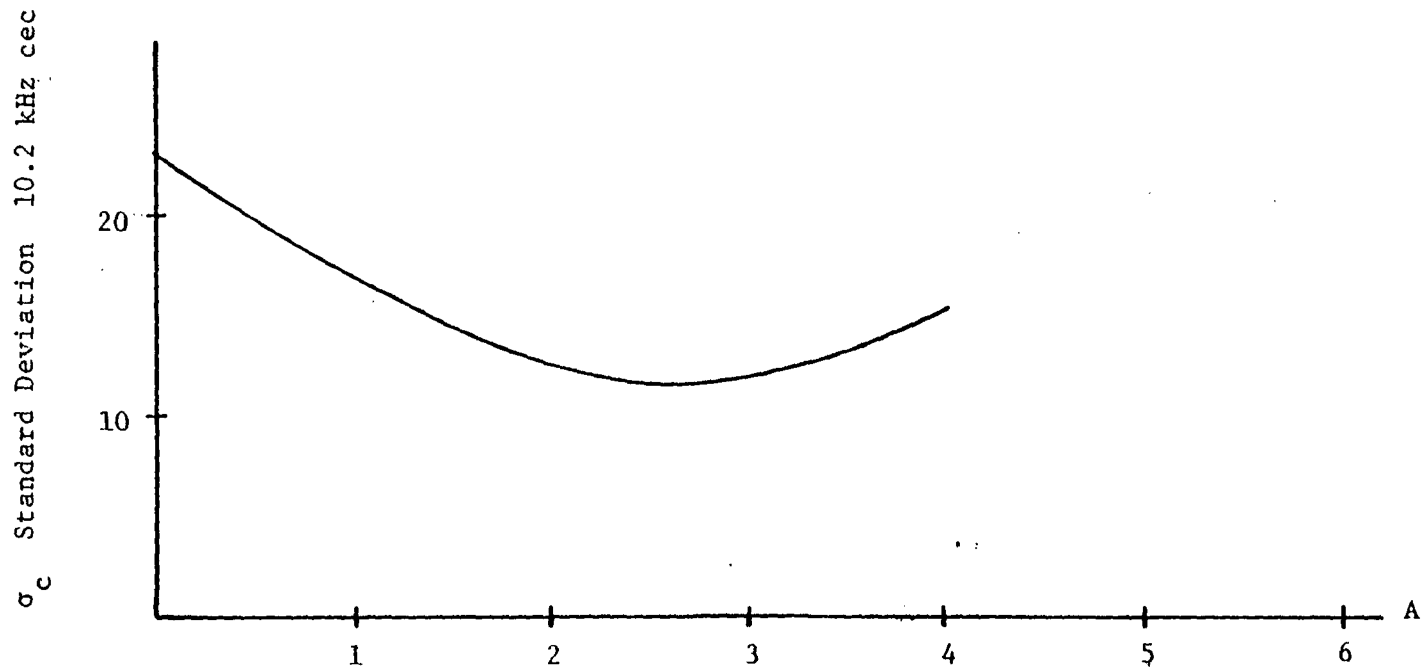

Figure 5-5. Composite Phase Standard Deviation vs. A(m) for Norway Data Set.

Using the relationship of (5-6) for the composite phase and the expression of (5-10) for the variance of this phase it is desired to consider the effects of various correlation coefficients.

First consider $R_{12} = 0$, i.e., the carrier phase values are uncorrelated; then from (5-10)

$$\sigma_c^2 = \frac{9}{16} m^2 \sigma_{13.6}^2 + (m-1)^2 \sigma_{10.2}^2 \, . \tag{5-15}$$

Normalizing by $\sigma_{10.2}^2$ yields

$$\left(\frac{\sigma_c}{\sigma_{10.2}}\right)^2 = \frac{9}{16} m^2 \left(\frac{\sigma_{13.6}}{\sigma_{10.2}}\right)^2 + (m-1)^2 \, . \tag{5-16}$$

Minimizing with respect to m yields

$$m_o = \left[\frac{9}{16}\left(\frac{\sigma_{13.6}}{\sigma_{10.2}}\right)^2 + 1\right]^{-1}$$

as the value of m at which the minimum occurs.

Reconsidering (5-10) it can be seen that the term involving the correlation coefficient R_{12} then modifies the uncorrelated phase variance so that a minimum occurs when $R_{12} = +1$ and a maximum occurs when $R_{12} = -1$. Therefore if uncorrelated variations in the carrier frequency phase are present they serve to increase σ_c^2 over what would be if variations were perfectly correlated, making uncorrelated noise undesirable. On the other hand if negative correlation exists, uncorrelated noise is desirable in that it serves to reduce σ_c^2. This of course assumes $m > 1$.

To further present the variation of σ_c with m consider Figure 5-6 which illustrates the minimum σ_c for various values of $\left(\frac{\sigma_{13.6}}{\sigma_{10.2}}\right)$ and correlation coefficient R_{12}. Values of R_{12} between 0.7 and 1.0 are given. It can be noted that as R_{12} increases for a given value of $\left(\frac{\sigma_{13.6}}{\sigma_{10.2}}\right)$ the m value, for which the minimum σ_c occurs, increases. As the variation in the 13.6 kHz carrier phase decreases with respect to the 10.2 kHz carrier phase variation, the 13.6 kHz is weighted more heavily in forming the minimum variance composite phase (smaller m). As correlation between the carrier frequencies increases, the carrier phase values are more equally weighted (larger m) in forming the minimum variance composite phase.

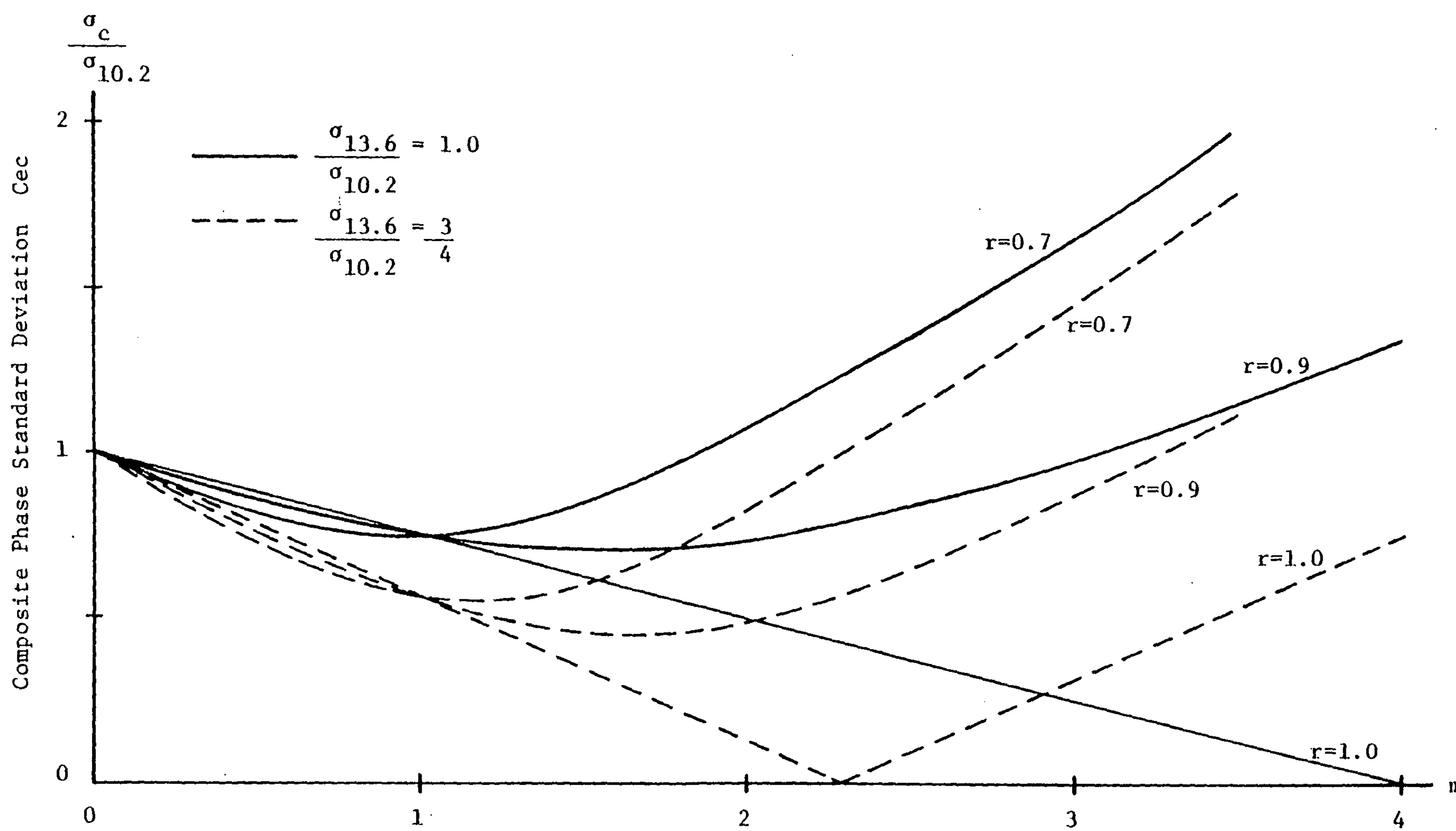

Figure 5-6. Composite Standard Deviation vs. m for Various Correlation Coefficient Values and Different Carrier Frequency Standard Deviations

Further analysis of Figure 5-6 shows that when $\sigma_{13.6}$ and $\sigma_{10.2}$ are very nearly equal and highly correlated an m value in the range 2.5,4.0 will yield minimum σ_c. This is consistent with results of data analysis presented in the previous section.

5.3 Summary

This chapter has presented a discussion of composite phase weighting constraints of carrier frequency phase to obtain 10.2 kHz phase units. Furthermore, specific data analysis has been used to determine the appropriate weighting of 10.2 kHz and 13.6 kHz phase for minimum variance composite phase over a long data period. Some additional data analysis of data combined in composite form has been carried out by NASA personnel. This primarily involved consideration of the 3.4 kHz difference frequency used in lane counting. Generally it was determined that the 3.4 kHz is useful for purposes of carrier frequency lane determination but is not as good as a carrier frequency for navigational accuracy.

"Page missing from available version"

CHAPTER 6

ANALYSIS OF PROPAGATION ANOMALIES

6.1 General

This chapter discusses modal interference, a potential source of error when using the OMEGA navigation system. This form of error is dependent only on propagation path considerations and appears as a phase error in the received phase from a particular transmitter. It is not currently considered in the published propagation corrections (ref. 19).

The representation of EM fields at OMEGA frequencies takes the form of a sum of propagating modes. One of these modes, the first quasi-TM mode, dominates strongly in most situations. Two factors determine the importance of a VLF mode at a given distance from the source. Those are the attenuation of the mode with distance, α_n, and the degree of excitation of the mode at the source, Λ_n. In general the higher quasi-TM modes attenuate with distance more rapidly than the lower, but can be strongly excited, while the quasi-TE modes are poorly excited. Because of the former, the use of a station for navigation is not recommended below a minimum separation. For propagation west to east at night, the second quasi-TM mode can become significant at relatively large transmitter receiver separation because of the decreased difference in mode attenuation parameters.

The purpose of this portion of the study was to verify that modal interference had been significant in the data gathered by NASA and analyzed by RTI over a three-year period (see ref 1), and to determine if the effect of higher order modes could be predicted accurately enough to improve navigation accuracy in the region covered by the experimental program.

As discussed in Chapter 2, the data base consists of phase and amplitude measurements for OMEGA signals from four transmitters, NORWAY, TRINIDAD, HAWAII, and NORTH DAKOTA. Measurements were made in a differential mode with a fixed receiver at Hampton, Virginia, and simultaneously with a movable receiver at sites located in the Maryland, Virginia and North Carolina area. Ten-second OMEGA measurements were made over 5-10 day set-ups with the receiver set-ups repeated at random intervals. Phase, relative to an uncalibrated stable reference, and amplitude were recorded at both receivers for the three frequencies and four transmitters involved.

6.2 Analysis of Data

Early in the data gathering period anomalous behavior was noticed in nighttime LOP phase measurements involving North Dakota transmissions most often at 13.6 kHz. This behavior (see ref. 4) involved large phase changes during the night in the form of phase shifts between largely differing values. *Often these changes appeared as level shifts which* remained for several hours at a time. At other times less coherent large scale phase fluctuations were observed. This phenomena appeared to be location dependent, occuring at many of the sites but to a much greater extent at only a few. This behavior was most clearly observed on the Trinidad-North Dakota LOP measurements. Using the OMEGA propagation prediction corrections the LOP phase differences can be predicted for the Trinidad-North Dakota LOP by:

$$\phi_{BD} = \phi_{C_{BD}} - \phi_{PPC_{BD}} = \left(\phi_{C_B} - \phi_{C_D}\right) - \left(\phi_{PPC_B} - \phi_{PPC_D}\right)$$

where $\phi_{C_{BD}}$ is the chart phase difference based on a phase velocity of 1.0026 times the speed of light, and $\phi_{PPC_{BD}}$ is the difference in propagation corrections at the receiver site for the two paths.

The difference between the hourly mean of measured LOP phase and the corresponding prediction was plotted as a function of time of day for large segment of the data. From these plots it was apparent that at night a time independent mean error was associated with LOP pairs involving North Dakota. This was exhibited at most of the receiver locations and was most prevalent at 13.6 kHz. Figures 6-1 through 6-9 demonstrate the day to day repeatability of the nighttime error for the B-D pair at 13.6 kHz.

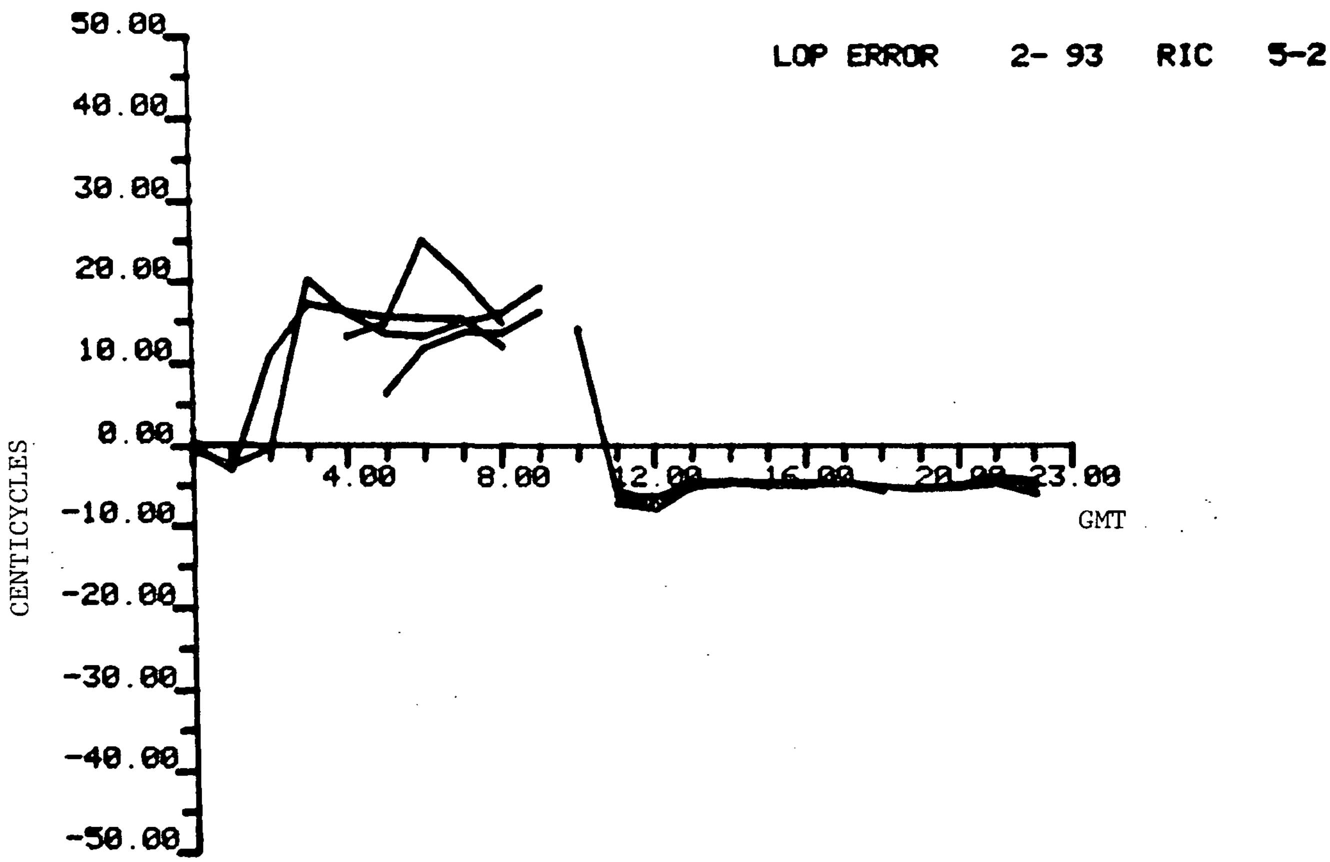

Figure 6-1. Trinidad - N. Dakota LOP Error Using Propagation Prediction Corrections at RMT. Hourly Means at 13.6 kHz.

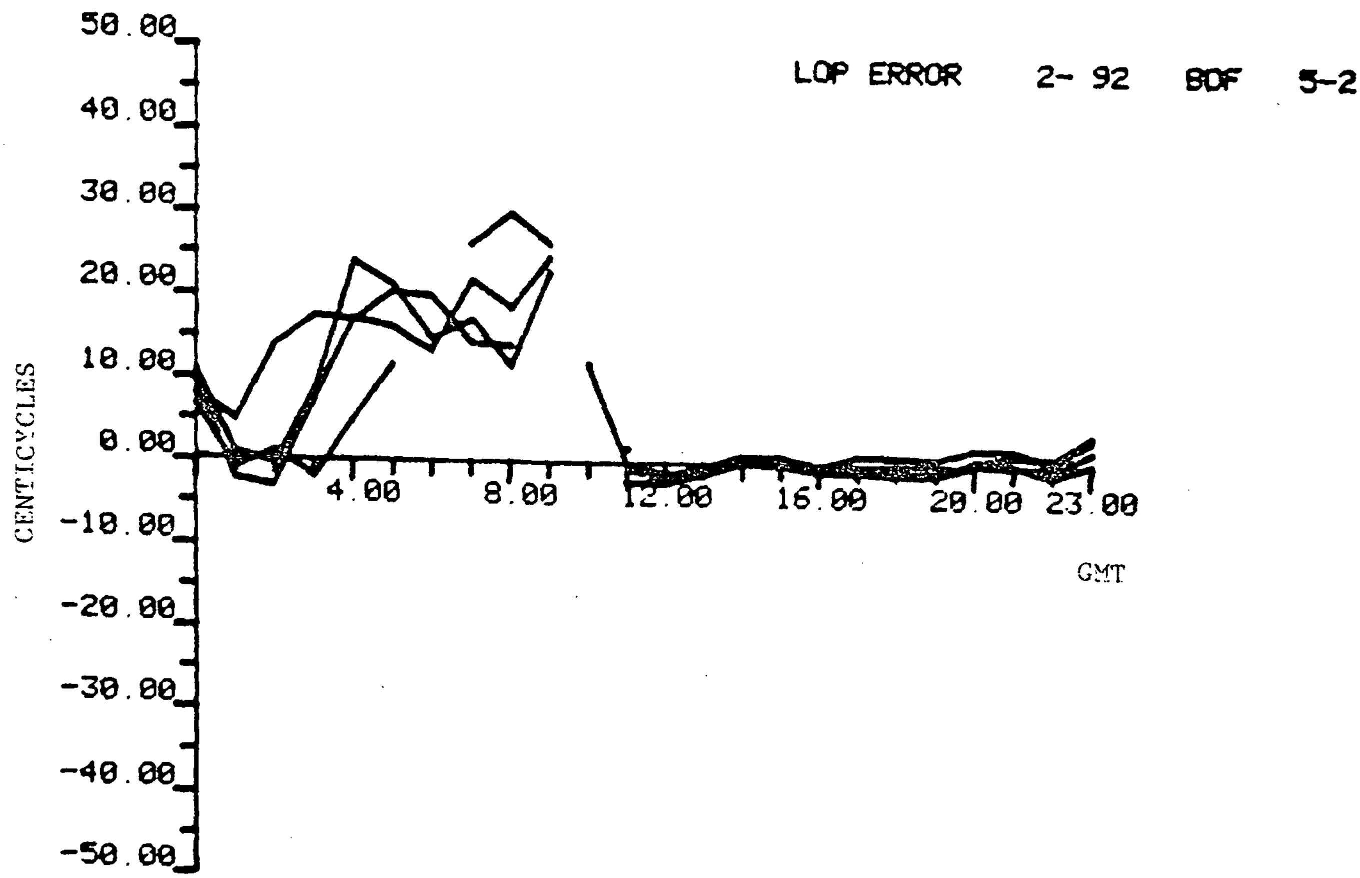

Figure 6-2. Trinidad - N. Dakota LOP Error Using Propagation Prediction Corrections at BDF. Hourly means at 13.6 kHz.

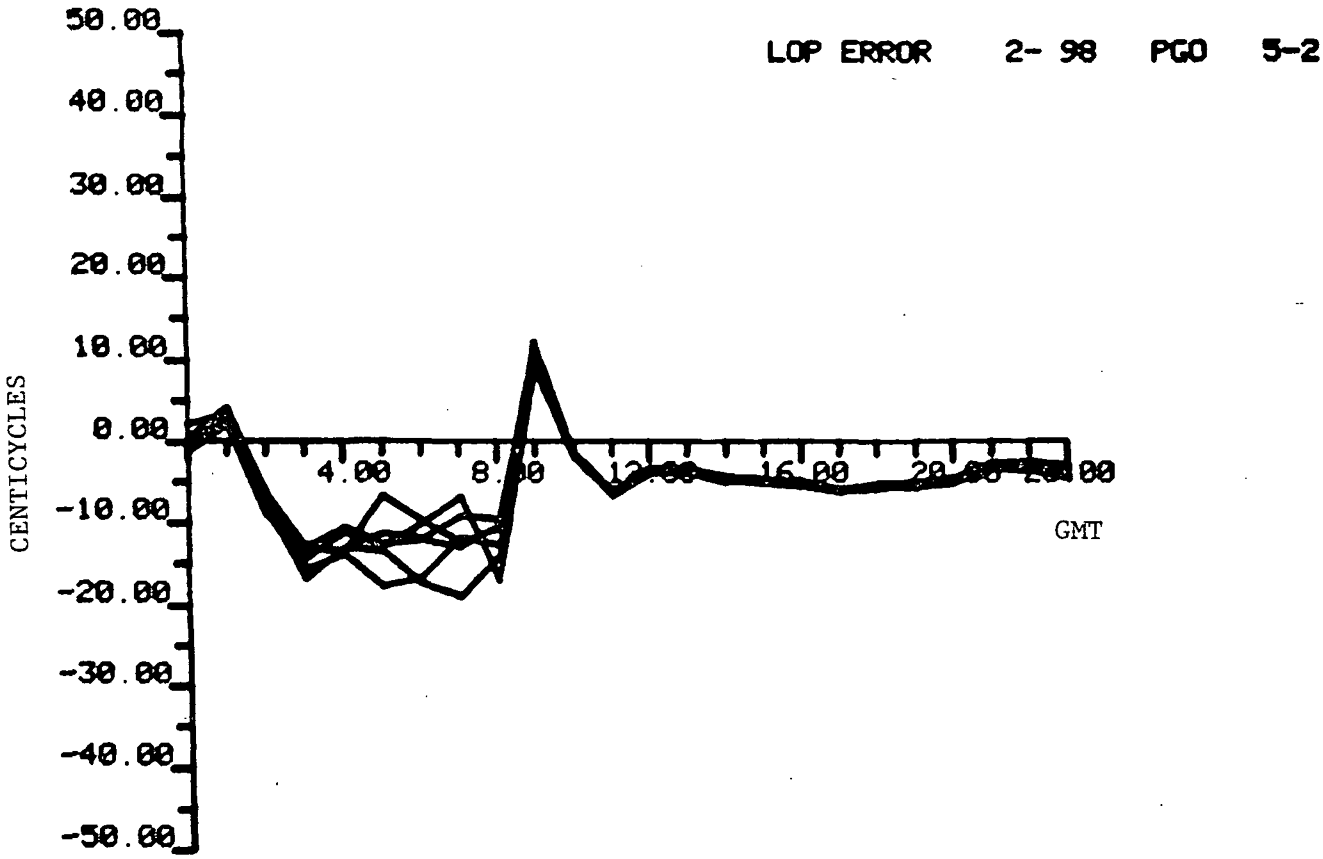

Figure 6-3. Trinidad - N. Dakota LOP Error Using Propagation Prediction Corrections at PGO. Hourly means at 13.6 kHz.

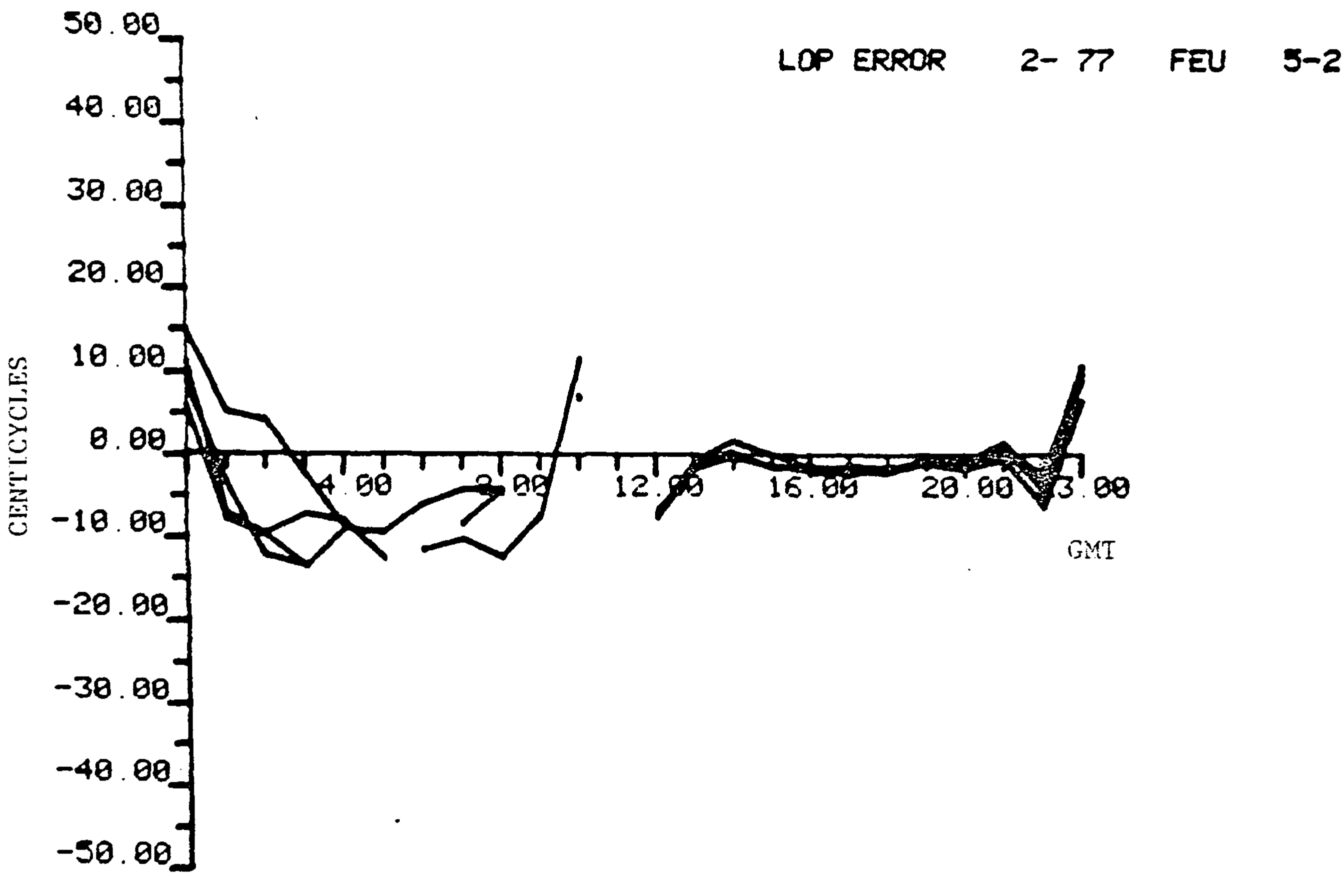

Figure 6-4. Trinidad - N. Dakota LOP Error Using Propagation Prediction Corrections at FEU. Hourly means at 13.6 kHz.

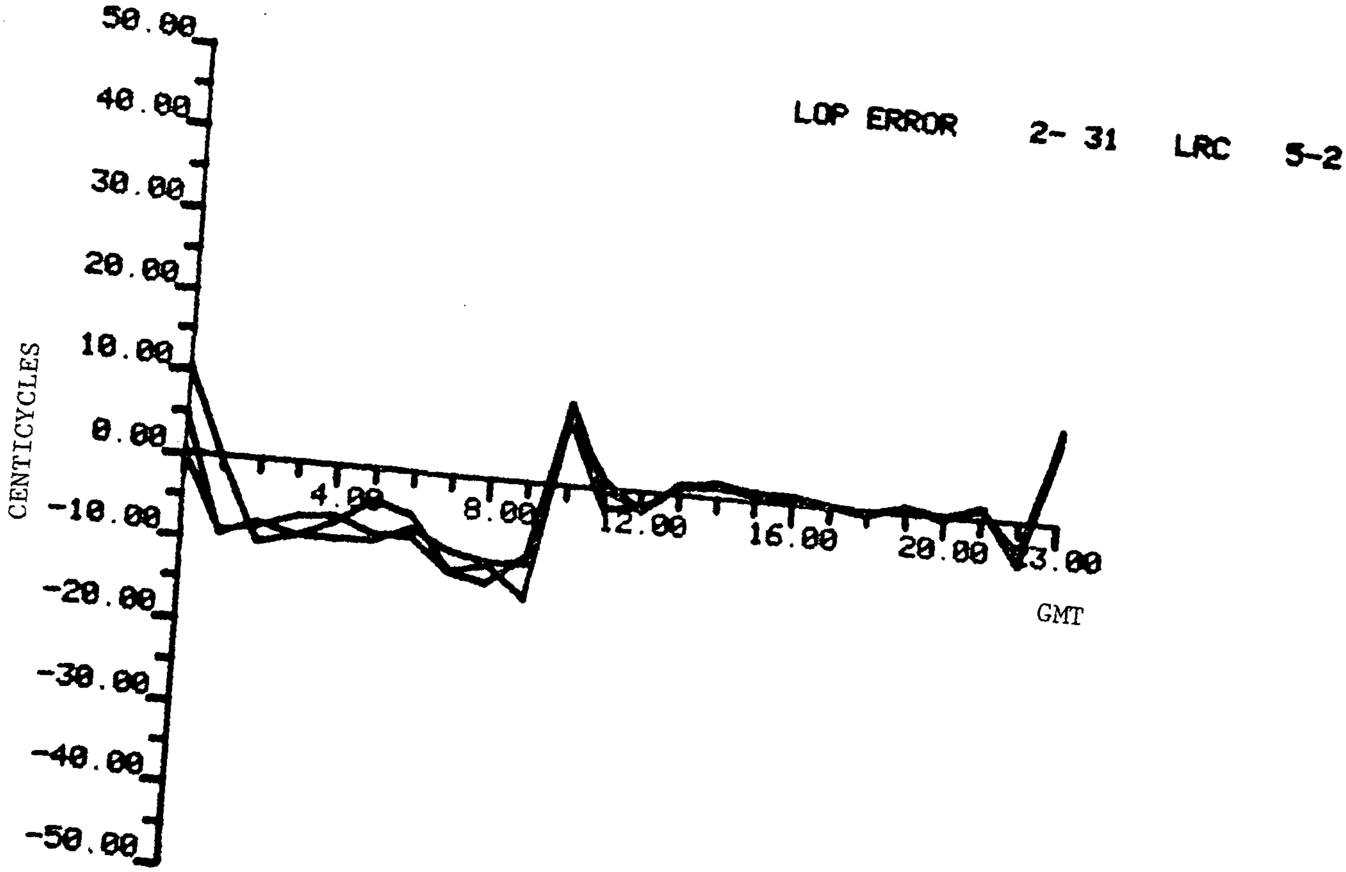

Figure 6-5. Trinidad - N. Dakota LOP Error Using Propagation Prediction Corrections at LRC. Hourly means at 13.6 kHz.

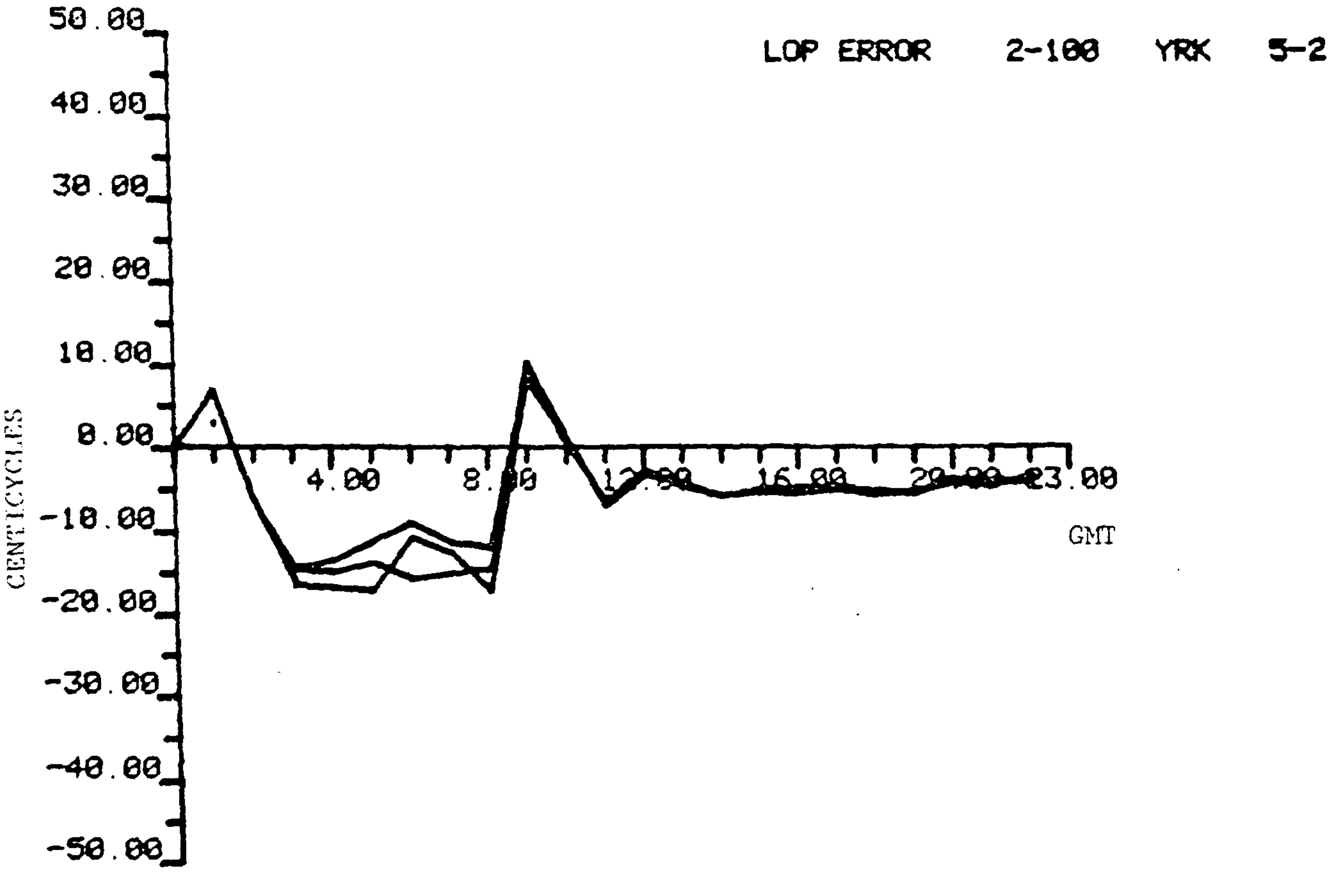

Figure 6-6. Trinidad - N. Dakota LOP Error Using Propagation Prediction Corrections at YKT. Hourly Means at 13.6 kHz.

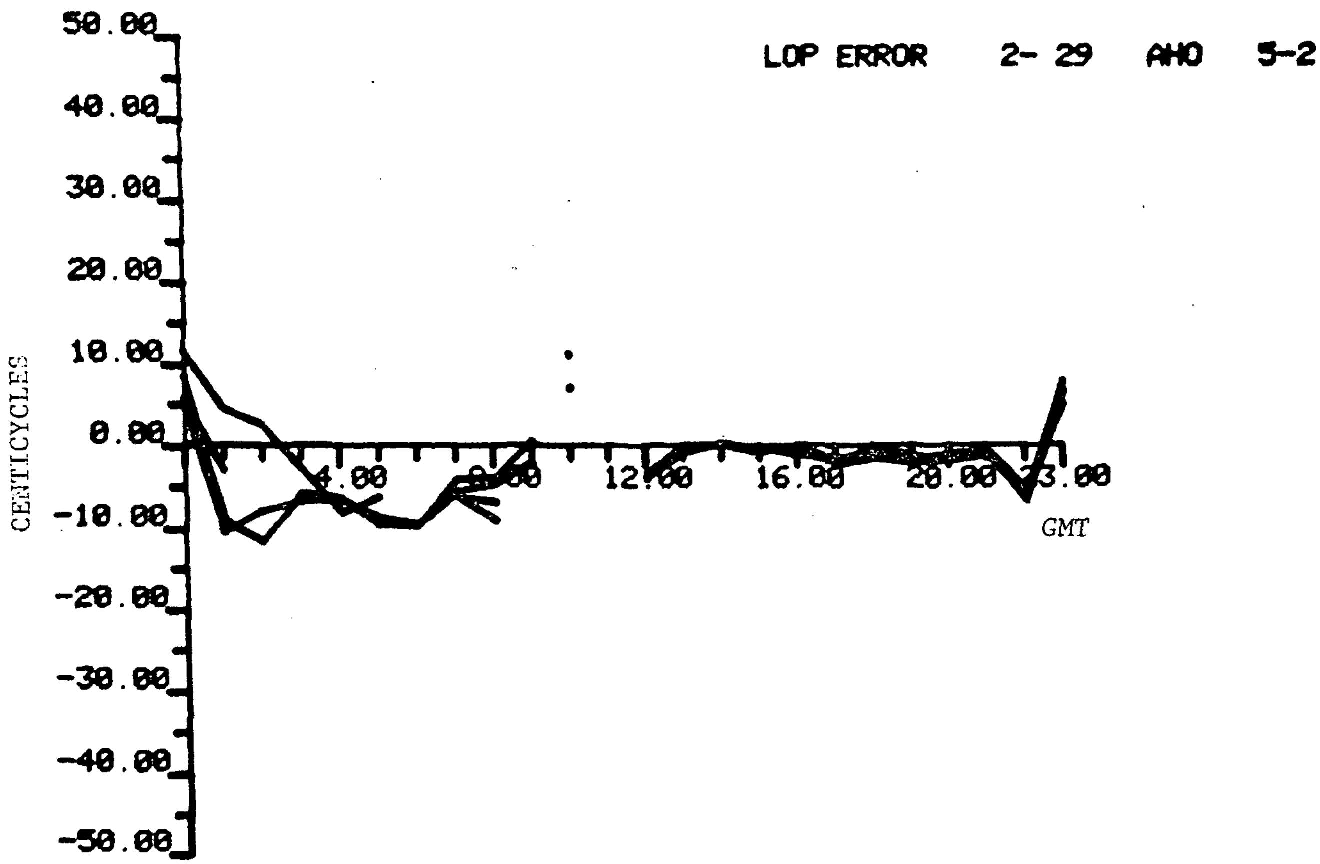

Figure 6-7. Trinidad - N. Dakota LOP Error Using Propagation Prediction Corrections at AHO. Hourly means at 13.6 kHz.

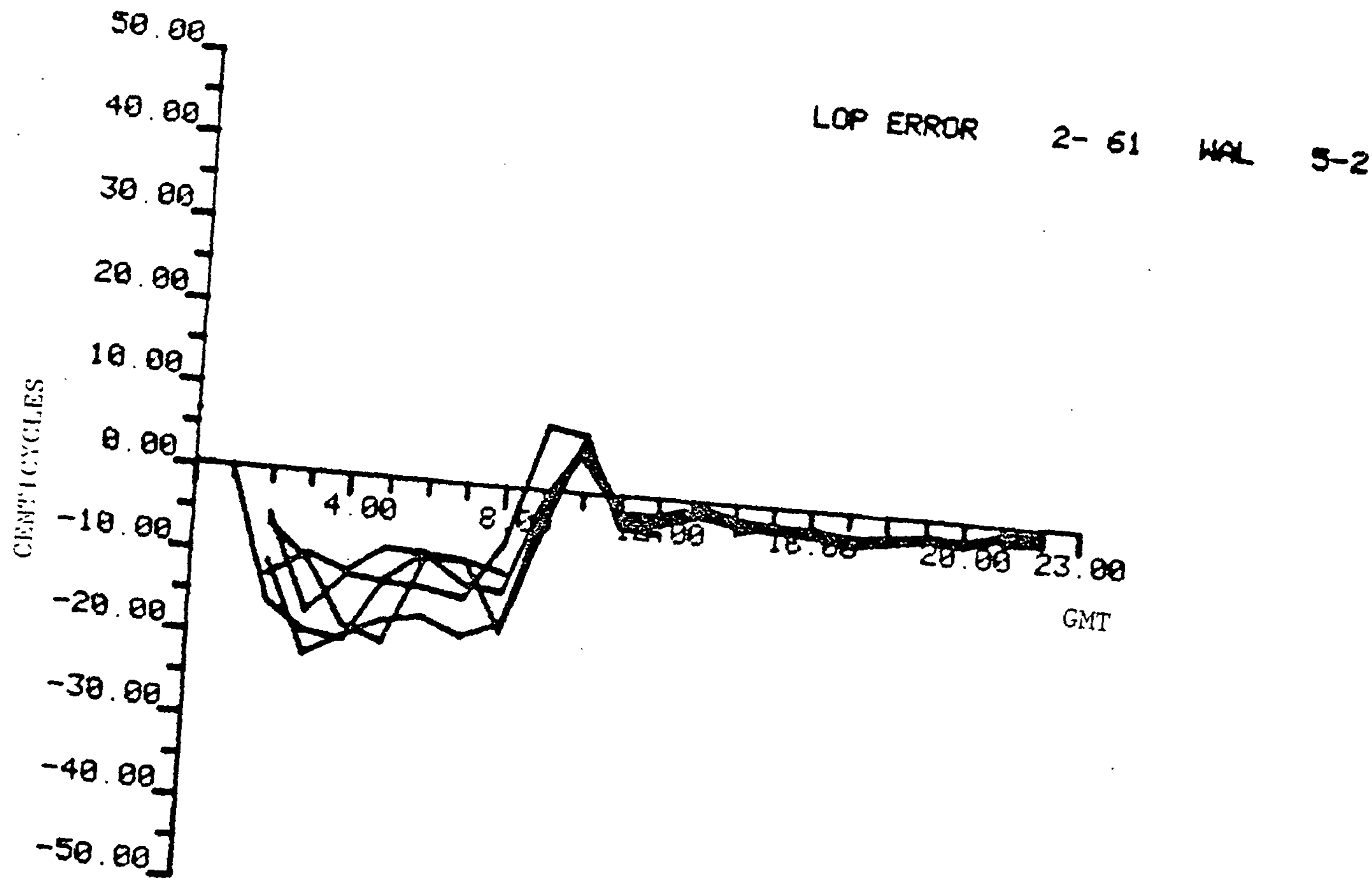

Figure 6-8. Trinidad - N. Dakota LOP Error Using Propagation Prediction Corrections at WAL. Hourly means at 13.6 kHz.

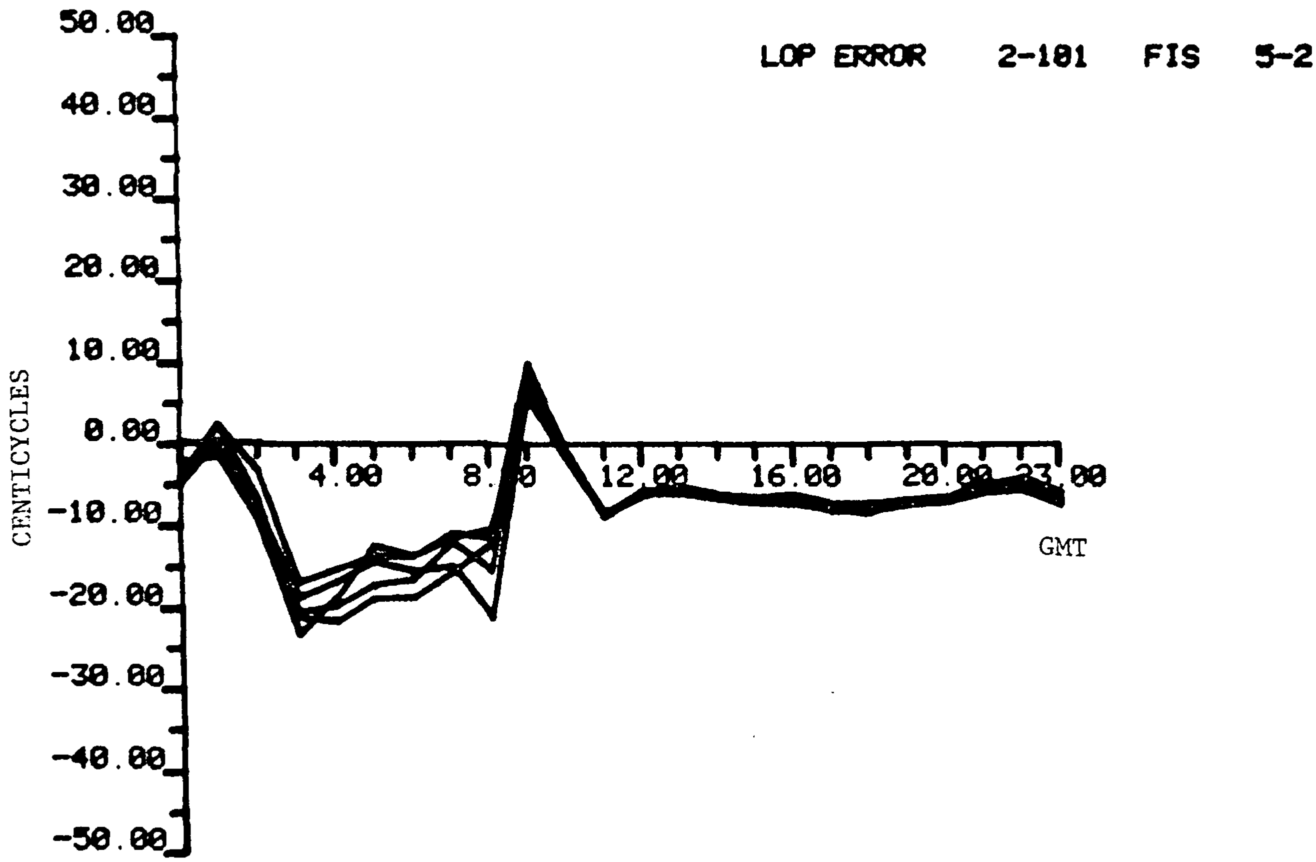

Figure 6-9. Trinidad - N. Dakota LOP Error Using Propagation Prediction Corrections at FIS. Hourly means at 13.6 kHz.

6.3 Predictability of Modal Interference

The average nighttime LOP phase error was plotted as a function of distance to North Carolina with the intention of comparing this plot to a theoretical plot of North Dakota second mode phase interference versus distance. The B-D nighttime phase error plot is shown in Figure 6-10 for 13.6 kHz. The data points are plotted as a dot or square corresponding to summer or winter. The propagation paths from North Dakota to the different receiver sites differ in azimuth from the NDK-Hampton path by less than 10°. This small change in path azimuth with respect to the earth's magnetic field was not predicted to have a significant effect on the North Dakota phase using the VLF propagation algorithm mentioned previously. This allows the inferred North Dakota phase to be treated as if taken along a single radial from the North Dakota transmitter to facilitate comparison with the theoretical plot. The accuracy with which the averaged Trinidad signal is corrected at each receiver site affects the agreement possible with a theoretical modal interference plot for North Dakota. However, Trinidad provides a stable signal in the Hampton area while providing propagation path conditions and sufficient distance to minimize the effects of modal contamination. The effect of the second TM mode of the Trinidad signal in the receiver area is predicted to be less than two cec with a maximum site to site variation close to one cec. A plot of the averaged nighttime data as described previously, produces the characteristic modal interference curve with a slight summer-winter trend noticeable. Important also was the steep slope between locations of mean positive and negative errors occurring in Figure 6-10 between 1.85 and 1.95 megameters. This was originally postulated as the cause of the large time varying phase shifts observed at receiver sites at about this distance from North Dakota (ref. 4). The shifts are apparently caused by a "breathing" of the propagation parameters resulting in a small shifting of the interference pattern. Expected variations in the nighttime ionosphere profiles were analyzed to determine if the observations are consistent with the proposed explanation. Morfitt (ref. 20) has fit VLF ground stations data to a exponential ionosphere VLF model described by

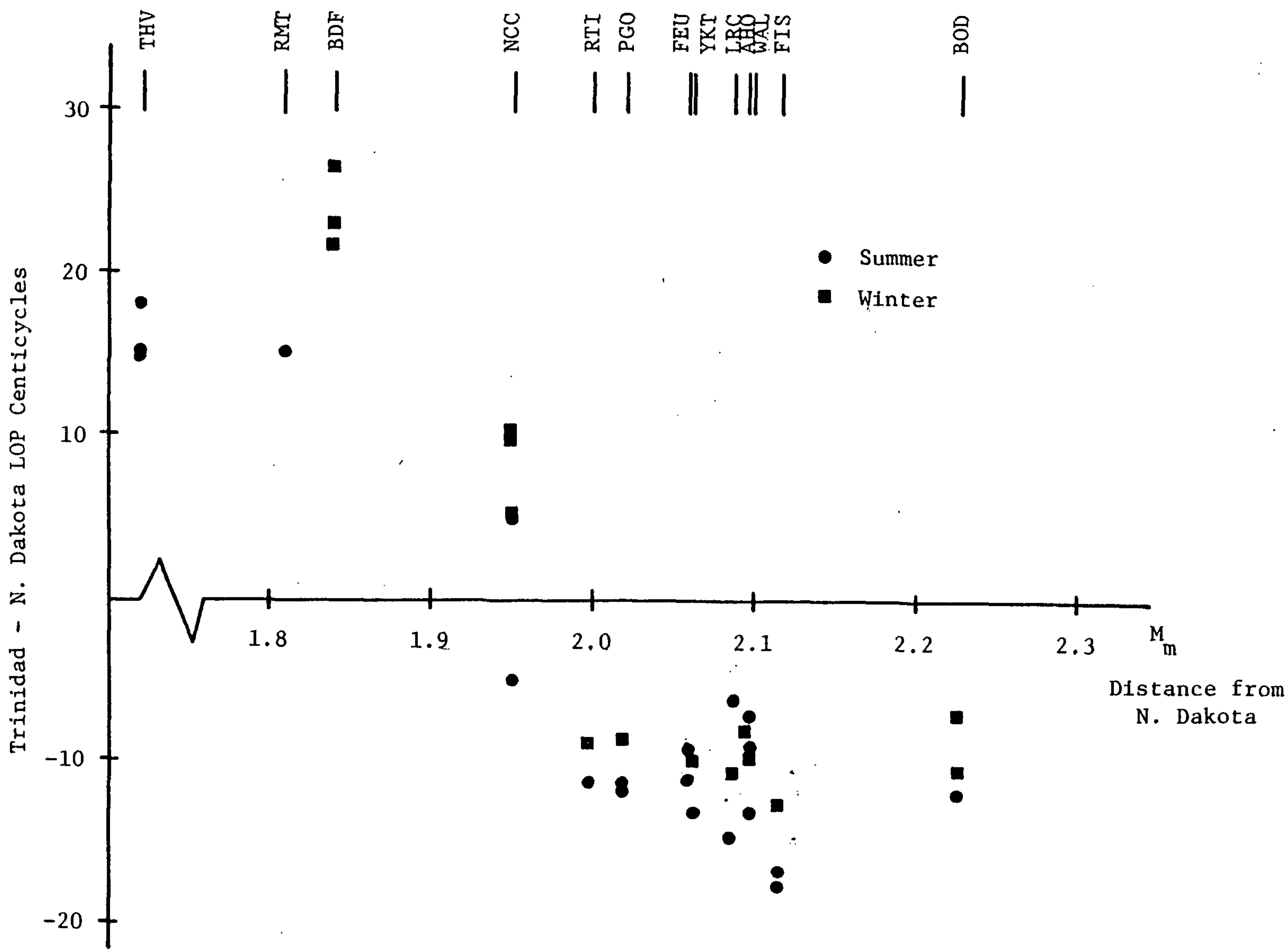

Figure 6-10. Error in Trinidad - N. Dakota LOP at Various Distances From N. Dakota Transmitter

$$N_e = N_0 e^{-\beta(z-h_0)}$$

where N_e is the electron density at height z, N_0 is the reference electron density, h_0 is the reference height, and β the electron density gradient. Parameter changes in h_0 and β were necessary to fit the data over the course of a typical night. Changes of this size, $\pm$ 20% for β = .7 and $\pm$ 1% for h_0, have been analyzed with the VLF propagation algorithm, and are quite adequate to shift the interference curve so that a receiver location near maximum positive phase error could shift to that near maximum negative phase error, or vice versa. This can result in a short term fluctuation of more than 50 cec at the location in question. Other locations, somewhat removed from the large error gradient would not expect to see the large fluctuations but would have a significant nighttime mean error as large as 20-25 cec, for this particular propagation path. At most of the sites studied this mean error appears to be a significant contribution to navigation accuracy and yet is not apparent to the OMEGA user as a signal with large phase variance. On the other hand, North Dakota provides a strong signal and good station geometry in the Atlantic Coast region which in the daytime tends to improve navigation accuracy over that obtainable using the other receivable stations only. This situation will be further reinforced by the planned phaseout of the Trinidad station. This stems from the greater distance and less favorable propagation path associated with the Liberia station.

The quality of the 13.6 kHz North Dakota signal and the general consistency of the second mode interference in the Middle Atlantic Coast region has led to an attempt to accurately model phase interference from higher modes to determine if navigation accuracy could be improved in this region. It is expected that the techniques investigated here would be applicable to other geographic areas. It should be noted however, that propagation path parameters as well as distance, dictate the extent of modal interference present so that the West Coast, for instance, can expect relatively little high order mode contamination of the North Dakota signal while being at comparable distance. An effort was made to fit the North Dakota-Trinidad data to the VLF propagation model mentioned previously. The ionosphere electron density profile has a major effect on the degree and location of model interference. This profile changes with the time of day, the sensor location, and the solar sunspot cycle a representative profile is shown in Figure 6-11. It was determined that the seasonal nighttime ionosphere models of Deeks (ref. 21) for sunspot minimum, produced too large a summer-winter deviation in the amplitude and location of the pattern although a mean ionosphere profile between the two given by Deeks fits the data well. Reducing the height of the profile results in an improved fit for the summer months, while an increase is necessary for the winter months. The changes necessary ($\pm$ 1 km) correspond to less than half of those indicated from the Deeks profiles. In raising and lowering the profiles, the shape was adjusted to approximate the seasonal trend. The primary effects of the profile shape on the interference pattern result from the height and slope of the main D region shelf at approximately 85 km above the earth. Varying the height to comply with the Deeks profile accounts for the observed direction in the shift of the interference pattern in distance. A shift in the shelf slope primarily affects the attenuation of the modes, influencing the second mode more strongly than the first. This results in a change in amplitude of the interference pattern. Height and slope changes with season intermediate to those of Deeks gave the best least square fit to the data. The profile shapes in the regions and below the main shelf were taken intermediate to the Deeks summer and winter figures depending on the height used. The mode parameters and interference pattern were not very sensitive to the exact profile shape in these regions.

A theoretical plot of the phase error due to second mode interference is shown in Figure 6-12 for a profile of intermediate height between the summer and winter extremes and corresponding to nighttime sunspot minimum. Figure 6-13 shows a portion of this plot superimposed on hourly average experimental nighttime B-D LOP phase error data. It is noted that a seasonal profile height variation as great as specified in the Deeks profiles produce a seasonal Mode 1 phase velocity variation which is quite

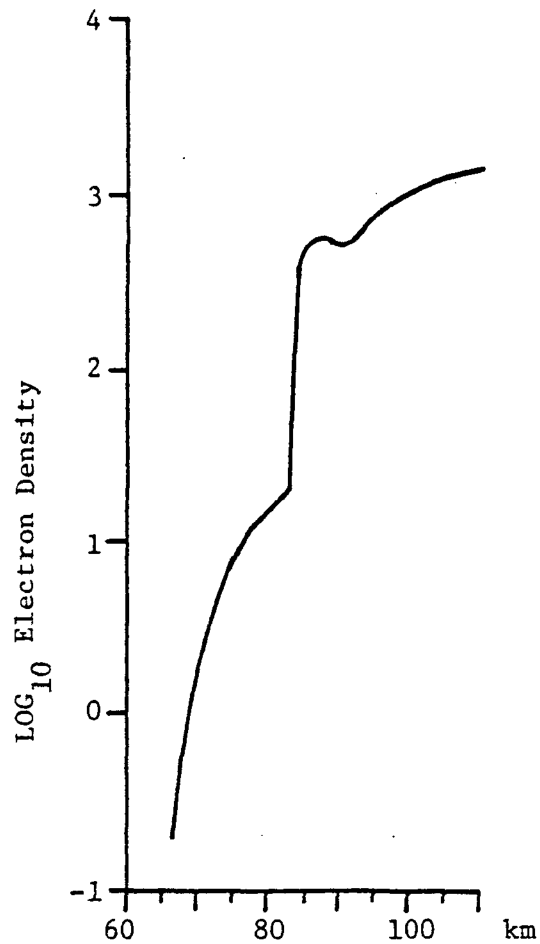

Figure 6-11. Deeks Winter Mid-Latitude Nighttime Sunspot Minimum Ionosphere Profile

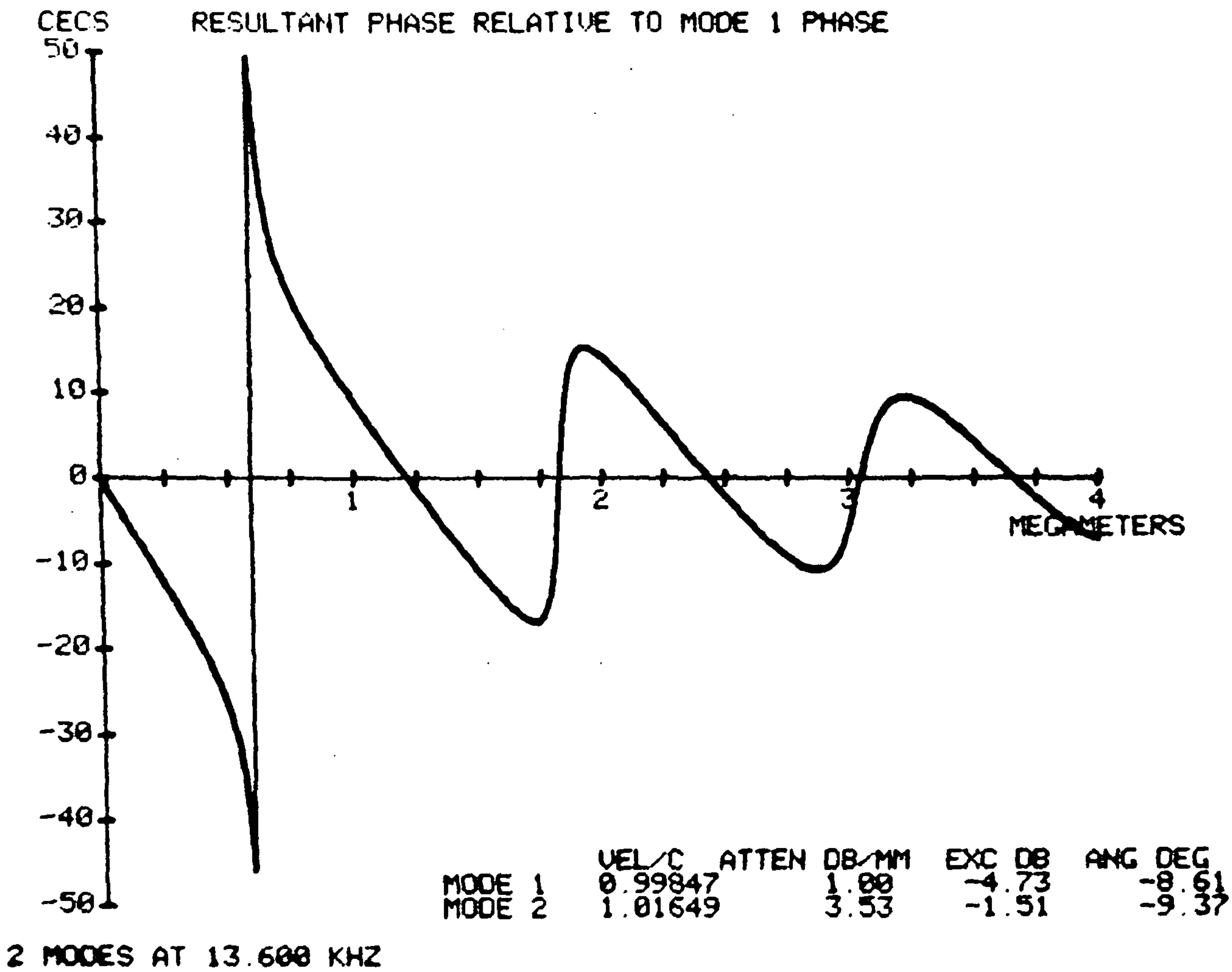

Figure 6-12. Resultant VLF Phase Relative to Mode 1 Phase vs. Distance from Transmitter

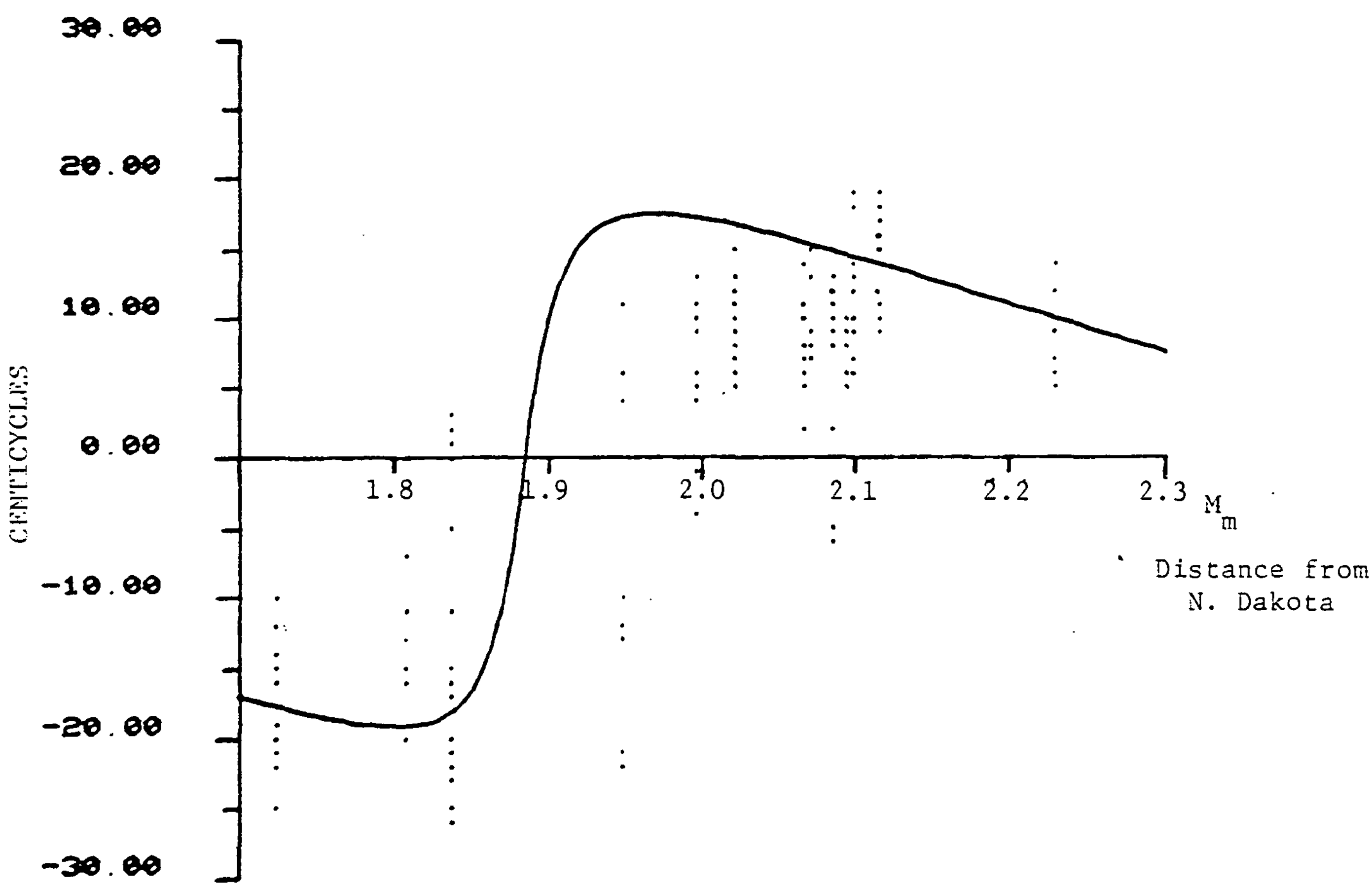

Figure 6-13. Trinidaa - N. Dakota LOP Error at Various Distances From N. Dakota

large. A variation of this size is not compatible with the published OMEGA propagation correction tables which are based in part on experimental data. It is interesting to note that the OMEGA skywave corrections obtained for 1974-1975, the time interval in which most of the data were taken, do not show any nighttime seasonal shift in phase velocity. The more recent tables do show a slight nighttime shift in the summer months, still much less than that which is predicted by the Deeks profiles.

"Page missing from available version"

CHAPTER 7

SUMMARY AND CONCLUSIONS

This ground-based experimental OMEGA program conducted by NASA-Langley Research Center has offered a number of contributions to the field. This represents probably the largest concerted effort in terms of time duration and geographic extent at collecting OMEGA phase data. Although a major goal of the program has been the study of the differential concept of operation, the data have provided considerable insight into ordinary OMEGA, composite OMEGA, local effects problems, receiver repeatability, and propagation anomalies. At the outset of the data gathering, the observed modal interference phenomenon was actually not expected. The available literature did not generally consider modal interference to be a significant problem in achieving good navigation accuracies except at positions close to a transmitter. To understand observations which contained significant errors caused by modal interference - particularly from North Dakota during nighttime periods - an unanticipated direction in the research and analysis resulted. It was necessary to understand the characteristics of VLF propagation to a much greater extent in order to explain why the observed phase perturbations were possible. This led to development of a VLF propagation model which retains enough detail so that phase variations actually observed could be predicted in terms of propagation parameters. For the area in which data were collected the model revealed a strong likelihood of modal interference with magnitudes of phase shift comparable to those observed. In the analysis no appreciable confidence in the ability to predict when this interference will occur has been obtained. However, to alert the navigation community to this problem is considered a significant contribution.

The differential OMEGA results which have been obtained are certainly as good or better than for any previous test. The conditions for this program were controlled. Phase correlation range was found to be larger than previously expected. Good correlation was observed with receiver separation ranges up to 600 n.mi. In fact, the largest limiting factor appeared as a random perturbation which existed even with the receivers co-located. Local effects are certainly important. This should not be a major contributor to error in an airborne

APPENDICES

environment, however. To expect position error to be within the often quoted figure of 0.5 n.mi. rms appears to be quite reasonable based on these results - even within differential regions extending to 150 n.mi. radius. With good receiver-antenna configurations errors on the order of several hundred meters are not unreasonable, particularly in daylight conditions.

Although analysis of the composite mode is not extensive, several general conclusions can be made. Difference frequency OMEGA is definitely a viable means to lane determination. Better position estimation accuracies can be obtained with carrier frequency operation with some means of providing propagation corrections. In general, various carrier frequency phase perturbations are highly correlated with the possible exception of modal type interference which usually is more evident at only one carrier frequency during a given period.

The implications for airborne use of OMEGA are quite good. With inexpensive programmable digital processors and the simplicity of the OMEGA signal format results of this effort show that attainable accuracies are quite reasonable particularly for the general aviation navigating community.

These data that have been collected and catalogued can be of continuing used to the OMEGA community. Certainly one obvious use is to serve as a means to improve published PPC tables and algorithms for stand alone systems. These data represent really a first look at navigation with the 11.3 kHz carrier which has received little attention in the past.

APPENDIX A

AMPLITUDE MEASUREMENT IN THE NASA OMEGA RECEIVER

Amplitude measurement of the received OMEGA signals is accomplished using the TRACOR receiver amplitude output signal. At the frequency selected on the TRACOR receiver for a particular receiver set-up this amplitude output is fed into an A/D converter and scaled so that an integer value in the interval (0, 100) is recorded on magnetic tape for each received OMEGA transmission. Only four transmitters may be monitored. A measurement value represents the amplitude of the respective OMEGA transmission in dB relative to the normal level of NDK at the Hampton, Va., receiver site. There is considerable range in the relative signal strengths of stations A, B, C, and D in the differential region used during the data gathering phase of the experimental program. Each receiver must measure amplitudes which may differ by as much as 50 dB between the level of North Dakota and Norway. The amplitude measurement characteristic of the receivers is not uniformly linear over this range and therefore must be considered when the recorded signal strength data is used to extrapolate the actual received signal strength at any given sample time.

This Appendix presents the receiver transfer characteristics for each channel at the 10.2 and 13.6 kHz frequencies used during the data gathering. A transformation to convert recorded values of signal strength to received signal strength are derived for each channel. The numerical values associated with parameters in the transformation are extrapolated from calibration curves associated with the amplitude measurement circuit. These calibration data were obtained at the end of the data gathering phase and represent the hardware configuration beginning with data set 56. Prior to the time of data set 56, the A/D gain was somewhat larger and the overall amplitude measurement transfer characteristic was undesirably non-linear for received amplitudes at the NDK signal level.

Recovered amplitude measurements will be used to determine if correlation exists between received amplitude and measured phase in the experimental data.

A.1 Receiver Amplitude Measurement Characteristics

Each of the TRACOR OMEGA receivers has an input/output transfer characteristic which is a function of an operator controlled gain setting on the front panel. This control determines the amplitude measurement outputs for a given signal level input. Internal to the OMEGA phase measuring and recording equipment is an analog-to-digital circuit with a preset non-operator controlled gain characteristic. The analog output of the TRACOR circuitry is sampled and recorded on tape at 10 sec intervals such that each of four channels is sampled once every 4 sampling intervals during periods of data recording.

The output of the A/D converter will be defined as the amplitude measurement output, an integer in the interval (0, 100), with units of counts which are linearly related to a dB value of the signal relative to the "normal" NDK signal. The input is signal strength of the particular OMEGA signal. The transfer function is the input/output characteristic plotted as output counts vs. input signal strength in dB relative to the "normal" NDK signal.

Figures A-1 and A-2 provide transfer function plots of receiver #1 (fixed base laboratory receiver) channels (A is 1, B is 2, etc.) at 10.2 kHz and 13.6 kHz respectively. Figures 3 and 4 provide the same functions for receiver #2 (mobile receiver complex). Each of the figures shows a set of curves for each of four gain settings which may be operator set. It can be noted that for each receiver the transfer characteristics are non-linear. Also the channels within receivers perform differently as do the different receivers.

For each channel, variation of input signal strength is normally within a few dB, so that, to calculate what the input was for any given output sample value it is adequate to consider each transfer characteristic in a piecewise linear fashion. A point on this curve can be associated with a nominal signal level of a channel with a given gain setting. The transfer characteristic in the neighborhood of this "nominal" point is then approximated by an estimate of the tangent of the curve at that point. Figure A-5 illustrates a nominal TRINIDAD level at -25 dB and 11 counts. The linear approximate characteristic slope indicates 1.5 dB/count, i.e. a 15 dB variation in input signal level yields a 10 count change in the recorded value of signal strength.

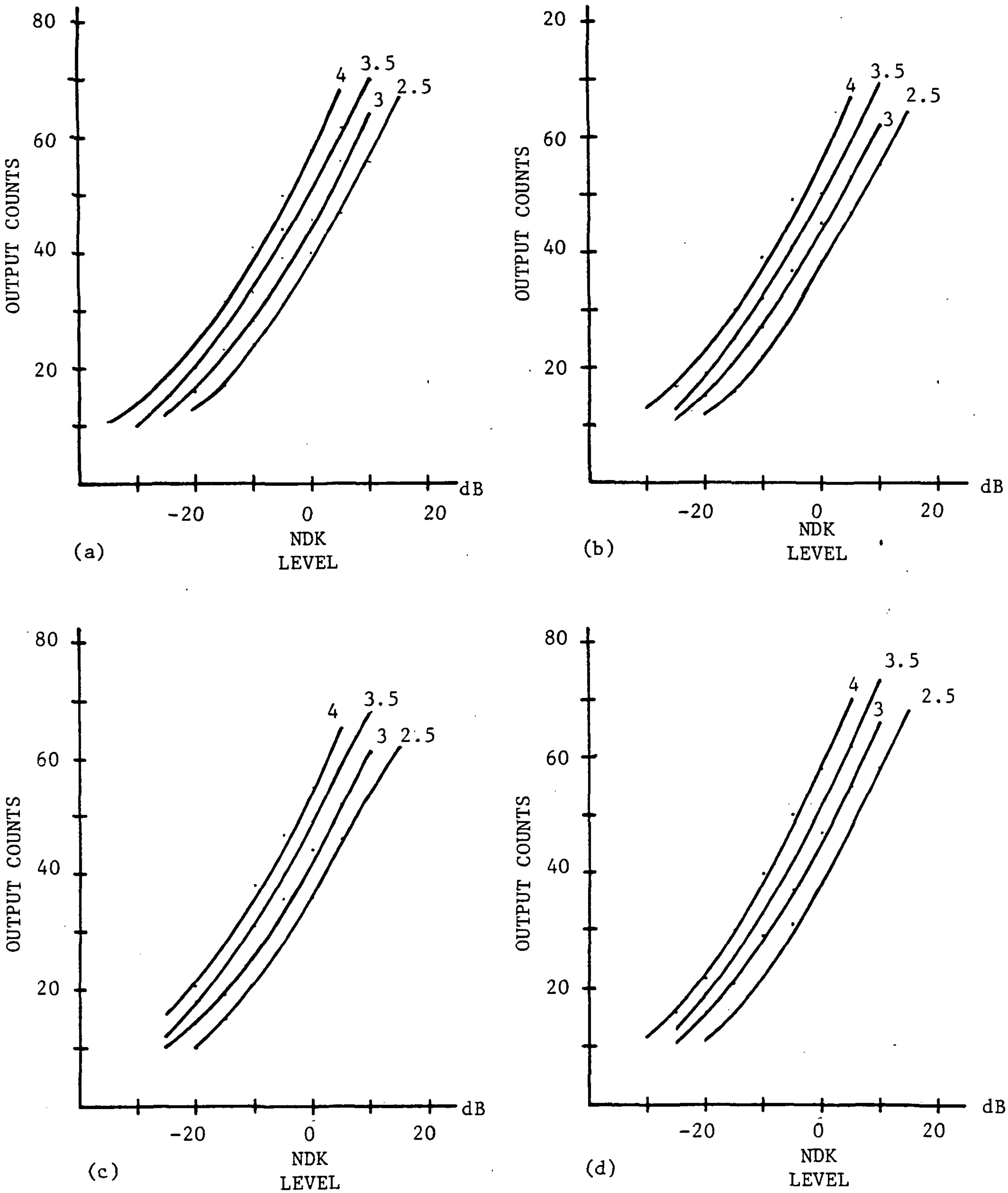

Figure A-1. Transfer Function of RCVR #1 Amplitude Measurement Circuit at 10.2 kHz for Front Panel Gain Settings 2.5, 3.0, 3.5, 4.0 a) Channel 1, b) Channel 2, c) Channel 3, d) Channel 4

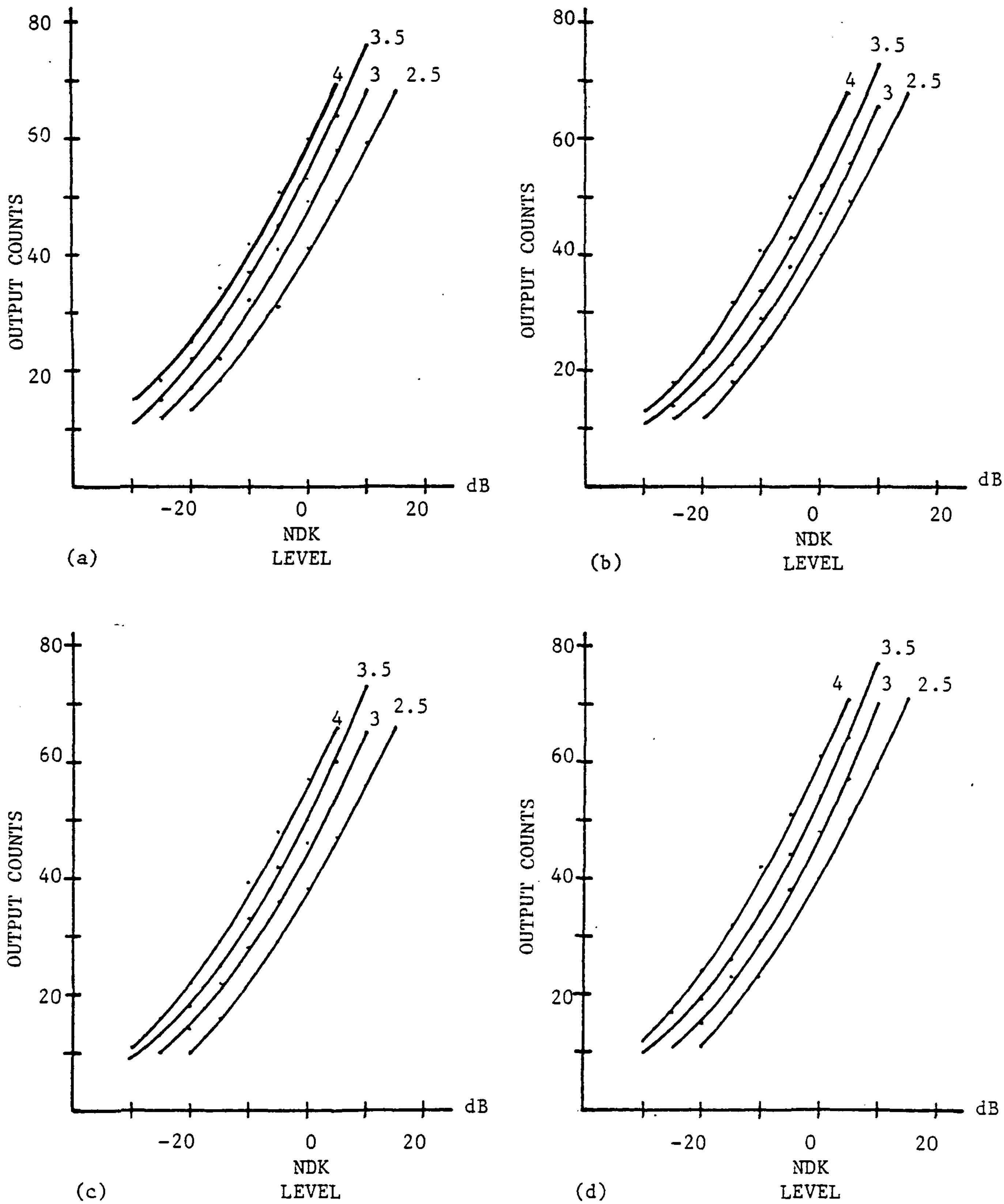

Figure A-2. Transfer Function of RCVR #1 Amplitude Measurement Circuit at 13.6 kHz for Front Panel Gain Settings 2.5, 3.0, 3.5, 4.0 a) Channel 1, b) Channel 2, c) Channel 3, d) Channel 4

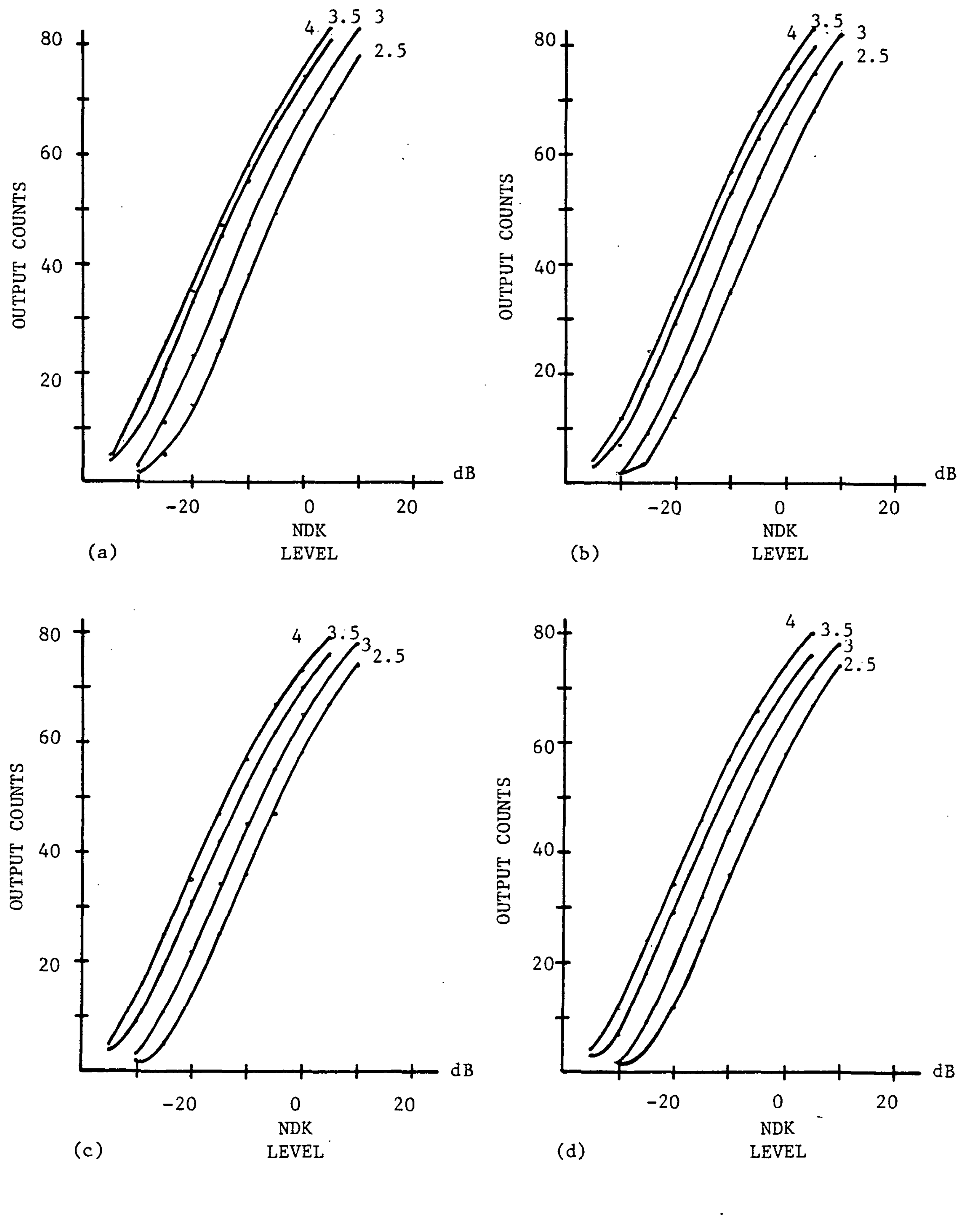

Figure A-3. Transfer Function of RCVR #2 Amplitude Measurement Circuit at 10.2 kHz for Front Panel Gain Settings 2.5, 3.0, 3.5, 4.0 a) Channel 1, b) Channel 2, c) Channel 3, d) Channel 4

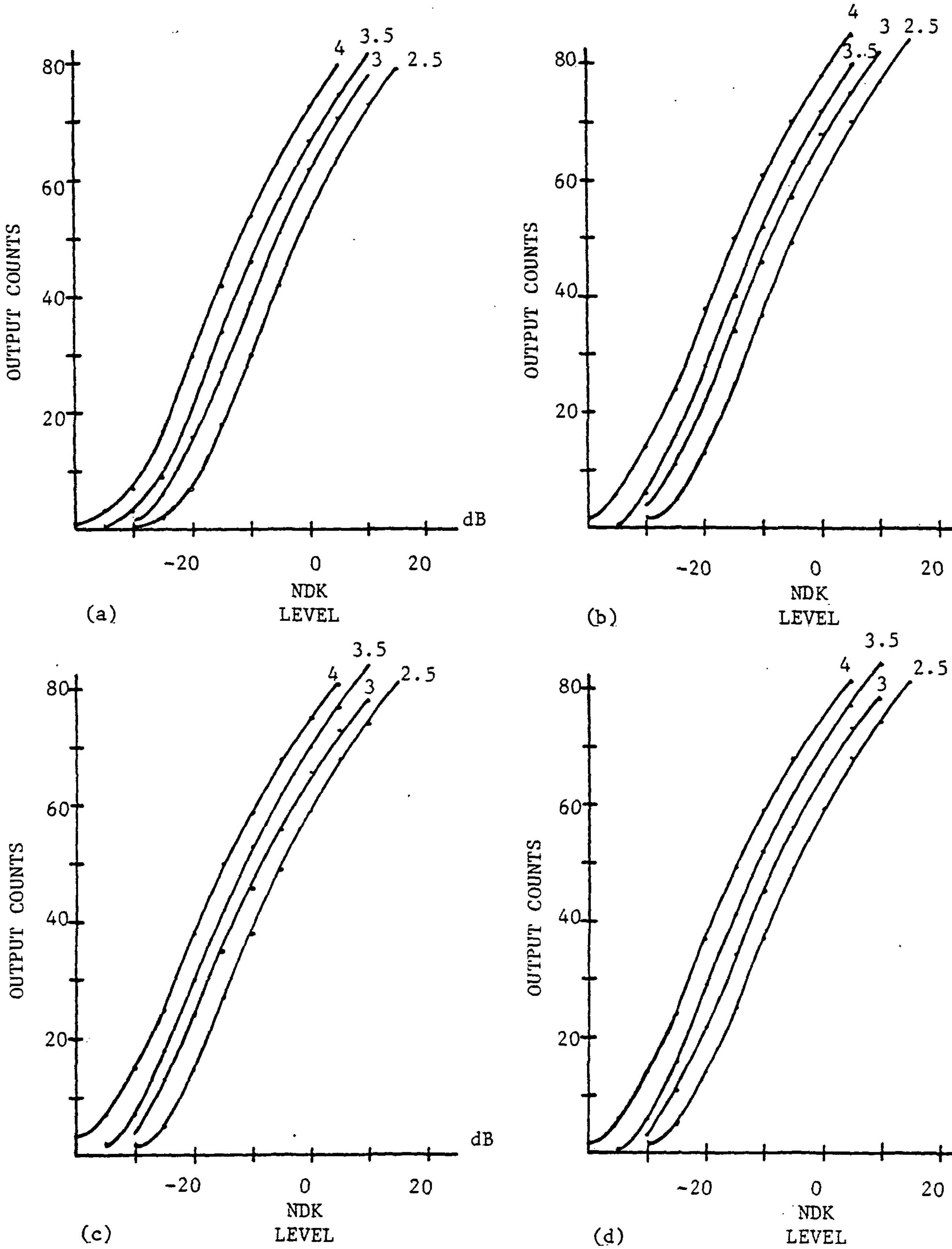

Figure A-4. Transfer Function of RCVR #2 Amplitude Measurement Circuit at 13.6 kHz for Front Panel Gain Settings 2.5, 3.0, 3.5, 4.0 a) Channel 1, b) Channel 2, c) Channel 3, d) Channel 4

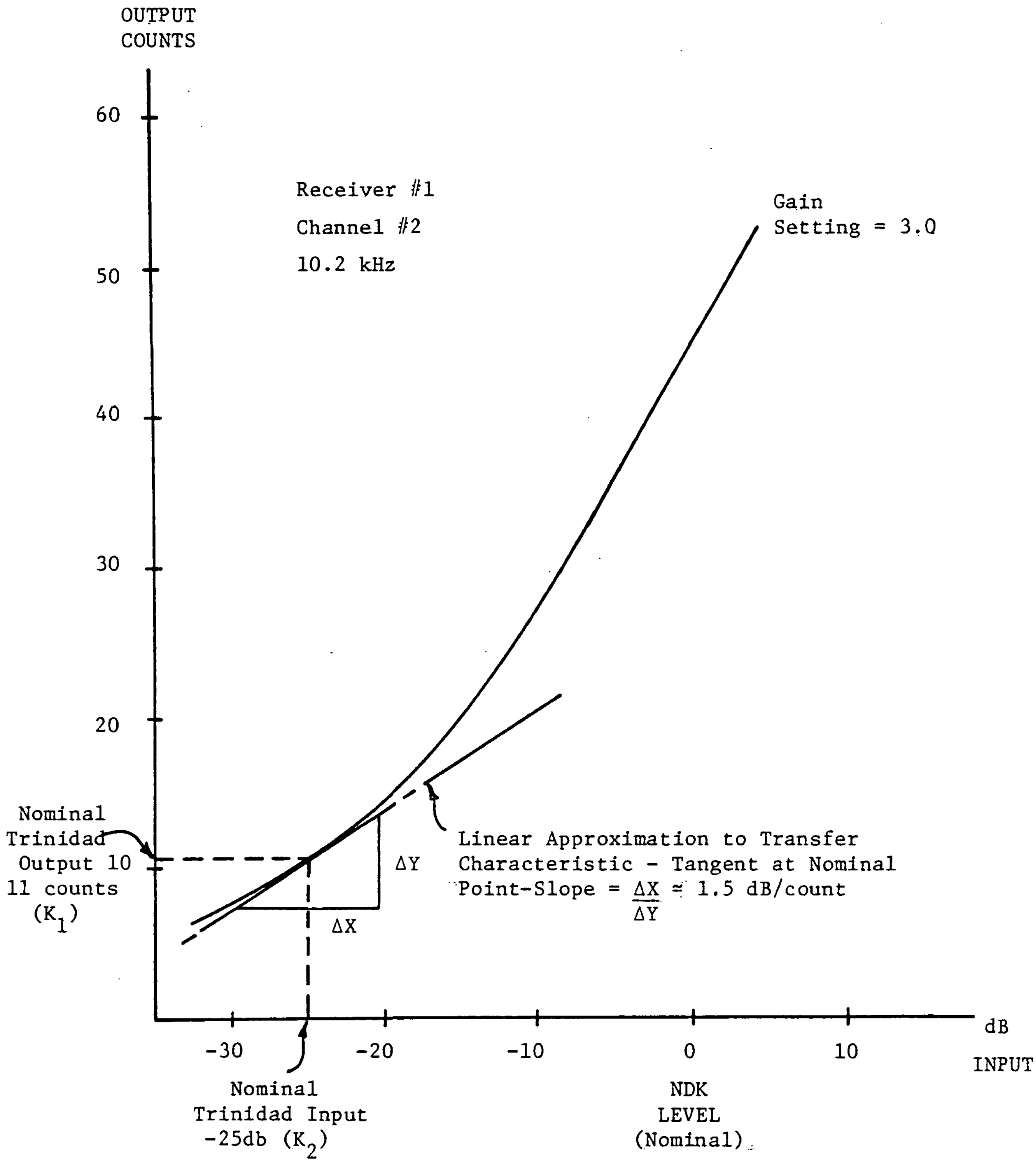

Figure A-5. Linear Approximation to Transfer Characteristic of Channel #2 Assigned to Trinidad Amplitude Measurement at 10.2 kHz.

A.2 Conversion of Recorded Data to Input Signal Strength

Let A_i be the recorded value in counts for a particular receiver measurement of the ith OMEGA transmitter signal strength at the selected frequency. Let S_i be the corresponding signal strength of this signal and S_o be the nominal NDK level or reference. The piecewise linear transfer function of the amplitude measurement characteristic is defined in terms of the parameters β_i, K_{1i} and K_{2i} where (K_{1i}, K_{2i}) defines a point on the transfer characteristic in output counts and input dB respectively and β_i is the slope in output dB per input count. Then

$$[A_i - K_{1i}] \times \beta_i + K_{2i} = 20\log S_i/S_o \qquad \text{(A-1)}$$

or

$$\frac{S_i}{S_o} = 10 ** \left\{ \frac{\beta_i}{20} [A_i - K_{1i}] + \frac{K_{2i}}{20} \right\} \qquad \text{(A-2)}$$

Table A-1 provides a tabulation of the parameter values for each of the data tapes corresponding to side-by-side runs from data set 56 on. These have been extrapolated from the calibration data. It should be noted that an operator log associated with receiver #2 (mobile receiver) was used to determine the operator controlled gain settings for each data tape. No such log exists for receiver #1 and the transfer characteristic parameter values have been estimated using the receiver calibration data and knowledge of the mean signal strength from the receiver #2 data. On the side-by-side runs, the two receivers should "see" the same signal so that this should provide a good estimate of the parameter values. Included in Table A-1 is the frequency at which amplitude measurements were made for each data set.

Figures A-6 and A-7 provide plots of average hourly estimated input signal strength vs. output recorded signal strength for the Trinidad and N. Dakota signals at 13.6 kHz contained on tape #56 for receiver #1. These represent plots of (A-2) using parameter values in Table A-1 over two ranges of recorded signal strength corresponding to received signal levels of Trinidad and N. Dakota at Hampton, Va.

TABLE A-1.

AMPLITUDE MEASUREMENT CONVERSION CONSTANTS

Note: Offset given in counts and dB; slope in dB/count

To convert RDG(count) - reading in counts - to AMP(dB) - amplitude in dB:

AMP(dB) = SLOPE(dB/count)[RDG(count) - OFFSET(count)] + OFFSET (dB)

		A - NOR			B - TRI			C - HAW			D - NDK			
		OFFSET			OFFSET			OFFSET			OFFSET			
Tape#	Gain	K_1 Count	K_2 dB	β Slope	K_1 Count	K_2 dB	β Slope	K_1 Count	K_2 dB	β Slope	K_1 Count	K_2 dB	β Slope	TRACOR Freq.
1.31														10.2
2.31	3.0													
1.41														10.2
2.41	3.0													
1.48														
2.48	3.5													13.6
1.52														13.6
2.52	3.0													
*ADC Gain changed here														
1.56	EST 3.5	15	-25	.909	26	-15	.714	25	-15	.667	54	0	.50	13.6
2.56	2.5	7	-20	.625	25	-15	.417	27	-15	.434	68	+5	.667	
1.59	EST 3.5	15	-25	.909	26	-15	.714	25	-15	.667	54	0	.50	
2.59	2.5	7	-20	.625	25	-15	.417	27	-15	.434	68	+5	.667	13.6
1.63	EST 3.	10	-30	1.0	25	-15	.769	24	-15	.769	52	0	.50	10.2
2.63	3.	10	-30	.43	29	-20	.425	42	-15	.48	70	0	.714	
1.68	EST 3.5	10	-30	1.0	25	-15	.769	24	-15	.769	52	0	.50	10.2
2.68	3.5	10	-30	.43	29	-20	.425	42	-15	.48	70	0	.714	
1.73	EST 3.5	15	-25	1.0	25	-15	.769	24	-15	.769	52	0	.50	10.2
2.73	3.5	10	-30	.43	29	-20	.425	42	-15	.48	70	0	.714	
1.76A	EST 3.5	15	-25	1.0	25	-15	.769	24	-15	.769	52	0	.50	10.2
2.76A	3.5	10	-30	.43	29	-20	.425	42	-15	.48	70	0	.714	

TABLE A-1. Continued.

AMPLITUDE MEASUREMENT CONVERSION CONSTANTS

Note: Offset given in counts and dB; slope in dB/count

To convert RDG(count) - reading in counts - to AMP(dB) - amplitude in dB:

AMP(dB) = SLOPE(dB/count)[RDG(count) - OFFSET(count)] + OFFSET (dB)

		A - NOR			B - TRI			C - HAW			D - NDK			
		OFFSET			OFFSET			OFFSET			OFFSET			
Tape#	Gain	K_1 Count	K_2 dB	β Slope	K_1 Count	K_2 dB	β Slope	K_1 Count	K_2 dB	β Slope	K_1 Count	K_2 dB	β Slope	TRACOR Freq.
1.81	EST 3.5	15	-25	1.0	25	-15	.769	24	-15	.769	52	0	.50	10.2
2.81	3.5	10	-30	.43	29	-20	.425	42	-15	.48	70	0	.714	
1.86	EST 3.5	10	-30	1.0	25	-15	.769	24	-15	.769	52	0	.50	10.2
2.86	3.5	10	-30	.43	29	-20	.425	42	-15	.48	70	0	.714	
1.91	EST 3.0	12	-25	.80	21	-15	.769	21	-15	.769	48	0	.53	13.6
2.91	3.0	6	-25	.50	34	-15	.417	24	-20	.45	73	+5	.769	
1.95	EST 3.0	12	-25	.80	21	-15	.769	21	-15	.769	48	0	.53	13.6
2.95	3.0	6	-25	.50	34	-15	.417	24	-20	.45	73	+5	.769	
1.101	EST 3.5	15	-25	.909	26	-15	.714	25	-15	.667	54	0	.50	13.6
2.101	2.5	7	-20	.625	25	-15	.417	27	-15	.434	68	+5	.667	
1.102	EST 3.0	12	-25	.80	21	-15	.769	21	-15	.769	48	0	.53	
2.102	3.0	6	-25	.50	34	-15	.417	24	-20	.45	73	+5	.769	13.6
1.103	EST 3.5	10	-30	1.0	25	-15	.769	24	-15	.769	42	-5	.526	13.6
2.103	EST 2.5	14	-20	.476	24	-15	.435	36	-10	.455	58	0	.50	

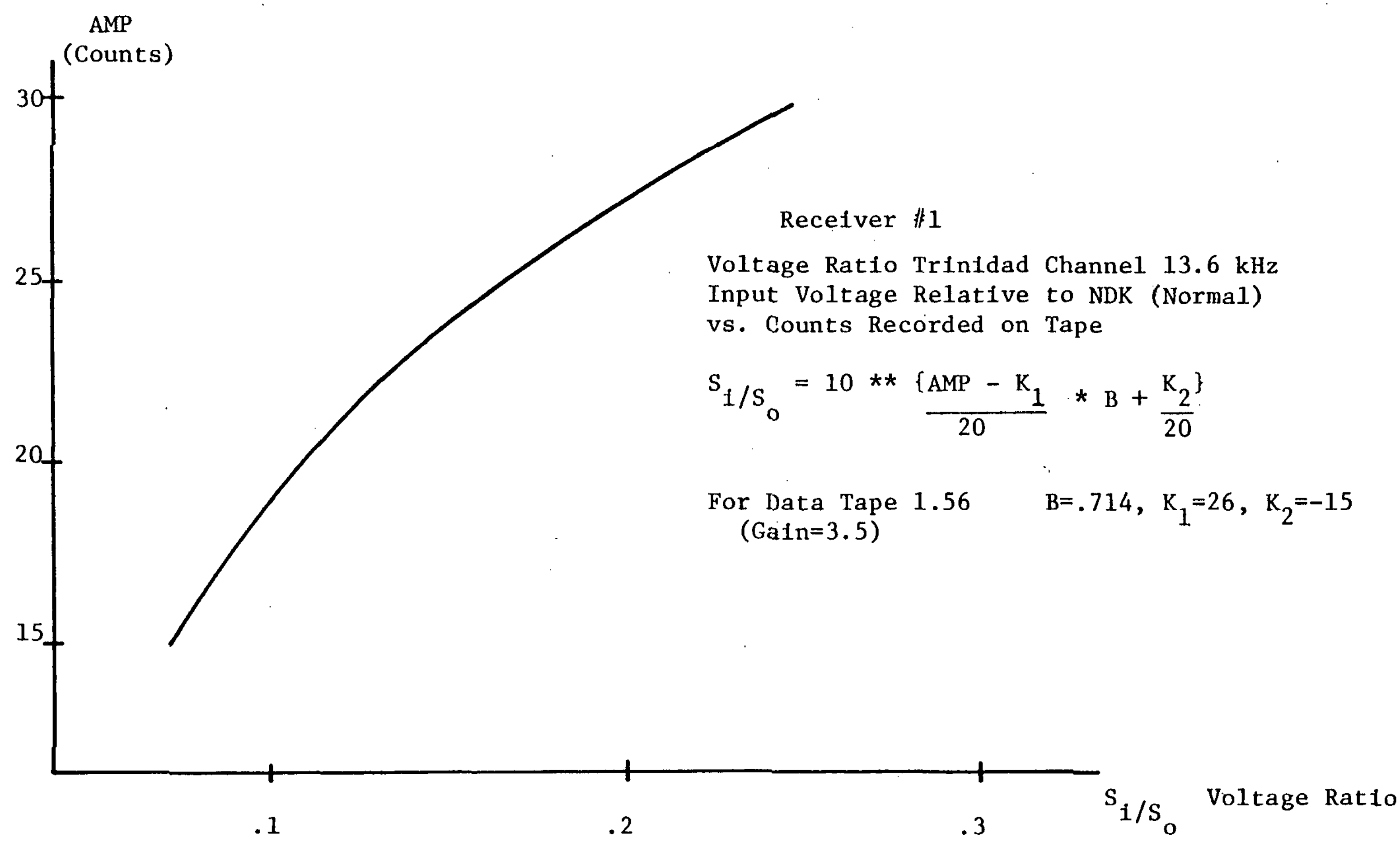

Figure A-6. Input Relative Signal Strength vs. Output Recorded Amplitude for Data Set 1.56 using TRI 13.6 kHz.

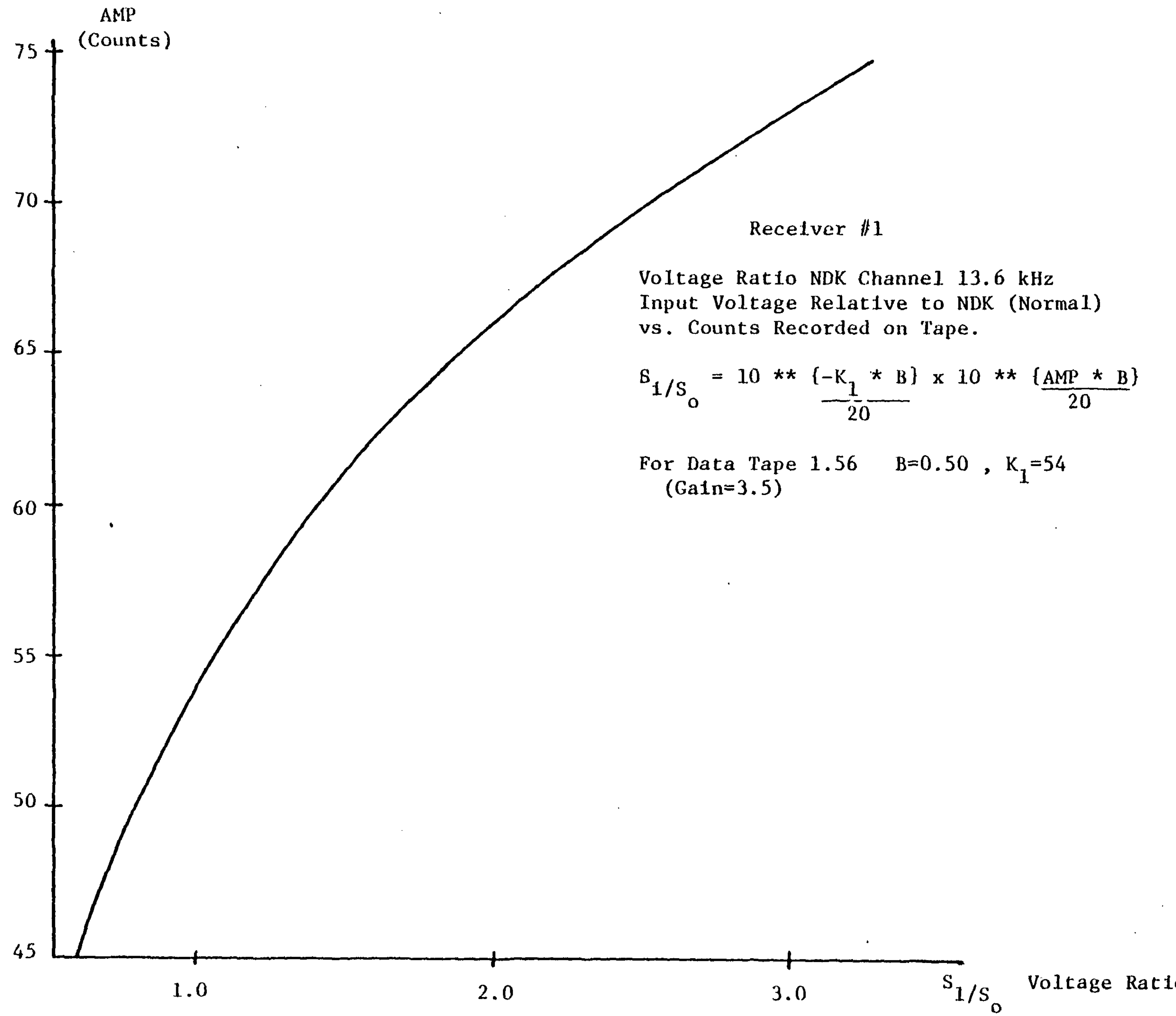

Figure A-7. Input Relative Signal Strength vs. Output Recorded Amplitude for Data Set 1.56 using NDK 13.6 kHz (K_2=0)

Using the procedure described in this Appendix, received amplitude variations in terms of estimated signal strength at the receiver can be compared to received phase to determine correlation. With the local oscillator phase drift removed, Figures A-8 through A-13 are scatter plots of input signal strength (dB) relative to the mean value versus measured phase in cec at the frequency of interest. Shown in these figures are the tabulated mean amplitude with the associated standard deviation, and the estimated linear correlation coefficient. Three data sets, 56, 81, and 91 are given for both receivers. Data sets 56 and 91 are at 13.6 kHz while 81 is at 10.2 kHz. Note that each data set is analyzed in terms of daytime periods and nighttime periods for each OMEGA transmitter which was monitored. There appears to be no consistent correlation between phase variations and amplitude variations for either receiver.

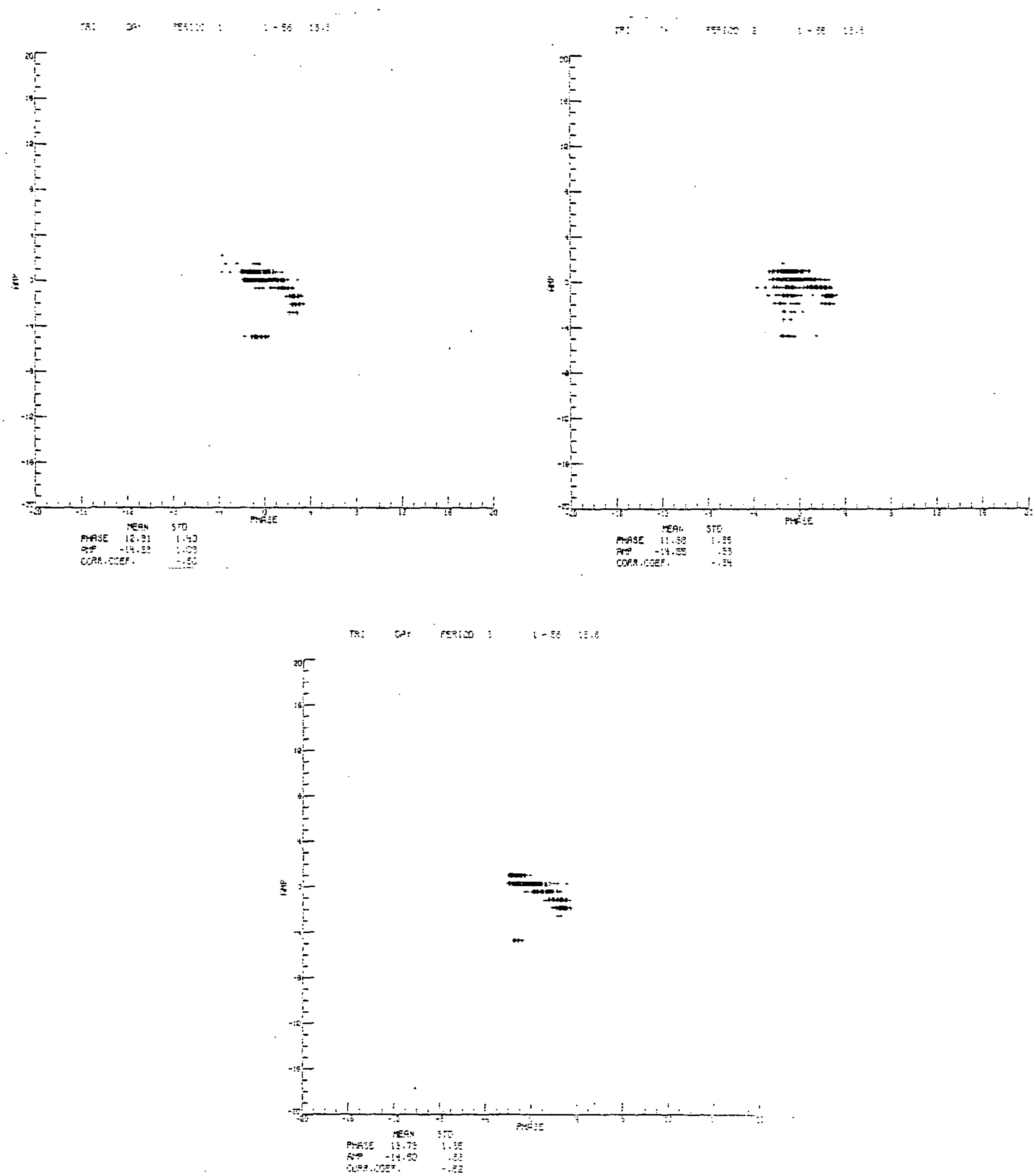

(a) Trinidad Daytime, Data Set 56, 13.6 kHz.

Figure A-8. Input Signal Strength (dB) Relative to Mean vs. Measured Phase in cec with Drift Removed (Base Receiver).

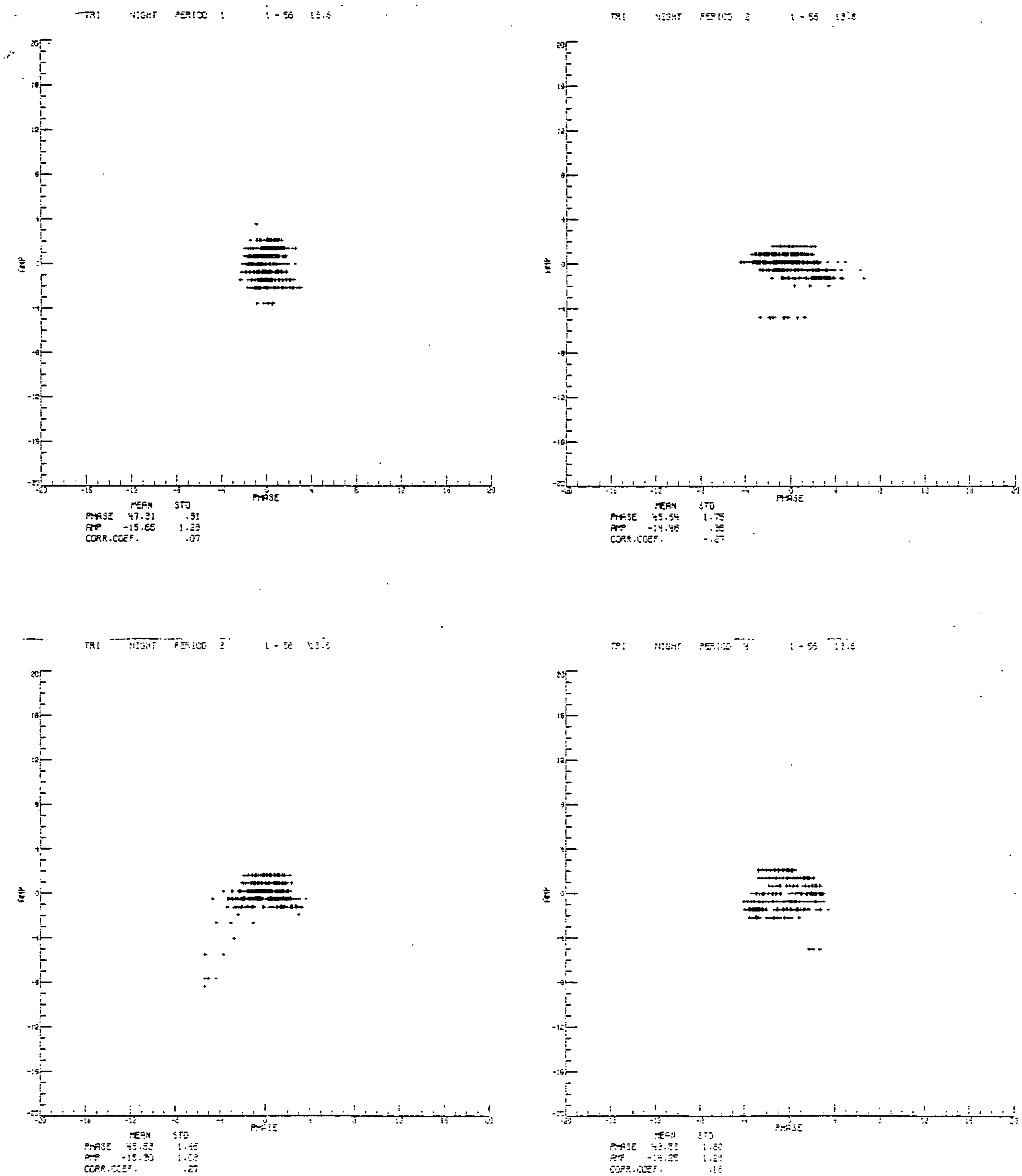

(b) Trinidad Nighttime, Data Set 56, 13.6 kHz.

Figure A-8. (Continued).

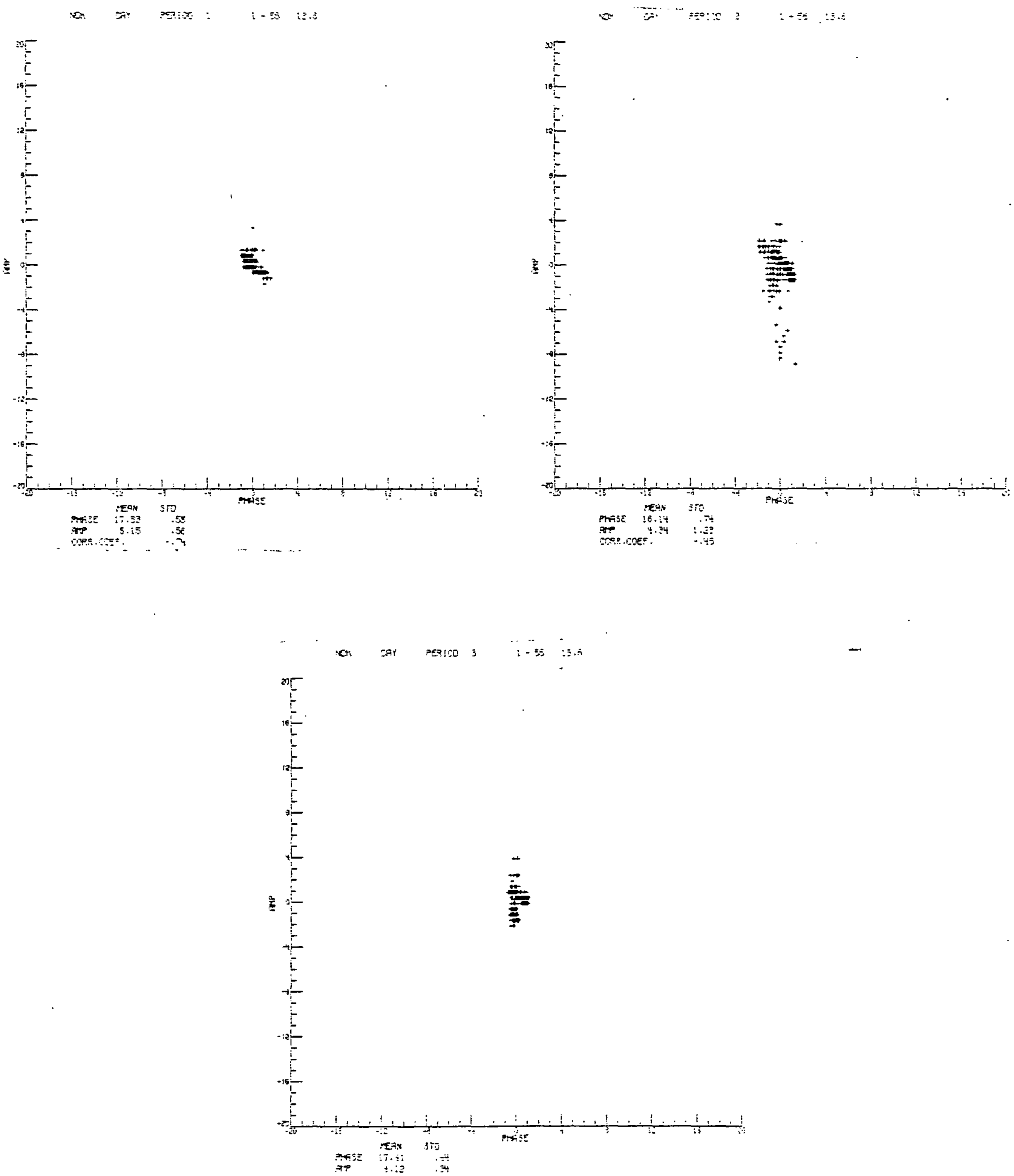

(c) N. Dakota Daytime, Data Set 56, 13.6 kHz.

Figure A-8. (Continued).

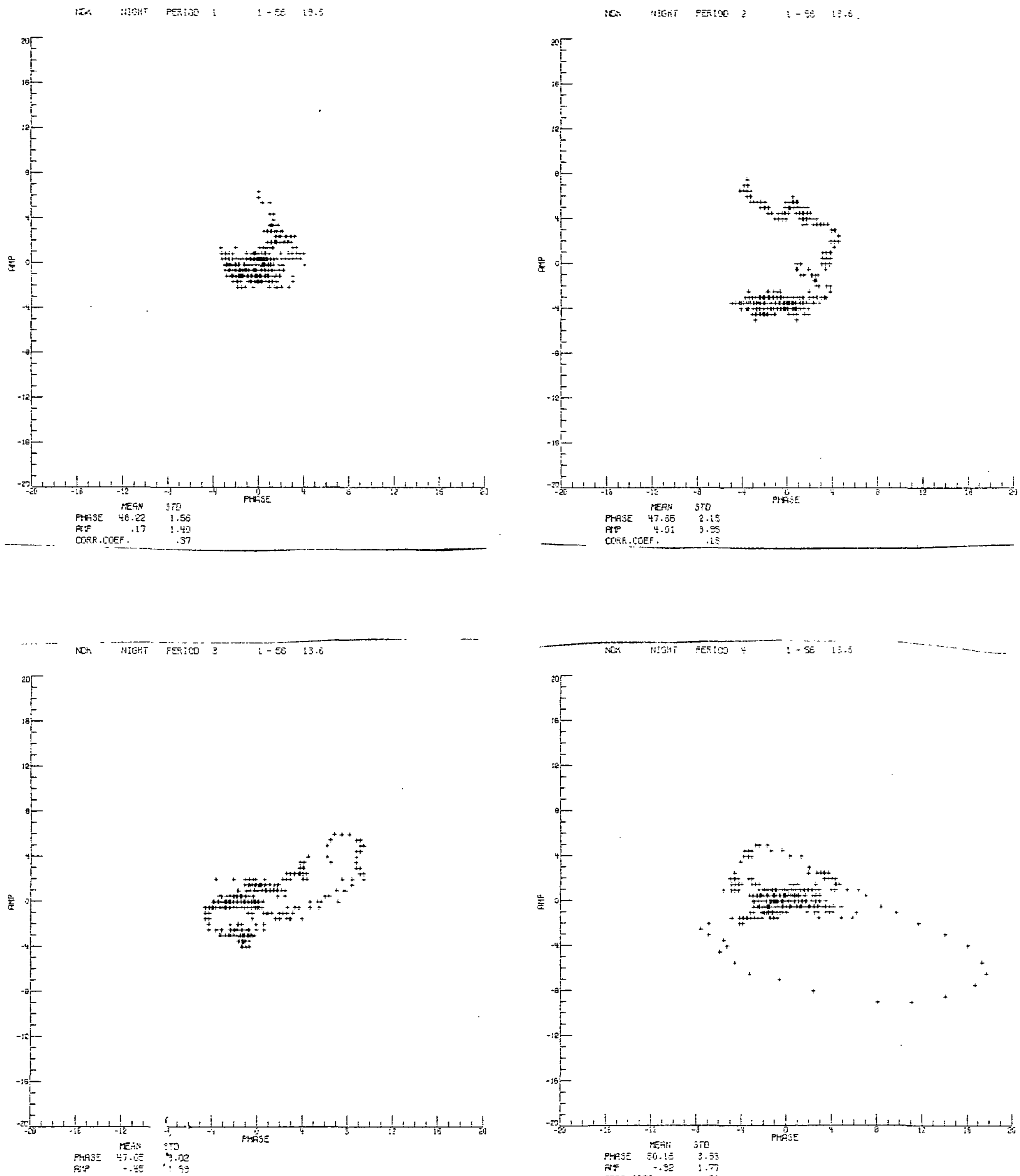

(d) N. Dakota Nighttime, Data Set 56, 13.6 kHz.

Figure A-8. (Continued).

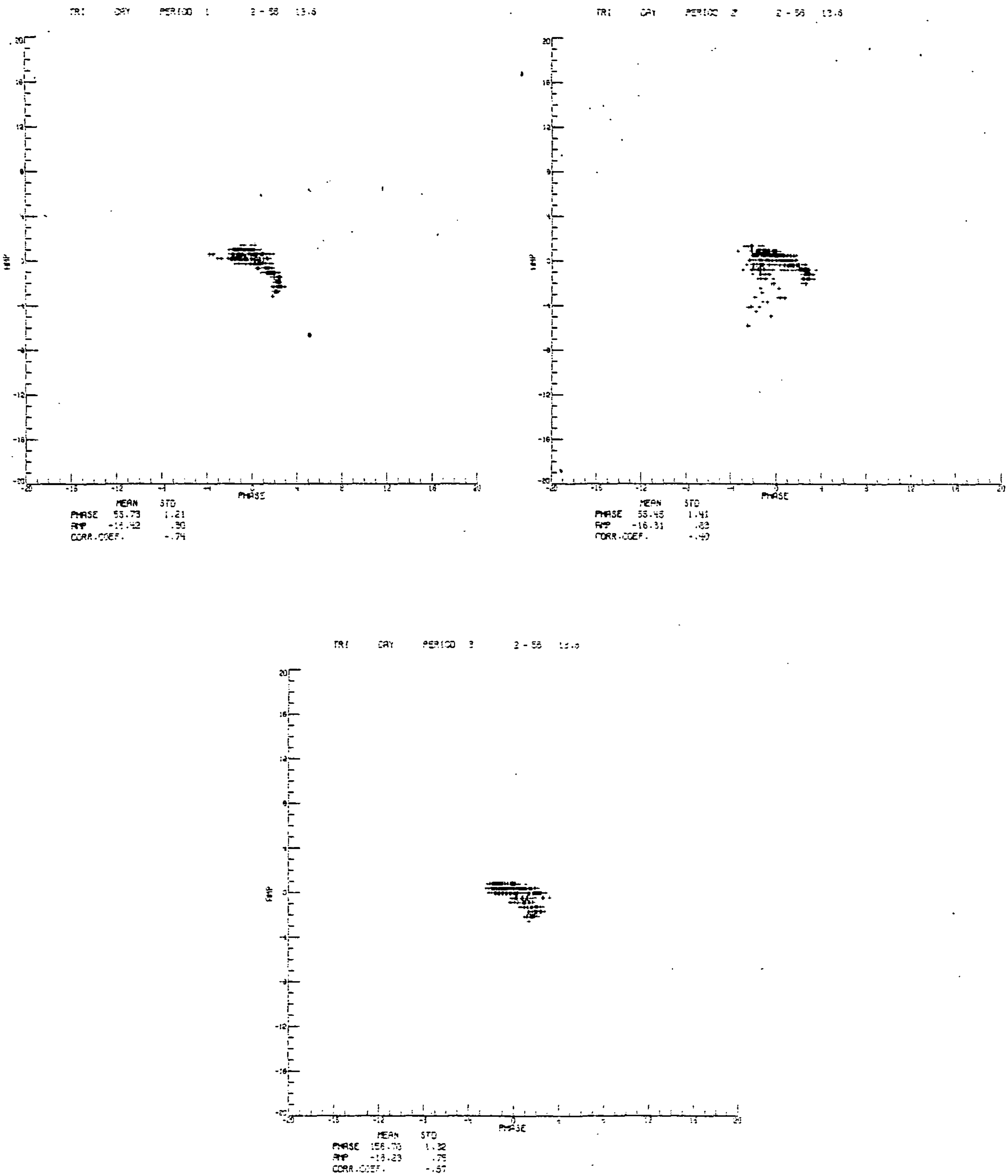

(a) Trinidad Daytime, Data Set 56, 13.6 kHz.

Figure A-9. Input Signal Strength (dB) Relative to Mean vs. Measured Phase in cec with Drift Removed (Mobile Receiver).

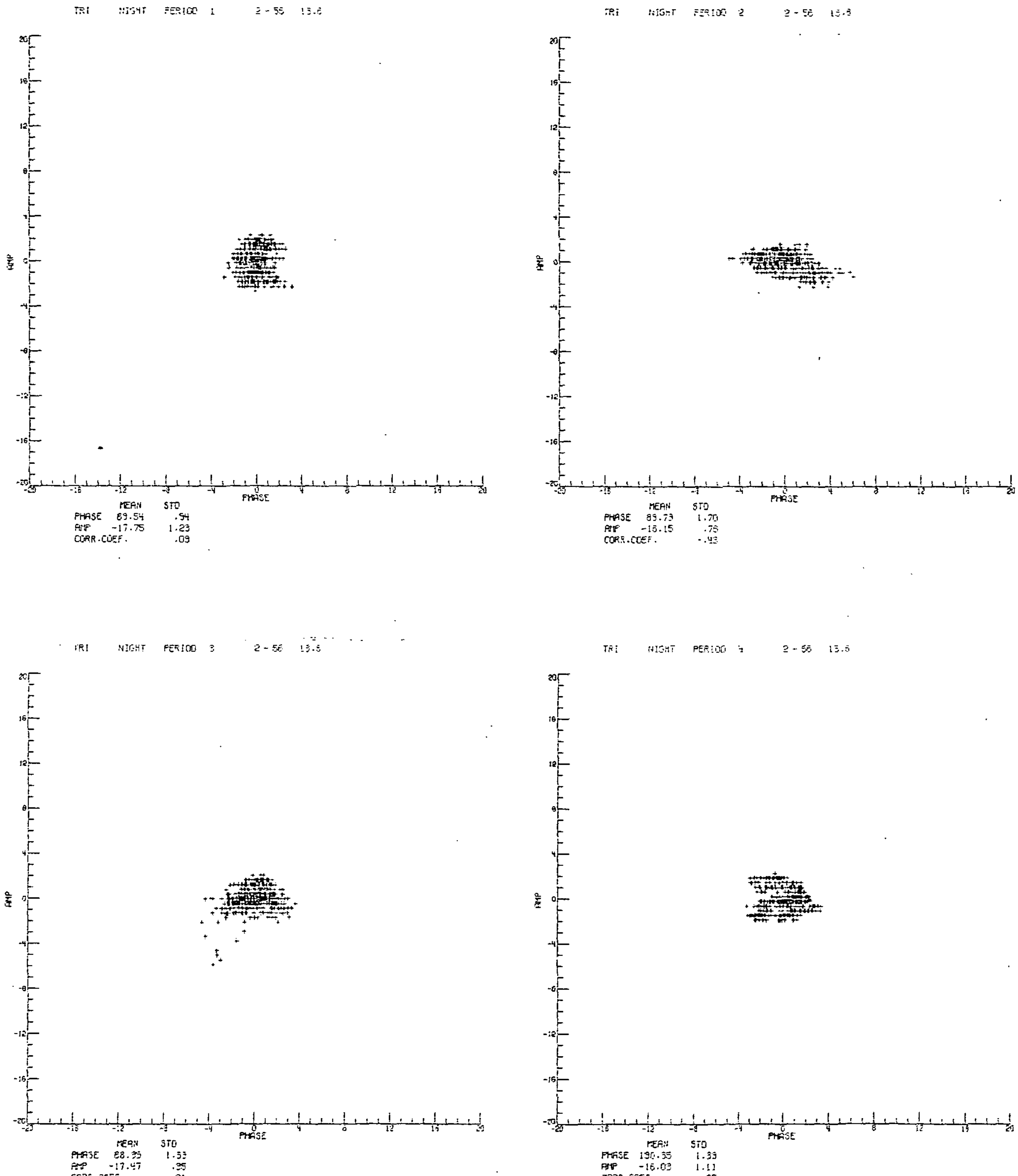

(b) Trinidad Nighttime, Data Set 56, 13.6 kHz.

Figure A-9. (Continued).

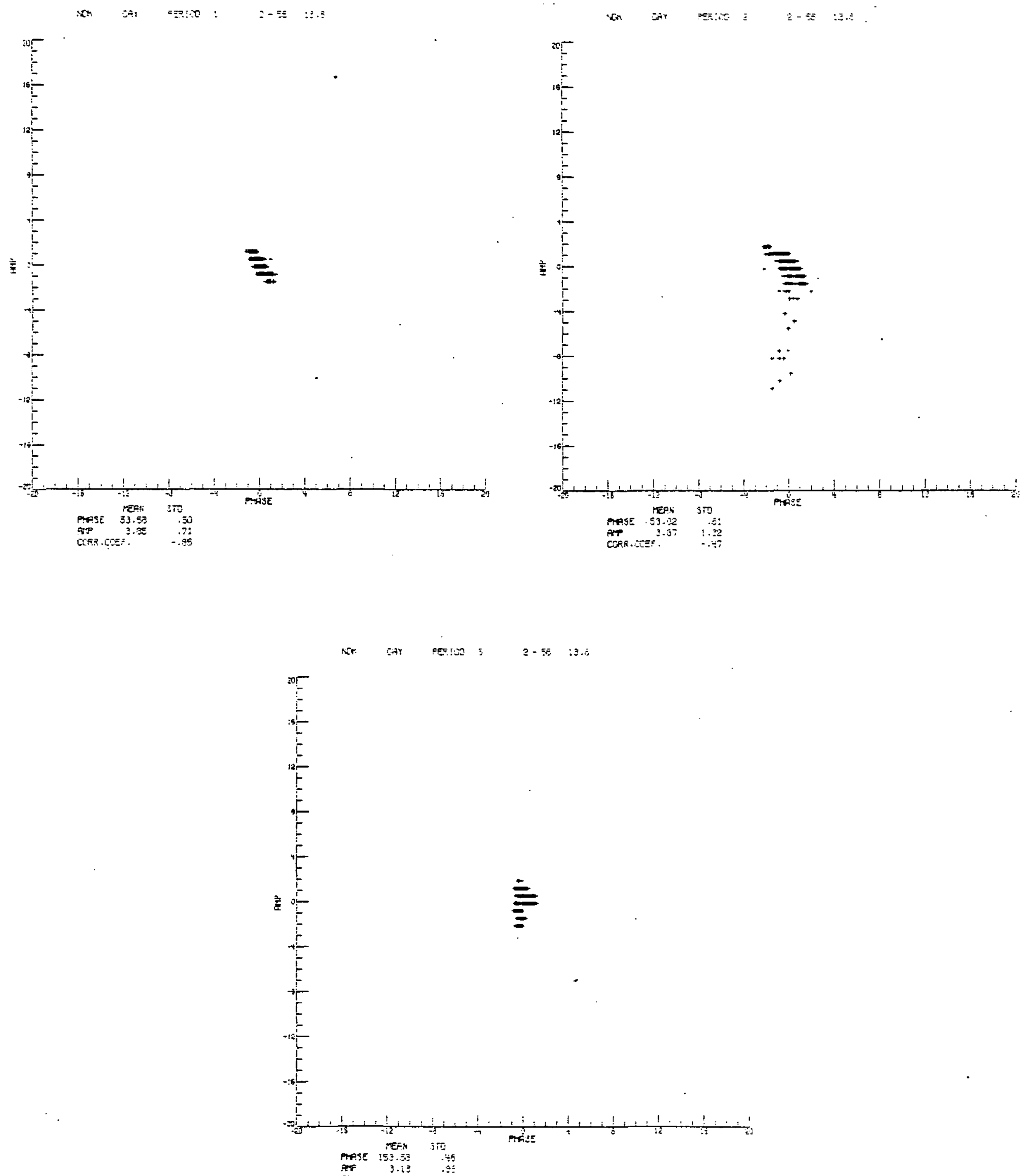

(c) N. Dakota Daytime, Data Set 56, 13.6 kHz.

Figure A-9. (Continued).

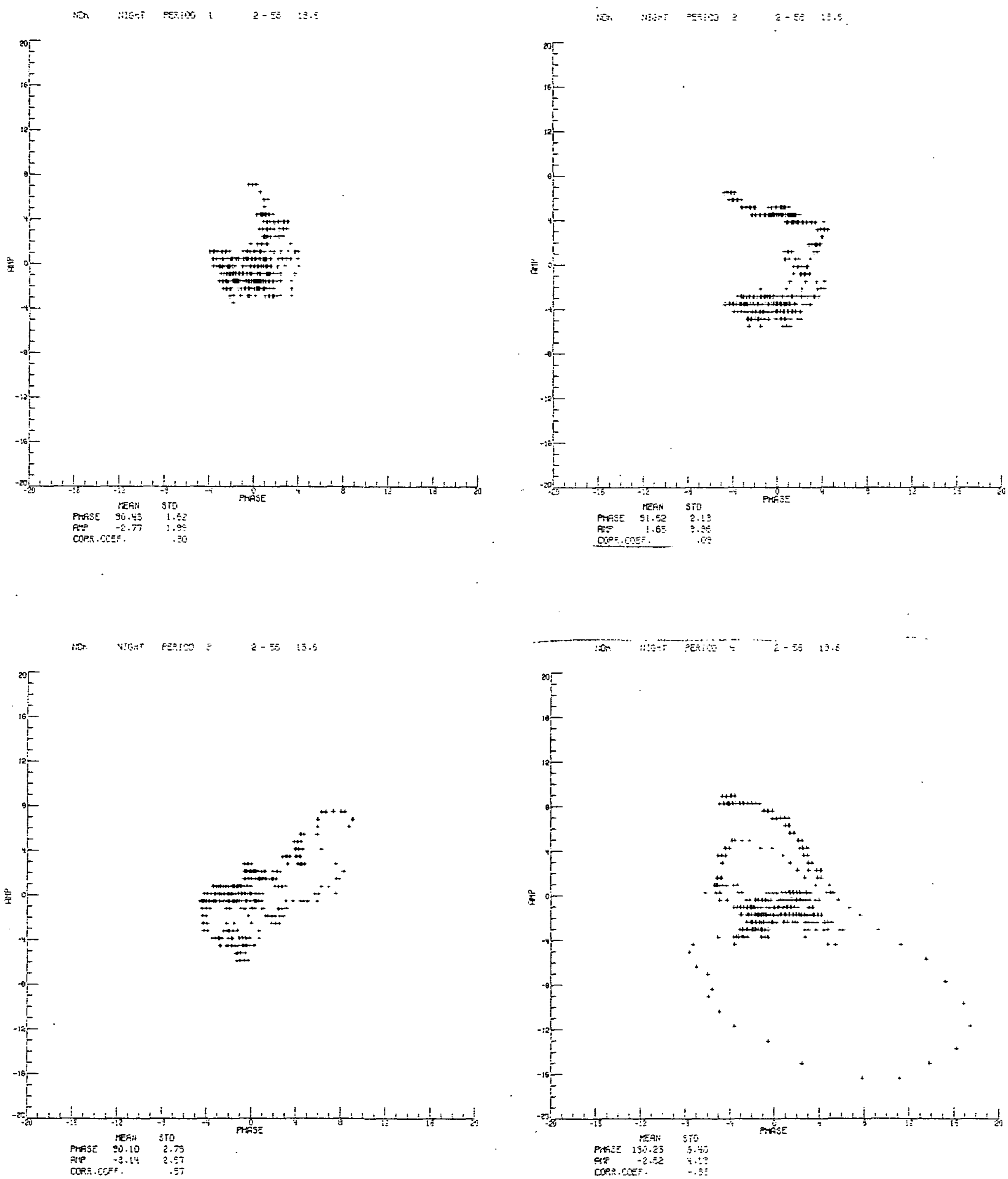

(d) N. Dakota Nighttime, Data Set 56, 13.6 kHz.

Figure A-9. (Continued).

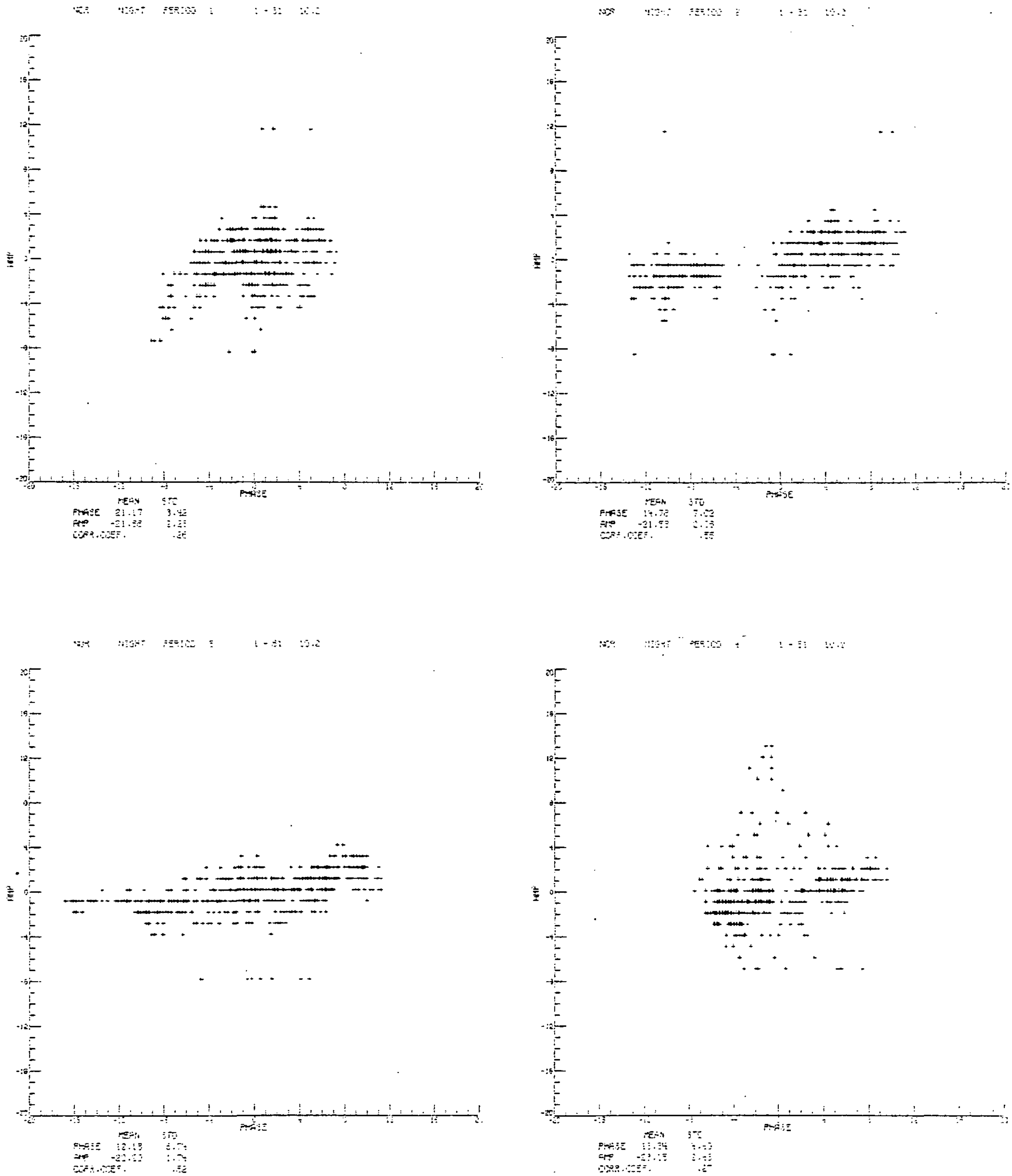

(a) Norway Nighttime, Data Set 81, 10.2 kHz.

Figure A-10. Input Signal Strength (dB) Relative to Mean vs. Measured Phase in cec with Drift Removed (Base Receiver).

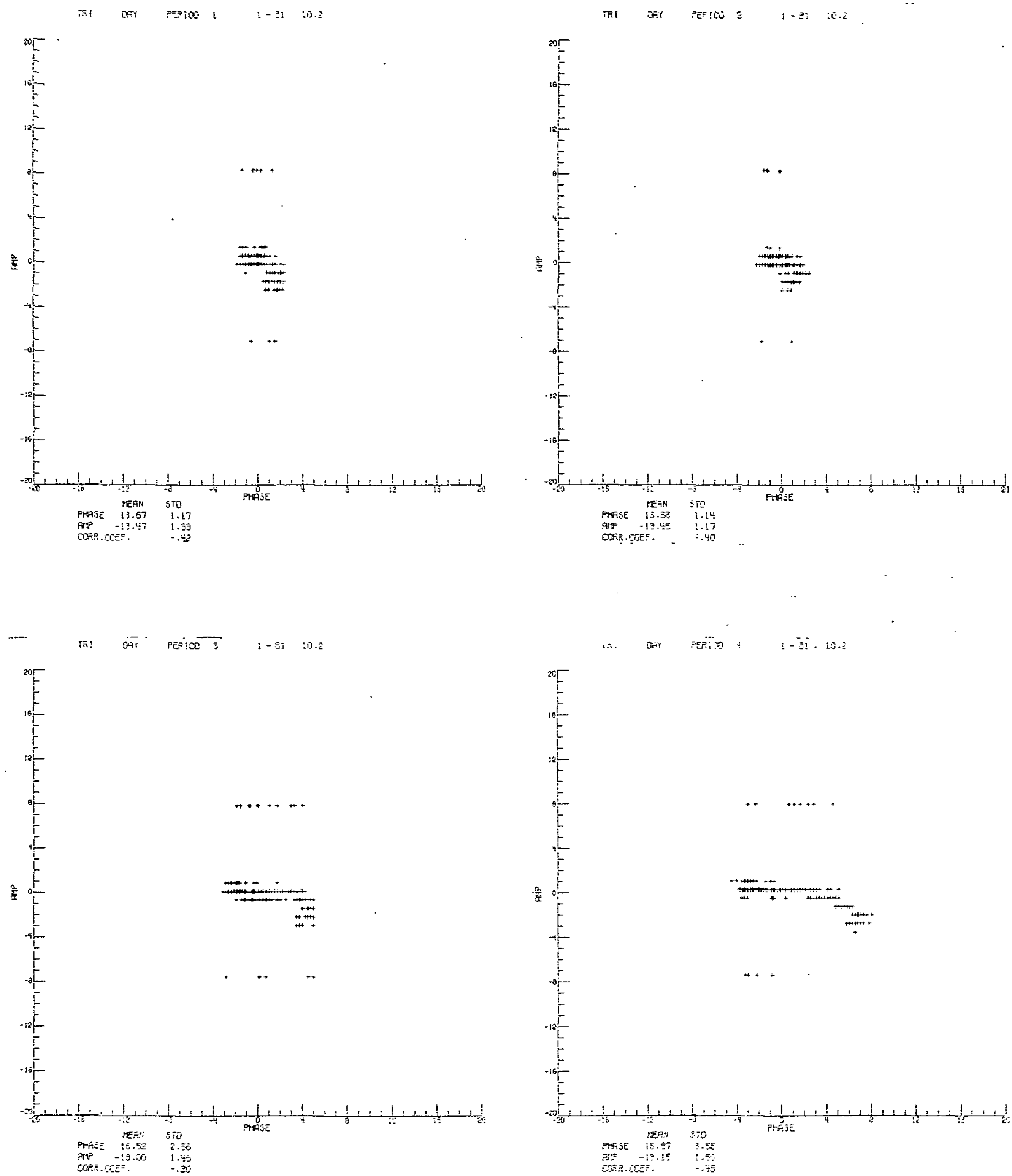

(b) Trinidad Daytime, Data Set 81, 10.2 kHz.

Figure A-10. (Continued).

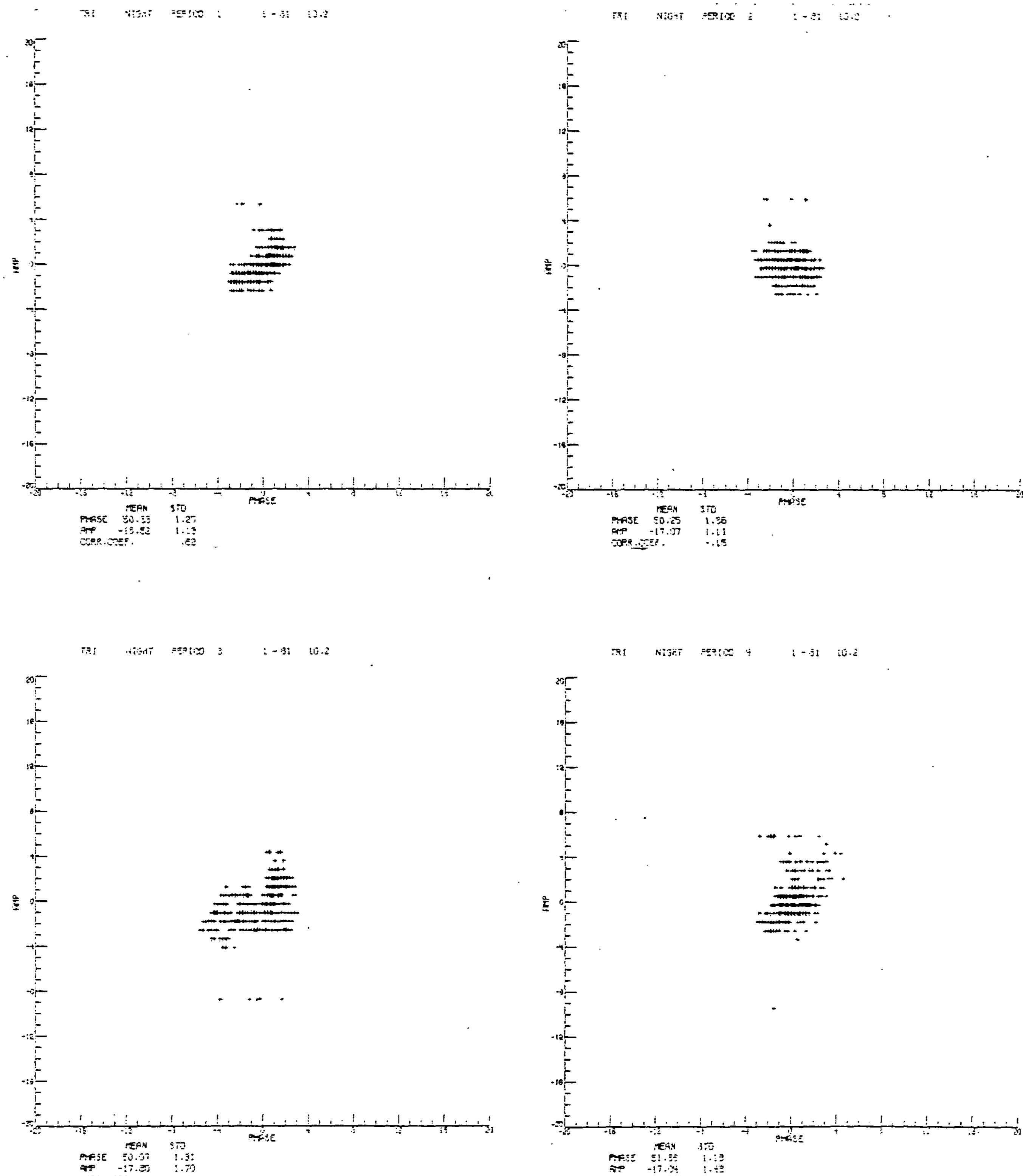

(c) Trinidad Nighttime, Data Set 81, 10.2 kHz.

Figure A-10. (Continued).

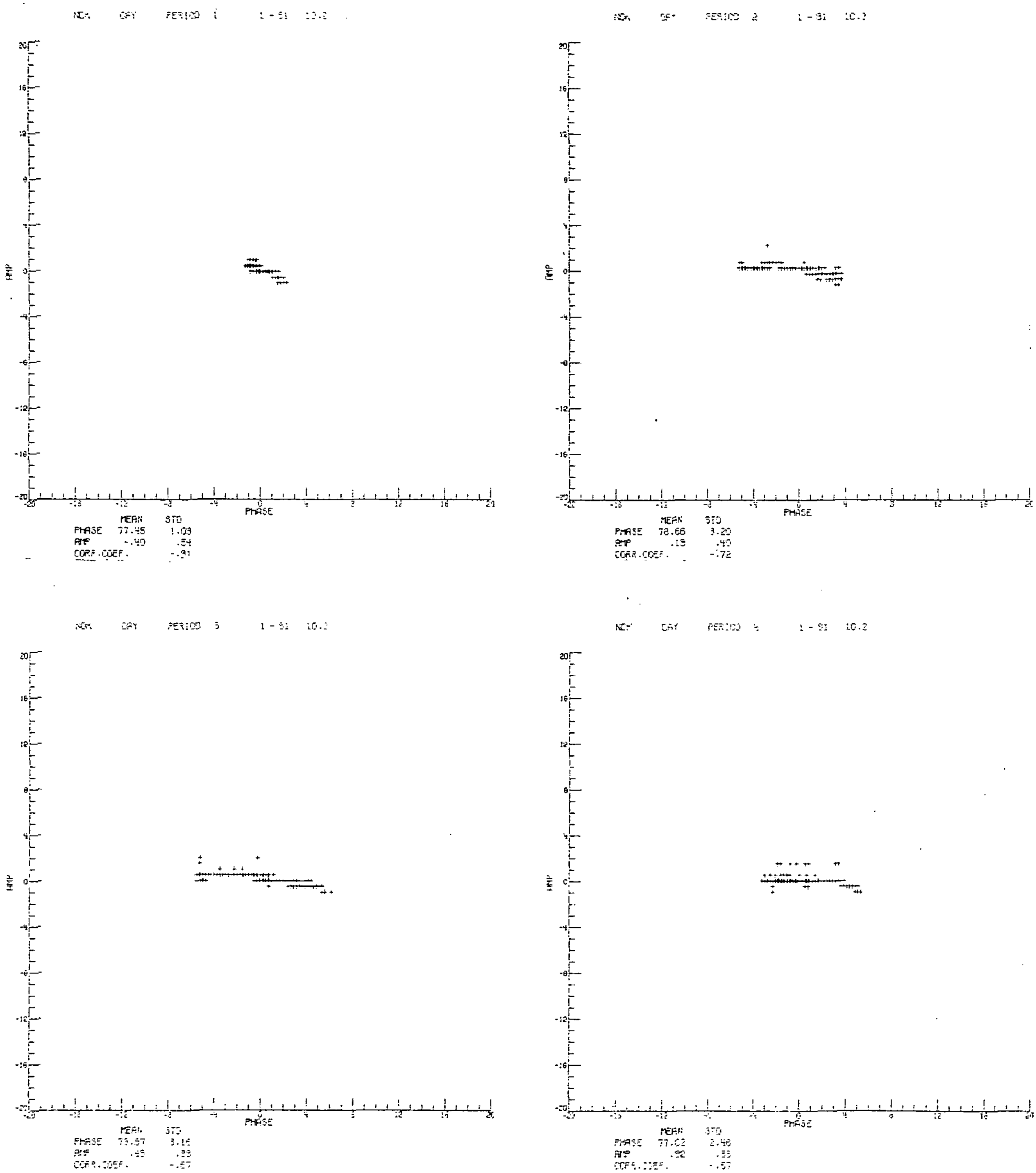

(d) N. Dakota Daytime, Data Set 81, 10.2 kHz.

Figure A-10. (Continued).

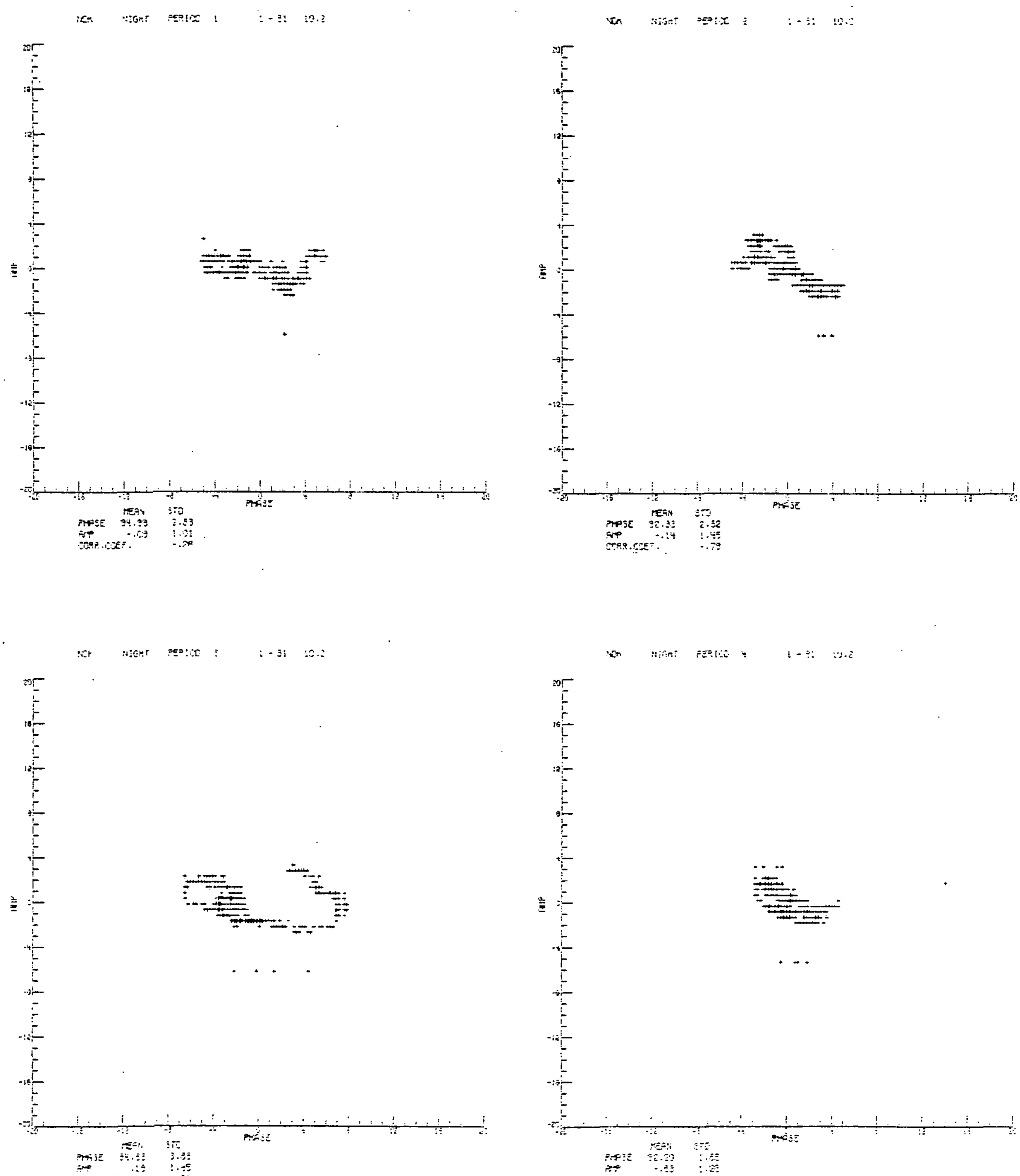

(e) N. Dakota Nighttime, Data Set 81, 10.2 kHz.

Figure A-10. (Continued).

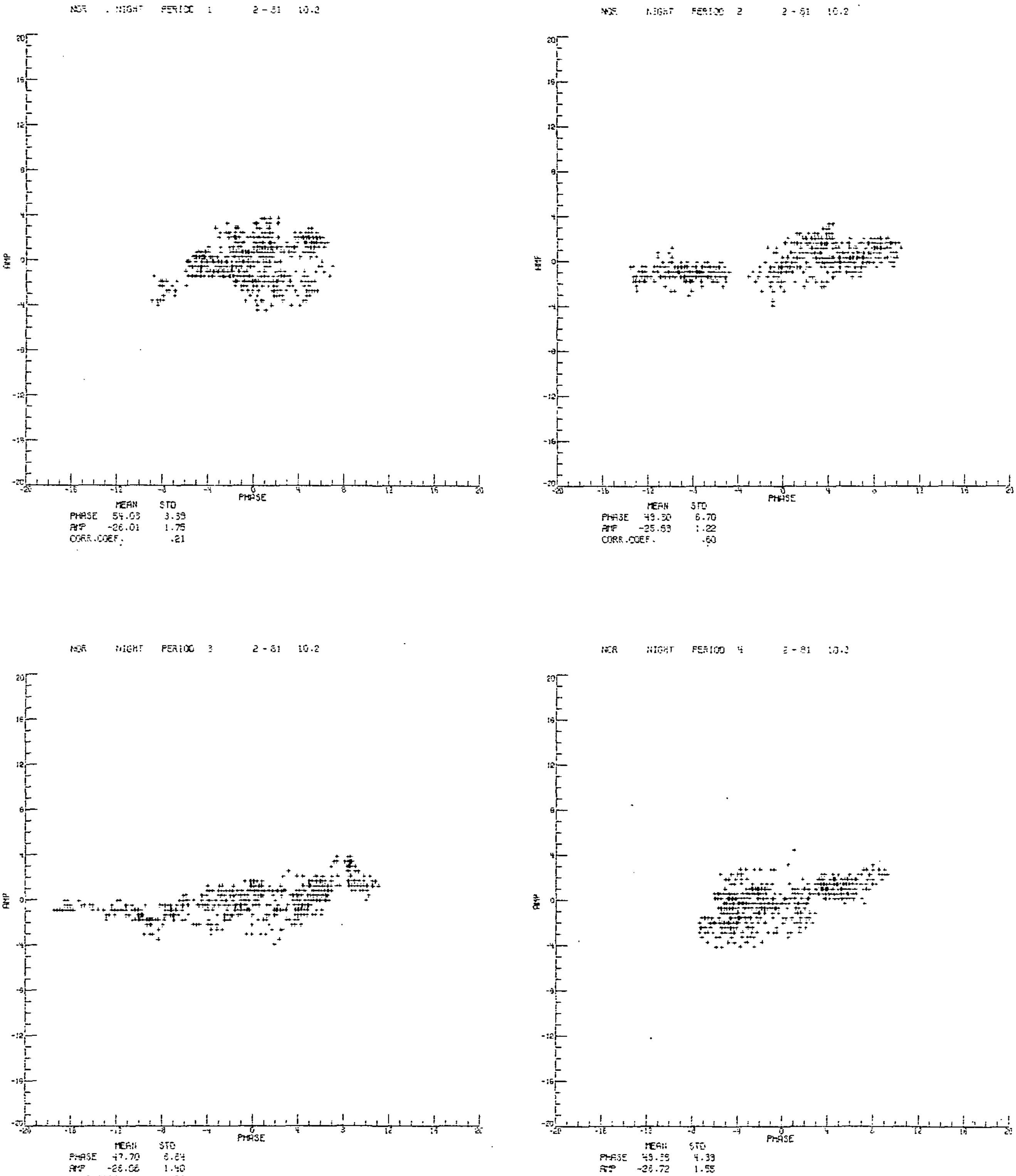

(a) Norway Nighttime, Data Set 81, 10.2 kHz.

Figure A-11. Input Signal Strength (dB) Relative to Mean vs. Measured Phase in cec with Drift Removed (Mobile Receiver).

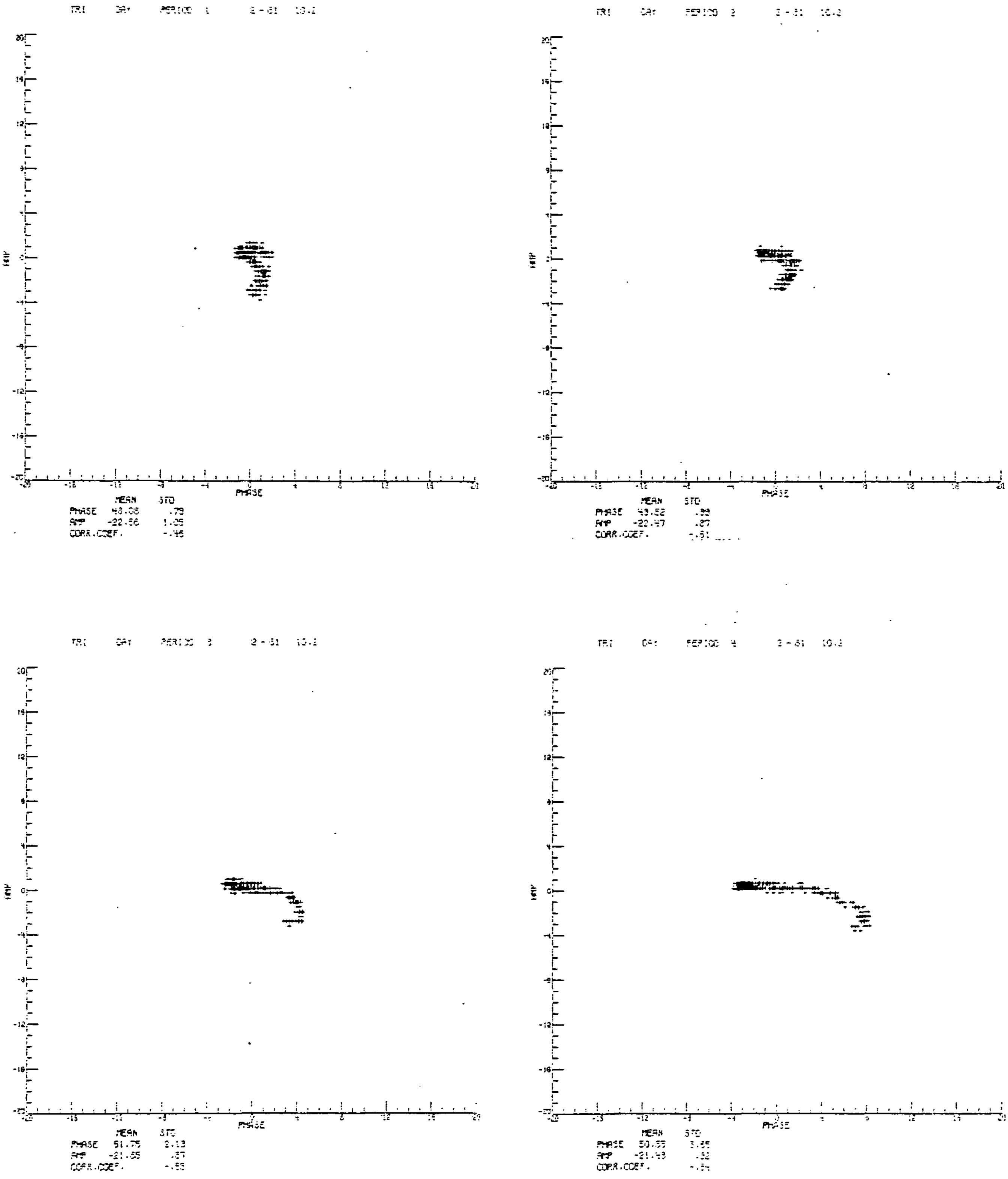

(b) Trinidad Daytime, Data Set 81, 10.2 kHz.

Figure A-11. (Continued).

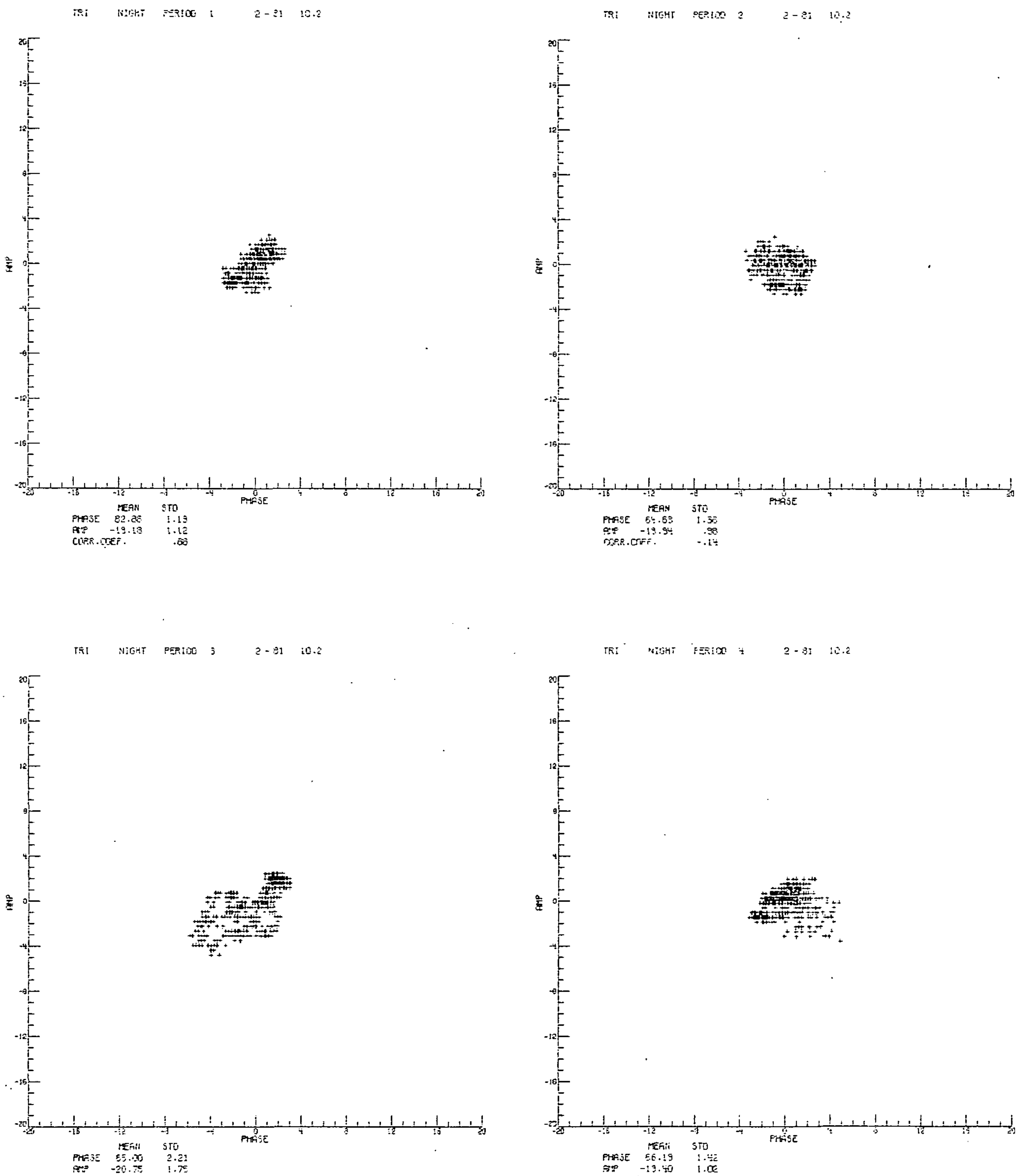

(c) Trinidad Nighttime, Data Set 81, 10.2 kHz.

Figure A-11. (Continued).

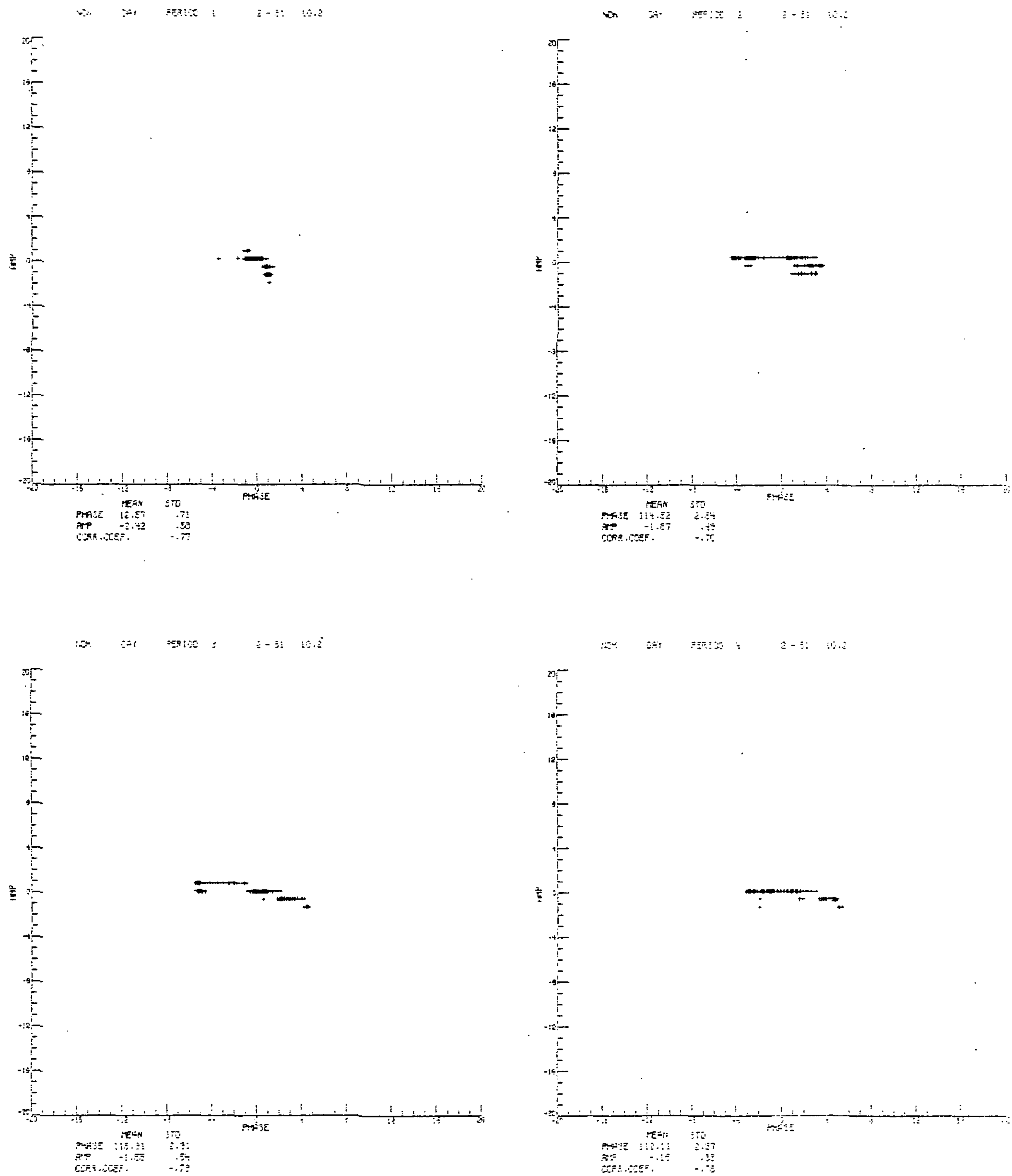

(d) N. Dakota Daytime, Data Set 81, 10.2 kHz.

Figure A-11. (Continued).

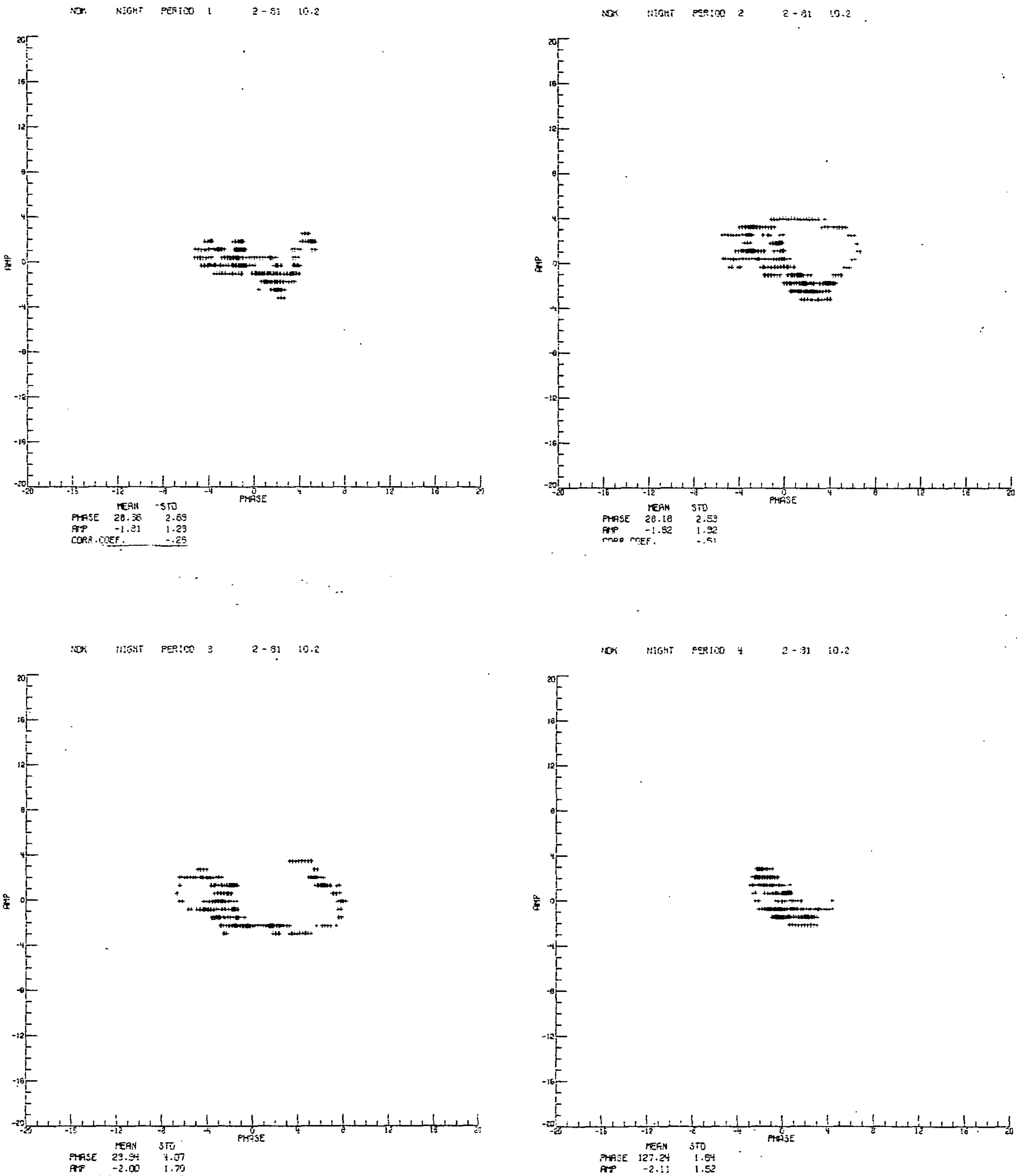

(e) N. Dakota Nighttime, Data Set 81, 10.2 kHz.

Figure A-11. (Continued).

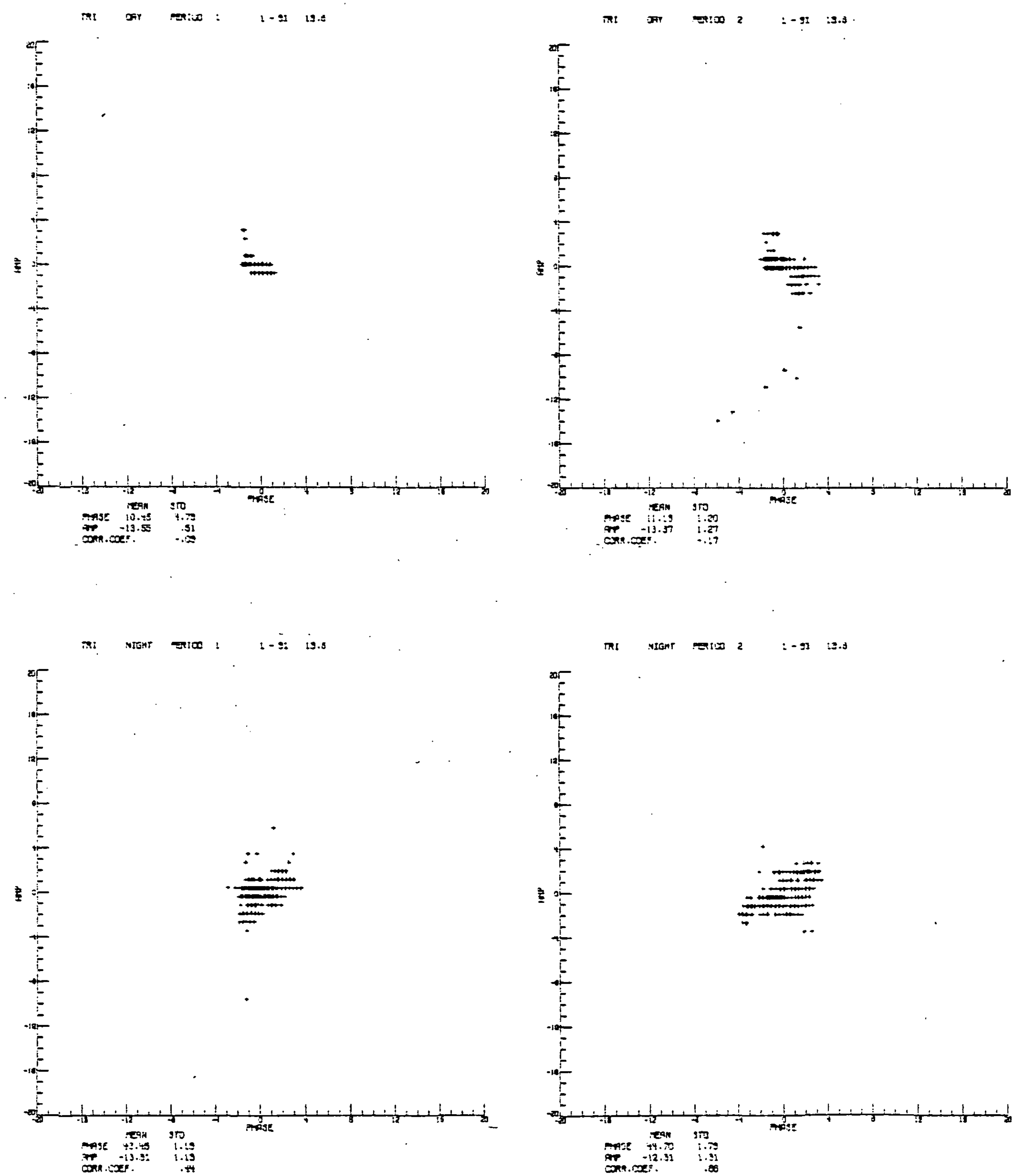

(a) Trinidad, Data Set 91, 13.6 kHz.

Figure A-12. Input Signal Strength (dB) Relative to Mean vs. Measured Phase in cec with Drift Removed (Base Receiver).

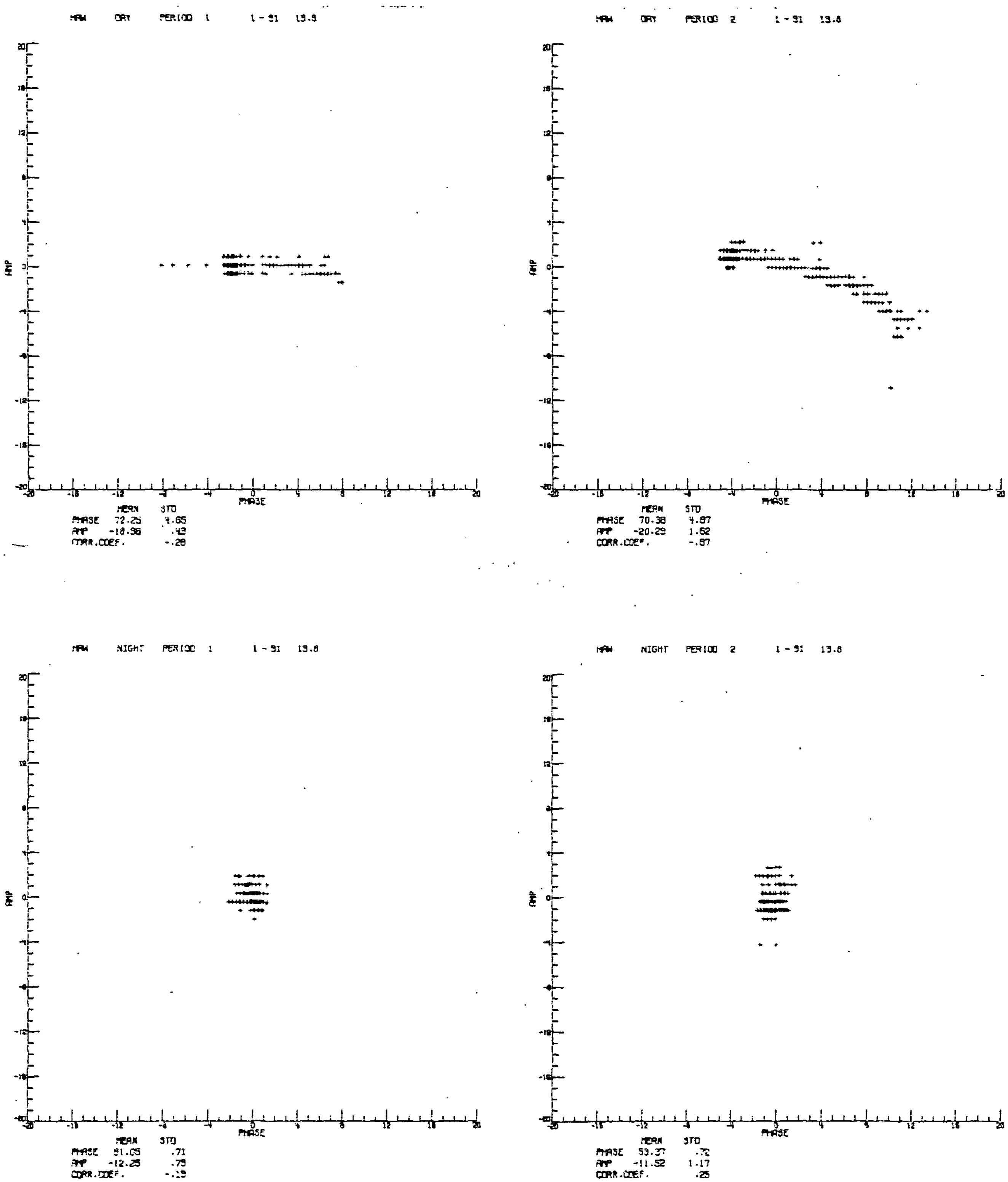

(b) Hawaii, Data Set 91, 13.6 kHz.

Figure A-12. (Continued).

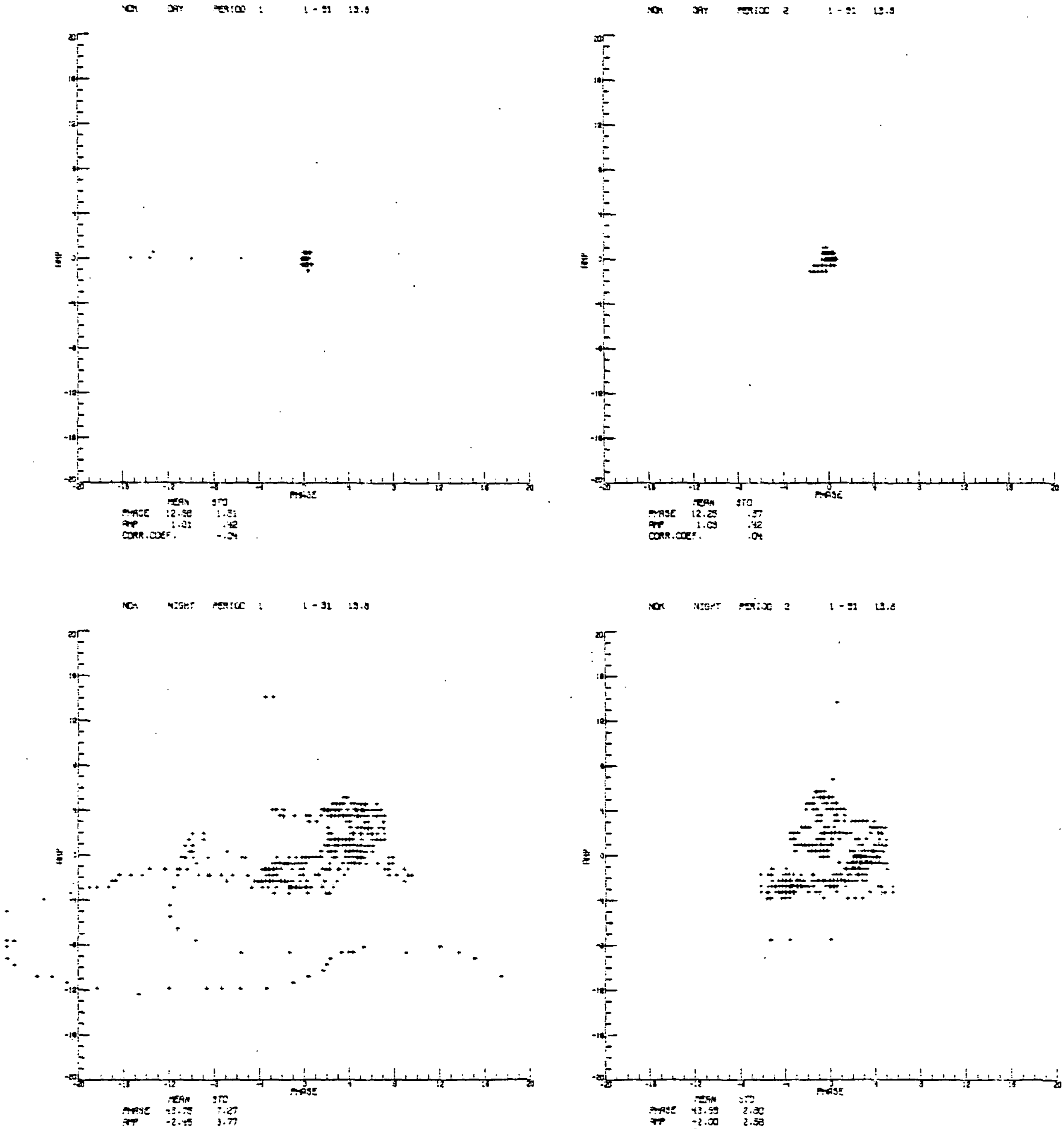

(c) N. Dakota, Data Set 91, 13.6 kHz.

Figure A-12. (Continued).

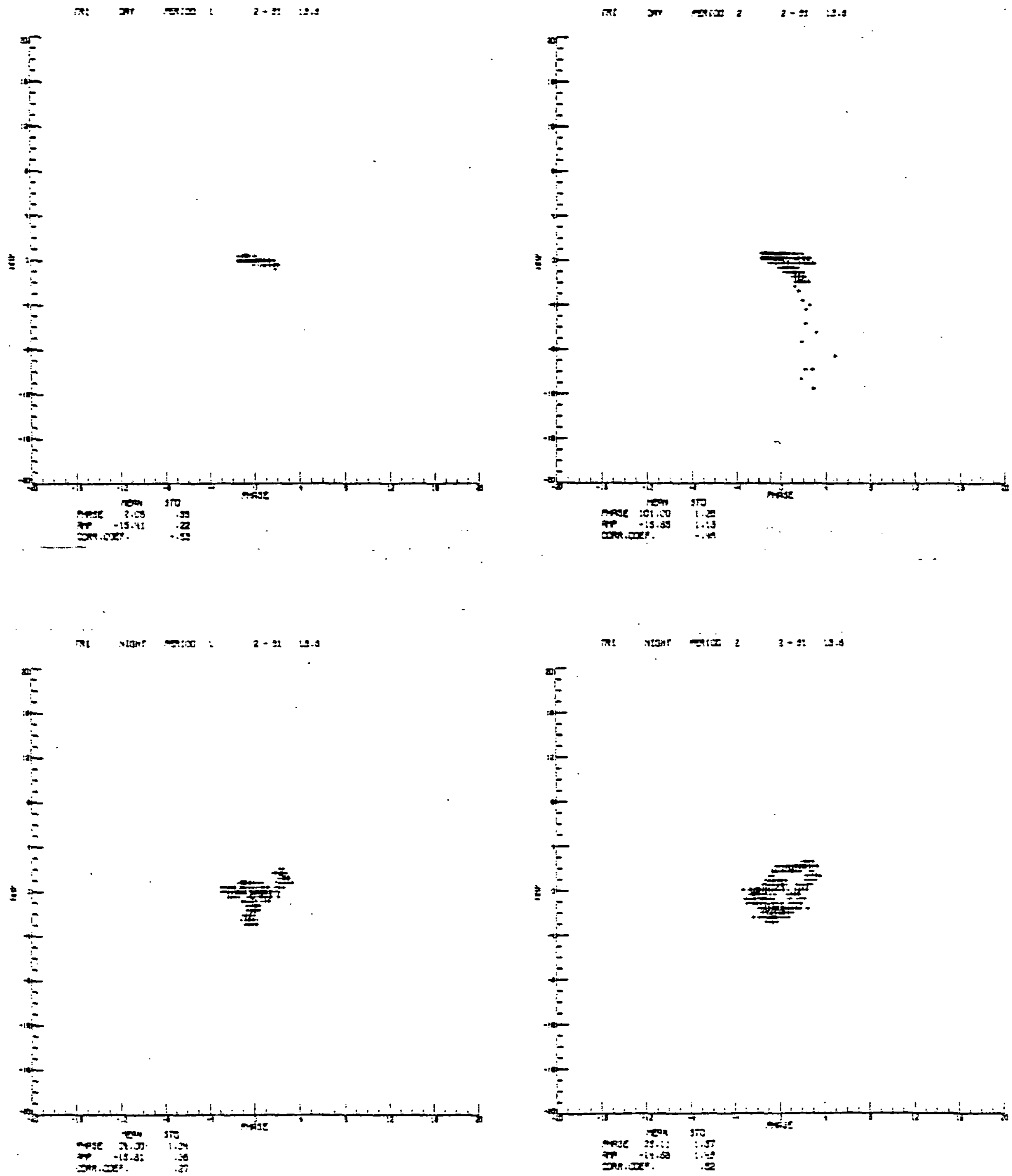

(a) Trinidad, Data Set 91, 13.6 kHz.

Figure A-13. Input Signal Strength (dB) Relative to Mean vs. Measured Phase in cec with Drift Removed (Mobile Receiver).

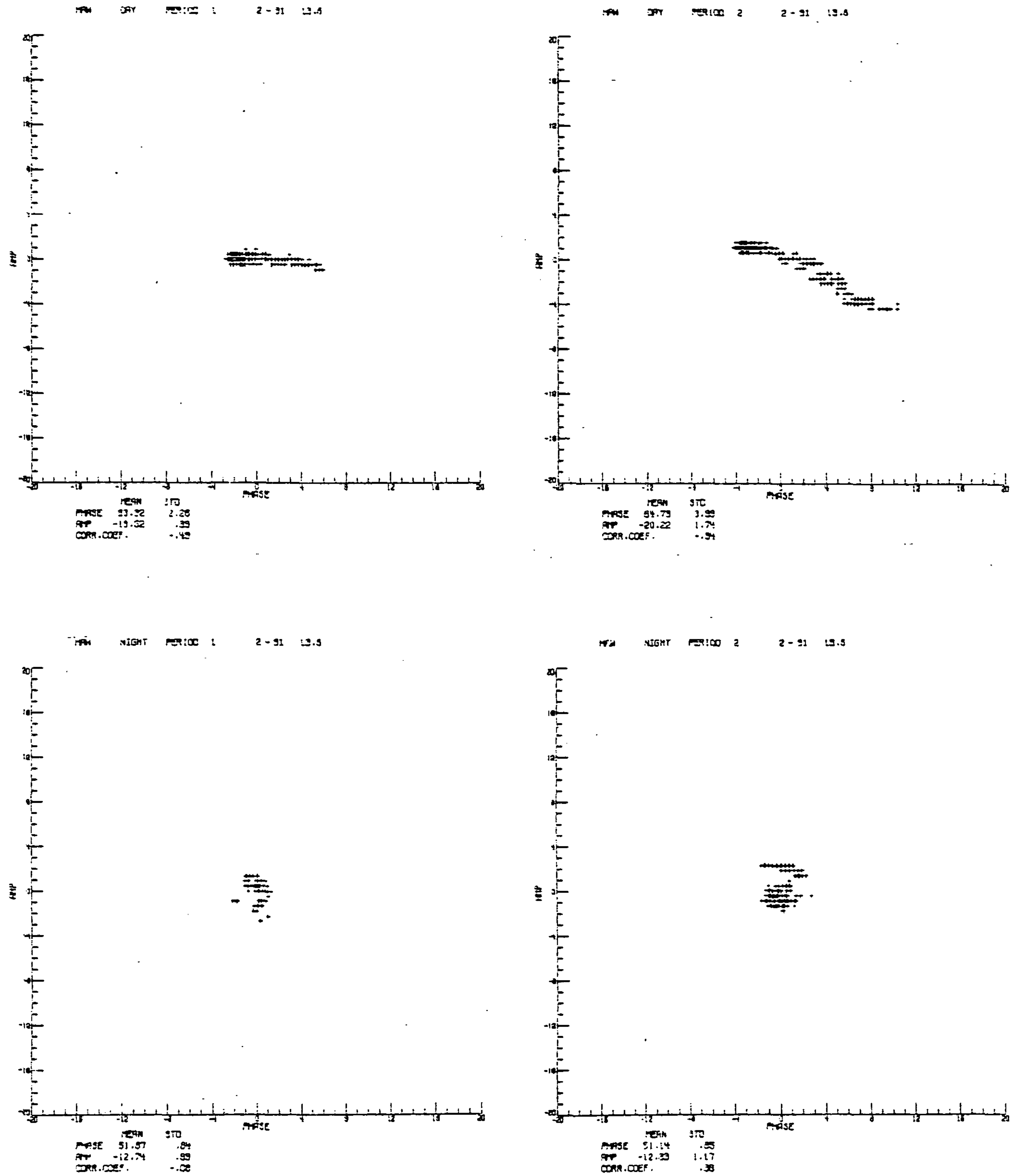

(b) Hawaii, Data Set 91, 13.6 kHz.

Figure A-13. (Continued).

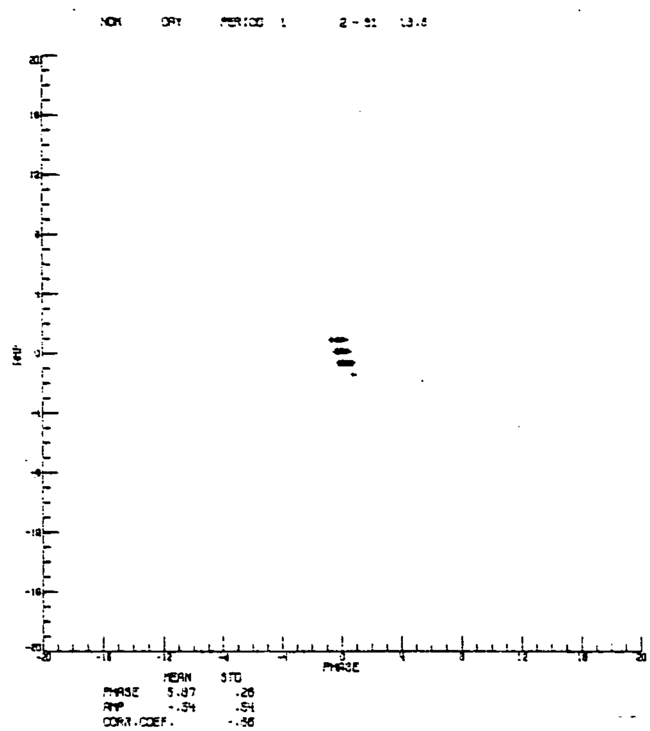

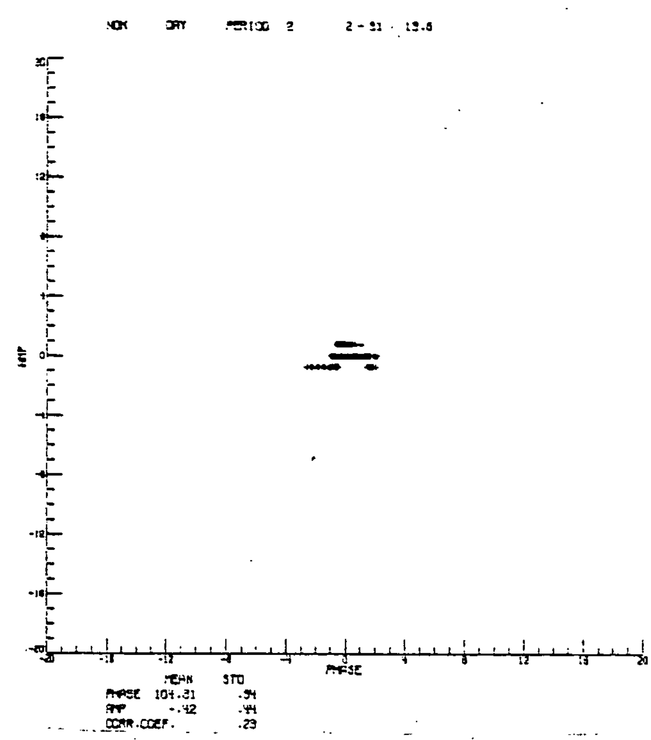

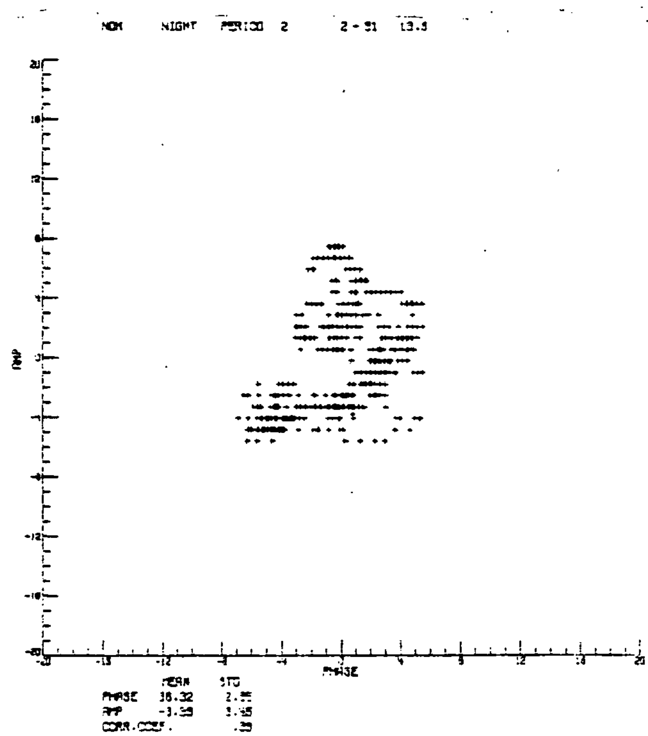

(c) N. Dakota, Data Set 91, 13.6 kHz.

Figure A-13. (Continued).

"Page missing from available version"

APPENDIX B

DEFINITION OF DAYLIGHT-TRANSITION-NIGHTTIME PERIODS

For purposes of the data analysis each 24 hour day has been divided into four time periods as described in this discussion. The four periods are designated as follows:

DESIGNATOR	PERIOD
1	Sunrise Transition
2	Daylight
3	Sunset Transition
4	Nighttime

Generally, these time periods are defined in terms of sunrise and sunset times at the two transmitters in a given station pair and the two receivers for which differential OMEGA analysis is being made (ref. 22). Considering these four positions the "sunrise transition period" is the time between the earliest and latest sunrise, i.e., the time between the full darkness situation and full daylight situation. The "sunset transition period" is correspondingly the time between the earliest and latest sunset. "Daylight" and "Nighttime" are when the four positions are in either simultaneous daylight or darkness respectively.

These periods are defined for analysis based on calculated sunrise and sunset times at each receiver and transmitter site. For each 24 hour day of data, four times (GMT) are used to define these periods: SRT, start of sunrise transition; DAY, start of daytime; SST, start of sunset transition; and NIT, start of nighttime. These times are tabulated in Table B-1 for each period for which data were taken (a data period is normally seven days or less). Using this tabulation of values a descriptive variable is defined for each hour in the 24 hour day for each day in the data period according to which of the daylight condition time periods the hour is to be included in. This variable DTIM has a value (1, 2, 3, or 4) for each hour in the data. This variable is assigned for each data hour (DAHR) as follows:

if $SRT \leq DAHR < DAY$, then $DTIM = 1$

$DAY \leq DAHR < SST$, then $DTIM = 2$

$SST \leq DAHR < NIT$, then $DTIM = 3$

otherwise $DTIM = 4$

It should be noted that several anomolous situations arise. In some cases either DAY=SST or NIT=SRT meaning that there is either no full daylight or full nighttime for that particular period. In the extreme there are occasions where the latest sunset occurs after the earliest sunrise (e.g., Norway - Hawaii at some times of the year). Here SRT and NIT have been set equal to the average of the two times. Similarly it is possible to have the earliest sunset before the latest sunrise so that it is necessary to set DAY=SST using the average of the two originally calculated values. There are no situations where the transition periods are nulled.

TABLE B-1

DAYTIME PERIOD TIMES (HOUR-GMT)

1 - Start of Sunrise Transition
2 - Start of Full Daylight
3 - Start of Sunset Transition
4 - Start of Nighttime

TAPE #	LOCATION	NOR-TRI				NOR-HAW				NOR-NDK				TRI-HAW				TRI-NDK				HAW-NDK			
	RCVR1/RCVR2	1	2	3	4	1	2	3	4	1	2	3	4	1	2	3	4	1	2	3	4	1	2	3	4
30-29	LRC/AHO	05	12	17	00	05	17	17	05	05	13	17	01	10	17	22	05	10	13	22	01	11	17	23	05
31-30	LRC/AHO	05	12	17	00	05	17	17	05	05	13	17	01	10	17	22	05	10	13	22	01	11	17	23	05
31	LRC/LRC	05	12	16	00	05	17	17	05	05	13	16	01	10	17	22	05	10	13	22	01	11	17	23	05
32	LRC/PGO	05	12	16	00	05	16	16	05	05	14	16	01	10	17	22	05	10	14	22	01	11	17	23	05
35	LRC/YKT	07	12	15	23	07	16	16	05	07	14	15	00	10	17	22	05	10	14	22	00	12	17	22	05
36	LRC/PGO	07	12	15	23	07	16	16	05	07	14	15	00	10	17	22	05	10	14	22	00	12	17	22	05
37	LRC/PGO	07	13	14	23	07	16	16	05	07	14	14	00	10	18	22	05	10	14	22	00	12	18	22	05
38	LRC/PGO	08	13	14	23	08	16	16	05	08	14	14	00	10	18	22	05	10	15	22	00	12	18	22	05
39	LRC/BDF	08	13	14	23	08	16	16	05	08	14	14	00	10	18	22	05	10	15	22	00	12	18	22	05
40	LRC/BDF	09	13	13	23	09	15	15	05	09	14	14	00	10	18	22	05	10	15	22	00	12	18	22	05
41	LRC/LRC	09	13	13	23	09	15	15	05	09	14	14	00	10	18	22	05	10	15	22	00	12	18	22	05
42	LRC/FEU	09	12	12	22	09	15	15	04	09	13	13	23	10	18	21	04	10	15	21	23	12	18	22	04
43	LRC/FIS	10	12	12	22	10	15	15	04	10	13	13	23	10	18	21	04	10	15	21	23	12	18	21	04
44	LRC/FIS	10	12	12	22	10	15	15	04	10	13	13	23	10	18	21	04	10	15	21	23	12	18	21	04
45	LRC/WAL	09	12	12	22	09	15	15	04	09	13	13	23	10	17	21	04	10	15	21	23	12	17	21	04
48	LRC/LRC	07	12	13	22	07	15	15	04	07	14	14	23	10	17	21	04	10	14	21	23	11	17	22	04
49	LRC/BOD	07	12	14	22	07	15	15	04	07	14	14	00	10	17	21	04	10	14	21	00	11	17	22	04
50	LRC/RTI	06	12	14	23	06	16	16	04	06	14	14	00	10	17	21	04	10	14	21	00	11	17	22	04
51	LRC/AHO	06	12	15	23	06	16	16	04	06	13	15	00	10	17	21	04	10	13	21	00	11	17	22	04
52	LRC/LRC	06	12	15	23	06	16	16	04	06	13	15	00	10	17	21	04	10	13	21	00	11	17	22	04
53	LRC/BDF	05	12	16	23	05	16	16	04	05	13	16	00	10	16	22	04	10	13	22	00	11	16	22	04

TABLE B-1. Continued.

TAPE #	LOCATION	NOR-TRI				NOR-HAW				NOR-NDK				TRI-HAW				TRI-NDK				HAW-NDK			
	RCVR1/RCVR2	1	2	3	4	1	2	3	4	1	2	3	4	1	2	3	4	1	2	3	4	1	2	3	4
54	LRC/PGO	05	12	16	23	05	16	16	05	05	13	16	01	10	17	21	05	10	13	21	01	11	17	22	05
55	LRC/YKT	04	11	16	23	05	17	17	05	04	13	17	01	10	17	22	05	10	13	22	01	11	17	23	05
56	LRC/LRC	04	11	17	00	04	17	17	04	04	13	17	01	10	17	22	05	10	13	22	01	10	17	23	05
57	LRC/FEU	04	11	17	00	04	17	17	04	04	13	17	01	10	17	22	05	10	13	22	01	10	17	23	05
58	LRC/THV	03	11	18	00	04	17	18	04	03	12	18	02	09	17	22	05	09	12	22	02	10	17	23	05
59	LRC/LRC	03	11	18	00	04	17	18	04	03	12	18	02	10	17	22	05	10	12	22	02	10	17	23	05
60	LRC/FIS	02	11	19	00	04	17	19	04	02	12	19	02	09	17	22	05	09	12	22	02	10	17	23	05
61	LRC/WAL	02	11	19	00	04	17	19	04	02	12	19	02	09	17	22	05	09	12	22	02	10	17	23	05
62	LRC/NCC	02	11	20	01	04	17	20	04	02	12	20	02	09	17	22	05	09	12	22	02	10	17	00	05
65	LRC/RTI	00	10	21	00	02	16	21	02	01	11	21	01	09	16	22	05	09	11	22	03	09	16	00	05
66	LRC/BOD	00	10	22	00	02	16	22	02	00	11	22	00	09	16	22	05	09	11	22	01	09	16	00	05
67	LRC/AHO	00	10	22	00	02	16	22	02	01	11	22	01	09	16	22	05	09	11	22	03	09	16	00	05
68	LRC/LRC	00	10	22	00	02	16	22	02	01	11	22	01	09	16	22	05	09	11	22	03	09	16	00	05
69	LRC/YKT	00	10	21	00	02	16	21	02	01	11	21	01	09	16	22	05	09	11	22	03	09	16	00	05
70	LRC/PGO	00	10	21	00	02	16	21	02	01	11	21	01	09	16	22	05	09	11	22	03	09	16	00	05
71	LRC/RMT	01	11	20	01	03	16	20	03	01	11	20	01	09	16	22	05	09	11	22	02	10	16	00	05
72	LRC/BDF	02	11	19	01	03	16	19	03	02	12	19	02	09	16	22	05	09	12	22	02	10	16	00	05
73	LRC/LRC	04	11	18	00	04	16	18	04	04	12	18	01	10	16	22	04	10	12	22	01	10	16	23	04
74	LRC/WAL	04	11	18	00	04	17	18	04	04	12	18	01	10	17	22	04	10	12	22	01	10	17	23	04
75	LRC/NCC	05	11	17	00	05	17	17	05	05	13	17	01	10	17	22	05	10	13	22	01	10	17	23	05
76	LRC/THV	05	12	17	00	05	17	17	05	05	13	17	01	10	17	22	05	10	13	22	01	11	17	23	05
77	LRC/FEU	05	12	17	00	05	17	17	05	05	13	17	01	10	17	22	05	10	13	22	01	11	17	23	05
78	LRC/BOD	06	12	17	23	06	17	17	05	06	13	17	01	10	17	22	05	10	13	22	01	11	17	23	05
79	LRC/RTI	06	12	16	23	06	16	16	05	06	14	16	01	10	17	22	05	10	14	22	01	11	17	23	05
80	LRC/RMT	06	12	15	00	06	16	16	05	06	14	15	00	10	17	22	05	10	14	22	00	11	17	23	05

TABLE B-1. Continued.

TAPE #	LOCATION	NOR-TRI				NOR-HAW				NOR-NDK				TRI-HAW				TRI-NDK				HAW-NDK			
	RCVR1/RCVR2	1	2	3	4	1	2	3	4	1	2	3	4	1	2	3	4	1	2	3	4	1	2	3	4
81	LRC/LRC	09	13	13	23	09	15	15	05	09	14	14	00	10	17	22	05	10	15	22	00	12	17	22	05
82	LRC/RTI	10	13	13	23	10	15	15	04	10	14	14	23	10	18	22	04	10	15	22	23	12	18	22	04
83	LRC/RTI	10	12	12	22	10	15	15	04	10	13	13	23	10	17	22	04	10	15	22	23	12	17	22	04
84	LRC/RTI	09	12	12	22	09	15	15	04	09	13	13	23	10	17	22	04	10	14	22	23	12	17	22	04
85	LRC/RTI	08	12	13	22	08	15	15	04	08	13	13	23	10	17	22	04	10	14	22	23	12	17	22	04
86	LRC/LRC	07	12	14	22	07	15	15	04	07	13	14	00	10	17	22	04	10	13	22	23	11	17	22	04
87	LRC/NCC	06	11	15	23	06	16	16	04	06	13	15	00	10	17	22	04	10	13	22	00	11	17	22	04
88	LRC/BOD	05	11	16	23	05	16	16	04	05	13	16	00	10	16	22	04	10	13	22	00	11	16	23	04
89	LRC/BOD	05	11	17	23	05	16	17	04	05	12	17	00	10	16	22	04	10	12	22	00	11	16	23	04
90	LRC/WAL	04	11	17	23	04	16	17	04	04	12	17	01	10	16	22	05	10	12	22	01	11	16	23	05
91	LRC/LRC	04	11	18	23	04	16	18	04	04	12	18	01	10	16	22	05	10	12	22	01	11	16	23	05
92	LRC/BDF	03	11	18	00	04	16	18	04	03	12	18	01	10	16	22	05	10	12	22	01	10	16	23	05
93	LRC/RHT	03	11	19	00	04	16	19	04	03	11	19	02	10	16	22	05	10	11	22	02	10	16	00	05
94	LRC/THV	02	10	20	00	03	16	20	03	02	11	20	02	10	16	22	05	10	11	22	02	10	16	00	05
95	LRC/LRC	01	10	21	00	03	16	21	03	02	11	21	02	10	16	22	05	10	11	22	02	10	16	00	05
96	LRC/AHO	01	10	21	00	03	16	21	03	02	11	21	02	10	16	22	05	10	11	22	02	10	16	00	05
97	LRC/RTI	01	10	21	00	03	16	21	03	01	11	21	01	10	16	22	05	10	11	22	02	10	16	00	05
98	LRC/PGO	00	10	22	00	03	16	22	03	01	11	22	01	10	16	22	05	10	11	22	02	10	16	00	05
99	LRC/REU	00	10	22	00	03	16	22	03	01	11	22	01	10	16	22	05	10	11	22	02	10	16	00	05
100	LRC/YKT	00	10	22	00	03	16	22	03	01	11	22	01	10	16	22	05	10	11	22	02	10	16	00	05
101	LRC/FIS	00	10	22	00	03	16	22	03	01	11	22	01	10	16	22	05	10	11	22	02	10	16	00	05
102	LRC/LRC	00	10	22	00	03	16	22	03	01	11	22	01	10	16	22	05	10	11	22	02	10	16	00	05
103	LRC/LRC	01	10	20	00	03	16	20	03	01	11	20	01	10	16	22	05	10	11	22	02	10	16	00	05
104A	LRC/FOU	02	10	20	00	03	16	20	03	02	11	20	02	10	16	22	05	10	11	22	02	10	16	00	05
104B	LRC/CHA	02	11	20	00	03	16	20	03	02	11	20	02	10	16	22	05	10	11	22	02	10	16	00	05

TABLE B-1. Continued.

TAPE #	LOCATION	NOR-TRI				NOR-HAW				NOR-NDK				TRI-HAW				TRI-NDK				HAW-NDK			
	RCVR1/RCVR2	1	2	3	4	1	2	3	4	1	2	3	4	1	2	3	4	1	2	3	4	1	2	3	4
104C	LRC/WAN	02	11	20	00	03	16	20	03	02	11	20	02	10	16	22	05	10	11	22	02	10	16	00	05
104D	LRC/MID	02	11	19	00	03	16	19	03	02	12	19	02	10	16	22	05	10	12	22	02	10	16	00	05
105A	LRC/BLC	02	11	19	00	03	16	19	03	02	12	19	02	10	16	22	05	10	12	22	02	10	16	00	05
105B	LRC/WEE	02	11	19	00	03	16	19	03	02	12	19	02	10	16	22	05	10	12	22	02	10	16	00	05
106	LRC/LRC	10	12	12	22	10	15	15	04	10	14	14	23	10	17	22	04	10	15	22	23	12	17	22	04

APPENDIX C

DIFFERENTIAL CHART VALUES

Table C-1. Calculated Differential LOP Chart Values (Values in cec at Frequency Shown)

Differential Pair	NOR-TRI A-B			NOR-NDK A-D			TRI-NDK B-D		
	10.2	13.6	11.3	10.2	13.6	11.3	10.2	13.6	11.3
LRC-YKT	78.11	4.16	86.79	77.66	70.21	75.17	99.55	66.05	88.38
LRC-FEU	36.45	48.61	40.51	18.40	91.21	9.33	81.95	42.59	68.83
LRC-FIS	94.02	92.03	93.35	60.15	13.54	77.95	66.14	21.51	84.59
LRC-AHO	89.88	19.85	33.20	72.45	63.27	36.05	82.57	43.42	2.85
LRC-WAL	43.85	25.14	4.28	48.81	98.42	98.68	4.97	73.28	94.40
LRC-RTI	84.42	45.90	4.91	41.59	88.79	23.98	57.17	42.89	19.07
LRC-PGO	63.65	84.87	70.73	88.38	84.51	53.75	24.73	99.63	83.03
LRC-BDF	34.11	45.48	71.23	43.90	58.53	15.44	9.79	13.04	44.20
LRC-NCC	81.46	41.95	1.62	7.01	9.35	7.78	25.55	67.40	6.16
LRC-THV	10.61	47.48	89.56	48.79	65.05	54.21	38.18	17.57	64.64
LRC-BIS	66.07	88.11	73.42	86.58	48.78	7.31	20.51	60.67	33.89
LRC-RMT	37.52	16.70	30.58	12.55	83.40	36.16	75.03	66.70	5.58
LRC-FOU	18.41	24.55	20.46	88.14	84.18	20.15	69.72	59.63	99.69
LRC-CHA	81.96	9.27	91.06	45.06	60.08	16.73	63.10	50.80	25.67
LRC-WAN	82.35	43.13	2.61	92.01	56.01	13.34	9.66	12.88	10.73
LRC-MI	80.84	41.12	34.26	87.13	49.51	41.26	6.30	8.40	7.00
LRC-BLC	85.10	13.47	27.89	46.96	62.61	85.51	61.86	49.14	57.62
LRC-WEE	94.86	59.81	49.84	57.93	77.24	64.37	63.07	17.43	14.52

	NOR-HAW A-C			TRI-HAW B-C			HAW-NDK C-D		
	10.2	13.6	11.3	10.2	13.6	11.3	10.2	13.6	11.3
LRC-YKT	89.62	86.16	88.47	11.5	82.01	1.68	88.03	84.04	86.7
LRC-FEU	14.19	85.59	4.66	77.74	36.99	64.16	4.2	5.6	4.67
LRC-FIS	80.15	40.69	0.58	86.5	48.67	7.22	79.63	72.84	77.37
LRC-AHO	19.61	59.49	66.25	29.73	39.65	33.04	52.83	3.77	69.81
LRC-WAL	1.73	2.31	68.80	57.89	77.55	64.32	47.07	96.1	30.08
LRC-RTI	4.0	38.68	48.90	19.59	92.79	43.99	37.57	50.1	75.08
LRC-PGO	56.7	42.27	18.56	93.05	57.41	47.84	31.67	42.22	35.19
LRC-BDF	34.65	12.87	94.06	0.54	67.39	22.83	9.24	45.65	21.38
LRC-NCC	5.04	73.39	27.83	23.58	31.45	26.21	1.96	35.94	79.95
LRC-THV	48.11	30.81	75.68	37.50	83.34	86.12	0.67	34.23	78.53
LRC-BIS	49.95	66.6	55.5	83.87	78.5	82.09	36.62	82.17	51.8
LRC-RMT	16.13	21.51	51.26	78.61	4.82	20.68	96.44	61.88	84.90
LRC-FOU	2.23	2.98	2.48	83.82	78.43	82.02	85.90	81.20	17.67
LRC-CHA	30.05	40.06	33.38	48.09	30.79	42.32	15.01	20.01	83.35
LRC-WAN	16.46	55.29	29.40	34.11	12.15	26.79	75.54	.72	83.94
LRC-MI	83.54	78.05	81.71	2.70	36.93	47.44	3.60	71.46	59.55
LRC-BLC	21.91	29.21	57.68	36.81	15.74	29.79	25.05	33.40	27.83
LRC-WEE	60.47	13.97	11.64	65.62	54.15	61.79	97.46	63.28	52.73

"Page missing from available version"

APPENDIX D

ESTIMATED AZIMUTH OF LOPS AT HAMPTON (LRC)

Consider the hyperbola defined by $x^2 - y^2 = a^2$. The slope at point (x_1, y_1) is defined taking the derivative

$$2xdx - 2ydy = 0$$

$$\frac{dy}{dx} = \frac{x}{y} \quad (x_1, y_1) \; .$$

Illustrated graphically as in Figure D-1 this slope can be found using the bisector of the angle between lines drawn from the point of interest to the respective foci.

This provides a method of estimating the slope of the LOPs at any point. The azimuth from LRC to each transmitter of a given pair is calculated using the CHART program (ref. 1). The mean of these two values is used to get the slope of the LOP at LRC.

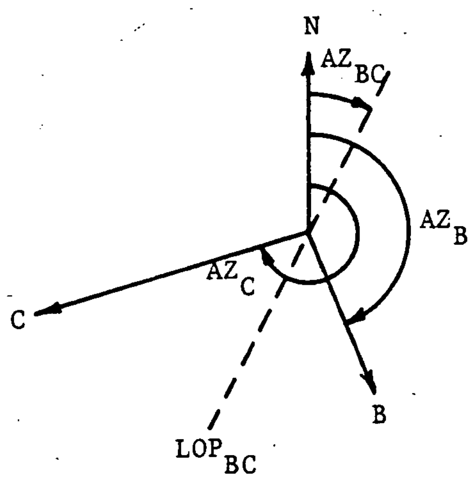

$$AZ_{BC} = \frac{AZ_C + AZ_B}{2} - 180^\circ$$ estimates slope of BC LOP at LRC.

The following table provides a tabulation of these slope azimuths.

	A	B	C	D
South AZ	208.79°	329.40°	102.78°	126.46°
N AZ From LRC	28.73°	149.40°	282.78°	306.46°

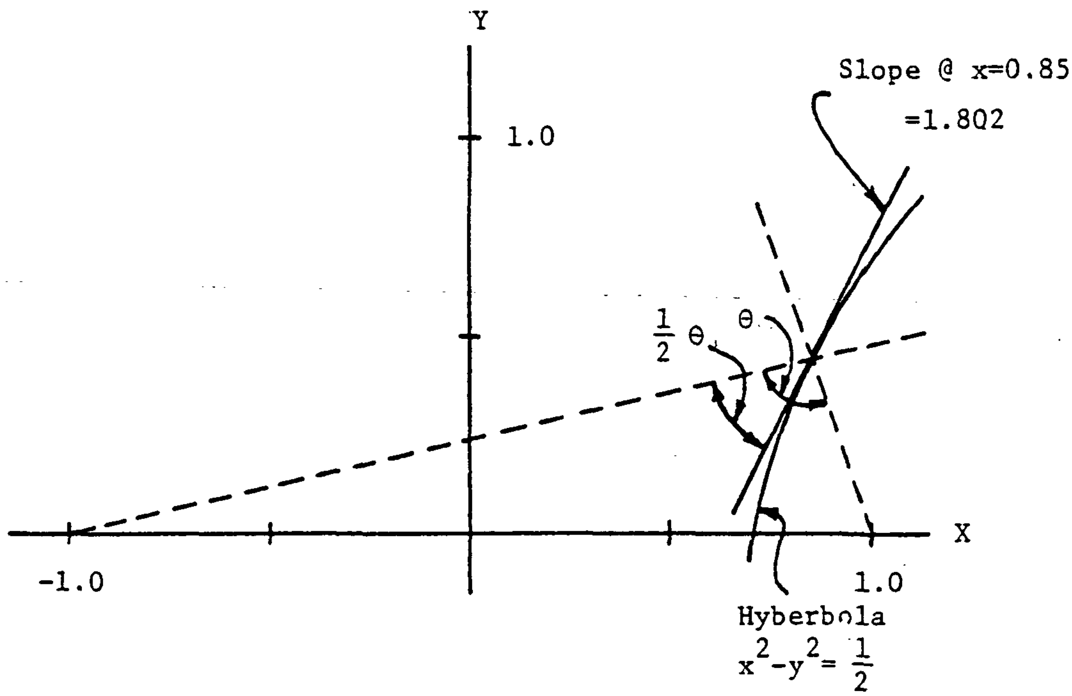

Figure D-1. Illustration of Hyperbola Slope at a Point.

Table D-1 summarizes slopes of the six LOPs at Hampton, Virginia (LRC) involving station A, B(TRI), C, and D.

TABLE D-1 LOP SLOPES AT LRC

LOP	SLOPE @ LRC (AZ)
A-B	89.07°
A-C	155.76
A-D	167.70
B-C	36.09°
B-D	47.93°
C-D	114.62°

"Page missing from available version"

PAGES 192, 193 &
194

REFERENCES

REFERENCES

1. Baxa, E. G., Jr.: "Implementation of an Experimental Program to Investigate the Performance Characteristics of OMEGA Navigation." Research Triangle Institute Final Report prepared under Contract NAS1-12043 for NASA Langley Research Center, CR-132516, September, 1974.

2. Baxa, E. G., Jr.: "Investigation of New Techniques for Aircraft Navigation Using the OMEGA Navigation System." Research Triangle Institute Final Report prepared under Contract NAS1-14005 for NASA Langley Research Center, February, 1978.

3. Baxa, E. G., Jr. and Piserchia, P. V.: "Recent Results on Parametric Analysis of Differential OMEGA Error." Journal of the Institute of Navigation, Vol. 22, No. 4, Winter 1975-76, pp. 309-323.

4. Baxa, E. G., Jr. and Lytle, C. D.: "On Observations of Modal Interference of the North Dakota OMEGA Transmission." Journal of the Institute of Navigation, Vol. 22, No. 4, Winter 1975-76, pp. 309-323.

5. Wright, J. R.: "Results of Differential OMEGA Test and Evaluation Program." A68-36444, Frequency, July, 1968.

6. Luken, K. et al.: "Accuracy Studies of the Differential OMEGA Techniques." AD 709 555, Naval Research Laboratory, Report 7102, June 29, 1970. AD-709 555.

7. Ruth, R. L. et al.: "Differential OMEGA Monitoring and Analysis." Vol. 1: AD 756 024, Vol. 2: AD 756 025, Vol. 3: AD 756 026. Beukers Labs, Inc. Final Report, Contract No. DOT-CG-22165-A, May 9, 1972.

8. Swanson, E. R.; Adrian, D. J.; Levine, P. H.: "Differential OMEGA Navigation for the U. S. Coastal Confluence Region." Part I: Overview and Part II: Requirements, Accuracies, and System Definition, Naval Electronics Laboratory Center, Technical Rpt. 1905 (Part I and II) January 2, 1974.

9. Vence, R. L.: "Implementation and Testing of a Proposed Differential OMEGA System." AD-745 878 Engineering Thesis, Naval Postgraduate School, Monterey, California, June, 1972.

10. Wait, J. R.: "Electromagnetic Waves in Stratified Media," Pergamon Press, 1970.

11. Galejs, J.: "Terrestrial Propagation of Long Electromagnetic Waves." Pagamon Press, 1972.

12. Budden, K. G.: "Radio Waves in the Ionosphere." Cambridge University Press, 1961.

13. Gossard, E. et al.: "A Computer Program for VLF Mode Constants in an Earth-Ionosphere Wave Guide of Arbitrary Electron Density Distribution." AD-800 856, U. S. Navy Electronics Laboratory Interim Report No. 671, September 1, 1966.

14. Morfitt, D. G.; Halley, R. F.: "Comparison of Waveguide and Wave Hop Techniques for VLF Propagation Modeling." Naval Weapons Center Technical Publication 4952, August, 1970.

15. Baltzer, O. J.: "Use of Composite OMEGA in Aircraft Applications." Proceedings of the First OMEGA Symposium, November, 1971, pp. 99-105.

16. Pierce, J. A.: "The Use of Composite Signals at Very Low Radio Frequencies." AD-666 567, Harvard University TR552, February, 1968.

17. Pierce, J. A.: "Lane Identification in OMEGA," AD-746 503, Harvard University TR 627, July, 1972.

18. Pierce, J. A.: "OMEGA: Facts, Hopes, and Dreams." AD-782 396, Technical Report No. 562, Engineering and Applied Physics, Harvard University, June, 1974.

19. Morris, P. B. et al.: "OMEGA Propagation Corrections: Background and Computational Algorithm." AD-A008 424 OMEGA Navigation System Operations Detail Rpt. No. ONSOD-01-74, December, 1974.

20. Morfitt, D. G.: "Computer Techniques for Fitting Electron Density Profiles to Oblique-Path VLF Propagation Data." AD-757 341, NELC Technical Report TR 1854, January 16, 1973.

21. Deeks, D. G.: "D-Region Electron Distribution in Middle Latitudes Deduced from the Reflexion of Long Radio Waves." Proc. Roy. Soc. 291 (1426), pp. 413-427, 1966.

22. Baxa, E.G., Jr.: "Investigation Into the Propagation of OMEGA Very Low Frequency Signals and Techniques for Improvement of Navigation Accuracy Including Differential and Composite OMEGA." Research Triangle Institute Final Report prepared under Contract NAS1-11298 for NASA Langley Research Center, CR-132276, February, 1973.